Investigations into the vortex lattice of Ni-chalcogenide and Fe-arsenide superconductors, using small-angle neutron scattering

by **Erik Jellyman**

UNIVERSITY OF BIRMINGHAM

A thesis submitted to
The University of Birmingham
for the degree of
DOCTOR OF PHILOSOPHY

Condensed Matter Group
School of Physics and Astronomy
University of Birmingham
Birmingham
B15 2TT
August 2018

exj001@bham.ac.uk

Abstract

This work summarises investigations into the superconductivity in 122-structure, *I4/mmm* symmetry materials; the heavy-fermion $TlNi_2Se_2$, and the iron-arsenides $(Ba_{0.5}K_{0.5})Fe_2As_2$ and KFe_2As_2. Small-angle neutron scattering (SANS) was used to study the vortex lattice (VL) of single crystal samples of these superconductors under temperature, field and angle modulation. We observe a linear response of the form factor to temperature variation for $TlNi_2Se_2$ and KFe_2As_2, concurrent with nodal and unconventional superconductivity. Weak VL anisotropy and no VL morphology were observed in $TlNi_2Se_2$ and $(Ba_{0.5}K_{0.5})Fe_2As_2$ respectively, whereas KFe_2As_2 experiences strong VL anisotropy. Observations of $(Ba_{0.5}K_{0.5})Fe_2As_2$ confirm Pauli paramagnetic effects (PPE) above $0.1H_{c_2}$. PPE are seen near T_c for KFe_2As_2, but not for $TlNi_2Se_2$. Literature review regarding the Fermi surface and electron bands confirms van Hove singularities (vHs) near the Fermi level (E_F) for all three materials. This provides some explanation of the variation in pairing symmetry for similarly structured superconductors. The tuning of the vHs with respect to E_F determines the symmetry of the gap function as well as the effective mass of the electrons for $TlNi_2Se_2$, $(Ba_{1-x}K_x)Fe_2As_2$ and KFe_2As_2.

ACKNOWLEDGEMENTS

First, I would like to acknowledge my supervisor Elizabeth Blackburn for the guidance and opportunities for more than three years of postgraduate research and three years of undergraduate study. Elizabeth has been invaluable to my success as a physicist. Elizabeth has been encouraging and honest with feedback, as well as compassionate during a low point in my mental health. On top of all that I have been able to travel extensively on experiments and conferences, occasionally with some complex funding applications, due to the extensive research opportunities provided by Elizabeth and this field. I wish her all the best at her new position in Lund and very much look forward to working with her again in the future.

I would like to acknowledge the Condensed Matter Group, particularly Ted Forgan for his work ethic and diligence on experiments. I don't think I will work with anyone more knowledgeable of experimental condensed matter physics or have more enthusiasm for experimentation. I would like to acknowledge Randeep Riyat for many lifts and interesting conversations at conferences and schools, Lingjia Shen for his dry sense of humour on long experiments and Emma Campillo for her company and conversation in a very empty office.

I would also like to acknowledge the many instrument scientists and collaborators I have met and worked with. Specifically, I acknowledge Bob Cubitt for his patience and good humour with a clumsy new PhD researcher. I acknowledge Jorge Gavilano for his perseverance and assistance in the face of dilution problems and a very shy neutron beam. I would also like to acknowledge Hazuki Kawano-Furukawa for her consistent cheery disposition on difficult experiments and bringing many tasty Japanese snacks to keep us going.

I would like to acknowledge the tremendous efforts of Stephen Pollard and Philippa Jefferies for being talented and enthusiastic undergraduates who helped a great deal on experimentation and analysis and covering some of the late shifts at

the ILL. I would like to acknowledge Minoru Soda for taking the lead on the initial EXED/HFM analysis due to my non-existent Python© coding skills.

I would very much like to acknowledge Ian Stevens, welfare tutor. His patience and knowledge of the welfare and counseling systems and the university helped me navigate through a difficult period of my academic life. His positive attitude and follow-up meetings have been most encouraging.

I acknowledge my Mum and Dad who, despite not understanding a word of my papers or my attempts to explain my PhD, have shown emotional and not insignificant financial support. I am sure that they, most of all, are glad of my completion of this thesis given that it means I will be able to start a career and will no longer be penniless. I am also sure that my Mum will be pleased that her prediction, that the moment I enter University I would never leave, has more or less come true. I also acknowledge my sister Marcie, who has provided me with the occasional new phone, money, and glib remarks. I would also like to acknowledge Simon, Beverley, Fiona and Lorna, who have regularly provided over the past four years the closest thing I can call a holiday. My visits to see them, be it in Texas, Lancaster or the Netherlands, have always provided a good deal of respite.

Most of all I would like to acknowledge my fiancée, Ellie Bennett. Together we have supported each other through our undergraduate and postgraduate studies, even though we have completely different disciplines (I like to think I've picked up some Assyriology along the way). Without each others mutual support and love during mental health problems, family loss and travelling for work I don't think we would have been as successful as we have been. I owe her a great deal. Now we are at the end of our studies, we can finally be employed and have that long awaited marriage ceremony we both deserve.

Contents

List of Figures

1 INTRODUCTION

The first two chapters of this thesis look at superconductivity theory in general, outlining the principles required in order to investigate the vortex lattice (VL) in a superconductor using small-angle neutron scattering (SANS). This is followed by the specific investigations into three superconducting materials that share a 122 chemical structure and an *I4/mmm* tetragonal space symmetry; one of which is a nickel-chalcogenide, while the other two are iron-arsenides.

The third chapter is a literature review and regards the electron band structure of $TlNi_2Se_2$ and
$(Ba_{1-x}K_x)Fe_2As_2$ compounds, with the latter varied in doping levels. In order to fully understand the variation between these very similarly structured materials a literary review of the available evidence is presented for comparison. The key feature is a van Hove singularity that commonly appears across all the materials presented in this thesis but varies in tuning level with respect to the Fermi level and specific location in the Fermi surface. It is this feature that heavily influences the appearance of nodes in the gap structure, the presence of heavy fermion behaviour and the pairing symmetry in the materials investigated.

The fourth chapter of this thesis presents investigations into the anisotropic VL and Pauli limiting behaviour in KFe_2As_2. Again, these studies are SANS investigations of the VL under field, temperature and angular variation. This material is known as a highly anisotropic unconventional superconductor with evidence for multiple gaps and nodes in the gap structure. Some previous investigations have attributed this to a *d*-wave gap symmetry but recent SANS studies (some of which are presented in this thesis) indicate a nodal *s*-wave pairing symmetry, with strong Pauli limiting effects.

The fourth chapter covers the investigations into the $(Ba_{0.5}K_{0.5})Fe_2As_2$ at very high fields. This is a relative of the compound, KFe_2As_2 and is the 50% doped

$(Ba_{1-x}K_x)Fe_2As_2$. This material has a high critical temperature of $T_c \approx 37$ K in comparison to the other two materials and an unmeasured upper critical field, estimated to be as high as $H_{c_2} \approx 140$ T. As such this material was subjected to high field SANS studies in two investigations covering fields up to 25.5 T. Similar to the previous two sections this material was investigated for field and temperature dependence to establish the superconducting pairing symmetry as well as any evidence for anisotropy with respect to field for comparison to KFe_2As_2. The evidence presented in this thesis indicates that $(Ba_{0.5}K_{0.5})Fe_2As_2$ is an s-wave superconductor, with no observable anisotropy or VL rearrangement but with emerging Pauli limiting behaviour at $T \to T_c$ for high fields ($B > 14$ T).

In chapter six investigations into the VL of Ni-chalcogenide $TlNi_2Se_2$ are presented. Preliminary SANS results are given, followed by a larger investigation using SANS with temperature, field and angle dependent results as well as some heat capacity data. This is done to approach the question of the pairing mechanism operational in this heavy-fermion superconductor. These results include angular dependent investigations to probe gap anisotropy in the superconductivity, which is considerable in similar materials of its space symmetry and structure. This material has only been synthesised as a superconducting single crystal material since 2013 and as such few investigations have been conducted. The literature that is available suggests potential multi-gap and d-wave pairing symmetry. The work presented in this thesis attempts to explore some of the previous conclusions by establishing pairing symmetry and behaviour of the VL with respect to temperature and field. Evidence presented in this thesis suggests a single nodal gap, but not necessarily d-wave given a lack of observed VL rearrangement or anisotropy. This contrasts with previous conclusions of multi-gap, nodeless superconductivity.

1.1 London model

The London Model was outlined by the London brothers in 1935 [1], who proposed a microscopic description for the behaviour of a superconductor in magnetic and electric fields, that was consistent with the observations of Onnes [2] and Meissner [3]. Here, we follow their model by considering a superconducting particle in a quantum mechanical context. However, Bardeen, Lewis *et al.* [4, 5] later added to this way of thinking by considering the superconducting sate as two fluids, a fluid of superconducting particles and a fluid of normal particles. The superconducting particle has charge e^* and mass m^*, moving through a vector potential $\mathbf{A}$, and will have a momentum

$$\mathbf{p} = m^*\mathbf{v}_s + e^*\mathbf{A}. \tag{1}$$

The * denotes the fact that we cannot assume that the mass and the charge are equivalent to an electron's mass and charge. In the ground state, the superconducting particle is assumed to have no net momentum, $\langle \mathbf{p} \rangle = 0$. We also hold this to be true when a finite external field is applied, thus imposing the field gauge $\nabla \cdot \mathbf{A} = 0$, known as the London gauge. We may then rearrange Equation 1 to find the particle velocity in the ground state:

$$\langle \mathbf{v}_s \rangle = \frac{-e^*\mathbf{A}}{m^*}. \tag{2}$$

This can be incorporated into the general equation for current density to generate an expression for the superconducting current density:

$$\mathbf{J}_s = n_s e^* \langle \mathbf{v}_s \rangle = \frac{-n_s {e^*}^2 \mathbf{A}}{m^*}. \tag{3}$$

where n_s is the superconducting particle density and the superconducting particle velocity is taken as an average over all particles. As we have established the London gauge in order to satisfy our zero net momentum ground state, the consequence is

that $\nabla \cdot \mathbf{J}_s = 0$. If we take the time derivative of the current density we then get the following:

$$\frac{\mathrm{d}\mathbf{J}_s}{\mathrm{d}t} = \frac{n_s {e^*}^2 \mathbf{E}}{m^*}. \tag{4}$$

This is the first London equation, and it implies perfect conductivity as the applied electric field accelerates the superconducting electrons as opposed to sustaining a steady state current flow.

If we take the curl of Equation 3 then we get the following:

$$\nabla^2 \mathbf{B} = \frac{1}{\lambda_L^2} \mathbf{B}. \tag{5}$$

This is the second London equation, which introduces an internal magnetic field $\mathbf{B}$ and the London penetration depth

$$\lambda_L = \sqrt{\frac{m^*}{\mu_0 n_s {e^*}^2}}. \tag{6}$$

By solving the second London equation it can be shown that for any applied magnetic field penetrating normal to the surface, the field will decay at an exponential rate over length scale of the London penetration depth, λ_L. This essentially means that any external magnetic field is expelled from the superconductor, as if in perfect diamagnetism. This is known as the Meissner effect, or Meissner state [3].

1.2 Vortex lattices in the London model

The London model is empirical by nature and so cannot account for emergent properties such as the vortex lattice (VL) and the existence of Type-II superconductors. Here we introduce the observation that superconductors can be split into two groups, Type-I and Type-II. So far we have operated on the assumption of Type-I, where the superconductor undergoes a single transition between the normal state and the superconducting state (Meissner state) via a first order phase transition. Here we

introduce the concept of the mixed state in Type-II superconductors. In the Meissner state, all flux is expelled up to a skin depth, defined by the penetration depth. In the case of Type-II materials, there is a mixed state between the Meissner and Normal state where some flux is permitted through the superconductor. This is screened by supercurrents to separate the flux lines, with some finite radius of normal state, from the superconducting bulk. These flux lines are observed to arrange as a regular, periodic vortex lattice (VL) in the superconductor. To understand the VL we must modify the London model to fit the empirical evidence. To do this we must return to the current density, Eq. 3.

Let us consider a single flux line. Outside of this flux line, Eqs. 3 and 5 hold true. To incorporate the flux core, we insert a two-dimensional delta function into the curl of Equation 3:

$$\nabla \times \mathbf{J}_s + \frac{n_s {e^*}^2}{m^*}\mathbf{B} = \Phi_0 \delta_2(\mathbf{r})\hat{\mathbf{z}}. \tag{7}$$

This can be rewritten as

$$\lambda_L^2 \nabla^2 \mathbf{B} - \mathbf{B} = -\Phi_0 \delta_2(\mathbf{r})\hat{\mathbf{z}} \tag{8}$$

where the delta function accounts for the position of the flux line, the unit vector $\hat{\mathbf{z}}$ attributes the flux line direction normal to the superconductor surface and $\Phi = hc/2e = 2 \times 10^{-15}$ Tm^2 is the magnetic flux quantum. The flux quantum is the amount of flux in a vortex in the mixed state in a Type-II superconductor. This flux is quantised and confirmed by experimentation [6, 7]. This does not formally forbid $n\Phi_0$ amount of flux being present in a flux core (as is the formal solution in Ginzburg-Landau theory for flux quantisation [8, 9]) as the premise of $n = 1$ is based on semi-classical arguments, the assumption of a ground state and the inexact London equations but a departure from flux quantisation of $n = 1$ has never been observed. The exact solution [10] for the case of a single flux line gives the spatial

variation of the magnetic field of the flux line:

$$B_z(r) = \frac{\Phi_0}{2\pi\lambda_L^2} K_0\left(\frac{r}{\lambda_L}\right). \tag{9}$$

where r is the radial distance from the flux line core and K_0 is the modified, zeroth order Bessel function. From this we must look at the two extreme cases, being close to the core and far from it, respectively.

$$B_z(r) = \begin{cases} \frac{\Phi_0}{2\pi\lambda_L^2} \ln\left(\frac{\lambda_L}{r}\right) & r \ll \lambda_L \\ \frac{\Phi_0}{2\pi\lambda_L^2}\sqrt{\frac{\pi\lambda_L}{2r}} e^{-r/\lambda_L} & r \gg \lambda_L \end{cases} \tag{10}$$

For $r \gg \lambda_L$, this is consistent with Eq. 5. By knowing the free energy per unit length of the flux line, we may understand the requirements for a stable VL by minimising the free energy. To do this we must take Equation 5 and by manipulating it with a vector identity and multiplying by B we obtain, $\lambda^2(\nabla \times \mathbf{B})^2 + B^2$ which is equivalent to the left hand side of Equation 8. We may therefore write the free energy as:

$$F = \frac{1}{2\mu_0} \int (B^2 + \lambda_L |\nabla \times \mathbf{B(r)}|^2) d^3\mathbf{r}. \tag{11}$$

Unfortunately this integral is divergent due to the field divergence as $r \to 0$ (the flux core). To have such a divergent field would require unsustainable and increasing supercurrents. To mitigate this we expand the flux core to a finite area, rather than a delta function. However, the premise of the London interpretation is that there is a local relationship between the supercurrent density and the vector potential at the same point. This is only possible if the flux line core size is negligible compared to the penetration depth. Otherwise we must include non-local corrections to the relationship between the vector potential and the supercurrents. This is discussed further in Section 1.2.2.

Nonetheless, the London model remains a powerful tool for describing VLs. To

this effect we may extend Equation 8 for an ideal VL:

$$\lambda_L^2 \nabla^2 \mathbf{B} - \mathbf{B} = -\Phi_0 \hat{\mathbf{z}} \sum_i \delta_2(\mathbf{r} - \mathbf{r}_i) \tag{12}$$

where i denotes the number of flux lines in the VL. The lattice is periodic in the distribution of vortices, which means that the internal field B is dependent on the position within the superconducting crystal. As such we must describe the field as $\mathbf{B}(\mathbf{r})$ and expand as a Fourier series to satisfy these aforementioned conditions.

$$\mathbf{B}(\mathbf{r}) = \sum_{\mathbf{q}} \mathbf{B}_q e^{i\mathbf{q}\cdot\mathbf{r}} \tag{13}$$

where $\mathbf{q}$ is the reciprocal lattice vector and $\mathbf{B}_q$ are the Fourier coefficients of the internal field. To get the Fourier coefficients in full we must substitute Equation 13 into Equation 12 and integrate with respect to the unit cell of the crystal. This yields

$$\mathbf{B}_q = \frac{\Phi_0 n_L}{1 + \lambda^2 \mathbf{q}^2} = \frac{\langle B \rangle}{1 + \lambda^2 \mathbf{q}^2} \tag{14}$$

where n_L is the number-density of vortices which when multiplied by the flux quantum gives $\langle B \rangle$, the average induction in the superconductor. These Fourier components are directly measurable, as we will discuss later and demonstrate. Consequently we may directly calculate the London penetration depth λ_L from this.

1.2.1 Anisotropic London theory

We have so far assumed an isotropic system with the London Model. However, there are many materials where this is not the case and anisotropic properties are observed. The London Model can be modified to incorporate anisotropy in the effective mass, while maintaining the invariance of the free energy. To do this we must replace the effective mass with a normalised mass tensor, m_{ij}[11]. This generates the following

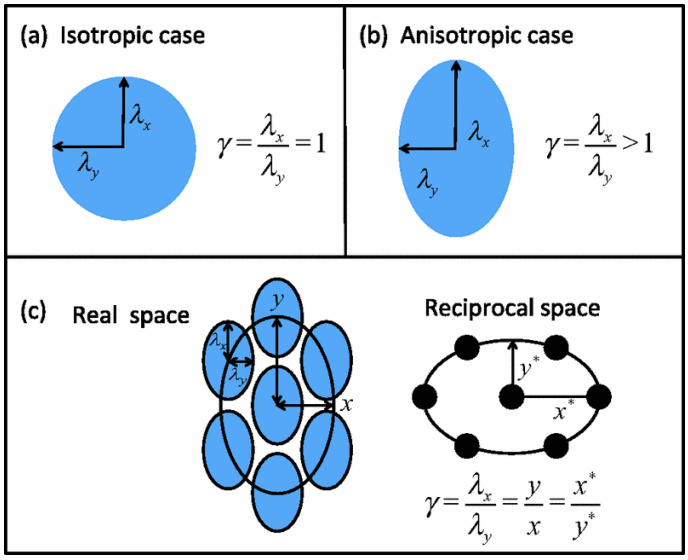

Figure 1: Sketches of the penetration depth in the $a-b$ plane for $H \parallel \mathbf{c}$ for (a) isotropic and (b) anisotropic cases from work in [12]. Panel (c) shows the VL in the case of $\gamma > 1$ for both the real and reciprocal representations; where $x^* \equiv k_x$, $y^* \equiv k_y$ are reciprocal axes.

analogue to Equation 11

$$F = \frac{1}{2\mu_0}\int [B^2 + \lambda_L^2 m_{ij}(\nabla_i \times \mathbf{B})(\nabla_j \times \mathbf{B})]d^3r. \tag{15}$$

For simplicity, λ has been altered to contain an average mass term, $\bar{m}$ rather than the effective mass term. We align the crystal axes with the principal directions of the mass tensor such that the mass tensor is diagonal with the following components: $m_{xx} = \frac{m_a}{\bar{m}}$, $m_{yy} = \frac{m_b}{\bar{m}}$ and $m_{zz} = \frac{m_c}{\bar{m}}$ then normalise the mass tensor $\bar{m} = m_a m_b m_c$. We will assume field penetration along $\hat{\mathbf{z}}$, such that we look at the inequality between only m_a and m_b. In the $a-b$ plane we may describe the anisotropy as a dimensionless ratio of the penetration depths: $\gamma_{ab} = \frac{\lambda_a}{\lambda_b}$. This anisotropy can also have an effect on the result in equation 14 by putting anisotropy into the Fourier components of the internal field modulation in the VL state.

In the case of an isotropic superconductor, the vortices of a VL can be aligned on a circle, demonstrating an isotropic hexagonal VL. For the anisotropic case, $\gamma \neq 1$, then an ellipse overlays the vortices for the VL. The circle of the isotropic case has

been distorted by a scalar transformation. The a direction has been distorted by $\sqrt{\gamma_{ab}}^{-1}$ and the b direction is distorted by $\sqrt{\gamma_{ab}}$. Figure 1 is a simplified representation of anisotropy in the VL. Any orientation of VL distortion satisfies the same free-energy requirements [13] outlined in equation 15. This is because the anisotropic VL can always be mapped back to the isotropic case by a scale transformation as outlined earlier. However, when an arbitrary angle is introduced to the applied field with respect to the crystal axes, the London model does make a prediction [13] as to the preferred alignment of the VL with respect to the crystal axes. The alignment is such that the nearest neighbour of a single flux line will be perpendicular to the axis of rotation for that arbitrary rotation of some angle for the superconductor with respect to the field.

1.2.2 Non-local London theory

Pippard [14] proposed a non-local relationship between the current density and the vector potential to generalise the London model. In the local London model, $\mathbf{J}_s(\mathbf{r})$ is proportional to $\mathbf{A}(\mathbf{r})$ at any point $\mathbf{r}$. Pippard's argument was that the current at a point $\mathbf{r}$ depends on $\mathbf{A}(\mathbf{r})$ throughout a volume of some radius l (an arbitrary length scale for the moment) about the point $\mathbf{r}$. Pippard argued that the length, l over which this was true was the Pippard coherence length, ξ_0. We can make an uncertainty-principle argument for the value of the coherence length as follows: Only electrons with energies which reside within kT_c of the Fermi energy can contribute at T_c as the superconducting phenomenon sets in at this point. Using the Fermi velocity, v_F, these electrons must therefore have a momentum range of $\Delta p \approx kT_c/v_F$. Thus we can make the uncertainty argument:

$$\Delta x \geqslant \frac{\hbar}{\Delta p} \approx \frac{\hbar v_F}{kT_c} \tag{16}$$

which gives the coherence length as:

$$\xi_0 = a\frac{\hbar v_F}{kT_c} \tag{17}$$

where a is an unknown constant. Pippard later fit this to aluminium and tin [15] to find an a value of 0.15 (later, BCS theory showed this to be 0.18). Now we have generated the coherence length and the penetration depth we can look at how the interplay between these two parameters defines the behaviour and type of superconductor. We may generate the following cases: Type-I superconductors where $\xi_0 > \sqrt{2}\lambda_L$ and Type-II superconductors, $\xi_0 < \sqrt{2}\lambda_L$. Within this we may also say that for $\xi_0 \simeq \lambda_L$ we have Weakly Type-II superconductors and at $\xi_0 \ll \lambda_L$, strongly Type-II superconductors. In Type-I superconductors there are only two stable phases, the normal and superconducting phase. The latter has the characteristic of expelling all magnetic flux. This is a consequence of the penetration depth being smaller than the coherence length. The flux lines are screened by the fact the larger coherence length generates a positive free energy requirement that screens flux lines from penetrating the surface of the superconductor due to the strong supercurrent response. In the Type-II case there is a mixed phase between the fully superconducting Meissner state and periodic flux cores of Normal state, whereby some flux lines are allowed to penetrate into the superconductor. This is because $\mathbf{A}(\mathbf{r})$ varies sharply over λ meaning the supercurrents that screen the fields are weaker. This permits flux lines to penetrate the surface of the superconductor.

When ξ is applied as a length scale, it can be interpreted as the length over which if $\mathbf{A}(\mathbf{r})$ varies from its maximum value, and then the response of the superconducting current is diminished and the penetration depth is enhanced as a result to a value much larger than the prediction from the local London model. This is the case when $\mathbf{r}$ is in proximity to a flux line core. Consequently, $\mathbf{A}(\mathbf{r})$ can still vary rapidly over a distance less than ξ_0 in the case of Type-I superconductors, and weakly Type-II su-

perconductors. For strongly Type-II superconductors non-local corrections become less important until they disappear for the limit $\lambda_l/\xi_0 = \kappa \to \infty$. As a result of this, Pippard proposed the following relationship:

$$\mathbf{J}_s(\mathbf{r}) = -\frac{3}{4\pi\xi_0}\frac{n_s e^{*^2}}{m^*}\int \frac{\mathbf{R}[\mathbf{R}\cdot\mathbf{A}(\mathbf{r}')]}{R^4}e^{-R/\xi}d\mathbf{r}' \tag{18}$$

where $\mathbf{R} = \mathbf{r} - \mathbf{r}'$. Here we also have ξ which is the coherence length in an impure material, and so Pippard assumes scattering of the electrons from imperfections occurs. This invokes the need to relate ξ to the mean free path of a normal metal, l. The coherence length of a pure material, ξ_0 is related to ξ and l by the following equation:

$$\frac{1}{\xi} = \frac{1}{\xi_0} + \frac{1}{l} \tag{19}$$

which demonstrates that for a sufficiently large mean free path, the coherence length has little dependence on the internal scattering, making it very important that a sample is pure, referred to as clean, to minimise unwanted scattering effects. In cases of high impurity or 'dirty' superconductors the mean free path, l becomes a more important parameter as it suppresses non-local effects by reducing ξ.

We have touched on how non-local effects can arise from the rapid variation of $\mathbf{A}(\mathbf{r})$ over distances less than ξ when ξ is sufficiently large compared to λ. However, there are non-local effects that arise in strongly Type-II superconductors predicted by Kogan [16, 17, 18] that affect the VL which we discuss in section 1.5.

1.3 Ginzburg-Landau (GL) model

Ginzburg-Landau theory is a phenomenological approach to superconductivity based upon thermodynamics and the use of an order parameter. This model describes the thermodynamic state of a superconductor and applies an order parameter to describe the collective behaviour of the superconducting quasi-particles. The Ginzburg-Landau model is also very powerful for dealing with spatial inhomogeneity, such

as at the interface between the normal and superconducting regions in the intermediate state of a Type-I or the mixed state of a Type-II superconductor.

We must introduce two concepts. The order parameter, ψ, is zero for $T \geq T_c$ and finite for all temperatures below the critical temperature, T_c. This order parameter can be described as a pseudowavefunction $\psi(\mathbf{r})$. This wavefunction describes the local density of superconducting electrons as part of a variational method, utilising the complex (and continuous) nature of the order parameter. The principle of the Ginzburg-Landau approach is the variational method; so long as ψ is small and varies gradually in space, the free energy density of such a system can be described by increasing powers of $|\psi|^{2n}$ and $|\nabla\psi|^{2n}$. We limit the powers to even numbers as the order parameter, ψ is complex. We begin the derivation of the model by writing the macroscopic free energy density:

$$F = F(T) + \alpha(T)|\psi(\mathbf{r})|^2 + \frac{\beta}{2}|\psi(\mathbf{r})|^4 + \cdots \tag{20}$$

The free energy can be minimised if α vanishes for $T \geq T_c$, so we give α a temperature dependence: $\alpha(T) = a(t-1)$ where $t = T/T_c$. Now if we minimise Equation 20 we obtain the following:

$$|\psi| = \begin{cases} 0 & T > T_c \\ \sqrt{\frac{\alpha(T)}{\beta}} & T < T_c \end{cases} \tag{21}$$

This accounts for the change of sign of α about T_c and the finite, positive value of $|\psi|$ below T_c. However, we have already established the premise that the Ginzburg-Landau approach can account for spatial inhomogeneity. Equation 21 does not include all the necessary information for spatial variance in ψ, so we must introduce energy gradient terms to account for this. Using the wavefunction definition, $\psi = |\psi|e^{i\phi(\mathbf{r})}$ and the Hamiltonian for a charged particle moving through an electro-

magnetic field we can define the following:

$$\frac{\hbar^2}{2m^*}|\nabla\psi(\mathbf{r})|^2 = \frac{\hbar^2}{2m^*}\left|\left(\nabla - \frac{ie^*\mathbf{A}}{\hbar}\right)\psi(\mathbf{r})\right|^2 \tag{22}$$

We can now modify the free energy density to include this term

$$F = F(T) + \frac{B^2}{2\mu_0} + \alpha(T)|\psi(\mathbf{r})|^2 + \frac{\beta}{2}|\psi(\mathbf{r})|^4 + \frac{\hbar^2}{2m^*}\left|\left(\nabla - \frac{ie^*\mathbf{A}}{\hbar}\right)\psi(\mathbf{r})\right|^2 \tag{23}$$

By minimising with respect to ψ and ψ^* we can reduce Equation 23 to the first of the Ginzburg-Landau differential equations

$$\alpha\psi + \beta|\psi|^2\psi - \frac{\hbar}{2m^*}\left(\nabla - \frac{ie^*\mathbf{A}}{\hbar}\right)^2\psi = 0 \tag{24}$$

To get the second Ginzburg-Landau differential equation we must minimise the free energy with respect to $\mathbf{A}$. This allows us to consider the supercurrent density.

$$\mathbf{J}_s = -\frac{i\hbar e^*}{2m^*}(\psi^*\nabla\psi - \psi\nabla\psi^*) - \frac{e^{*^2}}{m^*}|\psi|^2\mathbf{A} \tag{25}$$

These two equations above can be used to provide the length scales for the Ginzburg-Landau model in one dimension. If we assume an absence of any electromagnetic fields, and introduce our definition of $|\psi|$ from Equation 21 we may extract the Ginzburg-Landau coherence length.

$$\xi(T) = \sqrt{\frac{\hbar^2}{2m^*|\alpha(T)|}} \tag{26}$$

We must note that this coherence length is not the same as the Pippard coherence length in Equation 17, as the Ginzburg-Landau value diverges for temperatures approaching T_c, whereas the Pippard coherence length for non-local electrodynamics essentially remains constant. For pure metals well below T_c these two values are approximately similar, otherwise they differ. This Ginzburg-Landau coherence length

represents the shortest distance over which the order parameter will vary from it's maximal bulk value, $|\psi_0|$ to zero.

A second length scale can be extracted from the Ginzburg-Landau equations. If we take Equation 25 and assume we are at $T = T_c$, then $\psi(\mathbf{r}) = 0$ and the equation becomes

$$\mathbf{J}_s = \frac{-e^{*^2}}{m^*}|\psi|^2\mathbf{A} \tag{27}$$

Where we had previously defined in Equation 21 that $|\psi|^2 = \alpha(T)/\beta$. We may prescribe the term $|\psi|^2$ to be equivalent to the superconducting carrier density, $|\psi|^2 = n_s$. Thus if the superconducting carrier density falls to zero then there is no supercurrent. Now we may tie in to the London model and create a GL penetration depth defined as

$$\lambda(T) = \sqrt{\frac{m^*\beta}{\mu_0 e^{*^2}\alpha(T)}} \tag{28}$$

This means that in the GL approach the penetration depth and the coherence length are temperature dependent. So the dimensionless ratio for determining the extent to which a superconductor is Type-II in behaviour is now temperature dependent:

$$\kappa = \frac{\lambda(T)}{\xi(T)} \tag{29}$$

Now we shall return to the first GL equation, Equation 24, in order to expand to the Abrikosov solution to describe the Abrikosov or VL state of a Type-II superconductor. The phase transition from normal to the superconducting (mixed) state in a Type-II superconductor is second order. So we may assume that ψ is very small for fields just below H_{c_2} and zero at H_{c_2}. Thus we can drop the term $|\psi|^2\psi$ from equation 24 as it is small. Next we must choose a gauge for the fields. For simplicity we shall choose $\mathbf{B} = (0, 0, B)$ and $\mathbf{A} = (0, Bx, 0)$, also known as the Landau gauge.

If we also introduce the cyclotron frequency, $\omega_c = e^*B/m^*$ we may turn the first GL quation into the following:

$$\left(-\frac{\hbar^2}{2m^*}\nabla^2 - i\hbar\omega_c x\frac{\delta}{\delta y} + \frac{m^*\omega_c^2}{2}x^2\right)\psi(\mathbf{r}) = |\alpha(T)|\psi(\mathbf{r}) \tag{30}$$

which has the same form as Schroedinger's equation for a charged particle in a magnetic field. If we want eigenvalues for this system in order to describe the Abrikosov state, we must set up a trial function: $\psi = e^{i(k_y y + k_z z)}f(x)$. Where $f(x)$ is unknown but ψ describes a plane wave now in the y-z plane. If we substitute this trial function in Equation 30 we get the following

$$-\frac{\hbar^2}{2m^*}\frac{d^2 f}{dx^2} + \frac{m^*\omega_c^2}{2}\left(x + \frac{\hbar k_y}{m^*\omega_c}\right)^2 f = \left(|\alpha| - \frac{\hbar^2 k_z^2}{2m^*}\right) f. \tag{31}$$

As with the Schroedinger equation, our energy eigenvalues are associated with a simple harmonic oscillator (SHO)

$$|\alpha| = \left(n + \frac{1}{2}\right)\hbar\omega_c + \frac{\hbar^2 k_z^2}{2m^*}. \tag{32}$$

At $H = H_{c_2}$ we will have the lowest possible energy state available to us. This means we can set $n = 0$ and $k_z = 0$ for this field to describe the state, giving us $|\alpha(H = H_{c_2})| = \frac{1}{2}\hbar\omega_c$. To relate this to the field we can substitute in the definition of the cyclotron frequency, the GL coherence length and Φ_0 (the flux quantum) to get the upper critical field of the superconductor:

$$B_{c_2} = \mu_0 H_{c_2} = \frac{\Phi_0}{2\pi\xi^2} \tag{33}$$

This is an important result as it describes the distribution of the flux lines in the Abrikosov state. This equation describes one single flux line for every unit of area, $2\pi\xi^2$. This becomes even more important later for the conservation of the VL area when considering anisotropy with respect to applied field. This makes sense as ξ is

the length over which the order parameter decreases from its maximal value to zero. It will do this in the presence of a flux line. However, if the number density of flux lines were higher then the order parameter within the defined area would fall off to 0 a lot faster, meaning ξ no longer correctly describes the behaviour of the order parameter. We may also use this result to identify the difference between Type-I and Type-II superconductors as well as the condensation energy of the superconductor. We must go back to Equation 20 and substitute in the solution $|\psi| = -\alpha/\beta$, which gives the thermodynamic condensation energy defined by a critical field: $\mu_0 H_c^2/2 = \alpha^2/2\beta$. Now if we combine this with H_{c_2} we can arrive at a way of separating Type-I and Type-II superconductors with the following:

$$H_{c_2} = \sqrt{2}\kappa H_c \tag{34}$$

This equation creates a separation point of $\kappa = 1/\sqrt{2}$ for Type-I and Type-II materials. Type-II materials can now be identified by $H_{c_2} > H_c$ for $\kappa > 1/\sqrt{2}$ and Type-I by $H_{c_2} < H_c$ for $\kappa < 1/\sqrt{2}$. As H_c represents a condensation point, for Type-II superconductors the order parameter will gradually increase from H_{c_2} for a decreasing field implying a second order transition. Whereas for Type-I superconductors they remain in the normal state below H_c for a decreasing field until $H_{c_2} < H_c$ is reached and the order parameter will jump discontinuously from 0 to $|\psi|^2$.

We must now consider the case that we cannot ignore the cubic term in Equation 24, which is how Abrikosov [20] looked at Type-II materials. However the inclusion of $|\psi|^2\psi$ introduces non-linearity and the differential equation becomes harder to solve. The first step is to create a trial function that is consistent with the interpretation of a SHO system with Landau levels, and to consider only the lowest Landau level such that $n = 0$ and $k_z = 0$. Thus our trial function is

$$\psi = C \exp\left[\left(-\frac{\hbar k_y}{m\omega_c} - x\right)\frac{1}{\xi(T)^2} + ik_y y\right], \tag{35}$$

where C is a normalisation constant that is zero for $H \geq H_{c_2}$ and $\frac{\hbar k_y}{m\omega_c}$ is the shift in the lowest Landau level. This trial function is modelled as a Gaussian with its size in space determined by the coherence length, $\xi(T)$. This trial function cannot be left as it is in this form as we need to define the shift in the lowest Landau level by constraining k_y to non-infinite degeneracy by periodicity. If we define a new length parameter, l_y, over which k_y is periodic such that $k_y = 2\pi n/l_y$ and $n \in \mathbb{Z}$, we may now use the Landau correction

$$\frac{\hbar k_y}{m\omega_c} = \frac{2\pi\hbar n}{m\omega_c l_y} = \frac{\Phi_0 n}{B l_y} \tag{36}$$

such that the trial function becomes

$$\psi = \sum_{n=-\infty}^{n=\infty} C_n \exp\left[-\left(x + \frac{n\Phi_0}{B l_y}\right)\frac{1}{\xi(T)^2} + \frac{i2\pi n y}{l_y}\right] \tag{37}$$

C_n must be chosen in order to minimise the free energy. We have removed infinite degeneracy in y, so we must do the same with x by enforcing two conditions. Firstly, periodicity in C_n with $C_{n+\upsilon} = C_n$ and $\upsilon \in \mathbb{Z}$. Secondly a periodic length of $l_x = \upsilon\Phi_0/Bl_y$ where $\upsilon = 1$ is a square VL and $\upsilon = 2$ is a hexagonal VL (isotropic). The periodicity conditions phenomenologically account for the nucleation of the VL just below H_{c_2} with an arrangement of one flux quantum per unit cell of the VL. Abrikosov solved the first GL equation with this trial function to get the following free energy density [21]

$$F = F_0 + \frac{1}{2\mu_0}\left(B^2 - \frac{(B - \mu_0 H_{c_2})^2}{1 + \beta_A(2\kappa^2 - 1)}\right) \tag{38}$$

Where $\beta_A = \frac{\langle\psi^4\rangle}{\langle\psi^2\rangle^2}$ is the Abrikosov parameter. For constant values of ψ it has the value of unity, but becomes larger for functions which are more localised. Increasing values of β_A lead to less favourable values of free energy with regards to the shape of the VL. To explain, if we take an extreme example of a local solution, where

only a small fraction, f of volume is filled we can represent this as $\beta_A = f^{-1}$. This means the condensation energy of the VL is smaller than for a solution which fills more space and can be represented as $\beta_A \approx 1$. The numerical value of β_A is found through optimising the set of C_n for which β_A is smallest. The numerical solution for a square lattice was found by Abrikosov, $\beta_A = 1.18$ and the hexagonal lattice was calculated by Kleiner [22], $\beta_A = 1.16$. Consequently the hexagonal lattice is slightly energetically more favourable than a square lattice. We can come to the same conclusion via a close-packing argument. If we define the lengths $a_\square$ and $a_\triangle$ for the nearest neighbour distances of a square and hexagonal (or triangular) lattice, respectively. For a square lattice the nearest neighbour distance is

$$a_\square = \left(\frac{\Phi_0}{B}\right)^{1/2} \tag{39}$$

and for a hexagonal lattice

$$a_\triangle = \left(\frac{4}{3}\right)^{1/4} \left(\frac{\Phi_0}{B}\right)^{1/2} = 1.075 \left(\frac{\Phi_0}{B}\right)^{1/2} \tag{40}$$

which means that $a_\triangle > a_\square$. Given that flux lines mutually repel each other, this means that greater stability is achieved by a larger spacing between the flux lines. So, a hexagonal arrangement is marginally preferred over a square one. However, the difference between the two arrangements in energy terms is only $\approx 2\%$. This means that even a very small anisotropy in the system and the symmetries of the underlying crystal lattice can induce arrangements of flux lines other than isotropic hexagonal.

Brandt [23] analysed the results of the G-L theory to obtain a form factor ($F(q)$) description with field dependence for the VL close to the critical temperature. The following is valid for any κ value that qualifies as a Type-II superconductor in the

hexagonal VL arrangement.

$$F_{hk} = \frac{(-1)^{\nu} e^{\frac{\pi\nu}{\sqrt{3}}} (B - B_{c_2})}{1 + 1.16(2\kappa^2 - 1)} \tag{41}$$

where

$$\nu = (h^2 + hk + k^2) \tag{42}$$

with $[h, k, l]$ representing the Miller indices of the VL. As we approach T_c the form factor of the VL falls linearly to zero - this is strongly supported by measurements of Nb [24].

1.3.1 The Clem model

This model is not formally used in the analysis of the results conatined in this work, however the approach highlights some of the considerations needed for looking at Type-II materials and as such is added here for completion. Within the GL theory is the ability to provide an approximation that covers the divergent limit in the London model in the vicinity of a VL core. Clem [25] solved the second GL equation, equation 25, for a single flux line with a variational approach. Firstly we must define our coordinate system in cylindrical space: $\rho = \sqrt{(x^2 + y^2)}$, $\phi = \tan^{-1}(y/x)$ and z parallel to the field lines. Then we rewrite the second GL equation as

$$J_{\phi} = \frac{-\mu_0}{\lambda^2} \left(a_{\phi} - \frac{\Phi_0}{2\pi\rho} \right) f^2 \tag{43}$$

Where J_{ϕ} and a_{ϕ} are the supercurrent density and magnetic vector potential along $\hat{\phi}$, respectively. The unit vector is important as it needs to satisfy the London gauge and vanish at the flux line core. Here, ρ is the radial coordinate and $f(\rho)$ is a spacially varying function of ψ such that

$$\psi(\rho) = f(\rho) e^{-i\phi} = \left(\frac{\rho}{R} \right) e^{-i\phi} \tag{44}$$

Where $R = \sqrt{(\rho^2 + \xi_\nu^2)}$ and ξ_ν^2 is related to the GL coherence length such that ψ is a value which minimises the free energy. We may obtain a solution to a_ϕ by combining $\nabla \times \mathbf{B} = \mu_0 \mathbf{J}$ and $\mathbf{B} = \nabla \times \mathbf{A}$ and substitute in equation 43 for the current density then we get the following

$$\frac{d}{d\rho}\left[\frac{1}{\rho}\frac{d}{d\rho}(\rho a_\phi)\right] - \frac{f^2}{\lambda^2}a_\phi = -\frac{\Phi_0 f^2}{2\pi\lambda^2\rho} \tag{45}$$

We require modified Bessel functions, $K_n(x)$, in order to solve for a_ϕ. This yields the following solution

$$a_\phi = \frac{\Phi_0}{2\pi\rho}\left[1 - \frac{RK_1\left(\frac{R}{\lambda}\right)}{\xi_\nu K_1\left(\frac{\xi_\nu}{\lambda}\right)}\right] \tag{46}$$

Using $\mathbf{B} = \nabla \times \mathbf{A}$ we can generate the following magnetic field component

$$B_z = \left(\frac{\Phi_0}{2\pi\lambda\xi_\nu}\right)\frac{K_0\left(\frac{R}{\lambda}\right)}{K_1\left(\frac{\xi_\nu}{\lambda}\right)} \tag{47}$$

Now we need to introduce the reciprocal lattice vector for the VL, $\mathbf{G}$ by taking the Fourier transform of the field component

$$F_z(\mathbf{G}) = \frac{\Phi_0 K_1\left(\xi_\nu(\mathbf{G}^2 + \lambda^{-2})^{\frac{1}{2}}\right)}{(\mathbf{G}^2 + \lambda^{-2})^{\frac{1}{2}}\lambda K_1 \xi_\nu \lambda^{-1}} \tag{48}$$

which gives the form factor of the VL, the variation of the magnetic field of the vortices. However, we can simplify this expression by assuming a limit of large κ such that $\frac{\lambda}{\xi} \gg 1$, which gives the following

$$g = \frac{\xi_\nu\sqrt{1 + \mathbf{G}^2\lambda^2}}{\lambda} \tag{49}$$

$$F_z(\mathbf{G}) = \langle B\rangle \frac{gK_1(g)}{1 + \mathbf{G}^2\lambda^2}. \tag{50}$$

This is essentially the London model, and we can see parallels with equation 14, but with the addition of the Bessel functions and g to account for the contribution

of the cores. This is also why the field is given as an average induction over the z axis. As these equations are fundamentally derived from the GL theory they are consequently only valid near the critical temperature. This makes sense as the core corrections are not as important for well below T_c due to low flux line density. However, there is a lot of similarity between the Clem model and the London model due to the assumption that local electromagnetism is sufficient. This is maintained within the Clem model by the gK_1 term as it provides suppression of the contributions of the flux lines at small distances from the flux line cores. Both the Clem and London models support this assumption, provided the aforementioned condition of $\kappa \gg 1$.

The materials approached in this work do not fully fit the criteria for the Clem model being the most effective approach. With the emphasis of the investigations on low temperature features due to the interest in nodal and unconventional superconductivity and only $(Ba_{0.5}K_{0.5})Fe_2As_2$ satisfying $\kappa \gg 1$, this model is presented for completion and is not formally used in the analysis, as previously mentioned.

1.4 Bardeen-Cooper-Schreiffer (BCS) theory

So far we have approached superconductivity phenomenologically, where laws of thermodynamics and electrodynamics are applied to empirical data with certain simplifying assumptions and limiting cases in order to validate a reasonable description of superconductivity. If we want a deeper understanding of superconductivity and the ability to make predictions for behaviour, we require a theory that tackles superconductivity from a microscopic perspective; this requires invoking quantum mechanics and using the tools therein.

A comprehensive microscopic description of quantum mechanics was provided by Bardeen, Cooper and Schreiffer (BCS) [26] in 1957. Cooper [27] and Froelich [28] presented the framework for the BCS theory with the premise that electrons could form a bound state for an arbitrarily weak interaction potential. The justification

for this is the instability of the Fermi sea of electrons against the formation of a bound pair of electrons by the exchange of phonons. To explore the origins of the electron-phonon coupling that provides the binding mechanism, we create a two-particle wavefunction at the lowest energy state. Assuming no net momentum (spin up and spin down pair for equal and opposite momenta) we have the following wavefunction:

$$\psi_0(\mathbf{r}_1, \mathbf{r}_2) = \sum_{\mathbf{k}} g_{\mathbf{k}} e^{i\mathbf{k}\cdot(\mathbf{r}_1 - \mathbf{r}_2)} \tag{51}$$

where $g_{\mathbf{k}}$ is a weighting function. Given that the electrons must have equal and opposite spin for the lowest energy state, we must assume an antisymmetric case and consider only the sum of the products of $\cos \mathbf{k} \cdot (\mathbf{r}_1 - \mathbf{r}_2)$. This is the spin singlet case. The cosine components give a larger probability amplitude for the electrons to be near each other, implying an attractive interaction. The spin singlet wavefunction can be described by the following:

$$|\psi\rangle = \frac{1}{\sqrt{2}} |\uparrow\downarrow\rangle - |\downarrow\uparrow\rangle \tag{52}$$

This is an s-wave pairing with equal and opposite spin, consequently there is no net angular momentum; $l = 0$. To describe superconductivity we require a wavefunction that can take into account every electron in a Fermi level as one of a pair, with each pair contributing to a many-particle coherent wavefunction. To do this we must define a Cooper pair creation operator derived from electron creation operators for opposite spin. We define the following pair creation operator; $\hat{P}^{\dagger}_{\mathbf{k}} = c^{\dagger}_{\mathbf{k}\uparrow} c^{\dagger}_{\text{-}\mathbf{k}\downarrow}$, which is made up of two creation operators which generate electrons with opposite momenta and spin. This is assuming the lowest energy state, the vacuum state $|0\rangle$, as the supercodnucting state must be a ground state. This has been outlined in previous theory sections to some extent but is all them ore important here with a quantum mechanical treatment. Taking into account the probability of a pair state being unoccupied, $|u_{\mathbf{k}}|^2$ and occupied, $|v_{\mathbf{k}}|^2$ such that $|u_{\mathbf{k}}|^2 + |v_{\mathbf{k}}|^2 = 1$.

We may write the following wavefunction:

$$|\Psi_{BCS}\rangle = \prod_{\mathbf{k}} (u_{\mathbf{k}}^* + v_{\mathbf{k}}^* \hat{P}_{\mathbf{k}}^\dagger)|0\rangle \tag{53}$$

The wavefunction $|\Psi_{BCS}\rangle$ represents the superconducting ground state. This state is equivalent to the Fermi sphere for the following conditions: if $u_{\mathbf{k}} = 1$ for $|\mathbf{k}| > k_F$ or $v_{\mathbf{k}} = 1$ for $|\mathbf{k}| < k_F$. However, for $u_{\mathbf{k}}, v_{\mathbf{k}} \neq 1$ there is a distribution of occupation over the Fermi surface. This distribution has a width in reciprocal space equivalent to $\mathbf{k} = \xi_0^{-1}$ which is equivalent to the Pippard coherence length, previously discussed. But here the equivalence between the BCS value of ξ_0 and the Pippard length ξ is limited to $T = 0$ K. In the Pippard case the value of ξ doesn't vary much with temperature, but they essentially represent the same thing. In the Pippard approximation ξ represents the smallest size of the charge carrying wave-packet in a superconductor. In the BCS case ξ_0 varies smoothly with T and describes the separation between the states in the Fermi surface, in real space it describes the actual separation length of a Cooper pair.

In order to understand the Cooper pairs we need to investigate the binding energy of the pair and the energy state the pairs occupy. For this we set up a BCS Hamiltonian:

$$\hat{H} = \sum_{\mathbf{k}\sigma} \left(\frac{\hbar^2 \mathbf{k}}{2m} - \mu \right) c_{\mathbf{k}\sigma}^\dagger c_{\text{-}\mathbf{k}\sigma}^\dagger + \frac{1}{2} \sum_{\mathbf{k}\ \mathbf{k'}} c_{\mathbf{k}\uparrow}^\dagger c_{\text{-}\mathbf{k}\downarrow}^\dagger V_{\mathbf{k'},\ \mathbf{k}} c_{\mathbf{k'}\uparrow} c_{\text{-}\mathbf{k'}\downarrow} \tag{54}$$

where $V_{\mathbf{k'},\ \mathbf{k}}$ is the matrix element that describes the two-particle interaction of the Cooper pair and μ is the chemical potential. To solve the above we may treat the occupation probabilities as variables that need chosen values which minimise the total energy of the Cooper pair. By minimising the Hamiltonian we acquire the expression for the energy spectrum of excitations for a Cooper pair (treated as a quasiparticle) when introduced to the ground state in the BCS theory. Using

$\epsilon_{\mathbf{k}} = \frac{\hbar^2 \mathbf{k}}{2m}$, this expression is as follows:

$$E_{\mathbf{k}} = \sqrt{(\epsilon_{\mathbf{k}} - \mu)^2 + |\Delta_{\mathbf{k}}|^2} \tag{55}$$

$\Delta_{\mathbf{k}}$ is the superconducting gap function, which is uniform across k-space but is only dependent on the momentum. This value is actually half of the total binding energy of a Cooper pair, with the zero temperature value of the biding energy dependent on the critical temperature of the superconductor. BCS found this relationship to be

$$E_{gap} = 2\Delta(T = 0K) = 3.52 k_B T_c. \tag{56}$$

The gap function is analogous to the order parameter as BCS theory shows that the gap energy falls to zero at $T = T_c$. Gor'kov [29] later showed that the order parameter and the gap function were indeed directly related, with a further interpretation that the order parameter wavefuntion was in fact the wavefunction of the Cooper pairs, based on the motion of the centre of mass of the pair.

The gap, Δ, exists over the the whole Fermi surface. Below this energy, quasiparticle states are not not accessible. However, above this energy magnitude the nature of the the states is dependent on the occupation probabilities and the position in k-space. Well below the Fermi surface there is little to no occupation, so $|v_{\mathbf{k}}|^2 \simeq 1$ and the states are more like electrons. Well above the surface when $|u_{\mathbf{k}}|^2 \simeq 1$, the states are more like holes. But the image is not so binary nearer the Fermi surface where there are mixed characteristics for the quasiparticle states, behaving like electrons and holes. From [10] and [21] we have the means to find the mixed excitation energies using the Bogoliubov-Valatin fermion creation and annihilation operators to diagonalise the BCS Hamiltonian. The operators are

$$\hat{\gamma}_{\mathbf{k}\uparrow} = u^*_{\mathbf{k}} c_{\mathbf{k}\uparrow} - v^*_{\mathbf{k}} c^\dagger_{\mathbf{\text{-}k}\downarrow} \tag{57}$$

$$\hat{\gamma}^{\dagger}_{\text{-}\mathbf{k}\downarrow} = u_{\mathbf{k}} c^{\dagger}_{\text{-}\mathbf{k}\downarrow} + v_{\mathbf{k}} c_{\mathbf{k}\uparrow}. \tag{58}$$

The above operators diagonalise the BCS Hamiltonian with the same energy spectrum results as with the BCS wavefunction. This means we can describe single particle excitations above Δ as well as explain the emergence of Δ. Now we have a microscopic theory for an ideal system. In a real system there are perturbations, inhomogeneities in real space caused by the underlying crystal lattice, impurities, and flux lines. These spatial inhomogeneities are sources of scattering for quasi-particles and can be accounted for as a scattering potential, $U(\mathbf{r})$. The flux lines however can be accounted for as periodic fluctuations in the gap function caused by the flux cores. Consequently, the gap function is now a spatially varying parameter, $\Delta(\mathbf{r})$. We now have to change our operators to be position dependent rather than momentum dependent in order to account for the above inhomogeneities. To do this we define our Bogoliubov transformation in a more generalised manner

$$\hat{\Psi}_{\uparrow}(\mathbf{r}) = \sum_{n} \left[u_n(\mathbf{r}) \hat{\gamma}_{n\uparrow} - v_n^*(\mathbf{r}) \hat{\gamma}^{\dagger}_{n\downarrow} \right] \tag{59}$$

$$\hat{\Psi}_{\downarrow}(\mathbf{r}) = \sum_{n} \left[u_n(\mathbf{r}) \hat{\gamma}_{n\downarrow} + v_n^*(\mathbf{r}) \hat{\gamma}^{\dagger}_{n\uparrow} \right] \tag{60}$$

The above are annihilation operators with respect to position dependent functions, $u_n(\mathbf{r})$ and $v_n(\mathbf{r})$ which are chosen so that we may diagonalise the Hamiltonian. To do this the position dependent functions must satisfy the following, coupled, Bogoliubov-de Gennes equations:

$$\hat{H} u_n(\mathbf{r}) + \Delta(\mathbf{r}) v_n(\mathbf{r}) = E_n u_n(\mathbf{r}) \tag{61}$$

$$-\hat{H}^* v_n(\mathbf{r}) + \Delta^*(\mathbf{r}) u_n(\mathbf{r}) = E_n v_n(\mathbf{r}) \tag{62}$$

In order to satisfy this coupled pair of equations, we must determine $\Delta(\mathbf{r})$ from the available values of u and v. These equations can demonstrate that for a high κ value, Δ varies rapidly over a distance equivalent to the GL coherence length,

$\xi(T, \mathbf{r})$.

1.5 Non-local corrections

Non-local coupling effects can enhance the superfluid density in a superconductor. These effects of spin coupling are usually only seen in strongly coupled d-wave systems, where at the nodes of the gap on the Fermi surface the coherence length diverges due to the momentum dependence of ξ_0 such that $\xi_0(\mathbf{k}) \propto 1/\Delta_{\mathbf{k}}$ [96]. This creates loci of highly non-local points on the Fermi surface in the vicinity of the nodes where $\xi \gg \lambda_0$, even in strongly Type-II superconductors this can be very important and a non-local approach to looking at the superfluid density has been developed for looking at the d-wave cuprates by Amin *et al.* [101]. The extent to which non-local coupling effects are active in the material in determining the behaviour of the superfluid density with temperature can be an indication of interesting mechanisms that would not otherwise be noticeable. Small to negligible contributions of non-local coupling would be consistent with non-d-wave nodal gap structure or weakly coupled d-wave pairing [96, 101, 102, 109].

By using the approach by Amin *et al.*[101, 102] one may observe when non-local effects are influencing the superfluid density with respect to T variation. Generally, the low-T behaviour of ρ would become modified from a linear to a T^3 dependence with the presence of non-local coupling effects. This modification would become apparent below a characteristic temperature, $T^* = \Delta_0 \xi_0 q / k_B$ that usually indicates the temperature below which non-local coupling is an active effect. The consequence of the shift from linear to T^3 behaviour is the appearance of weak low-T dependence. This is in contrast to the work of Volovik *et al.* [32] that points to high sensitivity of unconventional superconductors to changes in temperature in low-T conditions. If we take $\rho(T)$ to be the unaltered (BCS), local superfluid density and define a new term

$$n(T) = 1 - (1 - \rho(T)) \left(\frac{T_c + T^*}{T_c} \right) \left(\frac{T^2}{T^2 + (T^*)^2} \right) \tag{63}$$

as the superfluid density calculations which we assume contain non-local contributions; where T^* is the previously defined cut-off temperature and $\rho(T)$ is the purely local superfluid density from the BCS theory [10]. We can keep in mind however, that White *et al.* [96] demonstrated that the T^* term was insensitive to fitting procedures and could vary considerably without detrimentally affecting a $n(T)$ fit.

The non-local term represents a fit to a low-T trend, rather than an equation with microscopic justification, and so represents a more phenomenological approach to supporting claims of non-local coupling effects, as a result of unconventional pairing mechanisms. To establish the presence of non-local coupling effects, we need to rearrange equation 63 to analyse just the non-local component of the data as a function of temperature as follows:

$$\frac{1-n(T)}{1-\rho(T)} = \left(\frac{T_c+T^*}{T_c}\right)\left(\frac{T^2}{T^2+(T^*)^2}\right). \tag{64}$$

$n(T)$ is the calculated value of the superfluid density using the available superfluid density data from an investigation and so is assumed to contain some non-zero, non-local contribution to the superfluid density even if this contribution is very small. ρ represents the BCS theory for the expected superfluid density, $\rho = 1-(T/T_c)^2$. Equation 64 places the two definitions of the superfluid density in a ratio of $n(T)$ and $\rho(T)$. This will leave a unitless magnitude that represents the strength of non-local coupling effects with the relationship roughly fitting a $y = x/(x+1)$ shape. Therefore the value of the non-local contribution tends towards unity with increasing temperature, which represents a complete match between ρ and n meaning zero non-local contributions (this is of course a low-T effect, so the coupling contribution should disappear for $T \to T_c$). This means that we should see a much stronger non-local contribution at low-temperature, which is in keeping with the predictions of Amin *et al.*[92, 102, 101] mentioned earlier. This approach will be used later in this work to look for non-local coupling contributions in order to analyse the likelihood

of the strong coupling d-wave case for explaining the presence of unconventional superconductivity.

1.6 Classification of superconductivity: d-wave and unconventional superconductivity

Returning to the quantum mechanical picture of superconductivity in BCS theory, we may classify the type of pairing for the Cooper pairs beyond the simple case of spin-up and spin-down electrons paired with equal and opposite momentum. We start with the pair amplitude [30] describing the pair formation in momentum-space using familiar creation and annihilation operators with spin states, σ and momentum, $\mathbf{k}$

$$g_{\mathbf{k}\sigma_1\sigma_2} \equiv \langle \hat{c}_{-\mathbf{k}\sigma_1} \hat{c}_{\mathbf{k}\sigma_2} \rangle \tag{65}$$

where the total momentum $k = (\mathbf{k}_1 - \mathbf{k}_2)$. The Pauli principle requires that under spin or momentum exchange, the pair amplitude is anti-symmetric such that

$$g_{\mathbf{k}\sigma_2\sigma_1} = -g_{\mathbf{k}\sigma_1\sigma_2}. \tag{66}$$

With this we may classify a superconductor with respect to its spatial parity and spin rotational symmetry. For the case of singlet pairing, where the total spin is $S = 0$, the pair amplitude is

$$g_{\mathbf{k}\sigma_1\sigma_2} = \begin{pmatrix} 0 & g_{\mathbf{k}} \\ -g_{\mathbf{k}} & 0 \end{pmatrix}_{\sigma_1\sigma_2} = g_{\mathbf{k}}(i\Sigma^2)_{\sigma_1\sigma_2} \tag{67}$$

Where we can equivalently relate $g_{\mathbf{k}}$ to Equation 52 as $g_{\mathbf{k}} = \frac{1}{2}[g_{\mathbf{k}\downarrow\uparrow} - g_{\mathbf{k}\uparrow\downarrow}]$ and Σ^2 is a Pauli spin matrix (Σ_x, Σ_y or Σ_z). Equation 66 requires that, with respect to the momentum, even parity is maintained. Simply put in spatial terms: $g_{-\mathbf{k}} = g_{\mathbf{k}}$. To get to the crux of the matter regarding the definition of s, d and p-wave

superconductivity we must look at the spherical harmonic description of our pair amplitude:

$$g_{\mathbf{k}} = \sum_{m=-l}^{m=l} a_{lm} Y_{lm}(\hat{\mathbf{k}}) \tag{68}$$

The spherical harmonics are described by Y_{lm}, with the orbital angular momentum l and the z-projection m. We can classify the pairing mechanism using the orbital angular momentum, l. For the case of singlet pairing ($S = 0$), l may take the values of 0, 2, 4, etc. We may label these states as s-wave ($l = 0$), d-wave ($l = 2$) and so on. So we may define d-wave pairing as spin singlet ($S = 0$) pairing with orbital angular momentum $l = 2$, consequently we will have a superconducting Cooper pair state with non-zero net momentum.

BCS pairing is often described as the s-wave case, previous defined by spin orbitals ($l = 0$). To be classified as a BCS superconductor the BCS transition must satisfy the following two characteristics simultaneously. Firstly, formation of bosons by the pairing of electrons (the Cooper pairs), and secondly the condensation of these bosons into a ground state which is distinctly characterised by being macroscopically phase coherent. This is similar to a Bose-Einstein Condensate (BEC). However, this doesn't preclude the case of the formation of Cooper pairs and condensation into phase coherence do not happen simultaneously. Thus it is possible to have pair formation above T_c but phase coherence setting in below T_c creating a pseudogap [31]. Higher orbitals, such as $l = 2$ in the d-wave case, can produce a non-isotropic gap over the Fermi surface. However, the presence of unconventional superconductivity is not limited to the higher orbital cases. Primarily the definition of unconventional superconductivity is an argument of symmetry in the gap structure with respect to the Fermi surface, which we will explore in the subsequent section.

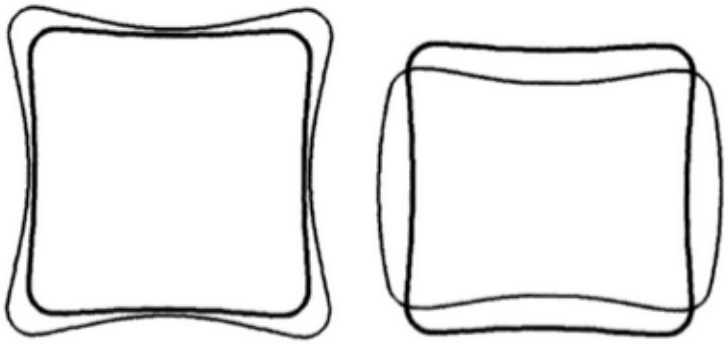

(a) (b)

Figure 2: Diagrams of the Fermi surface symmetry given the nature of the pairing mechanism. (a) The Fermi surface of a conventional superconductor. The thick line is the Fermi surface cross-section, the thin line is the amplitude of the order parameter. (b) The Fermi surface of an unconventional superconductor. The thick line is the Fermi surface, the thin line is the amplitude of the order parameter. The order parameter has less symmetry than the Fermi surface [66].

1.6.1 Classification of unconventional superconductors with respect to symmetry

As established in the BCS description of superconductivity, the Fermi sea is unstable to the formation of bound pairs, irrespective of how weak the binding strength of the pair is, provided that it is attractive. The pair potential is characterised by the attractive interaction $V_{\mathbf{k}p}^{(s)}$ and combines the pair amplitudes of the scalar and vector averaged pair amplitudes, $g_{\mathbf{k}}$ and $\boldsymbol{g}_{\mathbf{k}}$, respectively. These pair amplitudes are combined into the following pair potentials:

$$\Delta(\mathbf{k}) = -\sum_{p} V_{\mathbf{k}p}^{(0)} g_p \tag{69}$$

$$\mathbf{d}(\mathbf{k}) = -\sum_{p} V_{\mathbf{k}p}^{(1)} \boldsymbol{g}_p \tag{70}$$

These can also be referred to as the order parameters of the superconducting phase. We may now relate these to the maximum value of the temperature dependent pair potential $\Delta_0(T)$ with a momentum dependent orbital component $f(\mathbf{k})$

$$\Delta(\mathbf{k}) = \Delta_0(T) f(\mathbf{k}) \tag{71}$$

$$\mathbf{d}(\mathbf{k}) = \Delta_0(T) \mathbf{f}(\mathbf{k}) \tag{72}$$

With this description we can compare the symmetry of the orbital component of the pair amplitude to the symmetry of the Fermi surface. If the symmetries are the same then we may describe the superconductor as conventional. However, if there is different symmetry between the orbital component and the Fermi surface then we can classify the superconductor as unconventional.

To express this in terms of symmetry groups, we begin with the symmetry group G which describes the given point symmetry of the superconducting solid. Then there is the time-reversal symmetry of the superconducting transition, R and the gauge symmetry, $U(1)$. The superconducting gap defines a coherent state with Cooper pairs sharing a coherent phase, this phase is described by the wavefunction of the Cooper pair. To minimise energy costs at the phase gradients, we say the phase is practically constant within the system. This phase parameter defines a long-range-order that breaks gauge symmetry. Thus we develop the full symmetry of the normal state, described by $\Gamma = U(1) \times R \times G$. In a conventional superconductor only the gauge symmetry is broken at the superconducting transition. However in unconventional systems the point-symmetry properties are also broken. Consequently, this broken symmetry can lead to nodes or zeroes in the order parameter. These manifest as points or lines along the Fermi surface where the order parameter vanishes. This creates gapless points on the Fermi surface.

As a consequence we have to account for a gapless excitation spectrum across the Fermi surface. This has been shown to alter the low-temperature behaviour of physical properties in the superconductor. Specifically, it has been categorised by Volovik [32] that the heat capacity dependence, with respect to temperature, changes depending on the symmetry of the order parameter with respect to the Fermi surface.

For conventional superconductors an exponential relationship is observed: $C(T) = C_0 e^{(-\Delta/k_B T)}$, but for unconventional superconductors there is instead a power law: $C(T) \sim T^n$ where n is determined by the topology of the nodes or zeros in the order parameter. For example, T^2 behaviour of the specific heat in the superconducting state indicates line nodes, whereas T^3 behaviour is indicative of point nodes in the order parameter. This has been both confirmed by experimental fits and classified theoretically by Volovik and Gor'kov [32]. The crux of the theoretical framework is based on the availability of states at low temperature. In systems with nodes it is always possible to excite quasiparticles at any temperature. This means that line nodes have a greater capacity than point nodes for these types of excitations at low temperature. Overall, the net effect is nodal systems are much more sensitive to variation in temperature in the low-T regime.

1.7 Upper critical field in Type-II superconductors

There are two mechanisms for collapsing the superconducting mixed state in a Type-II superconductor. The first and most common form is through orbital-field limiting. The second, less common, mechanism is through Pauli limiting. The application of a field higher than either of the aforementioned limits will result in the destruction of the superconducting mixed state.

Orbital limiting describes the emergence of the VL and how the density of the VL determines the destruction of the mixed state. In the mixed state, supercurrents form in vortices around the flux line cores. This screens the bulk of the superconductor from the flux inside the core. In the mixed state, the size of the core doesn't increase with field, but the flux core density does increase. Eventually, the density of these cores is sufficient that the cores overlap. At this point the material is now composed of only normal regions (the flux cores) as the cores are no longer screened from the bulk. In this state we may say that the orbital limiting field has been reached and the material is no longer superconducting. We have previously found

this field by linearising the first GL equation 24, so we may re-write the solution as

$$\mu_0 H_{c_2}^{Orb} = \frac{\Phi_0}{2\pi\xi^2(T)} \tag{73}$$

The other mechanism, Pauli limiting, is caused by Zeeman splitting of single electron energy levels under a sufficiently high magnetic field. In the normal state under a magnetic field, spins align parallel or anti-parallel to the applied field lines through the material. However, the Cooper pairs in the spin singlet superconducting state must be negligibly susceptible to spin polarisation in order to maintain superconductivity. The field required to polarise a Cooper pair must be energy equivalent to the condensation energy or larger. Once this is field is reached, the Pauli-limited upper critical field, the superconductivity is destroyed. Chandrasekhar [33] and Clogston [34] estimated this field to conform to the following relation

$$\mu_0 H_{c_2}^{P} = \frac{\sqrt{2}\Delta}{g\mu_B} \tag{74}$$

Where g is the electron g-factor, $g = 2$, μ_B is the Bohr magneton and Δ is the previously defined superconducting gap. One may compare the effects of these two mechanisms in destroying superconductivity by the Maki ratio

$$\alpha_M = \sqrt{2}\frac{B_{c_2}^{Orb}}{B_{c_2}^{P}}. \tag{75}$$

For the majority of superconductors Pauli-limiting is a small contribution to the destruction of superconductivity at high fields, such that $\alpha_M \ll 1$. Materials that exhibit heavy fermion behaviour, where the effective mass of the electron is an order of magnitude larger than the electron mass, often exhibit strong Pauli-limiting behaviour (also referred to as a paramagnetic effect). Evidence for a material having dominant paramagnetic or orbital effects is in the nature of the transition from the mixed to the normal state near H_{c_2} and T_c. On approaching H_{c_2} if the phase

transition is of the second order then the orbital-limiting is the dominant mechanism, If the phase transition is first-order then Pauli-limiting is dominant.

1.8 Multigap superconductivity

Later in this thesis we will be looking at evidence for multiple gaps in superconductors, specifically $TlNi_2Se_2$. There are superconductors that have more than one superconducting gap function such as the borocarbides and oxypnictides. The G-L theory for this kind of system is outlined by Askerzade [35] and Orlova *et al.* [36], which we will briefly cover here.

Using the G-L theory and starting with equation 20 as a basis, we may write the free energy of a two-gap system as:

$$F[\Psi_1, \Psi_2] = \int d^3r (F_1 + F_{12} + F_2 + \frac{H^2}{8\pi}) \tag{76}$$

where F_i has the familiar G-L definition of

$$F_i = \frac{\hbar^2}{4m_i} \left| \left(\nabla - \frac{2\pi i \mathbf{A}}{\Phi_0} \right) \Psi_i^2 \right| + \alpha_i(T) \Psi_i^2 + \frac{\beta_i}{2} \Psi_i^4 + c.c. \tag{77}$$

and

$$F_{12} = \epsilon(\Psi_1 \Psi_2^* + c.c.) + \epsilon_1 \left(\left(\nabla + \frac{2\pi i \mathbf{A}}{\Phi_0} \right) \Psi_1^* \left(\nabla - \frac{2\pi i \mathbf{A}}{\Phi_0} \right) \Psi_2 + c.c. \right) \tag{78}$$

where i denotes either band one or two so F_i is the free energy of the separate bands. The coefficient α_i is similarly defined as for Equation 20, $\alpha_i = \gamma_i(T - T_{c_i})$, while γ_i is a constant of proportionality. Once again β has the same definition as previously defined in the G-L theory. The terms ϵ and ϵ_1 describe the inter-band mixing of the two order parameters and their respective gradients. In the same vein as Equation 24, we may minimize the free energy in order to yield the G-L differential equations for two-gap superconductors. We maintain one dimension as

before with $\mathbf{A} = (0, H_x, 0)$ for the following results

$$-\frac{\hbar^2}{4m_1}\left(\frac{d^2}{dx^2} - \frac{x^2}{l_s^4}\right)\Psi_1 + \alpha_1\Psi_1 + \epsilon\Psi_2 + \epsilon_1\left(\frac{d^2}{dx^2} - \frac{x^2}{l_s^4}\right)\Psi_2 + \beta_1\Psi_1^3 = 0 \tag{79}$$

$$-\frac{\hbar^2}{4m_2}\left(\frac{d^2}{dx^2} - \frac{x^2}{l_B^4}\right)\Psi_2 + \alpha_2\Psi_2 + \epsilon\Psi_1 + \epsilon_1\left(\frac{d^2}{dx^2} - \frac{x^2}{l_B^4}\right)\Psi_1 + \beta_1\Psi_2^3 = 0 \tag{80}$$

where the coefficient l_B is a characteristic length term that governs quantum phenomena in magnetic fields. It is also known as the magnetic length term. It is related to the applied field: $l_B^2 = \frac{\hbar}{eB}$. For example for an electron under $B = 1$ T, we get $l_B \approx 2.5 \times 10^{-8}$ m. If we consider using $\Psi_i(\mathbf{r}) = |\Psi_i(\mathbf{r})|e^{(j\phi_i(\mathbf{r})}$ in Equations 76 and 78, where ϕ_i is the phase of the order parameters, we may obtain the equilibrium values of the moduli squared of the order parameters without an applied magnetic field.

$$|\Psi_{10}|^2 = -\frac{\alpha_2^2(T)(\alpha_1(T)\alpha_2(T) - \epsilon^2)}{\epsilon^2\beta_2\alpha_1(T) + \beta_1\alpha_2^3(T)} \tag{81}$$

$$|\Psi_{20}|^2 = -\frac{\alpha_1^2(T)(\alpha_1(T)\alpha_2(T) - \epsilon^2)}{\epsilon^2\beta_1\alpha_2(T) + \beta_2\alpha_1^3(T)} \tag{82}$$

We may also define the phase difference between the two order parameters at equilibrium as well with the following:

$$\cos(\phi_1 - \phi_2) = \begin{cases} 1 & \text{if } \epsilon < 0 \\ -1 & \text{if } \epsilon > 0 \end{cases} \tag{83}$$

where ϕ here is the phase of a single gap.

There are additional consequences to having multiple gaps. The existence of more than one gap will generate a penetration depth associated with each gap, λ_i. These gaps will not likely have the same critical field and temperature associated with them. These additional variables need to be considered and account for the superconducting state acting like the superposition of two or more states, due to the

existence of multiple non-identical gaps. A consequence of this is that these gaps need not have the same value and thus H_{c_2} and T_c will be different for each gap. This introduces discontinuities in the superconducting state where one gap may be suppressed by a sufficiently high field but a larger gap is not, meaning a portion of the Cooper Pairs associated with the smaller gap are now normal. In addition, should one or more of these gaps be strongly associated with a particular orientation in the Fermi surface, this will introduce a directional dependence and anisotropy into the superconducting state. A good example of this is seen in KFe_2As_2, where two gaps are associated with the **c**-axis and **ab**-plane of the crystal structure, respectively; this introduces a high level of anisotropy as a result [91, 86]. It is also not necessary that two or more gaps share the same symmetry over the Fermi surface as well.

2 SMALL-ANGLE NEUTRON SCATTERING FROM MAGNETIC STRUCTURES - EXPERIMENTAL METHODS

2.1 Introduction to small angle neutron scattering

In the previous section we have introduced superconductivity and the concept of the VL. In order to investigate the superconductor and the VL we require a magnetic probe that is sensitive to the VL. It is in the use of neutrons that we find such a magnetic probe, given that neutrons have no charge, generally weakly interact with matter but have a magnetic moment. It is with the technique of neutron scattering that we may probe the VL and observe changes with respect to field, temperature and angle of rotation.

Small-angle neutron scattering (SANS) is an effective Bragg scattering method for probing structures of the order of $10^1 - 10^3$ Å. Neutrons possess a magnetic moment (they are spin 1/2) and so can be affected by the presence of magnetic fields, but without being perturbed by the presence of electric fields. Neutrons also have complex relationships for the scattering and absorption cross sections with respect to nuclear mass, this does makes neutrons suitable for heavier elements (unlike X-rays) but can make materials like hydrogen problematic.

We can derive the wavelength requirements for Bragg diffraction by calculating the lattice parameter for a VL using:

$$a = \sqrt{\frac{\Phi_0}{B}\sin(\beta)} \tag{84}$$

where a is the lattice parameter, Φ is the magnetic flux quantum, B is the applied field and β is the angle for the lattice shape (so 60° for a hexagon). If we choose a

field of $B = 1$ T for a hexagonal VL then $a = 480$ Å. This is significantly larger than the underlying lattice parameter of a crystal which will be of the order of $3 - 10$ Å. If we insert this into the Bragg equation:

$$n\lambda = 2d\sin(\theta_B) \tag{85}$$

with a thermal neutron wavelength of $\lambda \approx 10$ Å and setting $d = a$ then we get a Bragg angle of $\theta_B \approx 1°$. This technique is very useful for many mesoscopic structures, especially periodic magnetic structures such as superconducting VLs. An example of the neutron scattering apparatus can be seen in Figure 3.

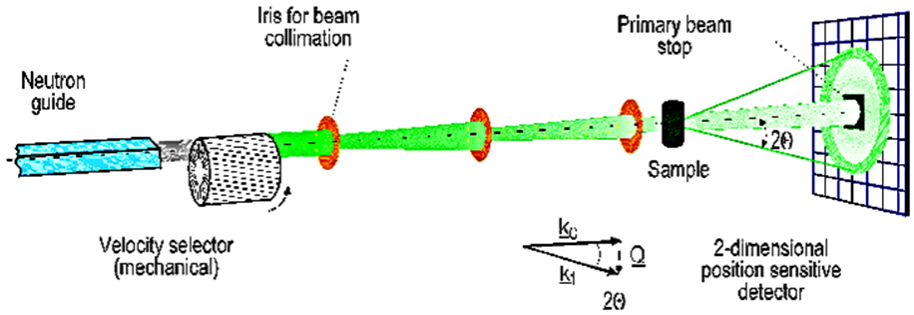

Figure 3: Instrumentation for a SANS investigation of a sample. This specifically shows the internal functioning of the SANS-I instrument at SINQ , PSI, Switzerland. Image sourced from [38].

2.2 Scattering theory for an ideal periodic potential

In order to set up scattering theory for SANS studies of the VL we must begin with a framework in quantum mechanics with some arbitrary periodic potential. Overall this can be described by the following Schrödinger equation for a neutron:

$$\left[\frac{-\hbar^2}{2m_n}\nabla^2 + V(\mathbf{r})\right]\Psi(\mathbf{r}) = E_n\Psi(\mathbf{r}). \tag{86}$$

Here we have the neutron mass m_n, the neutron energy E_n and the wavefunction $\Psi(\mathbf{r})$. To bring in a periodic scattering potential we use $V(\mathbf{r})$, but we need to maintain the case of weakly interacting scattering by applying the Born approximation,

so we use $V(\mathbf{r})$ as a perturbation. By doing this we keep the scattering amplitude simple and proportional to the Fourier transform of $V(\mathbf{r})$ with respect to reciprocal space q.

Following on from this premise, the probability of a change in neutron momentum can be described by Fermi's Golden Rule

$$\Gamma_{k_i \to k_f} = \frac{2\pi}{\hbar} \left| \langle \mathbf{k}_f | V(\mathbf{r}) | \mathbf{k}_i \rangle \right|^2 \rho_f \tag{87}$$

where $\mathbf{k}_i$ and $\mathbf{k}_f$ are the initial and final neutron wavevectors, respectively with $|\mathbf{k}\rangle$ as the wavefunction of the neutron. We represent the final density of states for the neutron to be ρ_f, with the assumption of energy conservation for the whole system and a lack of dependence on the neutron spin.

For a scattering event we must consider the time-dependent differential cross-section, which represents the probability for a given neutron to be scattered into a solid angle. We use the following,

$$\frac{d\sigma}{d\Omega} = \frac{1}{\phi_n d\Omega} \sum_{\mathbf{k} \in d\Omega} \Gamma_{\mathbf{k}_i \to \mathbf{k}_f}, \tag{88}$$

where $d\Omega$ is the solid angle and ϕ_n is the neutron flux. If we take equation 87 and write it in standard form (rather than Dirac notation) and insert it into equation 88 we obtain the following representation of scattering within the framework of quantum mechanics:

$$\frac{d\sigma}{d\Omega} = \left(\frac{m_n}{2\pi\hbar^2} \right)^2 \left| \int e^{(-i\mathbf{k}_f \cdot \mathbf{r})} V(\mathbf{r}) e^{(i\mathbf{k}_i \cdot \mathbf{r})} d\mathbf{r} \right|^2 . \tag{89}$$

The previous value of ρ_f has been normalised in the above calculation to give $\left(\frac{m_n}{2\pi\hbar^2}\right)^2$ [37]. To bring in a periodic potential we need to define $V(\mathbf{r})$ fully:

$$V(\mathbf{r}) = \sum_j^N \hat{V}(\mathbf{r} - \mathbf{R}_j) \tag{90}$$

where N is the number of weak scatterers in an array and $\mathbf{R}_j$ is the centre of the scattering array. Then we define $\mathbf{r}_f = \mathbf{r}_i - \mathbf{R}_j$ and insert the full description of the potential into equation 89 with the definition of the scattering vector $\mathbf{q} = \mathbf{k}_i - \mathbf{k}_f$ to get the following

$$\frac{d\sigma}{d\Omega} = \left(\frac{m_n}{2\pi\hbar^2}\right)^2 \left| \int \hat{V}(\mathbf{r}_f) e^{(i\mathbf{q}\cdot\mathbf{r}_f)} d\mathbf{r}_f \sum_j^N e^{(i\mathbf{q}\cdot\mathbf{R}_j)} \right|^2 . \tag{91}$$

The above can be written for any scattering system with a periodic potential of weak scatterers and condensed in the simpler representation as

$$\frac{d\sigma}{d\Omega} = |F(\mathbf{q})|^2 S(\mathbf{q}) \tag{92}$$

where $S(\mathbf{q})$ is the structure factor and $F(\mathbf{q})$ is the form factor. The structure factor describes how the neutrons are scattered by the periodic potential

$$S(\mathbf{q}) = \left| \sum_j^N e^{i\mathbf{q}\cdot\mathbf{R}_j} \right|^2 . \tag{93}$$

The form factor describes the scattering amplitude of a single scattering element in the array of weak scatterers

$$F(\mathbf{q}) = \frac{m_n}{2\pi\hbar^2} \int \hat{V}(\mathbf{r}) e^{(i\mathbf{q}\cdot\mathbf{r})} d\mathbf{r} \tag{94}$$

and effectively describes the Fourier transform of the scattering potential.

2.3 Small-angle neutron scattering from a VL

We now need to develop the general scattering theory in the previous section in such a way that it applies to scattering from a periodic magnetic potential, in our case a VL. This means developing the previous differential scattering cross section from equation 92 to contain magnetic field terms for the periodic potential. The

scattering potential can be described by the following

$$\hat{V}(\mathbf{r}) = -\gamma\mu_N B(\mathbf{r}) \tag{95}$$

where $\gamma = 1.92$ is the unitless gyromagnetic ratio for a neutron, μ_N is the nuclear magneton and $B(\mathbf{r})$ is the field distribution of the VL. For a VL, in the ideal case, there is only a single field component along the $\mathbf{c}$ axis as a result of a field applied along $\mathbf{z} \parallel \mathbf{c}$ so $\mathbf{B} = (0, 0, B)$. We can now begin to adopt equation 92 to describe the VL case for the differential cross section:

$$\frac{d\sigma}{d\Omega} = \left(\frac{m_n}{2\pi\hbar^2}\right)^2 \gamma^2\mu_N^2 \left| \int B(\mathbf{r}) e^{(i\mathbf{q}\cdot\mathbf{r})} \right|^2 S(\mathbf{q}). \tag{96}$$

We have provided a form factor by defining the periodic potential of the VL, we now need to define the structure factor. This means summing over the scattering potential of the VL at each of their positions, signified by $\mathbf{R}_j$. Given that the vortices are parallel to the field direction in $\mathbf{z}$ and can be interpreted as finitely-sized rods, we can use the following vector: $\mathbf{R}_j = \mu a\hat{\mathbf{x}} + \nu b\hat{\mathbf{y}}$. The structure factor can therefore be defined as

$$S(\mathbf{q}) = \left| \sum_{\mu=0}^{M-1} e^{(i\mu a q_x)} + \sum_{\nu=0}^{M-1} e^{(i\nu b q_y)} \right|^2 \tag{97}$$

where $M = \sqrt{N}$ (where N are the number of points at which there is a vortex), μ and ν are the dummy variables for the x and y directions and a and b are also the respective magnitudes for this vector description. As this description of the structure factor is a series of exponentials, we may combine these into trigonometric functions and instead write

$$S(\mathbf{q}) = \frac{\sin^2(aq_xM/2)\sin^2(bq_yM/2)}{\sin^2(aq_x/2)\sin^2(bq_y/2)} \tag{98}$$

We can simplify the conditions by assuming N is very large and at these N

points the structure factor is very sharp and delta-like and zero everywhere else. The locations of these points of sharp amplitude can be described with Miller indices notation as a vector,

$$\mathbf{G}_{h,k} = 2\pi \left(\frac{h}{a}, \frac{k}{b} \right) \tag{99}$$

where $\mathbf{G}_{h,k}$ is a reciprocal lattice vector for the VL. For N number of vortices and the assumption that the amplitude is effectively a delta-function at $\mathbf{G}_{h,k}$ we may write the simplifying case:

$$S(\mathbf{q}) = \frac{8\pi^3 N}{V} \sum_{\mathbf{G}} \delta^{(2)}(\mathbf{q} - \mathbf{G}). \tag{100}$$

where V is the volume of a reciprocal lattice unit cell, and the prefactor is obtained by integrating over this unit cell. Now that we have both the structure and form factor, we may now substitute these expressions into the differential cross-section in equation 96 to give

$$\frac{d\sigma}{d\Omega} = \left(\frac{\gamma}{4} \right)^2 \frac{8\pi^3 N}{V \Phi_0^2} \sum_{\mathbf{G}} |F(\mathbf{G})|^2 \delta^{(2)}(\mathbf{q} - \mathbf{G}) \tag{101}$$

where we have included $\Phi_0 = h/2e$, the magnetic flux quantum by rearranging the prefactor in equation 96. The delta function, $\delta^{(2)}(\mathbf{q} - \mathbf{G})$ represents the condition by which elastic scattering and Bragg scattering is satisfied i.e. when $\mathbf{q} = \mathbf{G}$. This means the momentum vector of the scattering neutrons matches a reciprocal lattice vector in the VL array, whilst the Bragg condition of elastic scattering, $|\mathbf{k}_i| = |\mathbf{k}_f|$, is also held.

The presence of the delta function suggests that when the Bragg condition is satisfied in elastic scattering conditions our differential cross-section become infinite. In reality this is not the case and a Bragg reflection is finite in size. This is due to imperfections in the VL and limitations on instrumental resolution. This means we instead approach the differential cross-section with a finite volume in the reciprocal

space over which the Bragg conditions are applied. We do not measure the partial differential cross-section in an experiment though, instead the integrated intensity is measured as the reciprocal lattice vector is rotated with respect to the Ewald sphere; a concept which will be explored later in this thesis.

To generate the aforementioned integrated intensity, the partial differential cross-section needs to be integrated over all directions in real-space. This produces the total cross section of a scattering event, σ_T. This total cross section then needs to be integrated as a function of the angle of rotation that the reciprocal lattice vector goes through. From an experimental viewpoint, the differential scattering cross-section represents the final state of the neutron and the likely position it will be detected on the detector bank. What is measured is the intensity as counts per pixel on the detector, essentially setting a resolution on the detector bank as a limit to the total cross-section. Here we give the final results of the two previously mentioned integrations:

$$I(G) = \left|\frac{d\sigma}{d\Omega}\right| \frac{\lambda_n^2 \phi_n}{4\pi^2 G \cos\zeta} = \frac{2\pi V \phi_n \lambda_n^2}{\Phi_0^2 G \cos\zeta} \left(\frac{\gamma}{4}\right)^2 |F(G)|^2 \tag{102}$$

where λ_n is the neutron wavelength, ϕ_n is the neutron beam flux per unit area and ζ is the Lorentz angle; the angle between the reciprocal lattice vector and the normal to the axis of rotation. In experimental terms ϕ_n is acquired via a measurement of the direct beam. If we hold Bragg conditions and successful scattering to be true then $\mathbf{q}$ and $\mathbf{G}$ are equivalent and interchangeable. $I(G)$ represents the intensity over some parameter, usually the Bragg angle. Equation 102 is sometimes known as the Christen formula, with the notation of $q \equiv G$ [37][62] . In this case it is good practice to define the reflectivity of the VL, normalised to the neutron flux of the beam

$$R(G) = \frac{I(G)}{\phi_n A}. \tag{103}$$

where we define A as the area of the sample face illuminated by the neutron beam. A

common result can be seen in the above equations, the integrated intensity and the reflectivity are both proportional to $|F(G)|^2$ and $1/G$, respectively. Although $F(G)$ dominates the behaviour of a measured integrated intensity, it is not wholly reliable to predict a value for the form factor or integrated intensity for a given sample, as it relies on parameters that are difficult to determine. A good estimate can be predicted from sample and instrument information. For a SANS investigation of the VL, the integrated intensity is extracted from direct measurement and analysis through GRASP software (see Appendix 8.1). This process if followed by rearrangement of equation 102 for the form factor of the VL.

2.4 Ewald sphere theory

To provide a geometric and visual framework for the two previous sections it is useful to invoke the Ewald sphere interpretation of elastic scattering in reciprocal space, illustrated in Figure 4. The size of the sphere is defined by the wavevectors $\mathbf{k}_i$ and $\mathbf{k}_f$ where these are the incident and final vector of a scattering event, respectively. We define the incident wavevector as $k_i = 2\pi/\lambda_n$ and invoke the elastic scattering condition: $k_i = k_f$. The radius of this sphere is $r = k_i$. This means that if all possible $\mathbf{k}_i$ and $\mathbf{k}_f$ originate from the same point then the ends of these wavevectors all lie on the surface of a sphere. To satisfy the Bragg condition for scattering the scattering vector must be equivalent to a reciprocal lattice vector. The difference between the incident and final wavevector is known as the scattering vector: $\Delta\mathbf{k} = \mathbf{k}_f - \mathbf{k}_i$. This means, geometrically, that as the two vectors, $\mathbf{k}_f$ and $\mathbf{k}_i$, are the same length then the scattering vector must lie on the surface of the sphere with a radius of $2\pi/\lambda$. This sphere is known as the Ewald sphere.

This model works such that if the tip of the vector $\mathbf{k}_i$ is placed at the point of origin, O, of the reciprocal space then diffraction may only ever occur on points that directly lie on the surface of the Ewald sphere. Thus as one rotates a crystal the Ewald sphere rotates about the origin point of the reciprocal lattice and points

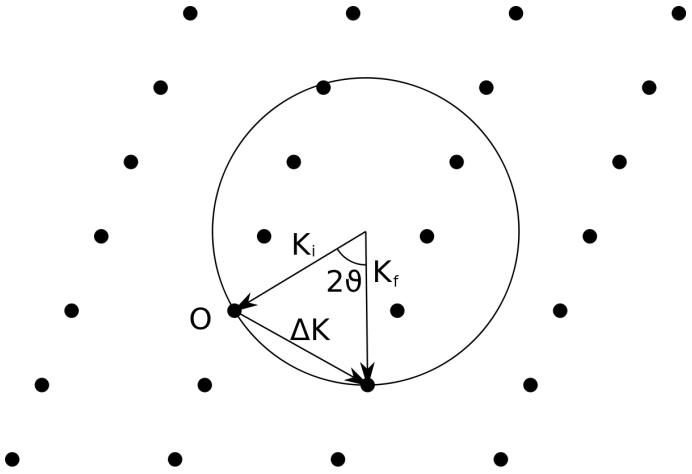

Figure 4: The array of black spots indicate the reciprocal lattice. k_i and k_f are the incoming and outgoing wavevectors, respectively. The origin, O, of the diffraction is also the point about which the sphere originates, in the sense that the initial point of scattering occurs at O (in this case a 2-D circle is used). In the case presented above only one spot satisfies the Bragg condition by lying on the Ewald sphere surface and generating the scattering vector Δk, which is equal to the reciprocal vector between the two points in the lattice. The Bragg angle of scattering is given as 2θ, which is the angle between k_i and k_f [39]. Image taken from work in [66].

of scattering within the lattice pass through the Ewald sphere, so as one rotates a crystal, peaks of scattering are detected as the sphere cycles through reciprocal lattice points within the lattice and scattering vectors are created that equal a reciprocal lattice vector as discussed before.

To connect again to the Bragg condition, the angle between the incoming and outgoing wavevectors is $2\theta_B$, where we have previously defined θ_B as the Bragg angle. In the case of SANS this angle is very small, no larger than the order of a degree. We can deduce from figure 4 that as the angle of rotation is increased more lattice vectors are satisfied. In the case of SANS, especially when looking at a VL, it is advantageous to satisfy multiple reciprocal lattice vectors at once by having an Ewald sphere that crosses through multiple points of scattering with rotation for a given radius of the sphere.

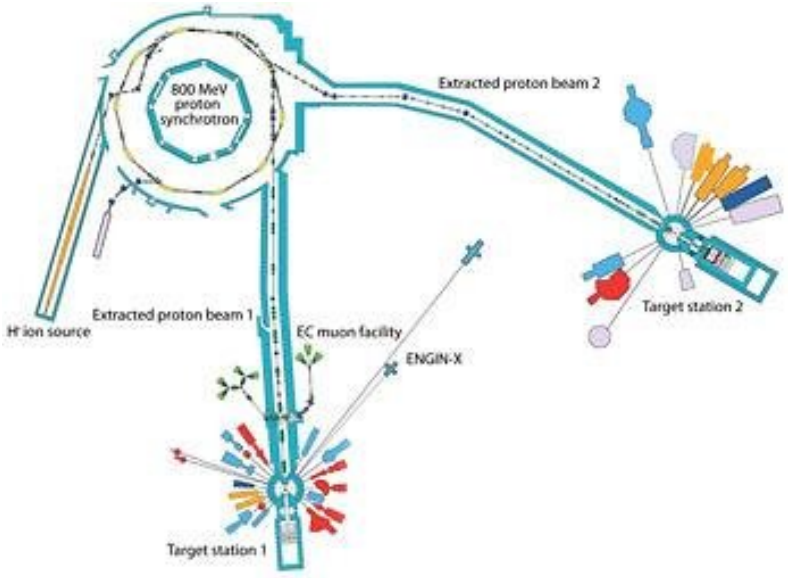

Figure 5: The layout of the ISIS spallation system with proton accelerator, target stations, and instrumentation. [42]

2.5 Instrumentation

For SANS, neutrons can be produced by two possible sources, fission and spallation. In the case of fission, this requires a nuclear fission reactor with an opening in one side. The opening will have a moderator in it to mediate the speed of the neutrons (and so their wavelength) which leads to one or more beam guides for transporting the neutrons towards scattering instruments. In the case of spallation, this process is not provided by reactor fuels. Hydrogen is ionised to produce protons, these are accelerated in pulses that collide with a target such as mercury (Oak Ridge National Laboratory [41]) or lead (Paul Scherrer Institute [40]). Upon striking the target neutrons are produced. These are similarly directed into a moderator and then into beam guides. Examples of the layout of these types of facilities are shown in Figures 5 and 6 for spallation and fission, respectively.

The instrumentation between the beam guides and the detector is summarised in Figures 3 and 7 as examples at PSI and ILL, respectively. Before the neutrons reach the detector they must first pass through a velocity selector. This is a rotating device covered in blades approximately parallel to the beam that absorb neutrons.

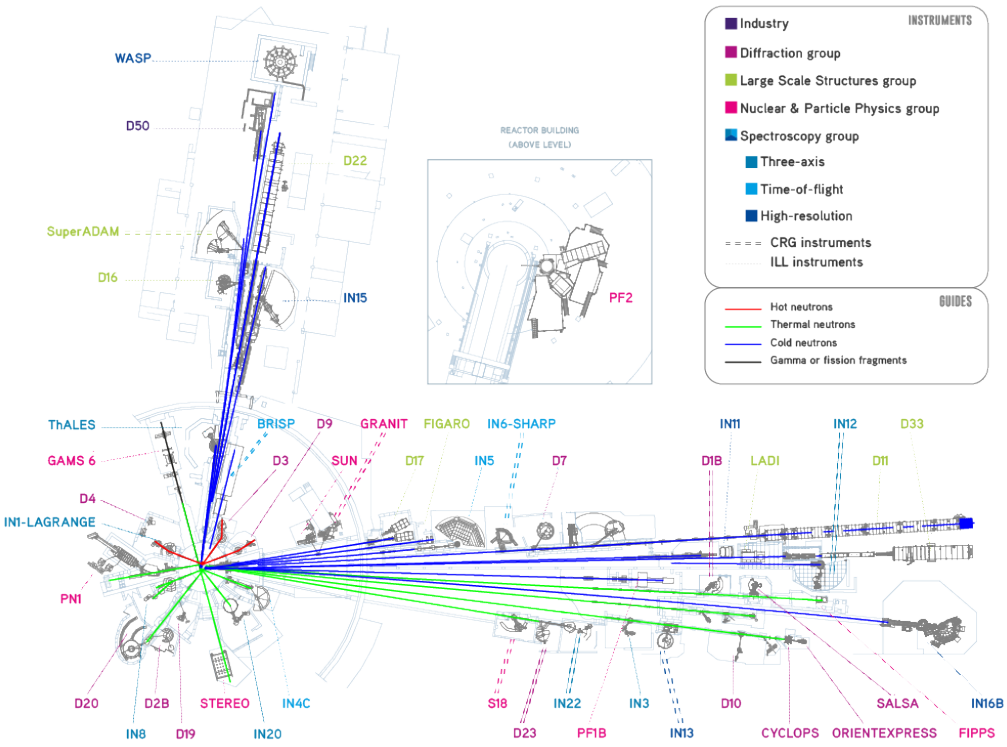

Figure 6: Layout of the fission reactor source, beam guides and instrumentation at the Institute Laue-Langevin, Grenoble, France [44].

By rotating at a set frequency, one may select neutrons of a particular wavelength with a width of about 10%. The beam is then incident upon a standard monitor: a low efficiency detector to give a measure of the incident beam. The neutrons then pass through the collimator. The collimator is divided into sections of between 1 m to 3 m of either waveguides coated in super-mirrors (highly reflective at low angles) or a collimator with a highly absorbing coating. By selecting the right combination of these sections one may control the divergence of the beam that interacts with the sample and the detector. For example, if one replaced each section of guide with the absorbing sections from the beam output towards the velocity selector, the divergence would be greatly reduced. However, this procedure also greatly reduces the flux. This often leads to a value judgement while conducting an experimental investigation on SANS beamlines to balance the count time with the resolution, given the amount of beam time available and the strength of the signal being investigated.

The detector needs to be between 4-20m from the sample in order to screen out

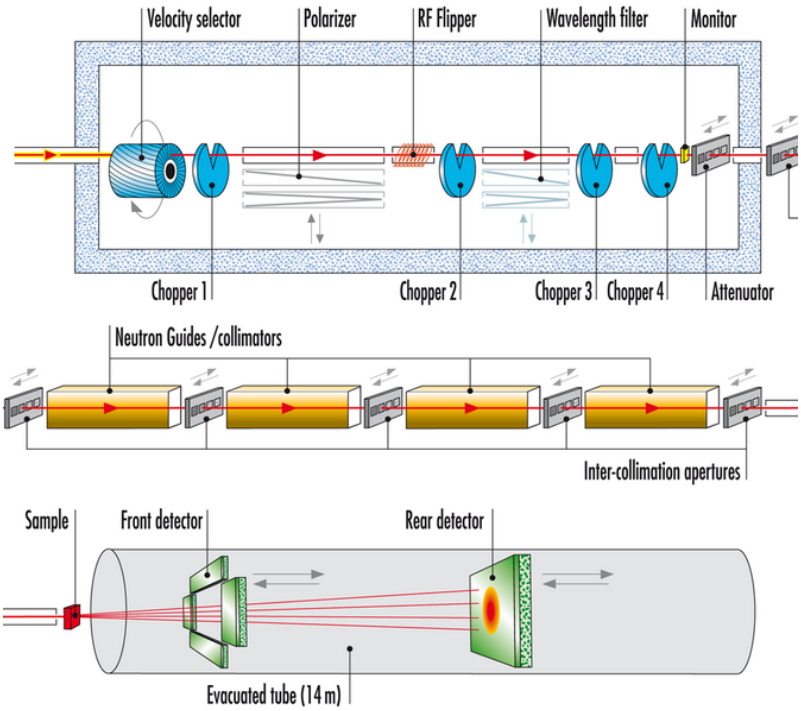

Figure 7: D33 instrumentation at the ILL, Grenoble, France. The top image shows the velocity and choppers used to select the wavelength and resolution of the wavelength. The middle image shows the collimation sections and apertures used to align and attenuate the neutron beam. The bottom image illustrates the neutron path after diffraction. The detectors are adjustable to match the q range available. The image is taken from [43].

as many direct, undiffracted neutrons as possible (additionally there is a cadmium or boron beam-stop in order to prevent the detector saturating from undiffracted neutrons). These aspects are shown in Figure 7 which illustrates the detector tube for D33, ILL, Grenoble, France (as one of the instruments used in the following investigations in this thesis) to be around 14m long. This tube is evacuated with the detector mounted on railings that can position the detector along the length of the tube, parallel to the beam. The detector contains ^{3}He which produces a 764 KeV proton and ^{3}H on absorbing a neutron. The protons then pass through a gas in the detectors which ionises when protons interact with it. This ionisation event is detected as a pulse by a grid of high voltage wires, which can pinpoint the location of the original neutron event. This grid arrangement works very intuitively building pixels to form a 2D image.

2.6 Sample and sample environment

Superconductivity investigations require that the sample be held at low, variable temperature with a variable field. This can be achieved using a cryomagnet. There are multiple designs but are generally configured by a vacuum jacket surrounding a liquid nitrogen layer, with a liquid helium bath around the evacuated sample space and potentially the magnet (depending on design and if the magnet is superconducting). The helium bath can sometimes be pumped on to achieve as low as 2 K or a dilution refrigerator insert can be used to reduce the temperature to ≈ 100 mK.

In the case of many VL experiments in SANS as with this one, the samples are arranged as a mosaic with their axes co-aligned on an Al plate, including a Cd window to reduce the total background signal, as seen in Figure 8 . The sample plate is fixed on the end of a sample stick and inserted into the sample space, which is then evacuated. The position of the sample is aligned with two Al windows on either side of the sample so there is less attenuation for the beam. Cryomagnets for this type of investigation are built with a superconducting magnet surrounding

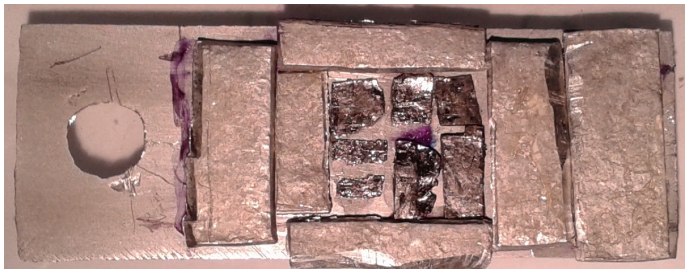

Figure 8: $TlNi_2Se_2$ mozaic made from 6 samples of approximately 2 mm by 3 mm surface area and 0.13 mm thickness. They are aligned with the **c** axis perpendicular to the mounting plate and the a and b axes co-aligned along the length and width of the mounting plate, respectively. This image is the sample setup for the preliminary measurements conducted at PSI, November 2015.

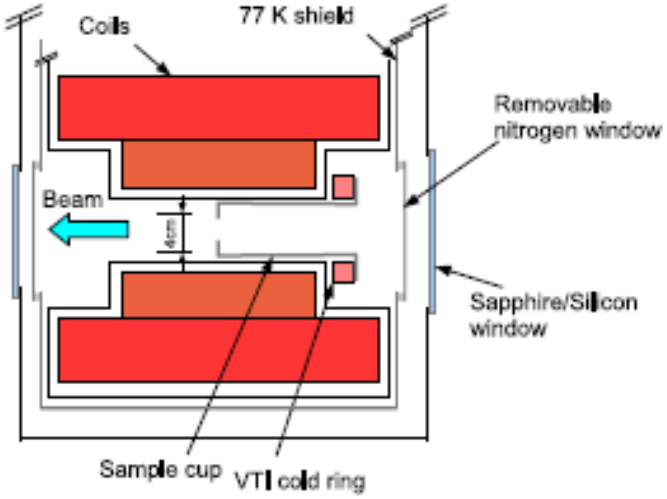

Figure 9: Side-cut view of the 17 T magnet bore for inserting the variable temperature insert (VTI). Shown here is the orientation of the magnet and sample space as well as the direction of an incoming beam of particles [63].

the sample and cooled by liquid helium. These magnets are usually a single long solenoid or a pair of solenoids that produce a field parallel to the beam, this sets up a vortex lattice in an orientation conducive to Bragg scattering with neutrons.

To adjust the angle of the cryomagnet, when using a monochromatic beam and satisfying Bragg conditions, the entire cryomagnet is mounted on an adjustable table that can move the cryomagnet in **x**, **y**, the polar angle ϕ and the azimuthal angle ω. The sample can also be rotated in ω independent of the field to a fixed displacement angle, labelled as Ω here by the use of a motor attached to the sample rod at the top of the cryomagnet.

For the preliminary investigation for $TlNi_2Se_2$ at SANS-I the MA7 (which has a maximum field of 7 T) magnet was used although the field only needed to be able to drive up to 1T. For the main investigation of $TlNi_2Se_2$ and the first investigation up to 16 T for $(Ba_{0.5}K_{0.5})Fe_2As_2$ the D33 beamline was used. The University of Birmingham 17 T cryomagnet was used for both investigations [63] with a dilution insert for $TlNi_2Se_2$. This cryomagnet has an outer vacuum jacket, then a 77 K shield of liquid nitrogen. A 4.2 K liquid helium bath surrounds the magnet [63]. To control the temperature of the sample a variable temperature insert (VTI) is applied, which the sample is connected to. The VTI consists of a thermally isolated gold-plated copper ring, which is cooled by a brass tube fed from the helium bath. The flow of helium to the VTI is regulated by a computer controlled needle valve. The cryomagnet can achieve fields of $B < 17$ T with the field aligned horizontally so that the field can be aligned approximately parallel to the neutron beam; this is shown in Figure 9. The temperature and field stability of this cryomagnet is very good and the dilution insert is stable for temperatures from 100 mK up to approximately 4 K. An Attocube© attachment allows rotation of the sample rod with respect to field alignment in the azimuthal ω plane while the cryomagnet at D33 is mounted on a table capable of adjusting the position of the instrumentation in x, y and the polar angle ϕ.

2.6.1 Dilution refrigeration in the 17 T cryomagnet

In order to support stable mK range temperature access for field and temperature scans, a dilution refrigeration insert was used for both the PSI and ILL investigations, and so we will cover the physics and function of dilution refrigeration systems here.

Dilution refrigeration is made possible by the phase separation of He when mixed as ^{3}He and ^{4}He upon cooling below a certain temperature. Referring to the phase diagram of ^{3}He/^{4}He mixtures vs temperature in Figure 10, we see that there is a λ

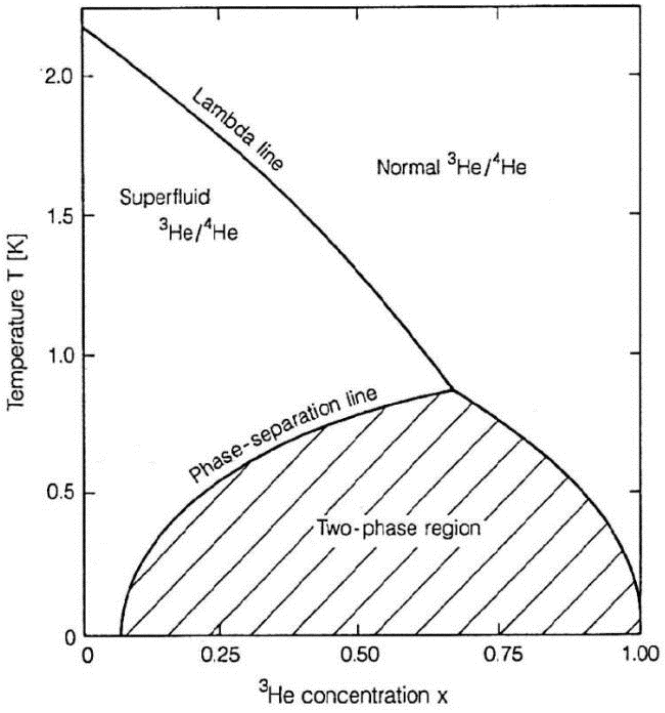

Figure 10: Phase diagram of a ^{3}He/^{4}He mixture with respect to temperature and concentration of ^{3}He as a molar fraction [64, 65].

point, or tri-critical point, at $T_\lambda = 0.86$ K for a concentration of $x_\lambda \approx 68\%$ ^{3}He [64]. The shaded region is not accessible so therefore at $T < T_\lambda$ the mixture separates into a ^{3}He rich phase and a ^{4}He rich phase, this is also called the ^{3}He dilute phase, hence dilution refrigeration. At $T < 0.86$ K we see in the Figure that there is a concentration of $x \approx 6.6\%$ where there will always be a finite fraction of ^{3}He in the dilute phase. As the ^{3}He rich side has a lower density it floats to the top and sits above the dilute phase, separated by a phase boundary. This phase boundary effectively separates an ordered, majority ^{3}He phase from a disordered majority ^{4}He phase.

The cooling power of this arrangement lies in the transfer of ^{3}He atoms from the ^{3}He rich phase to the dilute phase underneath. This is achieved by pumping on the mixture. ^{3}He will preferentially evaporate; this breaks the equilibrium in the dilute phase. We can see from the phase diagram that even at $T = 0$ K there is a finite percentage of $x \approx 6.6\%$ ^{3}He in the dilute phase. This means that while pumping on the mixture, the finite number of ^{3}He atoms in the dilute phase will

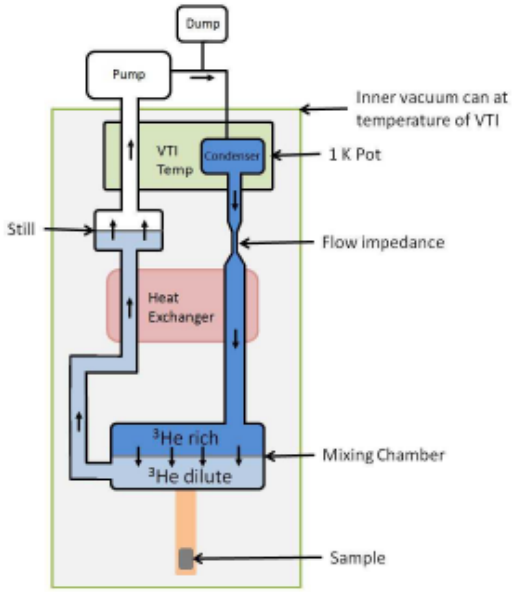

Figure 11: Schematic of a dilution refrigeration insert equivalent to that used in the $TlNi_2Se_2$ experiments for SANS at ILL and PSI. The pumps at the top are external and at room temperature [66]. The green box is the inner vacuum can which is placed into the variable temperature insert (VTI) of the cryomagnet.

evaporate, thus breaking equilibrium. To restore equilibrium ^{3}He atoms from the ^{3}He rich phase will have to cross the phase boundary to the dilute phase to replace the lost ^{3}He atoms. This process of crossing the phase boundary is endothermic [65], and the heat supplied to the ^{3}He atoms comes from the wall of the mixing chamber in contact with the mixture. For the purposes of continuous refrigeration ^{3}He is supplied to the mixing chamber using ^{3}He atoms evaporated from the dilute phase in a cyclical process. This cooling cycle can be applied for all temperatures as there is always a finite fraction of ^{3}He in the dilute phase, as seen in Figure 10. This dilution refrigeration mode was adopted for the dilution refrigeration system on the preliminary PSI experiment and the main ILL experiment for $TlNi_2Se_2$, covered later in this work.

We see in Figure 11 a schematic for a dilution refrigeration system. The diagram shows the essential components for maintaining the continuous cycle required for cooling. The 1 K pot provides initial condensation of the mixture, but is insufficient to reduce the mixture to the 0.86 K required for phase separation of the mixture.

Additional cooling of the mixture is provided by heat exchangers between the still and the ^{3}He going to the mixing chamber. Between the 1 K pot and the mixing chamber is a flow impedance, this is to apply additional pressure to the mixture to ensure condensation of the gas.

Another consideration is that the mixture ratio of the ^{3}He to ^{4}He should be chosen such that the phase separation boundary resides in the mixing chamber and, as shown in the schematic, the surface of the liquid dilute phase is in the still. This arrangement allows for ease of pumping on the liquid surface where the ^{3}He will evaporate from the dilute phase (as previously described). A technique for accelerating the cooling process is to heat the still to accelerate ^{3}He evaporation, which would accelerate the rate of endothermic exchange of ^{3}He atoms across the phase boundary if performed carefully. As described in the caption, the pumping system is external and at room temperature; evaporated ^{3}He gas passes through these pumps to be filtered and recycled back through an initial 77 K cold trap for pre-cooling before reaching the 1 K pot.

2.6.2 Preliminary calculations

To determine the suitability of SANS for an investigation the scattering and absorption cross-sections of the sample for neutrons must be known as well as an integrated intensity estimation. As an example we will use $TlNi_2Se_2$ which features later in this work and was investigated on the D33 (ILL) beamline. $TlNi_2Se_2$ has an approximate thermal neutron cross-section of 0.358 cm^{-1} and a linear attenuation factor of 1.245 cm^{-1} [45]. The samples are approximately 0.13 cm thick, mounted on 0.6 mm thick Al, so there should be few neutron losses from scattering or absorbing from the sample.

To determine the integrated intensity prediction for a measurement we look back

to the integrated intensity in equation 102,

$$I(q) = 2\pi V \lambda_n^2 \phi_n \left(\frac{\gamma}{4}\right)^2 \frac{|F(q)|^2}{\Phi_0^2 q \cos\zeta} \tag{104}$$

where $I(q)$ is the integrated intensity measured in counts $s^{-1}A^{-1}$ (where A is amps), V is the total volume of sample under investigation, λ_n is the neutron wavelength (≈ 1 nm), γ is the neutron g-factor, ϕ_n is the flux for the neutron beam. $|F(q)|$ is the form factor of the VL and is calculated later in this section in Equation 105. Here q is the magnitude of the associated reciprocal vector for the scattering and a is the maximum size of the VL. $\cos\zeta$ is the Lorentz factor, where ζ is the angle between the reciprocal lattice vector and the plane normal to the axis of rotation for the rocking curve. The magnetic flux quantum is Φ_0. However, we would need to estimate the form factor $|F(q)|$ and the Lorentz factor, by making some assumptions regarding the penetration depth and the coherence length for the former and assuming we're looking at a scattering vector normal to the axis of rotation for the latter.

The motivation for investigation is to extract the form factor of the VL, used in Equation 104 as $|F(q)|$. The form factor for the isotropic London model is [124]:

$$|F(q)| = \frac{Be^{cq^2\xi^2}}{1 + q^2\lambda_L^2} \tag{105}$$

where B is the applied field, q is the scattering vector for the VL, λ_L is the London penetration depth, ξ is the coherence length and c is an empirical core cut-off parameter taken between 0.5 and 2. The value for this is obtained from fitting the form factor data. The form factor is important as it is proportional to the superfluid density, $|F(q)| \propto \rho_s$ and the superfluid density is inversely proportional to the penetration depth squared, $\rho_s \propto 1/\lambda_L^2$. By knowing the behaviour of the superfluid density and penetration depth we may gain a deeper understanding of the superconducting state. We can also more accurately determine the coherence length with

this investigation using the following:

$$\xi(T) = \sqrt{\frac{\Phi_0}{2\pi B_{c_2}(T)}}. \tag{106}$$

By observing the melting of the flux lattice at the boundary between the normal and superconducting states we can increase the precision with which we know the coherence length.

2.7 Identification of pairing mechanisms

In order to properly model the likely pairing mechanisms we need to develop a means of analysing $I(q)$ and $F(q)$ with respect to temperature variation. For the results of the investigations of superconductors presented in this work, the temperature dependent results for the integrated intensity should be directly compared to ideal models of $I(q)$ and $F(q)$ with temperature variation, for all relevant parameters within the Christen formula. Subsequently the penetration depth can be characterised for two main pairing mechanisms: s-wave and nodal/d-wave pairing (including gap structures with line and point nodes). To do this we must apply a known framework for these pairing mechanisms. The models we will use in this work have been applied using the framework summarised by Prozorov [92], which is an accumulation and simplification of the groundwork for the more general theoretical case by Izawa, Maki *et al.* for nodal pairing with point nodes and line nodes [99, 100]. To develop the more general model that includes point and line nodes, we start with the two-fluid model of the penetration depth developed by Bardeen, Lewis *et al.*, mentioned earlier in the discussion of the London Model [5, 4, 10]

$$\lambda(T) = \frac{\lambda(0)}{\sqrt{1-t^4}}; \tag{107}$$

where $t = T/T_c$. This approach gives reasonable estimates for $\lambda(T)$, but it only represents an ideal for a clean, local BCS superconductor.

In order to develop the theory to cover a broad array of superconductors we use the framework of Prozorov, which builds upon the Lewis approach using empirical fits. The Prozorov approach describes the temperature dependent penetration depth much like the BCS two-fluid model, but with a key variation. The new framework introduces a phenomenological variation of the power law for the penetration depth as such:

$$\lambda(T) = \frac{\lambda_0}{\sqrt{1 - \left(\frac{T}{T_c}\right)^p}} \tag{108}$$

where λ_0 is the London penetration depth at zero temperature and p is a power that typically has a value between 1 and 4. In the classic BCS theory the power is often given as $p = 4$ for s-wave pairing over the superconducting gap [10]. However, as outlined by Prozorov *et al.* [92, 93, 94], previous attempts to model the penetration depth have shown that a power law, with p allowed to vary for a fit, is quite robust and when fitted can be indicative of the pairing mechanism dominant in the material. The framework outlined by Prozorov demonstrates that p takes the following values for a given pairing mechanism: $p = 2$ for s-wave and $p = 4/3$ for line and point nodes in the gap structure, including d-wave superconductivity. Empirical fits of Prozorov and two-fluid approaches have shown that $p = 4$ is not universal [92, 10, 4], with $p = 2$ being a better representation of s-wave behaviour.

If we take the $I(q)$ data and $|F(q)|$ calculations and plot them versus temperature, rather than a fit of these data sets, we can apply a null hypothesis. By using equations 104, 105 and 108 we can set the power laws for the penetration depth to represent the ideal case for each of the pairing mechanisms then see how the data compares. These elements combined in their ideal cases for each pairing mechanism, for the conditions of the investigation at the ILL on D33, produce models for the integrated intensity and form factor behaviour with respect to temperature.

The penultimate step is to insert the form factor function (equation 105) into the Christen formula (equation 104) with the other conditions of the investigation

to produce models for how the integrated intensity should look with respect to temperature variation. Looking at the form factor is useful but has its limitations due to the lack of knowledge surrounding the evolution of ξ and other terms, but by rearranging the Christen formula to calculate the form factor from the data, we do not need to know specific information about some of the terms. This null hypothesis approach is fairly robust as it avoids integrated intensity or form factor fits with large numbers of parameters, some of which not much is known about. Finally, following from this we may rearrange equation 108 to calculate the penetration depth from the form factor and apply direct fits; given the small number of parameters in equation 108 this should be trivial. This section of theory will be referenced later in the analysis of both $(Ba_{0.5}K_{0.5})Fe_2As_2$ and $TlNi_2Se_2$.

2.8 Perfecting the VL by oscillating the field

To measure at a given field-temperature point, the superconductor must be field cooled (FC), so that the field is only changed when the sample is in the normal state. This reduces the probability that the sample will be damaged when the field strength is changed or the angle of the sample is changed due to a lack of pinned flux in the normal state. However, FC can lead to imperfections in the VL because of pinning to crystal defects and impurities. This makes a reliable measurement of VL structural transitions less likely as a lack of coherence in the VL will impede the interference between scattered neutrons to produce Bragg peaks.

Dewhurst *et al.* [67] performed an investigation into oscillating or wiggling/shaking the field around the desired field in order to unpin vortices from pinning sites by applying longitudinal (shaking) and transverse (inverse shaking) procedure for the applied field in order to reduce the VL closer to a well ordered state for the field and temperature conditions applied. The longitudinal or shaking procedure is where the AC field is parallel to the applied DC field. This is applied by a sinusoidal variation of the current in the magnet. In the case of the transverse- or inverse-shaking pro-

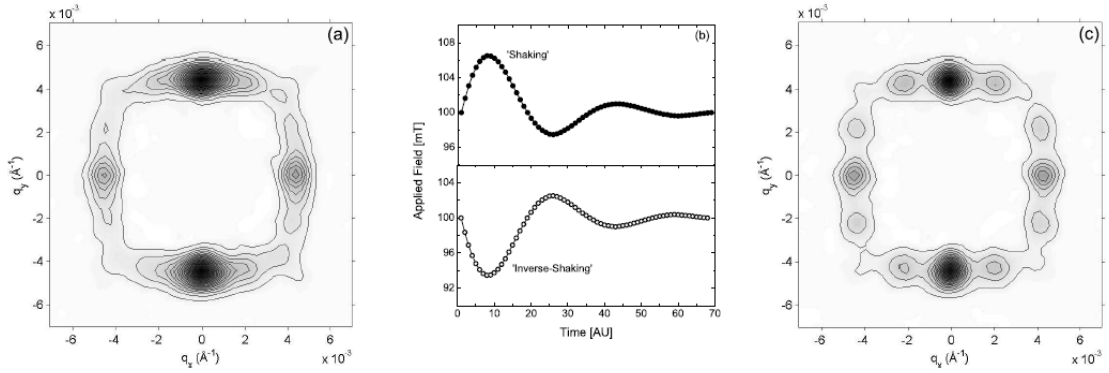

Figure 12: SANS images of the VL in YNi_2B_2C with inset of longitudinal shaking and inverse shaking field oscillations. Image (a) shows a 100 mT FC to 2 K without any shaking procedure. Image (c) shows the VL after a 10% longitudinal inverse shake after FC showing better resolution of the hexagonal vortices as they have become mobile and settled to equilibrium. Image (b) shows the shaking and inverse shaking field oscillations associated with the wiggling procedure. Image taken from work in [67].

cedure a separate split coil has to be mounted around the sample such that the AC shaking field is perpendicular to the DC applied field. There is an initial decrease in the amplitude of the field in the transverse case before following the same sinusoidal amplitude variation as the longitudinal procedure; illustrated in Figure 12.

Dewhurst found that wiggling with a frequency of 10 Hz to 100 Hz at an amplitude of 10 mT to 100 mT was sufficiently effective. This procedure works through the oscillating field acting as an alternating torque across vortices pinned to pinning sites. The torque is only felt if the vortex is pinned, so when the VL is reduced to equilibrium, no torque is felt. However, although the procedure improves orientational order for the VL, if competing forces such as the surface or background pinning are strong, then the shear and bulk moduli of the VL will be greater than the tilt modulus of the wiggling procedure. This will lead to vortices bending rather than unpinning, reducing longitudinal order for the sake of orientational order.

It was also observed that inverse wiggling (an initial reduction in the field in a cosine^2 manner) was more effective than wiggling. This is likely due to the initial reduction in field lowering the magnetic pressure and improving mobility for the

vortices. Figure 12 illustrates this procedure, as it shows an initial 'square' VL image under FC conditions with no wiggling, where the hexagonal spots are poorly resolved. Subsequently after warming again and then applying an FC cooling following by a 10% longitudinal inverse-wiggle the VL appears as a hexagonal lattice as it has now achieved equilibrium.

3 THE ROLE OF THE FERMI SURFACE AND ELECTRONIC STRUCTURE IN DETERMINING THE PAIRING SYMMETRY

As all three compounds being investigated by SANS in this thesis have the same 122 structure, also known as the $ThCr_2Si_2$-type structure [68], whereby they have the same arrangement of atoms in space but the sites are occupied by different elements. In the case of the Fe-based superconductors this is denoted by the chemical formula $AEFe_2Pn_2$ where AE is alkaline earth metal from group 2A of the periodic table. These are typically Ca, Ba, Sr or Eu. Pn is a pnictide, an element from group 15 of the periodic table. In this class of superconductor it is typically As or P. These crystals, $TlNi_2Se_2$ and the Fe-based superconductors, form in a tetragonal structure with the *I4/mmm* space group symmetry.

Since 2008 a wide family of Fe-base superconductors has emerged with structures including: 1111, 122, 111, 112, 245, 11 and others. Fe-base superconductors have a number of advantages such as high upper critical fields induced by doping, as we will see later in this work. In particular the 122 family of Fe-based superconductors that takes the specific form of $(Aa_{1-x}Bb_x)Fe_2As_2$ is of great interest given the particularly high sensitivity to doping. In this work we look at the substitution of Ba and K for Aa and Bb, respectively. This yields the parent compound $(Ba_{1-x}K_x)Fe_2As_2$, with $BaFe_2As_2$ as the fully overdoped and KFe_2As_2 the fully underdoped limits. In fact $BaFe_2As_2$ is not superconducting and requires pressure or doping to enter the superconducting regime [69].

It is vitally important to know what the variations are in the Fermi surface (FS) and band structure in each compound in order to draw comparisons. The overlaps

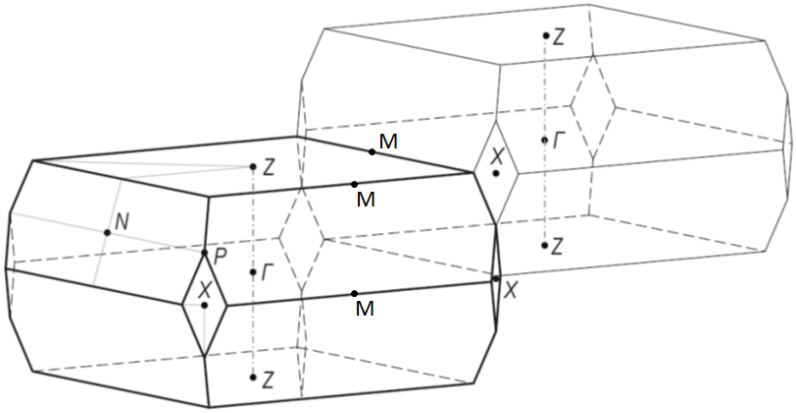

Figure 13: 1st and 2nd Brillouin Zone (BZ) of a tetragonal crystal structure [70]. This outlines the points of reference and lines of symmetry in reciprocal space when exploring the Fermi surface and band structure of the 122 materials in this work.

between the three compounds in this thesis suggests that there is likely one or more common features in the electronic structure that may explain the pairing symmetry in the superconducting state, or one or more of the superconducting properties. Similarly, investigating the differences in band structure will highlight why the variations between these very similarly structured superconductors exist. This kind of approach will allow us to make much more general statements regarding the effects of band structure and magnetic ordering on the development of the superconducting phase in materials with this common crystal structure. Overall this will allow us to contextualise any SANS findings regarding the pairing symmetry and the gap structure.

3.1 Electronic structure in KFe_2As_2

In this chapter we will illustrate and compare the electronic band structures in KFe_2As_2 using local density approximations (LDA) and angle-resolved photoemission spectroscopy (ARPES) results. In the subsequent diagrams we label bands with α, β, γ, δ, ϵ etc. These indicate the size of the surface area of the electronic band in the Fermi surface with α being the largest area. IT is common, when looking at doping effects, that these bands will shift in size and position. In these instances

the band labels are maintained for clarity, rather than reordering the band labels based on size. In Figure 13 we also show the 1st and 2nd BZ of a tetragonal crystal to illustrate the lines of symmetry and points of reference in reciprocal space when we later refer to FS and band structure measurements.

A saddle point in the electronic band structure of a material introduces interesting properties and effects, with interplays between the effective electron mass, the symmetry of the gap structure in a superconductor and the relation between these and charge/spin density waves (CDW/SDW). The flat parts of the saddle curve can be characterised as van Hove singularities (vHs) [71], as they create a singularity or non-smooth point in the density of states (DOS) due to being a point of divergence caused by the point of zero gradient in the energy spectrum $\nabla E = \hbar^2 k/m = \hbar\sqrt{2E/m}$, where the DOS is proportional to the inverse of the energy gradient, $g(k) \propto 1/\nabla E$.

ARPES measurements of KFe_2As_2 [72] indicate a vHs at -3.9 meV below the Fermi surface (E_F) with an asymmetrical peak in the density of states (DOS) due to the larger contribution from the occupied states compared to unoccupied states (which is consistent with hole-dominated systems such as KFe_2As_2). The vHs appears along the Z-A symmetry line with the saddle specifically appearing at V$(0.5\pi/a, 0)$ as shown in Figure 14. If we take the perpendicular cut we see a hole-like lobe instead with its maximum at V. Additionally these results indicate no dispersion in k_z, making this a 2-D feature dominated by the d_{xy} orbital. However, we have a temperature dependent factor on the size/height of the electron-like lobe of the saddle point. The peak position of the vHs (the bottom of the saddle in V) shifts from -3.9 meV at 0.5 K to -5.4 meV at 10 K. When these two data sets are overlapped and subtracted to account for the superconductivity, we see a superconducting gap emerge in the 0.5 K data. Crucially, the vHs is present in both the normal and superconducting phase, with a 1 meV gap feature, that disappears above 4 K, corresponding to a superconducting gap.

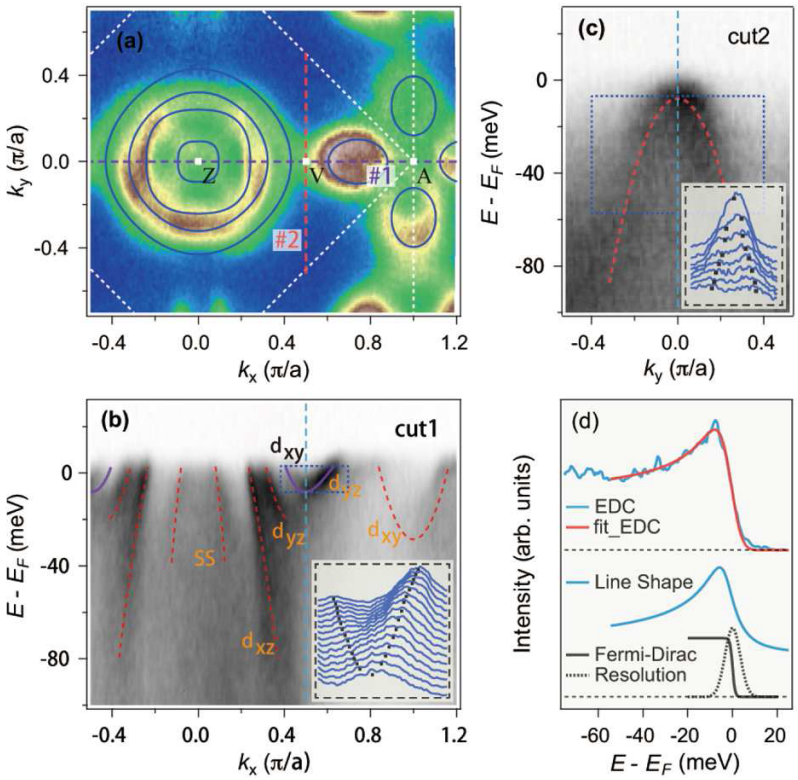

Figure 14: (a) ARPES results showing the Fermi surface intensity with $k_z = \pi$. The blue lines indicate the Fermi surfaces as a guide to the eye. (b) ARPES intensity plot for the blue dotted line direction in (a) labelled #1 and corresponding to the Z-A symmetry line. This data set shows a saddle point at V$(0.5\pi/a, 0)$, highlighted by the dotted blue square. (c) ARPES intensity plot along the direction in (a) labelled #2, which is aligned to the $(0.5\pi/a, k_y)$ symmetry line. The insets in (b) and (c) are momentum distribution curves (MDCs) taken from the areas highlighted by the dotted blue boxes. (d) Energy distribution curve going through the saddle point in (b). The lower portion of (d) indicates the theoretical components for modelling the energy distribution (an asymmetric shape, as previously discussed) [73]. All of the above measurements were made at 7 K and the images were taken from work in [72].

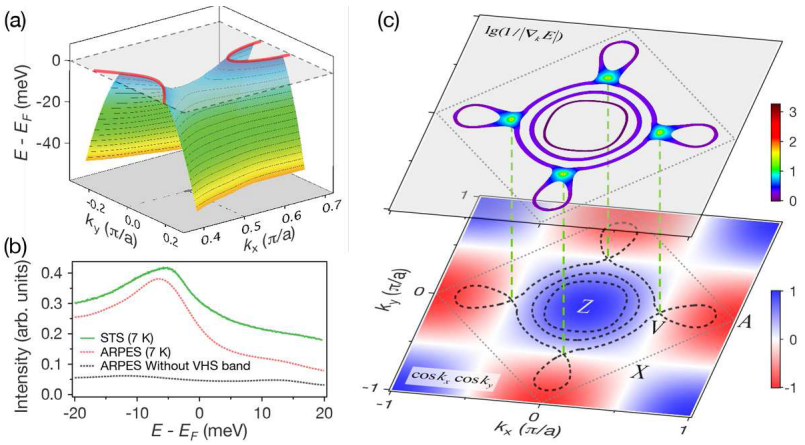

Figure 15: (a) 3-D fit from the ARPES data showing the saddle point and the band dispersion around it. (b) Comparison between DOS calculated from ARPES results and from scanning tunnelling spectroscopy (STS). (c) Top image shows the intensity plot of $\log(1/|\nabla E|)$ calculated form the ARPES results for band dispersion, corresponding to k-dependence. This is integrated with limits of ± 5 meV around the saddle point at V. The lower image is the corresponding energy contours as dotted lines showing the binding energy of the saddle points overlaid on the gap function, assuming the highly likely $s\pm$ pairing symmetry. Images taken from work in [72].

From Figure 15 we can see there is clearly a bright spot indicating a large peak in the DOS at the V point from image (c), indicating a vHs associated with each of the 4 saddle points. Additionally, the overlay on the gap function in (c) shows that the V point vHs sits exactly on the white lines, which represent the line nodes in nodal s-wave pairing, also known as $s\pm$ pairing, in the gap function. From the DOS calculations in the 1st BZ, we find that 80% of the states at E_F come from the 4 saddle points. Whilst at the same time, as we enter the superconducting state, it is found that the suppression of the DOS at zero energy is only 20%, which means that the majority of the DOS at the Fermi level are un-gapped in the superconducting state. However, in [72] it is established that the sample is very clean and as such this large amount of un-gapped DOS cannot be due to scattering from impurities.

The presence of four vHs means that the electron lobes contribute greatly to the DOS, explaining the large specific heat coefficient value γ, the Sommerfeld coefficient for free electrons. Simultaneously, the presence of the vHs at the line nodes as shown in Figure 15 means we can say that the vHs must have some sort of role in the

pairing symmetry. Previous investigations [74] indicate a multi-gap structure with the largest nodeless gap appearing on the inner hole pocket on the FS, an unconventional superconducting gap sits in an intermediate position of the FS with octet-line nodes and then on the outermost part of the FS there is a small, almost zero, gap. The octet line nodes refers to an eightfold reversal of the sign of the pairing symmetry along the node. There is evidence to suggest that Fe-pnictides show much greater overlap between nodal s-wave gap structure and the FS than other potential pairing mechanisms. Specifically in this case, and also seen in $Ba_{0.6}K_{0.4}Fe_2As_2$, we find that a gap function of $\cos k_x \cos k_y$ closely matches the FS of the Fe-pnictide family [76, 77]. The pairing function of $\cos k_x \cos k_y$ has nodal lines going through the four vHs as shown in Figure 15(c), which provides an excellent framework for describing the superconducting pairing mechanism of KFe_2As_2 and other Fe-pnictide superconductors. In [74] and [72] it is assumed that the vHs do not actually contribute much to the pairing mechanism and the $s\pm$ pairing is robust and unaffected, otherwise the vHs would contribute an additional unconventional pairing that would coexist with the $s\pm$ symmetry. This is not unreasonable as a pairing of $d_{x^2-y^2}$ would have a mechanism of $\cos k_x - \cos k_y$, which also has line nodes going through the four vHs points. We will demonstrate later with the SANS studies that the $s\pm$ picture is very strong, with weak evidence supporting any kind of d-wave pairing.

3.2 Electronic structure in doped variations of $(Ba_{1-x}K_x)Fe_2As_2$

KFe_2As_2 represents the most underdoped case for the compound $(Ba_{1-x}K_x)Fe_2As_2$, otherwise referred to as the $x = 1$ case. The doping of $BaFe_2As_2$ with K produces vastly different properties in terms of the variation in H_{c_2} and T_c due to a high level of sensitivity to doping. This would indicate that this compound is very sensitive to small changes in the electron doping levels; suggesting drastic variations in electronic band structure with little variation in the doping level, x.

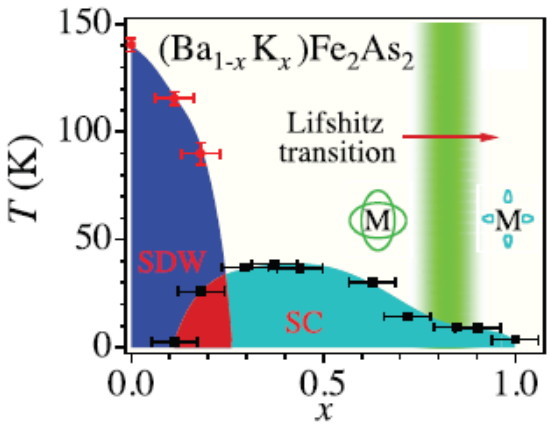

Figure 16: Phase diagram of $(Ba_{1-x}K_x)Fe_2As_2$ with respect to doping levels for various temperatures. The Lifshitz transition around the M point is highlighted in green and shows the shift in band structure around M. Image taken from work in [75].

For the case of $x = 0.4$ [75, 78], the optimally doped case ($T_c = 37$ K) for the superconducting phase and very close to our experimental case of $x = 0.5$, LDA calculations predict 3 hole-like FSs at the centre of Γ and 2 electron-like FSs centred near M; with the features dominated by the Fe 3d electrons. However, there were discrepancies found between the LDA calculations and the ARPES results, mainly due to the fact that ARPES shows, in the case of $x = 0.4$, to be strongly correlated. This is evidenced by the presence of a strong EDC peak within 1 eV of E_F from the Fe 3d orbitals (DMFT calculations on the other hand accurately predict the value of 1 eV).

As can be seen in Figure 17, the LDA calculations do not account for the saddle like feature at Γ that produces two hole-like lobes from the α and β bands around a central electron-like pocket. These lobes are also measured in the superconducting state. The α band reaches at most a peak of ≈ 20 meV above E_F.

Figure 18 (c) shows near the M bands a clear saddle point in the γ and δ bands, with the troughs of the saddles sitting at approximately 15 meV and 60 meV, respectively, below E_F. When compared across the bands, the top of the α band and the trough of the γ band saddle are only separated by ≈ 35 meV, unlike the 120 meV predicted by LDA. The bands can be summarised as: (α,β) hole-like; centred

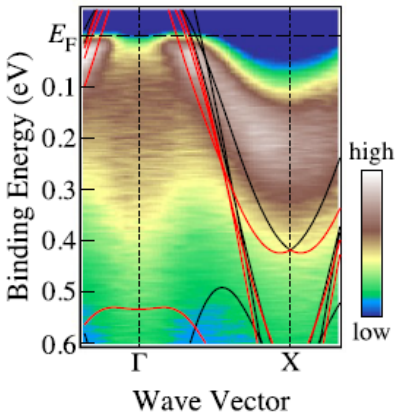

Figure 17: EDCs of $(Ba_{0.1}K_{0.9})Fe_2As_2$ from ARPES measured at $T = 50$ K. Measurements are made along the Γ-X direction with LDA calculations presented as red lines ($k_z = 0$) and black lines ($k_z = \pi$). Image taken from work in [78].

at Γ, (γ,δ) electron-like; centred at M. Investigations using ARPES conducted by Ding *et al.* [78] suggest a coherence length of $\xi_0 \approx 9 - 14$ Å, with a Fermi velocity of around $v_F \approx 3.2 \times 10^4$ ms^{-1}. A later section in this work will demonstrate that this is not far from the results of SANS investigations for $x = 0.5$, estimating the coherence length to be $\xi_0 \approx 15$ Å given an estimate of $H_{c_2} \approx 140$ T. This is not vastly different, but the value of the coherence length varies little for high critical field values due to the inverse square root dependence of ξ_0 on the field strength of the upper critical field.

We also see from the ARPES results at $x = 0.4$ in Figure 18 that the superconducting gaps are identical at α, β, γ and δ with an approximate gap value of $\Delta \approx 5.6$ meV. The following effective masses are also measured in units of m_e: $m^*_\alpha = 4.8$, $m^*_\beta = 9.0$, $m^*_\gamma = 1.3$, and $m^*_\delta = 1.3$. These values as well as the similar gaps shows there is strong band coupling and thus effective interband scattering between the FSs. Ding *et al.* suggests this likely plays a dominant role in the pairing mechanism for this material. What we can also obtain from these results is the free electron coefficient of the specific heat, $\gamma = \pi N_A k_B^2 a^2 m^*/3\hbar^2$ for each band [78]: $\gamma_\alpha = 7.2$ mJmol^{-1}K^{-2}, $\gamma_\beta = 13.6$ mJmol^{-1}K^{-2}, $\gamma_\gamma = 2$ mJmol^{-1}K^{-2} and $\gamma_\delta = 2$ mJmol^{-1}K^{-2}. The total free electron coefficient in the superconducting state is $\gamma^{SC}_{Total} \approx 32$ mJmol^{-1}K^{-2} and in the normal state is $\gamma^{N}_{Total} \approx 64$ mJ^{-1}K^{-2}mol.

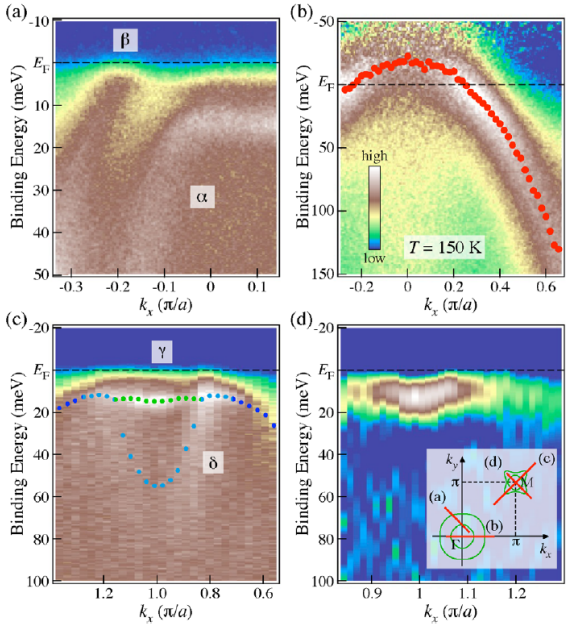

Figure 18: Intensity plots of the band structure of $(Ba_{0.6}K_{0.4})Fe_2As_2$. All dots in the following sub-plots are from energy distribution curve (EDC) peaks. (a) Plot near Γ ($T = 15$ K). (b) Plot near Γ ($T = 150$ K). (c) Plot near M ($T = 15$ K). (d) Second derivatives of the spectra near M. The inset indicates the locations of the ARPES measurements in the BZ in relation to the sub-plots (a)-(d). Images taken from work in [78].

Studies in [75] and [78] show the cases of varying $x = 0.9$ to $x = 0.4$ and the Lifshitz transition that occurs in-between. A Lifshitz transition is a change in the topology of the Fermi surface in momentum-space (k-space) [79]. We see with doping that T_c can shift from above 30 K to as low as 3 K due to the FS topology evolving with doping levels. Other ARPES studies have shown that doped compounds of $(Ba_{1-x}K_x)Fe_2As_2$ have a complex nodal superconducting gap near Γ [74], we shall see something similar in the SANS results for KFe_2As_2 later in this work. This result is consistent with investigations into the thermal conductivity at low temperature as well [80] [81]. Given the high probability of nodal s-wave pairing in high K doping compounds and the SANS investigations presented later in this work showing evidence that at $x = 0.5$ we see BCS s-wave pairing, it would be reasonable to suggest that there is likely a fundamental change in the superconducting order parameter between $x = 1$ and $x = 0.5$. An investigation by Xu *et al.* [82] suggests

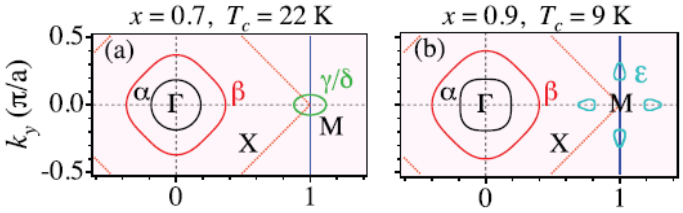

Figure 19: (a) FS of $(Ba_{1-x}K_x)Fe_2As_2$ for x = 0.7. (b) FS of $(Ba_{1-x}K_x)Fe_2As_2$ for x = 0.9. Images taken from work in [82].

that the fundamental change occurs somewhere below $x = 0.9$ in the doping regime, with $x = 0.4$ exhibiting nodeless gap behaviour similar to the $x = 0.5$ compound studied under SANS in the previous chapter.

In [82] it is demonstrated that as the doping level enters the range $0.8 < x < 0.9$ upon increasing x, in the vicinity of the centre of M, four small off-centre FS pockets emerge as hole-like lobes that are then measurable at $x = 0.9$. At this doping level the superconducting gaps at $T = 0.9$ K are isotropic, with $T_c = 9$ K. The emergence of the lobes and the evolution of the FS is evident in Figure 19. This critical temperature is not too far from the value for KFe_2As_2 which demonstrates that either side of the FS topology rearrangement, the Lifshitz transition, the pairing symmetry of the superconducting gap does not change very much as a result according to the inference in [82]. Later in this work we will be analysing the SANS investigations into $x = 0.5, 1$ compounds and comparing their pairing symmetries to the work discussed in this chapter. A shift in the pairing symmetry between $0.5 < x < 1$ would likely be a result of this Lifshitz transition.

Further to this, in [82] it is demonstrated that due to the Lifshitz transition the intensity of the off centre M electron-like lobes that cross E_F is similar between the $x = 0.9$ and $x = 1.0$ case compared to the $x = 0.7$ case. In addition, the lobes at M peak slightly below E_F in the $x = 0.7$ case. This suggests that doping more K pushes the electronic bands above E_F. In fact Xu *et al.* [82] cannot rule out a small electron pocket nested at M caused by hole doping towards $x = 1.0$. We have already demonstrated the existence of a saddle point and a van Hove singularity in

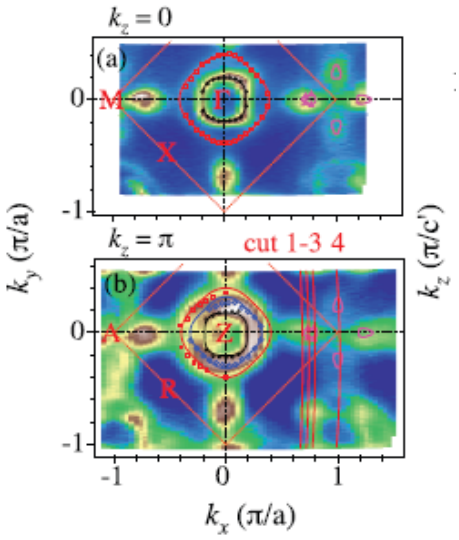

Figure 20: (a) ARPES FS intensity map, $k_z = 0$. (b) ARPES FS intensity map, $k_z = \pi$. The symbols indicate the positions of k_F and the red lines in (b) designate cuts through the FS for ARPES intensity analysis, which is given for cuts 1-4 in Figure 21 for $x = 0.9$. Images taken from work in [82].

KFe_2As_2 earlier in this chapter. This suggests that above the Lifshitz transition, not only do we have an evolution of the pairing mechanism but also a creation of a saddle point and van Hove singularity that may very well underpin the nodal symmetry of the gap function, as previously discussed.

If we look at Figure 21 we can see the saddle points for the ϵ bands potentially crossing the Fermi level. The peak of this band is very close to E_F and the band is narrow at this resolution, making it difficult to judge for certain how far below the trough of the saddle sits under E_F and by how much the peaks sit above E_F. This interpretation of the evidence in Figure 21 is consistent with what has been seen previously for $x = 0.4$ and $x = 1.0$; where in the former case we know that this compound has saddle points in the electronic bands and in the latter case we know that these cross the Fermi surface.

The superconducting gaps detected via the ARPES method are as such: $\Delta_{\alpha/\alpha'}^{k_z=0} = 3.6$ meV, $\Delta_{\beta}^{k_z=0} = 2.7$ meV, $\Delta_{\alpha}^{k_z=\pi} = 2.7$ meV and $\Delta_{\alpha'}^{k_z=\pi} = 2.5$ meV. These results demonstrate that the superconducting gap is approximately isotropic, with all measurements in [82] along Γ-M suggesting little change in the superconduct-

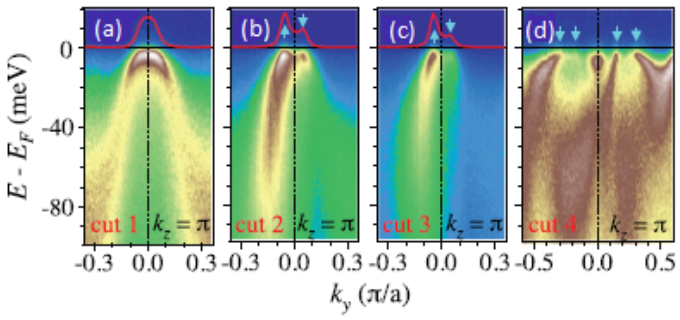

Figure 21: (a) ARPES intensity plot for cut 1, $k_z = \pi$ for ϵ pockets. (b) ARPES intensity plot for cut 2, $k_z = \pi$ for ϵ pockets. (c) ARPES intensity plot for cut 3, $k_z = \pi$ for ϵ pockets. (d) ARPES intensity plot for cut 4, $k_z = \pi$ for ϵ pockets. Cuts here refer to Figure 20 for the case of $x = 0.9$. Images taken from work in [82].

ing gap along k_z in the case of the Γ-centred hole-like FS for $x = 0.9$. As seen in KFe_2As_2, discussed in the previous section, the global pairing function is likely to be $\cos k_x \cos k_y$ from the strong coupling approach [76, 77].

ARPES studies also highlight the absence of nodes around Γ, much like in the case for the fully overdoped $x = 1.0$ case, discussed previously. This again indicates an inconsistency with a d-wave interpretation of the gap symmetry of $x \geq 0.9$. We do however, observe nodes in ϵ that cannot be explained by a simple gap function due to the position of the ϵ FS lobes being far from the nodal lines. Overall this createsa complex picture of the FS. We will see later in this work that SANS investigations do not strongly support a d-wave interpretation. However, we will also see SANS results for $x = 0.5$ demonstrate a lack of evidence for nodal superconductivity.

3.3 Electronic structure in $TlNi_2Se_2$

ARPES studies by Xu *et al.* [83] go some way to revealing the band structure of $TlNi_2Se_2$ and attempt to explain the heavy fermion behaviour of this superconductor. By comparing density functional theory (DFT) calculations with ARPES measurements we can describe the band structure. Previous investigations into $TlNi_2Se_2$ [83] have pointed to an unusual saddle point (referred to as a camelback-shape in [83]) near E_F at the Z point. In most Fe-pnictides [70] this saddle point

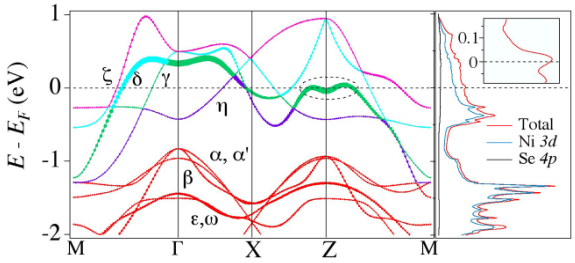

Figure 22: LDA band structure corresponding to lines of high symmetry for $TlNi_2Se_2$. The width of the line indicates the spectral weight of the Se $4p$ orbitals. The dotted line oval indicates the saddle feature of interest. The right hand side inset shows the DOS from the LDA calculations. It can be seen from the secondary inset, in the top right, that there is a peak in the DOS caused by the saddle point at the Fermi surface. Image taken from work in [83].

is usually sitting entirely in the unoccupied states. Once again, like we have seen in the Fe-based superconductors, there are van Hove singularities in the FS. In this case however the Fermi level actually crosses the saddle point created by the γ band, generating a lobe at the Z point. This looks like an electron-like pocket at the Z point surrounded by a concentric hole-like pocket. In fact we will see at the Z point that there are four γ band lobes centred on Z, very similar to the fourfold lobes seen previously in KFe_2As_2.

Figure 22 indicates from calculations that a saddle point should sit very close to the Fermi level, with the peaks of the saddle actually crossing E_F while the trough does not. The saddle is roughly centred at $k = (0, 0, \pi)$, the Z point of the 1st BZ.

In Figure 23(b) four lobes become apparent in the FS around the Z point, between which are flat parts. The peak intensity of the hole-like lobes are in concordance with the four-fold symmetry of the underlying lattice. The peaks at the top of the γ band near the saddle point lie at $\approx$ 15 meV above E_F at $T = 150$ K and the trough sits at $\approx$ 18 meV below E_F. These saddle points create vHs as previously discussed for the case of KFe_2As_2 as they cause a divergence in the DOS. This effect can be seen in the inset of Figure 22. Thus we have four vHs in this band structure in the vicinity of E_F. These points are likely the explanation for the heavy fermion behaviour in this compound as the vHs just below the Fermi level will drive

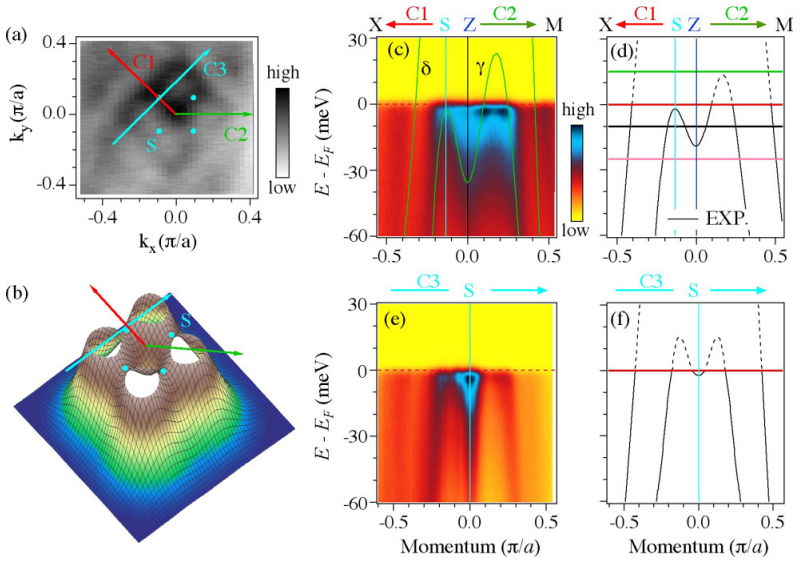

Figure 23: (a) Plot of the FS at the Z point. Coloured lines indicate directions for analysis of the FS in ARPES. (b) 3-D plot of the band structure at Z. (c) ARPES results taken along the C1 and C2 directions indicated in (a). These were taken at $T = 5$ K. (d) Dispersion of bands in (c). (e) ARPES results taken along the C3 direction as indicated in (a). (f) Dispersion of bands in (e). Images are taken from work in [83].

up the effective masses at the saddle point and for all the electrons associated with the central electron-like lobe. This is due to the gradient of the dispersion curve being inversely proportional to the electron mass: $\nabla E = \hbar^2 k/m^*$, and the DOS is inversely proportional to ∇E.

Figure 24 is a clearer ARPES illustration of the FS and band structure for both the $k_z = 0$ and $k_z = \pi$ planes. Here we can clearly see the fourfold nesting of the electron-like lobes of the γ band within the hole-like δ band. Specifically, Figure 24c shows the fourfold nested lobes creating the saddle point at the FS. The DOS near E_F is identified as being mainly contributed by the Ni $3d$ electrons [83], as shown in Figure 22. The saddle point at Z is considered to originate from the hybridisation of the Ni-d_{xy} and Se-p_z orbitals as this is a very common feature in metal pnictides and chalcogenides. We see this directly by observing that the band structure, as calculated from the ARPES results, of $TlNi_2Se_2$ is very similar to the Fe-pnictide $BaFe_2As_2$ and the Co-pnictide $BaCo_2As_2$ [78, 84]. This suggests a universal band structure (with small variations) for $TlNi_2Se_2$, $BaFe_2As_2$ and $BaCo_2As_2$.

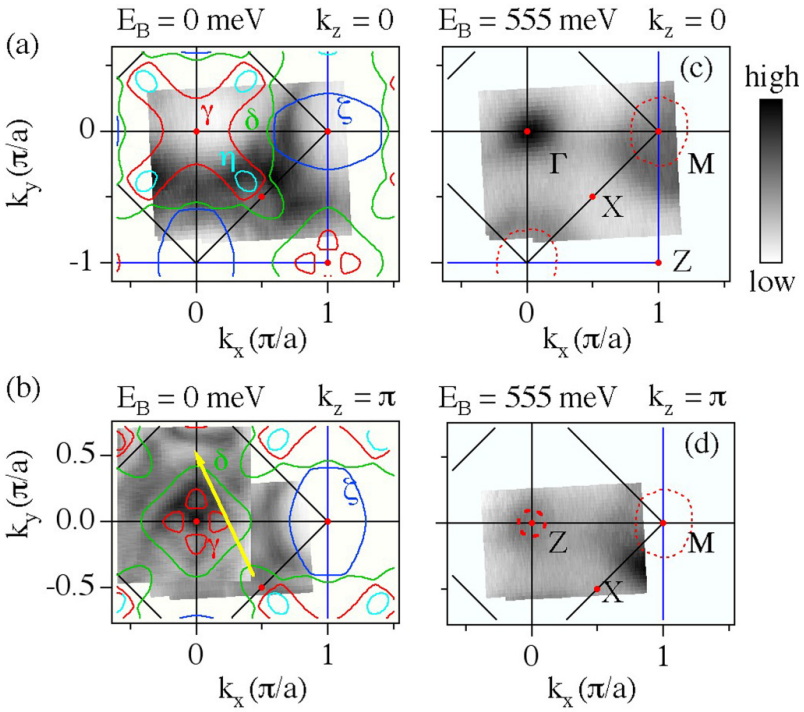

Figure 24: Maps of the FS for the $k_z = 0, \pi$ planes. These are the integrated intensities of the ARPES measurements in [83] within ± 5 meV of E_F, with electronic bands overlaid for clarity. (a) $k_z = 0$ plane centred on Γ. (b) $k_z = \pi$ plane centred on Z. (c) and (d) are taken at 555 meV below E_F. E_B denotes the sampling energy below E_F. Images are taken from work in [83].

However, in the case of $TlNi_2Se_2$, the chemical potential is shifted such that E_F crosses the saddle point. Specifically the chemical potential sits in the range 2 meV $< E_B <$ 17 meV, where E_B is the binding energy of the chemical potential μ. This allows the γ band to cross the chemical potential along the Γ-X and Z-M directions. This effect is largely due to the presence of more $3d$ electrons in $TlNi_2Se_2$ ($3d^{8.5}$) compared to $BaFe_2As_2$ ($3d^6$) and $BaCo_2As_2$ ($3d^7$), allowing the existence of the small electron-like pockets surrounded by concentric hole-like pockets, the consequences of which are seen in Figure 24. However, this small range of tuning available to the chemical potential explains the dramatic change in the band structure with chemical potential tuning for this family of superconductors. This can be seen in KNi_2Se_2 [133] which has a T_c of 0.8 K, 4 times smaller than in $TlNi_2Se_2$, for a chemical potential shift of less than 30 meV for the Lifshitz transitions between these materials [79]; this means that T_c is incredibly sensitive to doping.

3.4 Comparing the 122, *I4/mmm* superconductors

In terms of explicit similarities of $TlNi_2Se_2$ to $(Ba_{1-x}K_x)Fe_2As_2$ and KFe_2As_2, all three have large specific heat capacity coefficients, with KFe_2As_2 having $\gamma \approx 94$ mJmol^{-1}K^{-2} [85] compared to $\gamma \approx 40$ mJmol^{-1}K^{-2} [48] and $\langle\gamma\rangle \approx 43$ mJmol^{-1}K^{-2} (from this work) for $TlNi_2Se_2$ (notwithstanding the $\gamma \propto H^{0.5}$ behaviour). Similar response to pressure has also been observed for $TlNi_2Se_2$ [134] and KFe_2As_2 [87], with T_c being suppressed with increasing pressure. As discussed previously, we have established that a vHs is considered responsible for the nodal superconductivity in KFe_2As_2 [86, 87, 72], as is highly likely in the case of $TlNi_2Se_2$.

Figure 25 illustrates a simplified picture of the FS in KFe_2As_2, $(Ba_{0.5}K_{0.5})Fe_2As_2$ and $TlNi_2Se_2$, respectively. In Figure 25, KFe_2As_2 and $(Ba_{0.5}K_{0.5})Fe_2As_2$ the FS is centred on Γ, with the lobes centred on the M point, while the FS of $TlNi_2Se_2$ is centred on Z, with the lobes centred around Z. We can see the similarity clearly between the fourfold lobes found around the M point in KFe_2As_2 and the Z point

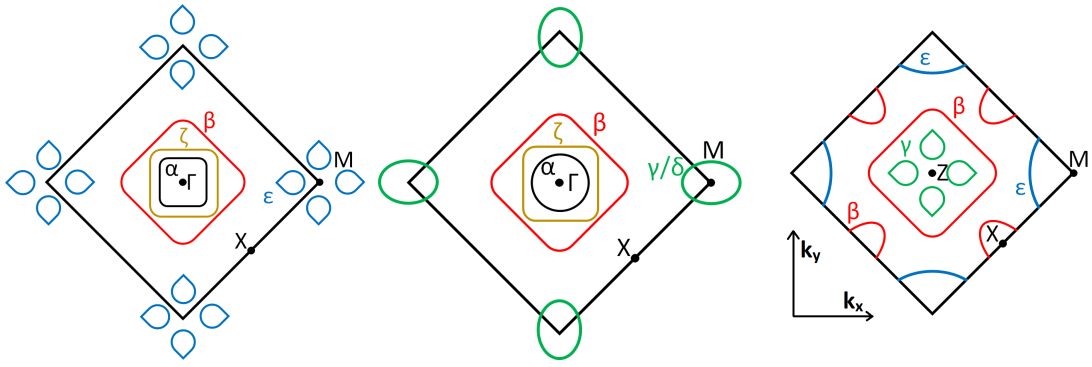

Figure 25: Schematics of the FS of KFe_2As_2, $(Ba_{0.5}K_{0.5})Fe_2As_2$ and $TlNi_2Se_2$, respectively. (a) FS of KFe_2As_2. (b) FS of $(Ba_{0.5}K_{0.5})Fe_2As_2$. (c) FS of $TlNi_2Se_2$, here we label β instead of δ used previously in Figure 24 in order to illustrate the similarities between the concentric cyclinders in (a) and (b) at Γ with those in $TlNi_2Se_2$ at Z. The FS is centred on Z in the 1st BZ in (c), unlike (a) and (b) which are centred on Γ in the 1st BZ.

in $TlNi_2Se_2$. It is these lobes that generate the vHs within a fine tuning range of chemical potential that are responsible for the heavy fermion behaviour and very likely responsible for the unconventional superconductivity observed in these materials. Another similarity can be drawn between the β bands in Figure 25, where we see the three concentric cylinders around the Γ point in the FS of KFe_2As_2 [88] and $(Ba_{0.5}K_{0.5})Fe_2As_2$, while we see one cylinder centred on the Z point in $TlNi_2Se_2$, nesting the saddle point and the fourfold lobes of the γ band. We can also see the transition in electronic energy levels with doping between Figures 25a and 25b, where we have lost the saddle points, the vHs, of the ϵ bands at E_F. They now sit below E_F, removing the effects of the vHs on the formation of Cooper pairs at the FS.

3.5 Conclusions

It is reasonable to suggest that the common feature of nodes in the gap function between $TlNi_2Se_2$ and $(Ba_{1-x}K_x)Fe_2As_2$ is due in large part to the vHs present near the Fermi surface in each respective material and the doped variations of the lat-

ter. The saddle features observed in the electronic bands of each of the compounds explains the heavier effective masses measured for these materials, with the largest effective mass measured for $TlNi_2Se_2$; where more $3d$ electrons are contributed at the saddle points and the trough of the saddle in $TlNi_2Se_2$ sits closest to E_F, comparatively. What we also observe is that in the case of $TlNi_2Se_2$ and KFe_2As_2, where the Fermi level does cross through the saddle points, we measure nodal pairing symmetry in the SANS results and from the ARPES results. However, in the case of $(Ba_{1-x}K_x)Fe_2As_2$ for $x < 0.9$ we see a Lifshitz transition in the ϵ bands. Later we will compare this with observed pairing behaviours with decreasing K content in the SANS investigations. Also in the case of $x < 0.9$ we observe that E_F shifts to above the peak of the saddles of the electron bands. This means we no longer have nested electron-like lobes inside hole-like lobes, but we still have the high effective masses and specific heat coefficients associated with the vHs.

What we also can draw comparisons with is the nature of the nested lobes produced by the unusual saddle bands in the case of $TlNi_2Se_2$ and KFe_2As_2. In KFe_2As_2 we saw four vHs surrounding the Z point at V (along the Z-A line). This happens to also align with the pairing symmetry line nodes for a nodal pairing function of $\cos k_x \cos k_y$, indicating that this symmetry alignment likely has a role to play in the pairing symmetry of the superconducting phase. The fourfold symmetry of the $TlNi_2Se_2$ hole lobes surrounding the electron lobe at the vHs will become important for comparison later with the SANS results, in the same way we have established some explanations for the interactions between the FS and gap structure for KFe_2As_2. Given the pairing symmetry of KFe_2As_2, it would suggest that not only do the presence of vHs explain the heavy fermion similarities between these compounds, but the alignment of the vHs with underlying symmetry appear to have a role to play in the pairing mechanism (and it's evolution with doping) in these 122, I4/mmm structures. At the same time, the ARPES results have demonstrated the immense sensitivity the saddle alignment has to the Fermi level, due to the

small window of energy within which E_F can cross between the trough and peak of a dispersion curve saddle point. Later in this work we present SANS studies that complement the literature review of ARPES investigations, and reinforce many of the conclusions drawn here.

4 ANISOTROPY IN THE VL OF KFe_2As_2

In this section figures are included from related work of collaborators and from work conducted in [86] of which the author of this thesis was a contributing author and investigator during the SANS investigations into KFe_2As_2. The provenance of the figures is included in the captions for the sake of clarity and transparency.

4.1 Properties of KFe_2As_2 and motivation for SANS studies

Iron-based superconductors were discovered in 2008 with the high T_c material $LaFeAsO_{1-x}F_x$, $T_c = 26$ K [110]. This was a surprising development as the large magnetic moment of iron is usually a prerequisite for long-range spin-ordering in materials for (anti)ferromagnetic phases and this is often thought of as a competing phenomena with the spontaneous emergence of paired electrons in superconductivity [111]. The appearance of, and subsequent research into, Fe-based superconductors dispelled the idea that Fe was antagonistic to superconductivity.

KFe_2As_2 is a 122 iron pnictide material with *I4/mmm* space symmetry. It belongs to a broader family of iron-based superconductors, and is the fully over-doped version of the $(Ba_{1-x}K_x)Fe_2As_2$ materials. Previous work [112, 113] on this material has pointed to nodes in the superconducting order parameter, indicating possible nodal s-wave pairing or d-wave pairing.

This material has a critical temperature of $T_c \approx 3.6$ K and an upper critical field of $B_{c_2}^{ab}(0) = 8.6$ T and $B_{c_2}^{c}(0) = 1.8$ T determined by Abdel-Hafiez *et al.* [85]. KFe_2As_2 also has a large Sommerfeld coefficient, $\gamma_n = 94$ mJ mol^{-1}K^{-2} and some evidence to suggest there might be multiband effects [12, 85, 86, 109]. Previous SANS investigations into KFe_2As_2 with $\mathbf{B} \parallel \mathbf{c}$ have shown a distorted VL for all fields and temperatures accessed, even up to $H \to H_{c_2}$. In this upper field regime, similar tetragonal materials like $CeCoIn_5$ [89] have displayed a great sensitivity of the VL to the gap structure.

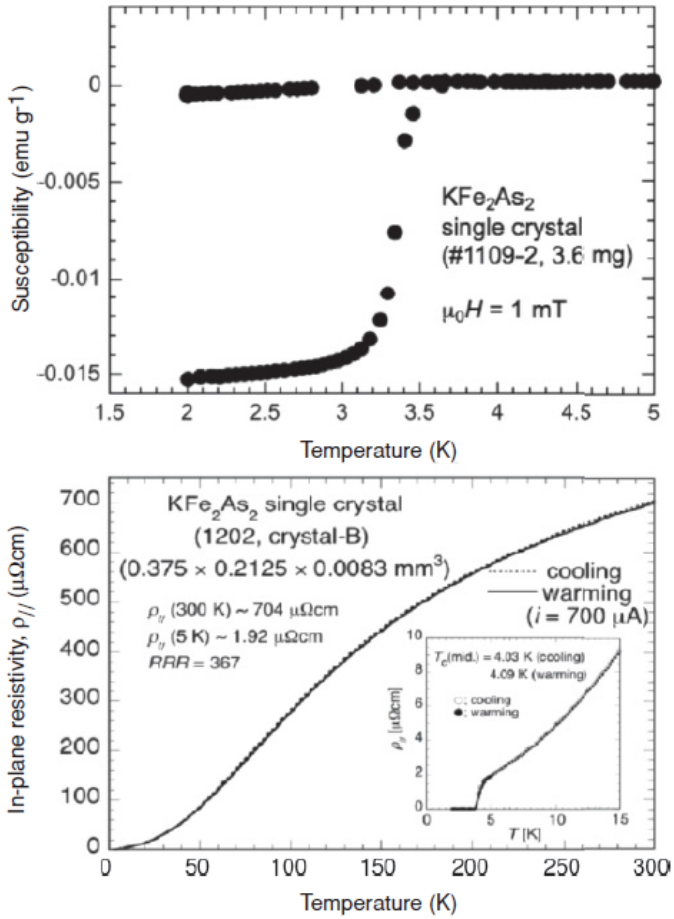

Figure 26: Magnetisation and resistivity measurements taken for sample characterisation. For the magnetisation, a field of 1 mT was applied, with the upper curve presenting field cooling and the lower curve zero-field cooling. The sample information is contained within the resistivity graph, alongside the residual resistivity ratio (RRR). Figure taken from work in [109]

This material was also observed to have nodal behaviour in the superfluid density. Although one could posit a d-wave symmetry for this behaviour, previous ARPES studies [74] did not see line nodes on all the Fermi sheets, nor is there evidence to suggest that the optimally doped $(Ba_{1-x}K_x)Fe_2As_2$ ($x \approx 0.4$ for highest T_c) has any nodes, precluding a smooth transition under doping.

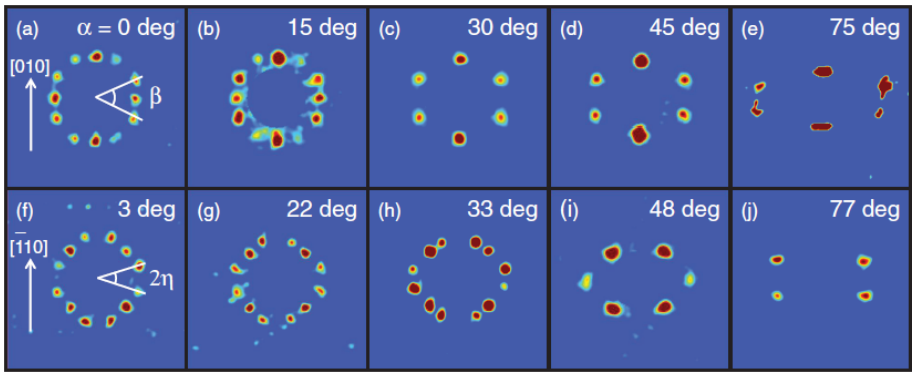

Figure 27: VL diffraction patterns of KFe_2As_2 at 2 K and 0.2 T for both the [010] (a)-(e) and [$\bar{1}$10] (f)-(j) orientations. In the work by Kawano-Furukawa *et al.* [12] the angle Ω is denoted more generally as α, while the angles β and η are defined in images (a) and (f), respectively. Figure taken from work in [12]

4.2 Previous investigations in KFe_2As_2

Previous investigations in this material have been conducted by Kawano-Furukawa *et al.* since 2011, primarily focused on SANS studies of the VL at the SANS-I beamline, SINQ, Paul Scherrer Institute (PSI), Switzerland. Samples were grown [109] in a potassium flux with a FeAs precursor at 900°C for 10 hours in a vacuum. This is then mixed in the following atomic ratio K:As:FeAs = 3:2:2. This mixture is heated again in an aluminium crucible sealed in a steel tube, heated to 900°C for 10 hours, as before. This was then cooled at a rate of -1K/hour to 650°C before being finally quenched. The samples produced in this way are plate-like single crystals with typical dimensions of $7 \times 7 \times 0.5$ mm^3. These were then prepared as a mosaic, with co-aligned axes, on aluminium plates for SANS studies. Samples in the initial experiments [12] were grown at the Karlsruhe Institute of Technology (KIT) while crystals in later experiments (the majority of the work presented here [86]) were grown at the National Institute of Advanced Industrial Science and Technology (AIST) by Kunihiro Kihou. Samples of both sources provided results that were qualitatively very similar. The sample quality was confirmed by Kawano-Furukawa *et al.* [12] using magnetisation and resistivity measurements, presented in Figure 26.

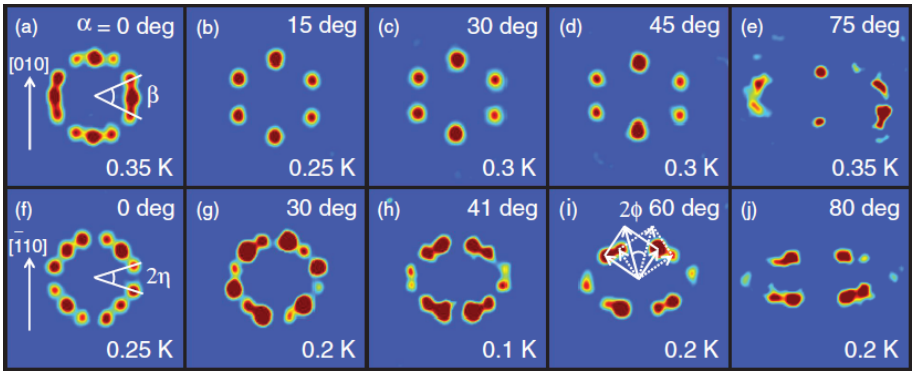

Figure 28: VL diffraction patterns of KFe_2As_2 for $T < 0.35$ K and 0.2 T for both the [010] (a)-(e) and [$\bar{1}$10] (f)-(j) orientations. In the work by Kawano-Furukawa *et al.* [12] the angle Ω is denoted more generally as α, while the angles β and η are defined in images (a) and (f), respectively. Here another misalignment angle ϕ is also defined due to the weak signal for measuring η. Figure taken from work in [12]

The results in Figure 27 show VL diffraction patterns for a range of applied fields and angles at a fixed temperature of 2 K. Here a displacement angle of α is defined. This describes the angle between the normal of the sample face (the c-axis) and the applied field. In images (a) and (f) we clearly see the degenerate second domains for the case of the angle $\alpha = 0°$. For the case of (a) to (e), in the [$h0l$] orientation, the rotation of the field towards the [100] (or a) axis suppresses the second domain rapidly. We also see that both domains maintain their orientation with respect to angle, with the first domain becoming more distorted with increasing angle for (a) to (e). However, in the case of the diffraction patterns (f) to (j) we see the degeneracy remains for higher angles in the [hhl] case, with the domains changing their orientation with respect to angle. Essentially, the two domains distort and rotate until they overlap as one aligned domain.

In Figure 28 we see the low temperature regime for the same field as in Figure 27. Once again we see in the [$h0l$] case, images (a) to (e), that the second domain rapidly disappears with an increase in angle while the first domain becomes increasingly distorted. For images (f) to (j) in the [hhl] orientation we see the second domain once again persist up to large angles, with both domains respecting the underlying crystal symmetry. For images (f) to (j) the signal for measuring η becomes very

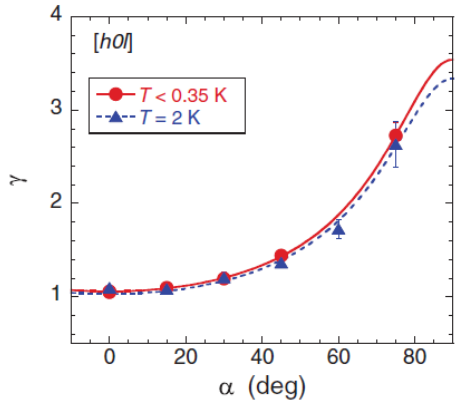

Figure 29: γ, the anisotropy, versus the applied angle α for the $[h0l]$ orientation. Separate data sets are given for the $T < 0.35$ K and $T = 2$ K measurements. Figure taken from work in [12]

weak with angle and so ϕ is defined as a new misalignment angle.

The anisotropy given in Figure 29 can be calculated by fitting the VL to an ellipse and extracting the major and minor axis ratio for each field. This method remains valid provided the VL symmetry remains the same such as in the $[h0l]$ case, but unlike the $[hhl]$ orientation where we see significant reorientation with respect to angle, α. The γ used in this work is defined in the anisotropic London model, referred to at the beginning of this work but fully outlined by Kogan [11]. This anisotropy is given as

$$\gamma(\alpha) = \left(\frac{1}{\gamma^2(\alpha = 90°)} \sin^2 \alpha + \frac{1}{\gamma^2(\alpha = 0°)} \cos^2 \alpha \right)^{-0.5} \tag{109}$$

We may simplify this equation by taking the London simplification of $\gamma^2(\alpha = 0°) = 1$ and including the fact that in both cases of (a) at $\alpha = 0°$ there is some visible distortion. To reflect this we rewrite equation 109 as

$$\gamma(\alpha) = A \left(\frac{1}{\gamma'^2} \sin^2 \alpha + \cos^2 \alpha \right)^{-0.5} \tag{110}$$

The above equation is used to fit the data in figure 29 for the case of $T < 0.35$ K and $T = 2$ K. The fits produce the following parameters for the temperature

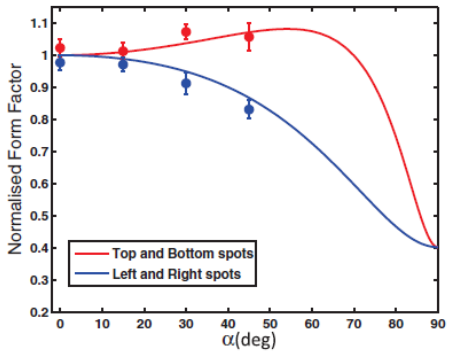

Figure 30: Normalised for factor of the two top/bottom spots and the four left/right spots in the $[h0l]$ configuration. Field is set to 0.2 T and $T < 0.35$ K. The form factors are normalised to the values at $\alpha = 0°$. The fits were produced using $\lambda = 203$ nm, $c = 0.52$ and $\xi = 13.5$ nm for $B_{c_2} = 1.8$ T and $T = 50$ mk. The anisotropy $\gamma = 3.35$ was also used. Figure taken from work in [12].

ranges, respectively: $A^{<0.35K} = 1.03 \pm 0.03$, $\gamma'^{<0.35K} = 3.24 \pm 0.21$, and $A^{2K} = 1.06 \pm 0.003$, $\gamma'^{2K} = 3.35 \pm 0.03$. This means the SANS results in [12] indicate an average anisotropy of $\gamma \approx 3.3$. This is in close agreement to previous resistivity measurements [129] that indicate $\gamma = \rho_{ab}/\rho_c \approx 3.52$.

The final calculations in the work by Kawano-Furukawa *et al.* in 2013 [12] looked into the angular dependence of the form factor. From the extensive data gathered on the anisotropy and the evolution of the VL with angle and field we can see from Figure 30 that the form factor, with respect to angle, varies for the top/bottom and left/right spots. The data shows that with rotation away from the **c** axis the left- and right-most spots experience the increase in the penetration depth by a decrease in the form factor; we can see this by comparing the VL diffraction patterns to Figure 1. However in the top and bottom spots, we do not see this effect. This is because the penetration depth here is mainly affected by the currents in the basal, or $a - b$, plane. An additional contributing effect is that by rotating away from **c** towards the basal plane increases B_{c_2}, which means for the top and bottom spots B/B_{c_2} reduces. The net effect is shown in figure 30 with an enhancement of the form factor for the top and bottom spots that increases with angle up to $\alpha \approx 60°$ (based on the fit) and with persistent enhancement over the left/right spots for the full

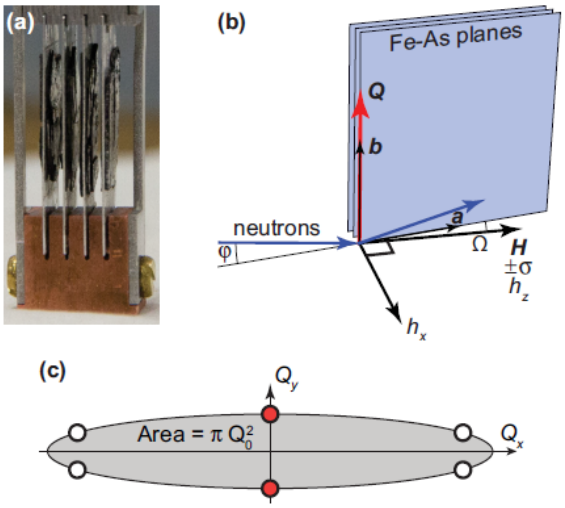

Figure 31: (a) Sample mosaic mounted on four parallel aluminium plates with a cadmium window. The total mass of the samples is ≈ 2 g. (b) Coordinate systems of the experiment. The directions are defined as **z** parallel to **H** and **y** parallel to **b**, also known as the basal plain [86]. The magnetic field is rotated by some angle Ω away from the $a-b$ plane. Neutron spins are denoted by $\pm\sigma$ and are parallel or antiparallel to **H**. The neutron beam is incident in the $z-y$ plane and at angle ϕ, to the field direction **H**. **Q** is the scattering vector of the VL. The transverse and longitudinal modulation components of the applied field are identified by $\mathbf{h}_x$ and $\mathbf{h}_z$. (c) Diagram of the hexagonal VL experiencing anisotropy. The VL spots lie on an ellipse in reciprocal space, with the anisotropy ratio, Γ_{VL} describing the major/minor axis ratio of the ellipse. The area of the ellipse is determined by $A = \pi Q_0^2$, where Q_0 is defined by equation 112. Given the anisotropy follows an ellipse, only the two red spots are needed to determine Q_0 and thus the area and Γ_{VL}. Figure published in [86].

angular range. The fit parameters were calculated in [12] and are given in Figure 30 for use in equation 105.

4.3 Anisotropy in the VL

4.3.1 Experimental setup

Figure 31 shows the schematics and sample setup for a series of SANS measurements conducted at the SANS-I beamline, PSI between 2014 and 2016. The samples in image (a) were co-aligned mosaics of smaller single crystals grown at at the National Institute of Advanced Industrial Science and Technology (AIST). This arrangement

was made so that the thickness of the sample presented to the neutron beam was minimised while the volume was maximised. Image (a) shows the samples in the $b-c$ plane, as shown in image (b). As in previous works [109, 12], the anisotropy will be defined by the distance between the top- and bottom-most spot. This is demonstrated in image (c) where this distance is the minor axis of the ellipse that the anisotropic VL spots lie on. Measurements were conducted in 2015 on the SANS-I beamline, SINQ, PSI, Switzerland. Measurements were taken at $T = 50 \pm 10$ mK with applied fields of 0.4 T to 2.6 T. The sample was cooled using a dilution refrigerator insert into a cryomagnet, with a horizontal magnetic field. The dilution refrigerator with mounted sample could rotate with the previously defined angle Ω in the $a-c$ plane, with the **b** crystal axis aligned vertically.

The sample was field cooled for each change in field and angle with a wiggle procedure added to improve the quality of the VL. The amplitude of the field modulation (wiggle) was ± 20 mT; additionally, Ω was changed before the value of B. A neutron wavelength of $\lambda_n = 8 \pm 0.8$ Å and $\lambda = 12 \pm 1.2$ Å was used. The detector was varied between 11 m and 18 m from the sample. The sample was also rocked about the angle ϕ, with horizontal axis perpendicular to the incoming neutron beam, to satisfy the Bragg condition. Equivalently rocked background measurements were taken in zero field for subtraction from the foregrounds.

4.3.2 Effects of field on the anisotropy

Figure 32 illustrates five fields applied to the VL at a fixed angle of $\Omega = 10^\circ$ with respect to the basal plane ($a-b$). In order to distinguish between the anisotropy and the increasing VL density with field, the axes in Figure 32 have been normalised to Q_0. Each image has also been normalised in the colour scale such that the significantly weaker signals are still visible for comparison. It is very clear that the anisotropy increases with increasing field as we see the minor axis of the VL decrease, as indicated by the white lines, from 0.4 T to 2.2 T. The central region has

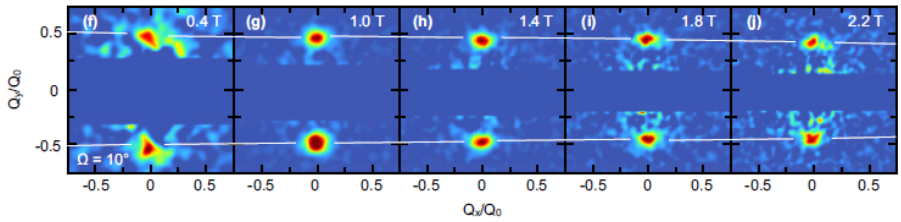

Figure 32: Measurements (f)-(j) are made at a fixed angle $\Omega = 10°$. The anisotropy clearly increases with increasing field. The white line has been added as a guide to the eye to show the decrease in the VL ellipse minor-axis in the same scale for increasing field. The central area has been masked in order to cover imperfect background subtraction while the colour scale for each image is adjust individually in order to make the spots for the larger fields clearly visible. Figure published in [86].

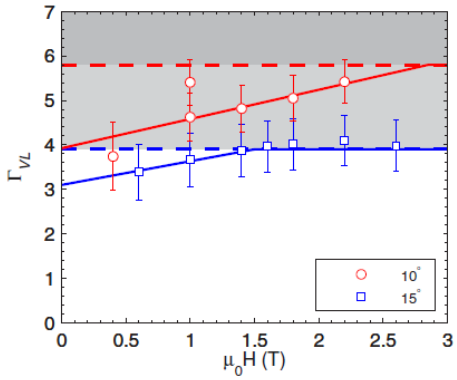

Figure 33: The VL anisotropy, Γ_{VL} variation with respect to the applied field. Two separate angles of rotation in Ω are included as well; being the two smallest angles of rotation available.The dashed lines with graded grey areas represent the relative maximum possible values of the anisotropy for the angle Ω, defined as $\Gamma_{VL}^{Max} = 1/\sin\Omega$. Figure published in [86].

been masked as it contains the direct beam, this is unreflected and has an intensity several orders of magnitude higher than the reflected intensity.

In Figure 33 the anisotropy with respect to the applied field is calculated from the reciprocal space diffraction patterns using equation 111. Although for both applied angles we see an increase in anisotropy with field, the effect is greater in the $\Omega = 10°$ case. This is because at $\Omega = 15°$ the anisotropy saturates for $B = 1.4$ T at $\Gamma_{VL}^{Max}(\Omega) = 1/\sin\Omega$, due to $\Gamma_{ac} \to \infty$ effectively in equation 113. Due to weak signal strength at high fields ($B > 2.4$ T), we were unable to accurately establish the anisotropic saturation point for the $\Omega = 10°$ case. Larger angles are not included

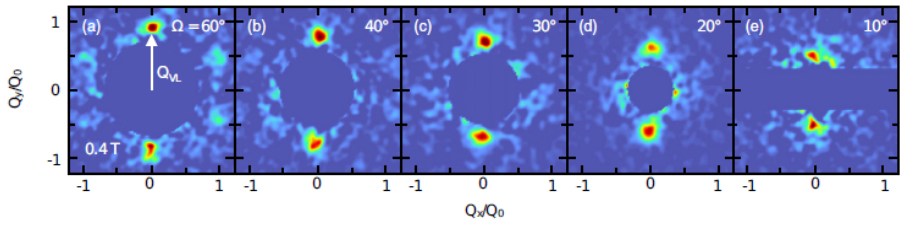

Figure 34: Measurements (a)-(e) are made at a fixed field $B = 0.4$ T. The anisotropy clearly increases with increasing angle. The central area has been masked in order to cover imperfect background subtraction, this beign a circular area from (a) to (d) and a strip in (e). The colour scale for each image is adjusted individually in order to make the spots for the larger fields clearly visible. Note that image (e) here is identical to image (f) in Figure 33. The strip is applied due to increased background scattering off of the Aluminium plates and crystal defects at small Ω.Image (a) still faintly shows the other 4 VL spots in the first domain. All images are normalised to Q_0 for both axes. Figure published in [86].

here due to the decreasing dependence of Γ_{VL} on Γ_{ac} for increasing Ω, which will become apparent in the next section.

At 0.4 T we see that the anisotropy surpasses $\Gamma_{H_{c_2}} \approx 3.3$ from previous studies [109, 12]. We would expect $\Gamma_{ac} = \Gamma_{H_{c_2}}$ for all directions in the crystal for a superconductor that has an orbitally limited upper critical field, typically associated with single-band superconductors. KFe_2As_2 is clearly a case where a single gap does not explain the observed phenomenon, especially given the strong H_{c_2} anisotropy.

4.3.3 Effects of rotation in Ω on the anisotropy

For the case of the VL of a superconductor, the anisotropy of such a structure can be characterised by the following unitless ratio:

$$\Gamma_{VL} = \left(\frac{Q_0}{Q_{VL}}\right)^2, \tag{111}$$

where Q_{VL} is the measured Q value in reciprocal space of the VL spots and Q_0 is the expected Q value of the VL spots in reciprocal space given the applied field, B. The expected value of the spot position in reciprocal space for a hexagonal VL is determined by the following equation [20],

$$Q_0 = 2\pi\sqrt{\frac{B}{\Phi_0 \sin\theta}} = 2\pi\sqrt{\frac{2B}{\sqrt{3}\Phi_0}}, (\theta = 60^\circ). \tag{112}$$

With regards to Ω dependent anisotropy, we would typically expect to see behaviour that conforms to the following relationship:

$$\Gamma_{VL} = \frac{\Gamma_{ac}}{\sqrt{\cos^2\Omega + (\Gamma_{ac}\sin\Omega)^2}} \tag{113}$$

where Γ_{ac} is the ratio between the major and minor axis of the VL in reciprocal space, which can also be taken from the zero angle results due to the fact that $\Gamma_{VL}(\Omega = 0) = \Gamma_{ac}$.

Figure 34 shows the variation of the VL with respect to the applied angle Ω. Once again we focus on the minor axis of the VL to find Q_{VL}, with Q_0 previously defined in equation 112. The relation of the anisotropy defined in equation 111 is evident in these results as the minor axis measured as Q_{VL} decreases towards $Q = 0$ with a decrease in Ω towards the basal $a - b$ plane under a constant applied field. A rotation in Ω will align the samples such that at small Ω the transverse field component ($\mathbf{h}_z$) will be closely aligned to the $a-b$ plane. This means VL scattering associated with this contribution dominates. Scattering with q-vectors parallel to h_x have an incredibly small signal due to these components not being aligned to the vertical axis. This means these components are not perpendicular to the scattering vector Q_{VL}. This motivated the use of ϕ scanning for the rocking curves and using only the top and bottom spots here.

Figure 35 shows the angular dependence of the VL anisotropy at fields of 0.4 T, 1.0 T and 1.4 T. The full fit values for equation 113 for Γ_{ac} are $\Gamma_{VL}(0^\circ) = 5.2\pm1.8$ for 0.4 T and $\Gamma_{VL}(0^\circ) = 10.8^{+21.9}_{-4.7}$ for the combined high-field data. The high gradient of the high-field data consequently produces an asymmetric error for the Γ_{ac} fit. This shows the VL of KFe_2As_2 to be exceedingly anisotropic for high field, compared to the consistent value of $\Gamma_{H_{c_2}} = 3.3$ found in previous low temperature experiments

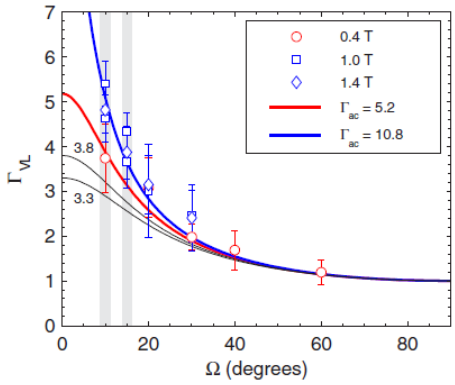

Figure 35: Γ_{VL} calculated as a function of Ω using equation 113 to generate the fit curves in red and blue, with respective y-axis intercepts of $\Gamma_{ac} = 5.2$ and $\Gamma_{ac} = 10.8$. The 1.0 T and 1.4 T data sets are combined for a fit, given their close overlap. The black lines are from fits obtained in previous work by Kawano-Furukawa *et al.* [12] at low fields. The grey bars represent the areas of Ω which are equivalent to the grey areas in Figure 33. Figure published in [86].

[109, 12]. This is given the fact that these values are extrapolations to the condition of the natural anisotropy at $\Omega = 0°$, Γ_{ac}.

4.4 Evidence of Pauli paramagnetism and multiband superconductivity

In superconductors, a phenomenological indication of whether Pauli paramagnetic effects will be present is obtained by comparing $H_{c_2}^{ab}$ in Tesla to T_c in Kelvin. If the field is greater in magnitude then Pauli limiting effects are highly likely to be observed [109, 12, 86]. A precise indication of Pauli limiting effects is the comparison of the orbital limiting field to the Zeeman splitting (characterised by the Pauli limiting field); this is described by the previous equations 73 and 74.

Previous results [85] and the results presented here indicate an anisotropic suppression of H_{c_2} in the basal $(a-b)$ plane, which suggests strong Pauli paramagnetic effects in the $a-b$ plane [90, 91], with fields suppressed below the orbital limit for KFe_2As_2. Work by Zocco *et al.* also highlighted a transition in $H_{c_2}(T)$ below 1.5 K going from a 2nd-order transition at $T > 1.5$ K to a 1st-order transition at $T \leq 1.5$ K that is attributed to Pauli limiting effects.

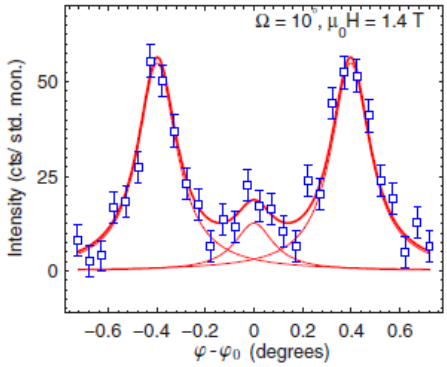

Figure 36: A VL rocking curve showing the scattered intensity versus the rocking angle, ϕ, relative to the rocking centre $\phi_0 = 0.8°$. Rather than a single central scattering peak aligned to ϕ_0 as we would expect, instead there are three peaks. There is the central non-spin-flip peak due to longitudinal field modulation ($\mathbf{h}_z$) and the two larger spin-flip peaks caused by Zeeman splitting from the transverse field modulation ($\mathbf{h}_x$). In this rocking scan $\lambda_n = 8$ Å and the spin-flipped peaks are located at $\pm 0.4°$. Figure published in [86].

Further evidence of Pauli paramagnetic effects is derived from the presence of spin-flipped with non-spin-flipped diffraction peaks while rocking in ϕ under some non-zero field. In Figure 36 we can see the emergence of spin-flipped peaks alongside the non-spin-flipped peak at $\Omega = 10°$, $B = 1.4$ T. The amplitude of the scattered intensity is proportional to the form factor, also known as the field modulation $|F(q)| \leftrightarrow |\mathbf{h}|$, such that $I(q) \propto |\mathbf{h}|^2$, as established by the Christen formula (equation 104). Typically the form factor is proportional only to the longitudinal modulation of the applied field $\mathbf{B}(\mathbf{r})$ in the plane of the superconductor that is normal to $\mathbf{B}(\mathbf{r})$. This field component is denoted as $\mathbf{h}_z$ and is labeled in Figure 31. However, when we look at highly anisotropic superconductors there is a strong preference for the currents in the vortex cores (also known as the screening currents) to flow within the $a-b$ plane. As the rotation angle Ω decreases, the $a-b$ plane tends towards a parallel alignment with the applied field. This rotation decreases the size of the $a-b$ plane seen by the neutron beam and drives up the dominance of the transverse field modulation $\mathbf{h}_x$ [114, 115]. The dominance of $\mathbf{h}_x$ leads to Zeeman splitting of the VL rocking curve, see Figure 36, as the incoming unpolarised neutrons feel the static modulation of $\mathbf{h}_x$ and equally align parallel or anti-parallel to $\mathbf{h}_x$. Still visible

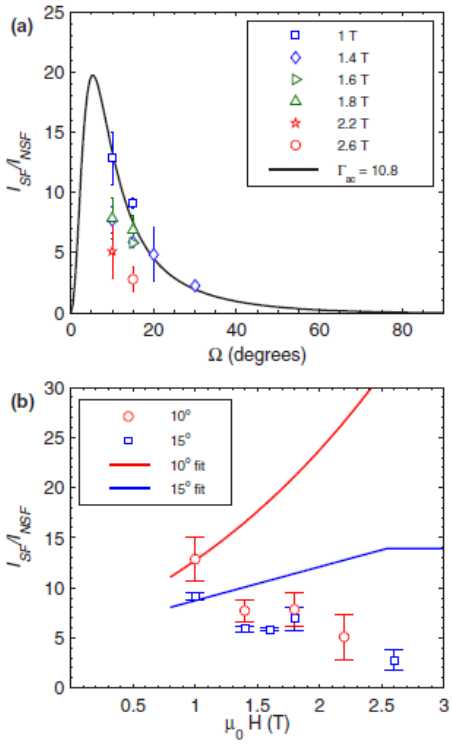

Figure 37: Intensity ratios of spin-flip to non-spin-flip peaks versus Ω (a) and applied field (b). Given that the spin-flip peaks correspond to only one spin orientation each, they are summed for a total integrated intensity of the spin-flip contribution. The fit line in (a) is calculated using equation 114 and the values in Figure 35. In (b) the fit lines are from the London model (Christen formula) and the field dependence of Γ_{VL} from Figure 37. Figure published in [86].

is the central non-spin-flip peak caused by those neutrons affected by the non-zero value of $\mathbf{h}_z$ [116, 117].

In order to compare the relationship between the spin-flip and non-spin-flip contributions, we can divide $|h_x|^2$ by $|h_z|^2$ and eliminate the core correction term (which cancels out due to its presence in both components) which leaves the only dependence being on Ω and Γ_{ac}. The calculation of the intensity ratio is outlined by Thiemann *et al.* [114]:

$$\frac{I_{SF}}{I_{NSF}} = \frac{|h_x|^2}{|h_z|^2} = \left(\frac{(1-\Gamma_{ac}^2)\sin\Omega\cos\Omega}{\cos^2\Omega + \Gamma_{ac}^2\sin^2\Omega} \right)^2 . \tag{114}$$

It is clear from Figure 37 that the spin-flip contribution scales as we would expect with the angle Ω with reasonable consistency with the black fitted line in (a). But

we do see a stronger spin-flip response for lower fields, which points to h_x dominating with angle, rather than overall field strength where h_z would also be stronger. In (b) we see a lack of conformity with the fitted models for field-dependent behaviour. The results for two angles show a consistent decrease of the intensity ratio with applied field increasing. This is additional evidence of Pauli limiting behaviour, alongside the deviation of the high field values in (a). This is due to the polarisation of the normal electrons in the screening currents in the vortex cores. When these electrons polarise [118, 119] they do so commensurate with the VL periodicity, this enhances the longitudinal form factor contribution h_z and thus enhances I_{NSF}, decreasing the value of the ratio for higher fields. We may then say that the non-spin-flip form factor can be split between the VL contribution and the Pauli limiting contribution such that $h_z = h_z^{London} + h_z^{Pauli}$.

By measuring this ratio we can show clear evidence of the Pauli limiting effects provided we separate the Pauli limiting contribution:

$$\frac{I_{SF}}{I_{NSF}} = \frac{|h_x^{London}|^2}{|h_z^{London} + h_z^{Pauli}|^2} \tag{115}$$

By rearranging the above we may present the Pauli paramagnetic contribution to the form factor with the following:

$$\frac{|h_z^{Pauli}|}{|h_x^{London}|} = \left(\frac{I_{SF}}{I_{NSF}}\right)^{-0.5}_{Measured} - \left(\frac{I_{SF}}{I_{NSF}}\right)^{-0.5}_{London} \tag{116}$$

Where the ratio denoted *London* represents the London calculation of $h_x^{London}/h_z^{London}$. The results of this analysis are presented in Figure 38 as a function of applied field. It is clear that the Pauli paramagnetic effects increase with applied field over the full field range with an exponential behaviour. There are no easily resolvable spin-flipped peaks below 1 T and above 2.6 T the overall signal strength is too weak; at higher fields we would expect signal saturation as $B_{applied} \to B_{c_2}^{Pauli}$ and then disappear, with $B_{c_2}^{Pauli} = 5$ T [120, 121].

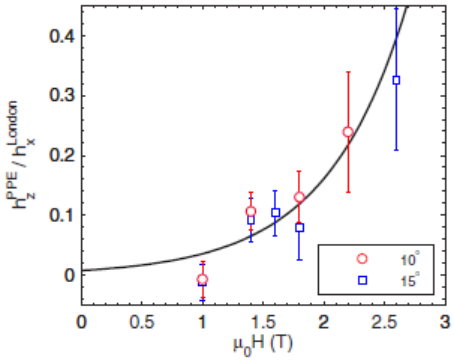

Figure 38: Ratio of the Pauli paramagnetic contribution to the form factor parallel to the vortices h_z, using equation 116. Also used are the ratio values from Figure 37(b). Included is a black line representing an exponential fit. Figure published in [86]

Multiband superconductivity is primarily evidenced by the existence of anisotropy; specifically $\Gamma_{ac} > 1$ and Γ_{VL} exhibiting field dependence. Intrinsic anisotropy in superconductors arises from the ease with which Cooper pairs may travel along a specific axis or within a specific plane in the underlying crystal. This is directly related to the Fermi velocities in the Fermi surface sheets that carry the superconducting Cooper pairs. In a single band superconductor the intrinsic anisotropy can be found by the following ratio: $\Gamma_{ac} = v_{ab}/v_c$. However, in the case of a multiband superconductor we would expect an intermediate value that sits within the range set by the multiple Fermi sheets that carry supercurrents [86, 122]. If these bands then have different Fermi velocity ratios associated with them, then there will be a field dependence of Γ_{ac} as each band has its own gap value which is suppressed by an applied field increase; bands with smaller energy gaps will be suppressed by fields $H < H_{c_2}$.

4.5 Conclusions

We see that SANS studies have been more that sufficient to explore the anisotropy, band structure and Pauli paramagnetic effects in KFe_2As_2. The available data so far demonstrates a superconducting anisotropy that is highly dependent on the applied field; this in turn is more evidence to suggest multiple superconducting bands. We

also see plenty of evidence demonstrating the existence of Pauli limiting effects. We see that Γ_{ac} exceeds the upper critical field anisotropy of 3.3 from previous results. This strongly supports the interpretation of Pauli paramagnetic effects occurring within the $a-b$ plane. We see this in previous results as well when looking at the form factor, where the left and right spots exhibit s-wave behaviour while the top and bottom spots shows clear enhancement from Pauli paramagnetic effects.

The form factor clearly signify Pauli paramagnetic enhancements (PPE) in KFe_2As_2, this sets a context for further potential observations of PPE in the other 122 materials in this thesis. The most obvious point of comparison will be in terms of anisotropy. In the KFe_2As_2 case we see very strong anisotropy, indicative of multi-band and Pauli limiting effects.

We will see in subsequent sections how this material compares to others in this work, $TlNi_2Se_2$ and $(Ba_{1-x}K_x)Fe_2As_2$. Despite having very similar structures, and values of T_c in the former case, we will see significant differences arising when comparing KFe_2As_2 to $TlNi_2Se_2$ and $(Ba_{1-x}K_x)Fe_2As_2$.

5 HIGH FIELD STUDY OF SUPERCONDUCTING $(Ba_{0.5}K_{0.5})Fe_2As_2$

5.1 Properties of $(Ba_{0.5}K_{0.5})Fe_2As_2$ and motivation for SANS studies

It has been previously demonstrated that by doping the K site with Ba in the iron-based compound KFe_2As_2, the T_c and H_{c_2} are driven to very high values [123, 125, 126]. We do not currently have a known, measured value of $H_{c_2}(T = 0)$ for $(Ba_{0.5}K_{0.5})Fe_2As_2$, or many of the other doping levels due to the incredibly high predicted upper critical field that is currently not easily accessible experimentally, especially not with a steady state horizontal field for SANS studies. Figure 40 represents a prediction of the behaviour of H_{c_2} with respect to the temperature, with the area to the left of the blue line representing the superconducting state. These predictions are based on the known values of the coherence length and some of the values for the upper critical field conducted at high T by the crystal growers. This prediction obviously has room for variation and later in this work we will demonstrate how the contributions of the SANS temperature scans contribute to a revision of these values. The other motivation for investigating this material is due to the Pauli limiting effects demonstrated in the previous section for KFe_2As_2. Given that the doping of 50% Ba to K has driven up T_c by an order of magnitude and H_{c_2} by approximately two orders of magnitude it means that Pauli limiting effects are even more likely to be detected at fields well below H_{c_2}.

Figures 39a and 39b show the resistivity measured on a similar single crystal sample of $(Ba_{0.5}K_{0.5})Fe_2As_2$ produced by the same crystal grower. These resistivity results seem to indicate a broader spread of T_c values along **c** compared to the **ab** plane with applied field strengths. This indicates that the superconducting state along **c** is more sensitive to changes in field and could suggest potential anisotropy

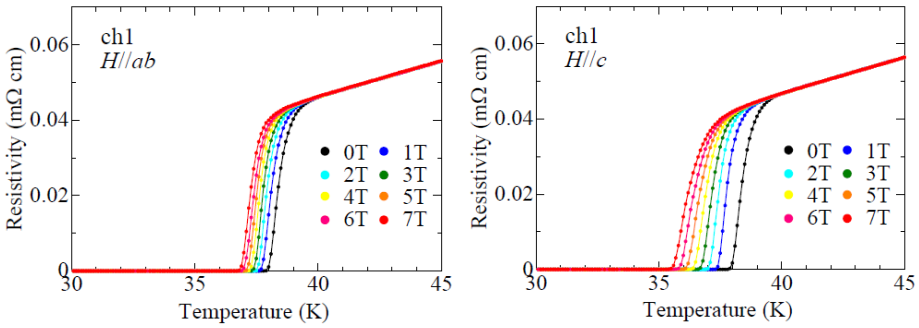

(a) (b)

Figure 39: (a) Resistivity measurements on grown samples of $(Ba_{0.5}K_{0.5})Fe_2As_2$ with the measurement of resistivity $\parallel ab$ at varying fields. (b) Resistivity measurements on grown samples of $(Ba_{0.5}K_{0.5})Fe_2As_2$ with the measurement of resistivity $\parallel \mathbf{c}$ at varying fields. There is a narrower spread of H_{c_2} values for each field for $H \parallel ab$, indicating that the **c** axis is more sensitive in the superconducting state to changes in field.

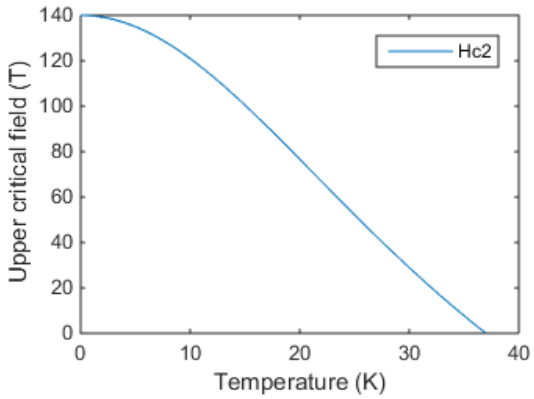

Figure 40: Prediction of the approximate H_{c_2} behaviour extrapolated from the London theory, details from the sample grower and the data available in this work.

in the VL that would be measurable below 7 T for temperatures below 38 K. The lower value of T_c for an equivalent field in the **c** plane suggests a larger evolving penetration depth for $\mathbf{B} \parallel \mathbf{c}$. This would be detectable in the form of anisotropy developing in the form factor as we change the angle with respect to the $a-b$ plane. In addition, the ω (azimuthal) and ϕ (polar) scans can generate penetration depth results that could indicate the existence of anisotropy in the basal plane. This factor is probed in $TlNi_2Se_2$ and presented in a later section (Figure 97).

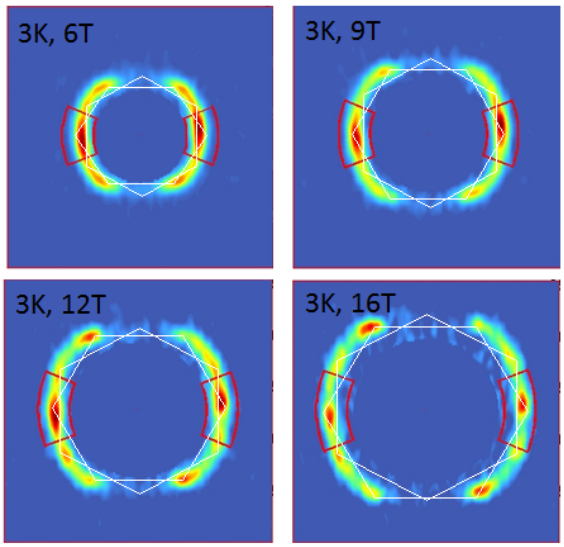

Figure 41: Comparative images of the diffraction patterns from azimuthal ω scans with a maximum rock of $\pm 3°$ for high fields and $\pm 2°$ for low fields. There is a second domain visible via the apparent spots above and below the left- and right-most spots at 12 T and 16 T. The second domain's signal is much weaker for lower fields. The diffraction pattern signal is clearly still very strong up to 16T. White hexagons are used to illustrate the apparent positions of the two visible domains at these field, temperature and angle settings.

5.2 Results for $(Ba_{0.5}K_{0.5})Fe_2As_2$: D33 beamline, ILL July 2016

For the investigation into $(Ba_{0.5}K_{0.5})Fe_2As_2$ on the D33 beamline at the Institute Laue-Langevin, Grenoble, France (ILL), high quality single crystal samples were grown using the self flux method described in [127] and [128] (similar to the method for KFe_2As_2) by Kunihiro Kihou of the National Institute of Advanced Industrial Science, Japan. The samples were grown using a KAs flux grown with controlled amounts of substituted compounds. The use of an FeAs flux is unsuitable for growing high quality crystals due to the high melting temperature of $T_m = 1030°$ C which causes a loss of the more volatile K vapour, which also has a tendency to interact destructively with the quartz container. Instead, with a KAs flux, $T_m = 625°$ C and a stainless steel container which can sustain the high pressures of the K vapour generated stable crystal growth. Typical crystals are grown to a size of 5

$\times$ 5 $\times$ 0.2 mm^3. These samples were then characterised by the grower, including characterisation of superconducting properties.Single crystals of $(Ba_{0.5}K_{0.5})Fe_2As_2$ were mounted on an Al plate. The total sample volume is 1.03×10^{-7} m^3, sample mass is 600 mg. If we include the Al plate, the sample area is 15×15 mm^2, with an additional Cd window around the mosaic. Inclusive of the Al plates, the total sample thickness is 4 mm. The mosaic was aligned such that the single crystal **c** axis was aligned parallel to **B** and approximately parallel to the neutron beam, as outlined for KFe_2As_2.

However, in this investigation the dilution refrigeration insert is not used, but the Birmingham 17 T magnet is. At 3 K we observe VL diffraction patterns between 6 T and 16 T and for 1 T, 1.4 T and 3 T there are weak VL signals with resolvable rocking curves for each field. The diffraction patterns for 6 T to 16 T are presented in Figure 41. Sector boxes are shown in red highlighting the area over which the intensity of a diffraction spot is integrated in order to produce results. These patterns clearly show the primary domain of the hexagonal VL, but with a greater intensity for the left- and right-most spots as these spots were rocked over in ω, the azimuthal plane, and so were exposed to a greater proportion of the neutron intensity. Rocking curves were sampled from the diffraction patterns using GRASP with sectors 30 pixels wide and 60° arc-length. This is to represent the fact that the 1st hexagonal domain of the VL should be easily segmented by 60° per spot on the diffraction pattern. We also see a second domain VL which increases in intensity, relative to the first domain, with increasing field. With this experimental set-up we have only probed the VL lattice with fields up to $\approx 0.11 H_{c_2}$ and as such with these results we cannot rule out the potential presence of Pauli paramagnetism, nor can we rule out structural changes in the VL with increasing field strength.

The integrated intensity data is extracted by the use of rocking curves as demonstrated in Figure 42 for the case of 16 T and 3 K. The red sectors previously shown apply the area over which the intensity is extracted from the sample rock. In this

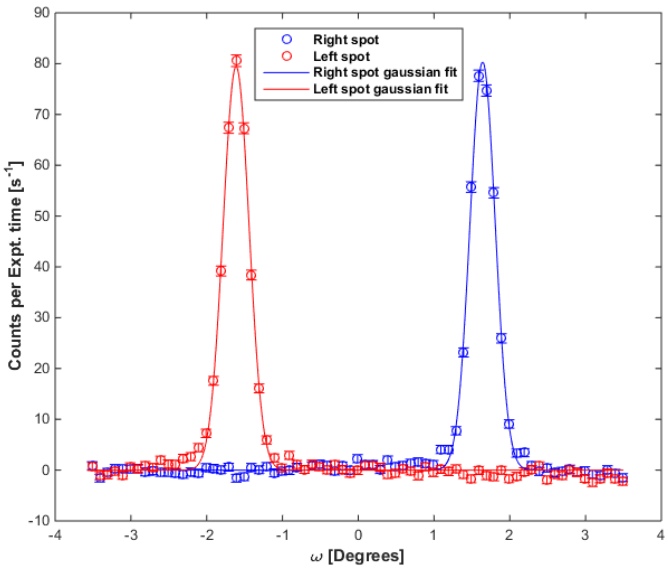

Figure 42: Rocking curves of the left- and right-most spots of the diffraction pattern from Figure 41. The spots under analysis are highlighted in Fig. 41 by the red sector boxes. For high fields a rock of $\pm 3.5°$ is used to contain some sufficient background. For lower fields smaller rocks of $\pm 2°$ were used instead to save time. The units for the y axis represent the number of counts per total amount of scan time per point within the red sector boxes in the analysis. The x axis is represented by the azimuthal angle ω.

case the rock is in the azimuthal plane. The rocking curves represent the intensities with respect to ω and are fitted with Gaussian functions in this case (Gaussian fits produced smaller errors than Lorentzian fits). From the Gaussian fit functions the integrated intensity is given by the GRASP software. See section 8.1, Appendix A for more details on this process.

5.2.1 Field dependence of the form factor

The first investigation was conducted at the D33 beamline at the ILL. Fields of 2 T, 6 T and 16 T were accessed as well as as temperatures up to $T_c \approx 37$ K. The results in Figure 43a demonstrate a very large form factor, $|F(q)|$, of 2 mT peaking at 6 T applied field, and with increasing field $|F(q)|$ only decreases by 10% between 6 T and 16 T. This suggests a trend of an unusually strong form factor signal that will persist for even larger fields, this allows for the possibility of Pauli limiting behaviour

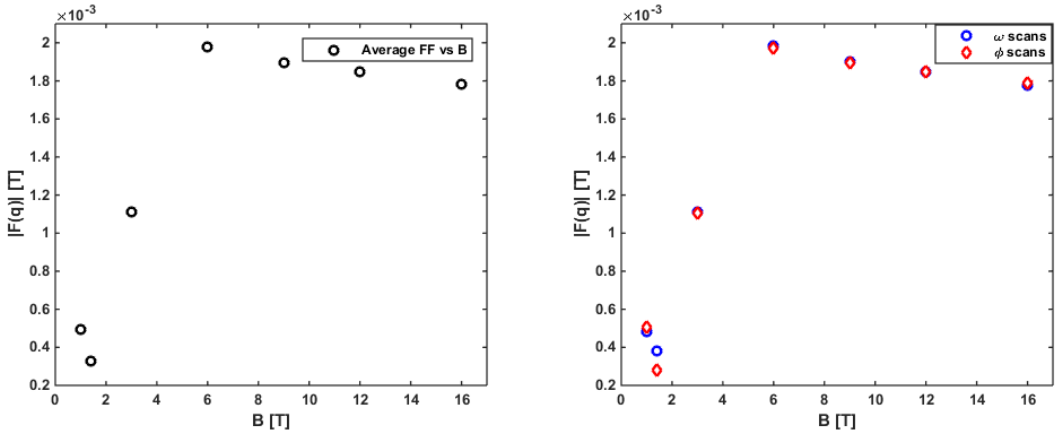

(a) (b)

Figure 43: (a) $|F(q)|$ vs field at 3 K averaged using multiple spots in the VL for better statistics. Above 6 T very little change in the $|F(q)|$ is observed, opening up the possibility of Pauli paramagnetic effects at stronger fields and ensuring that a VL will easily be observable for fields above 16 T. The low $|F(q)|$ below 6 T is possible due to disorder in the VL at low fields. (b) $|F(q)|$ vs field at 3 K. Similar to (a) except the ω and ϕ scans are not combined in an average, they are separated in order to look for potential disagreement with respect to direction of rotation.

for higher fields. What also stands out is the significantly weaker signal below 6 T. It seems that below this field there is significant disorder in the VL at low fields such as to limit the strength of the coherent VL signal, despite the standard wiggle-cool procedure being used here to ensure good ordering of the VL.

Given the small gradient of $|F(q)|$ with respect to the field, it is difficult with the data set in Figure 43b to be able to draw a good fit or a comment on the behaviour with respect to field. This is likely in part due to the very high value of H_{c_2}, such that we are looking at potentially only the lower $10 - 15\%$ of the accessible field relationship for this material.

We can also comment on the separated results in Figure 43b. If there were any potential *a*-*b* anisotropy in the VL then we might see a difference between the ω (azimuthal) and ϕ (polar) scans. Differences here could also indicate structural evolution in the VL or shifts in the pairing mechanism or multi-gap effects. However, the results between the two different rotational axes are strikingly similar and show strong agreement with each other. We can also see for both graphs of $|F(q)|$ vs B

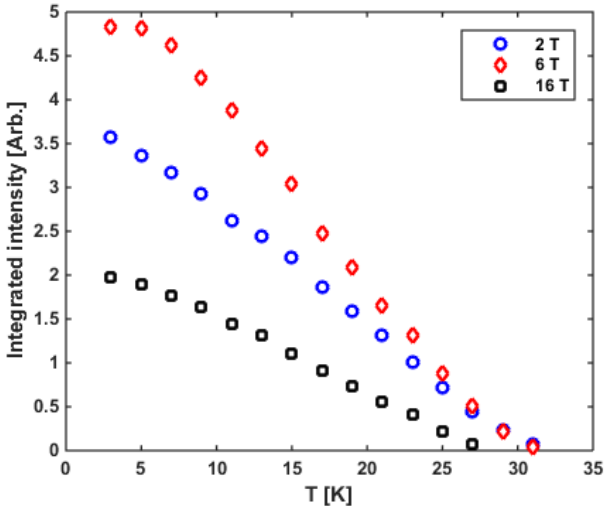

Figure 44: Integrated intensity ($I(q)$) results as a function of temperature. These results are the averages between the ϕ and ω scans. The integrated intensities are extracted from gaussian fits to the rocking curves, like those in Figure 42.

that the errors remain similar and small across the entire field range.

5.2.2 Temperature dependence of the form factor

Figure 44 shows the integrated intensity results averaged over the ω and ϕ scans. Here we can see the elevated signal in the 6 T results, concurrent with the observations under field variation in Figure 43a. We have seen that under field variation the signal peaks at $\approx$ 6 T, meaning 6 T would reasonably be the largest set of temperature dependent signals. While the signal strength varies unintuitively the intercept with the x-axis demonstrates the T_c variation with applied field conforms to expectations. The integrated intensity signal evolves between the sets such that the 6 T results follow an S-shape with a high gradient for intermediate temperatures, while the 2 T and 16 T follow a lower gradient, almost linear, evolution with T. The steeper gradient of the larger 6 T signal gives a stronger impression of T-dependent variations compared to the 2 T and 16 T sets. Another feature unique to the 6 T results is apparent plateauing of the integrated intensity at $T \leq 5$ K, however we don't have any lower temperature data points to see the plateauing in comparison to the potential low-T plateauing in the 2 T and 16 T sets for $T < 3$ K.

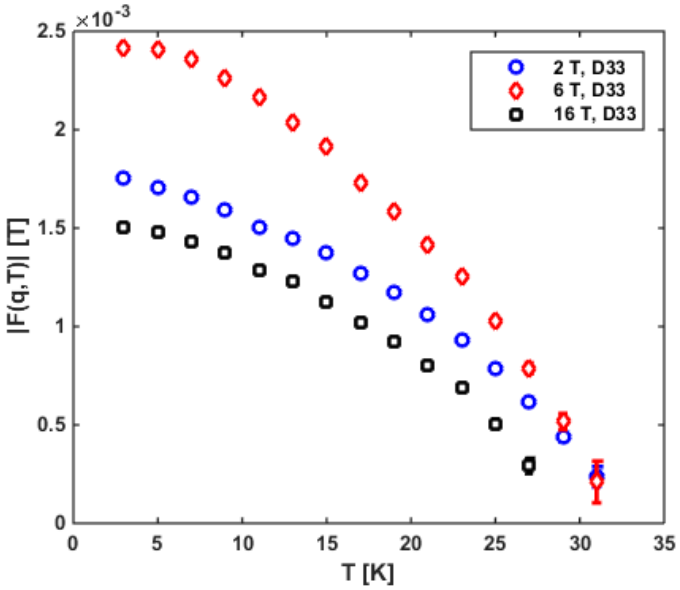

Figure 45: Form factor calculated from the temperature scan integrated intensities in Figure 44 using the Christen formula. A core correction term is used with $c \approx 0.52$ using the value from the related compound KFe_2As_s [109, 12] and an approximated Pippard coherence length of $\xi_0 \approx 1.53$ nm ($\kappa \approx 81$).

Figure 45 shows the temperature dependent form factor, calculated from the integrated intensity results and the rearranged Christen formula, equation 104. As with the integrated intensity we have an elevated signal strength over the other sets for 6 T that falls below the signal strength of 2 T for high temperature $T > 30$ K. These results also suggest that even at $T \approx T_c$ the form factor signal will be resolvable for high fields; given the signal strength is still in the mT range for 16 T. This suggests that even at double this field strength the form factor will likely be in the mT range. The weaker signal for the form factor at 2 T is most likely due to high levels of disorder in the VL at low field. Although the coherence length also varies with temperature, there is no available information outside of ideal models for how the coherence length evolves with temperature here, so the approximation of $\xi(T) \approx \xi_0 = 15.3$ Å (calculated by the sample growers) is used as this is accurate for most of the temperature range due to a comparatively low field compared to H_{c_2}.

Again, we see no significant dips or aberrations in the behaviour of the form

factor to indicate a rearrangement of the flux lattice from the results in Figure 45. This is in direct contrast to the related compound KFe_2As_2 covered in the previous section.

5.2.3 Identifying the pairing mechanism of $(Ba_{0.5}K_{0.5})Fe_2As_2$

By comparing the integrated intensity with ideal models using the Christen Formula, we can compare the results with the ideal case for each potential interpretation; a null hypothesis approach as discussed earlier in this work (section 2.7). Figure 46 shows the results for each set of $I(q)$ vs T data at 6 T, 12 T and 16 T compared to two models: s-wave and nodal pairing symmetry.

Figure 46 indicates that consistently, for every field accessed, the data strongly supports an s-wave interpretation. Equally the form factor calculations presented using the Christen formula in Figure 47 support a strong adherence to a BCS, s-wave behaviour for the gap symmetry. Not only is this result consistent across all the fields accessed but there are no visible anomalies within the data to suggest any kind of multiple gap structure or rearrangement of the gap symmetry or VL structure. However, we do see an evolution in the signal at $T \rightarrow T_c$ from 2 T up to 16 T in both the integrated intensity and the form factor. This is a small enhancement of the signal for 6 T above 22 K and a significant enhancement of the signal at 16 T above 15 K. This response is outside of the established signal size we would expect to see for the given models. This suggests that we are seeing an equivalent effect to what was demonstrated previously with KFe_2As_2; there is a Pauli paramagnetic effect enhancing the form factor signal at high fields. Given this, we would expect to see further enhancement at higher fields.

The conclusions drawn from the null hypothesis approach to the data are supported by the subsequent penetration depth calculations in Figure 48. Each set of $|F(q)|$ calculations is then put into equation 105 to get $\lambda(T)$.

As can be seen from the fits, the powers for each field set all sit within error of

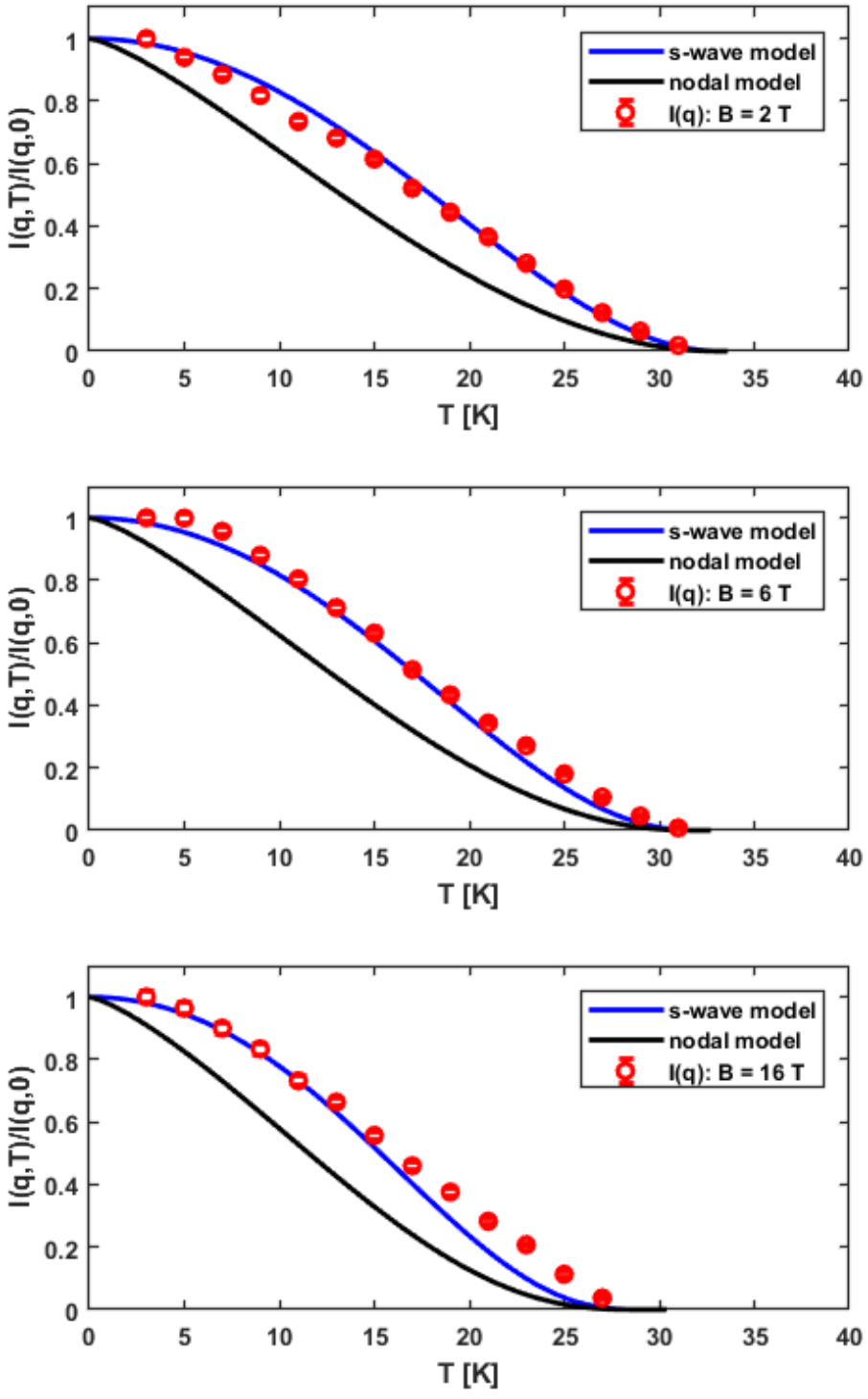

Figure 46: The normalised integrated intensity ($I(q)$) at 2 T, 6 T and 16 T vs temperature, compared to models of $I(q)$ behaviour according to the BCS theory for s-wave pairing, and a nodal model that also covers potential d-wave pairing.

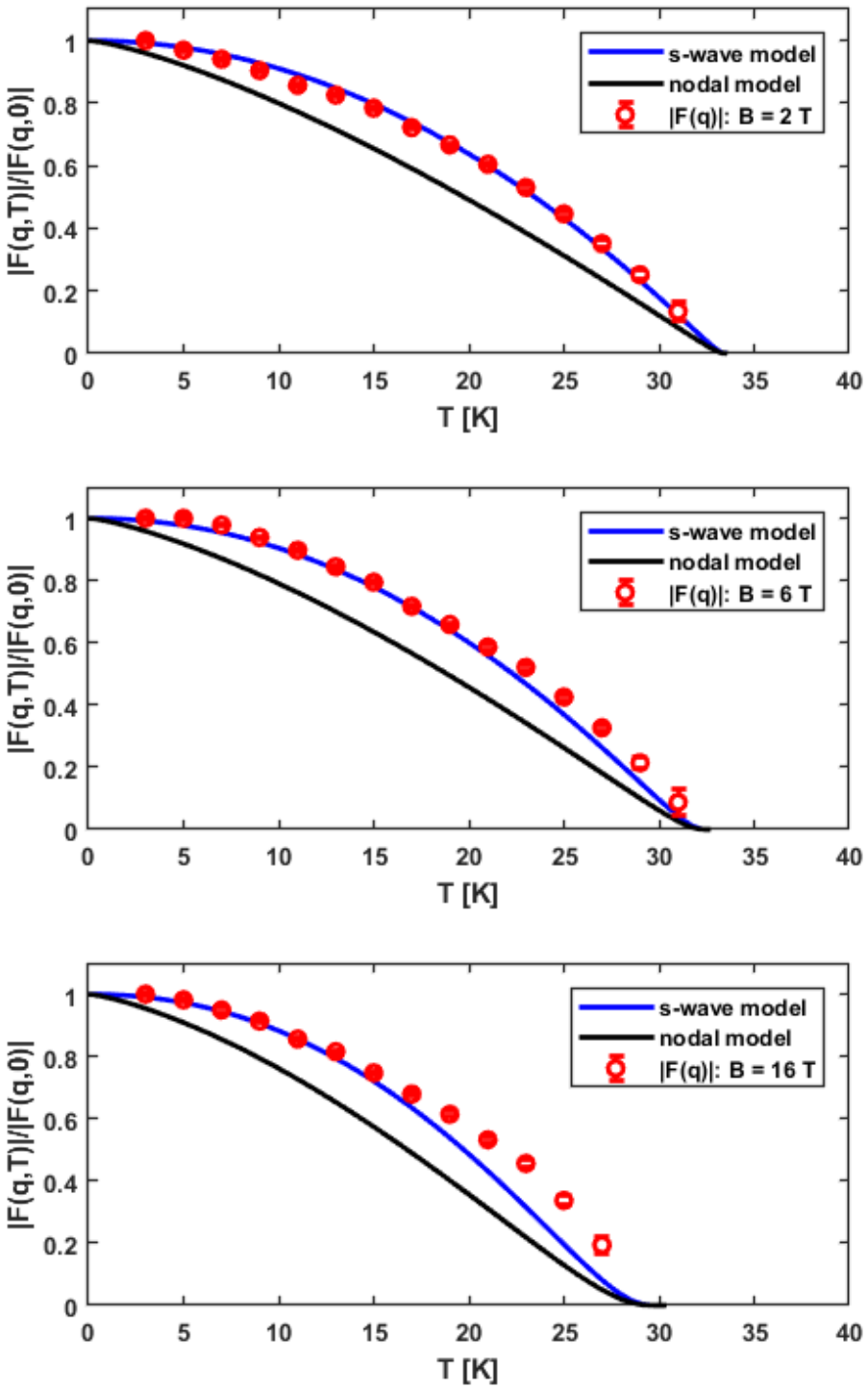

Figure 47: $|F(q)|$ at 2 T, 6 T and 16 T calculated using the Christen formula (equation 104) rearranged. Previously the $|F(q)|$ calculations contained a varying value of $\xi(T)$ with temperature, however here the core correction values are roughly cancelled out in normalisation. Once again, as with Figure 46, the data clearly indicates a strong adherence to s-wave behaviour.

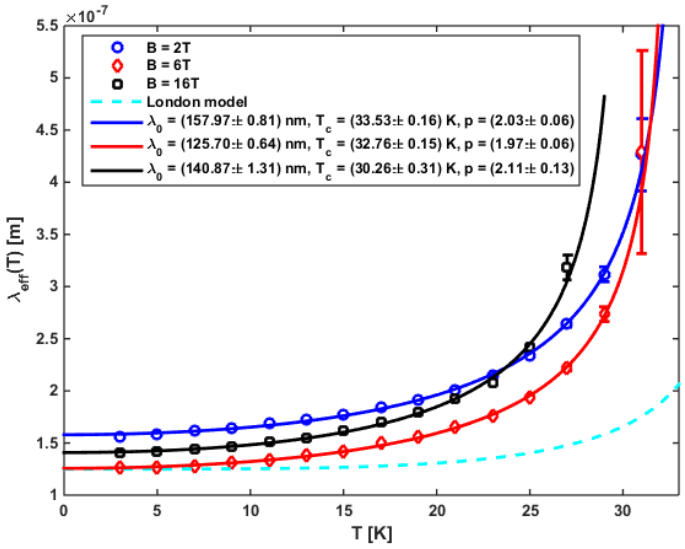

Figure 48: Calculations of $\lambda(T)$ from the modified London model (taking into account core corrections) for each applied field. These results are compared to the expected London calculation of the evolution of $\lambda(T)$ with fits for comparison. However the model diverges at $T = T_c$, whereas the application of a magnetic field means the results will diverge at a lower temperature which has been estimated from the form factor temperature data and confirmed by the fitting procedure.

$p = 2$. This comfortably aligns the data to the s-wave model, which is of course consistent with what we have already seen. Again there are no major anomalies other than the continued overlap between the 2 T and 6 T data, due to an enhanced 6 T signal. Despite the signal enhancement, the power law is still very indicative of BCS, rather than unconventional behaviour. We see at $T \to T_c$ the 16 T results shift such that they fall into a more expected penetration depth compared to the lower fields; this shift happens at 24 K. However, contrary to expectations we see the 6 T, rather than the 2 T results display the smallest penetration depth, with $\lambda(B = 6T)$ not increasing above the 2 T signal until 30 K, almost at T_c and with a large error compared to the rest of the temperature range.

5.2.4 Non-local corrections to the superfluid density

Although the superfluid density calculations in Figure 49 don't add to the analysis of pairing mechanisms, especially given the fits are the recalculated fits from the penetration depth, these results do very much highlight the stark difference in carrier

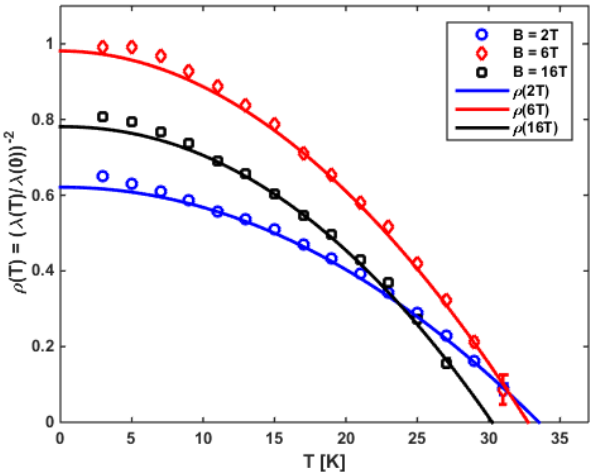

Figure 49: Calculated superfluid density using the previously calculated penetration depths from the temperature scan data. Core corrections have been taken into account with the form factor to produce the penetrations depths for these calculations. The model accompanying the data points is a modified version of the BCS model for the penetration depth; which is $(\lambda_{eff}(T)/\lambda(0))^{-2} = 1 - t^4$, but using the calculated parameters in the fitting procedure from Figure 48. The results have been normalised to the largest signal response, the 6 T data.

numbers between the 6 T results and the other two fields; with the 2 T and 16 T conforming to expectations for temperature dependence. It is not clear why the 6 T signal is so strongly enhanced over the other fields other than an argument of low field disorder for $B < 6$ T. The field dependent scans shown in Figure 43a and the VL patterns for low field scans indicate a greater amount of disorder for this regime in the VL signal compared to the upper field regime. This would normally generate much higher errors, compared to the high field regime. The following equation is used to calculate the normalised superfluid density

$$\rho(T) = \left(\frac{\lambda_0}{\lambda(T)}\right)^2 \tag{117}$$

where the value of λ_0 is taken as the intercept with the y-axis.

By using the approach outlined in section 1.5 we can try to establish the likelihood of strongly-coupled d-wave pairing being a driving mechanism in this material. The onset of non-local effects as outlined by this phenomenological approach only

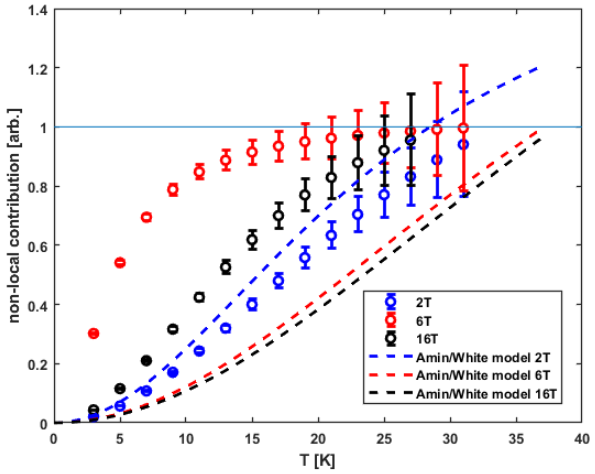

Figure 50: Non-local coupling contributions. This data represents residual ratio calculations of $n(T)$ and $\rho(T)$ for $(Ba_{0.5}K_{0.5})Fe_2As_2$ as before in this work, with $n(T)$ as the calculated superfluid density from the penetration depth data and $\rho(T)$ being the BCS model and equation 64 used to generate these results. Once again at $y = 1$ the non-local contribution is completely minimised, indicated by the black reference line. The dotted lines are the Amin/White models of the non-local contribution indicating the expected behaviour for each field [102, 96].

become apparent below a characteristic temperature, $T^* = \Delta_0\xi_0 q/k_B \approx 8.0$ K, below which non-local coupling is effective. The consequence of the shift from linear to T^3 behaviour is the appearance of weak low-T dependence. In this case, given $T^* \approx 8$ K, it would appear that a small portion of the superconducting regime should be affected by non-local coupling contributions. We now use equations 63 and 64 to establish a ratio by which we can observe any modulation in non-local effects.

We see in Figure 50 a varied response to non-local coupling in the superfluid density. The models predict the 2 T set to have the weakest response of non-local coupling, but calculations point to it having the strongest response but also the closest response to the Amin/White predictions. The 6 T set has the weakest non-local coupling response and the 16 T set falling in between. This means that the non-local coupling is approximately inversely proportional to the form factor response, while the Amin/White models predict a very different behaviour. Additionally we see the models indicating the 16 T and 6 T results being quite close together and of a similar shape of curve. Instead the calculations indicate some degree of similarity

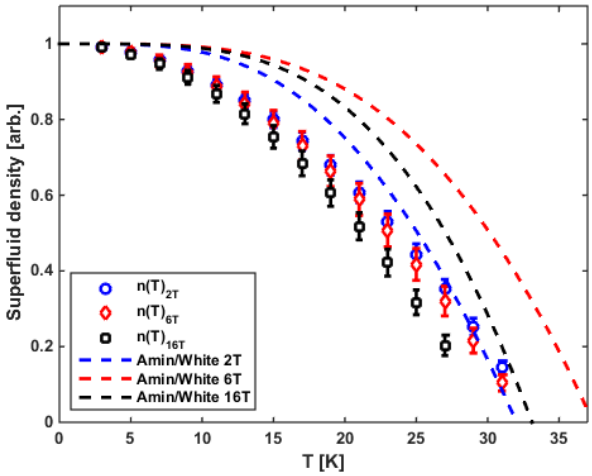

Figure 51: Superfluid density calculated from measured data compared to the Amin/White predictions using equation 63 with the non-local limiting temperature, T^* for $(Ba_{0.5}K_{0.5})Fe_2As_2$. The Amin/White models, plotted with dashed lines, produce larger values for the superfluid density than those calculated from the form factor. This comparison suggests a slightly weaker non-local coupling effect than predicted and a smaller superfluid density as a result.

between the 2 T and 16 T results with the 6 T set as the main outlier. In fact the 6 T set very rapidly converges to unity for the non-local coupling contribution; above 10 K the non-local coupling is within error of unity. Equivalently the 6 T and 2 T results converge on unity well before the models predict them to, suggesting weak non-local spin coupling.

When we look at the superfluid density calculations in Figure 51 we see a great degree of similarity between the different field sets. However, the superfluid density does appear to be slightly stronger for weaker fields, as one would expect. The Amin/White models predict a superfluid density that is more persistent at low temperatures compared to the calculations. Once again the 2 T results appear to be the closest match to the Amin/White model but still fall short. These calculations suggest there is not a particularly significant non-local coupling contribution at any field, this is in line with the previous conclusions that we are likely looking at an s-wave superconductor that is very strongly Type-II ($\kappa \approx 81$), so generally strong non-local coupling effects are going to be weak according to the London model and

the work of Volovik [10, 32], discussed earlier in this work.

5.3 Results for $(Ba_{0.5}K_{0.5})Fe_2As_2$: EXED beamline, High Field Magnet (HFM), HZB July 2017

A second investigation with $(Ba_{0.5}K_{0.5})Fe_2As_2$ took place in July 2017 at HZB using the small-angle neutron scattering beam-line for extreme environments and using the high field magnet (EXED/HFM). This was a time-of-flight (TOF) experiment that uses a range of neutron wavelengths, rather than rocking the sample in order to probe the Bragg conditions for the superconducting VL. Previously we have discussed the beam in monochromatic terms. In TOF the beam is pulsed, during flight in the beam-line the faster neutrons in the "white", polychromatic beam will arrive first, this broadens out the pulse to some known time. The breadth of this pulse and the bandwidth of neutrons can be selected by the use of chopper discs as discussed previously for controlling the width of monochromatic beams at PSI and ILL. This experiment used fields up to 25.5 T for similar temperatures to the ILL experiment. Fields accessed were 14 T and 16 T for an overlap with the ILL data as well as 20 T and 25.5 T for the high-field scans. The aim of this experiment was to probe for potential Pauli paramagnetic effects for higher fields by looking at the persistence of the VL signal up to 25.5 T compared to the peak signal previously seen at 16 T.

5.3.1 Instrumentation for EXED/HFM

As previously described, the high field measurements were conducted over a second experiment at HZB using the EXED/HFM instrumentation [104]. The TOF setup allows for neutrons to be available from 0.7 to 15 Å. Due to the chopper setup, the system can operate between a narrow 0.6 Å beam and broad 14.4 Å beam. Choppers are available from $\Delta t \approx 6\mu s$ up to $\Delta t \approx 5000\mu s$ for balancing intensity and resolution. The diffraction pattern is picked up by six ^{3}He linear position detector

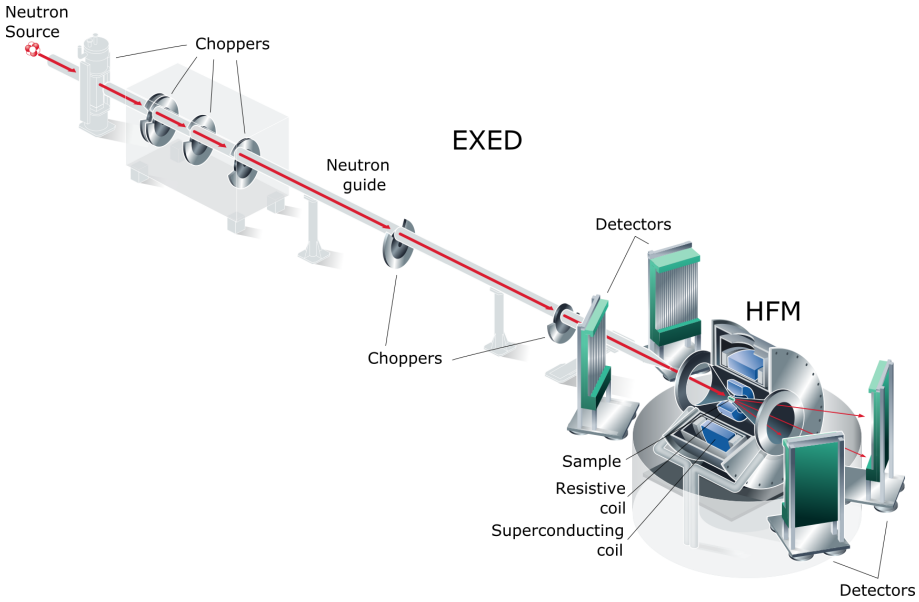

Figure 52: Schematic of the EXED beamline including the HFM and detectors. During the experiment all four detectors were positioned behind the HFM relative to the beam guide. This is because we are not measuring any large angle scattering, as our Q vector is in the realm of small angles $\approx 1°$. This image was sourced from [103].

banks that subdivide 204 linear position detector tubes. The cryomagnet is a hybrid system with a water cooled resistive coil inserted in a room temperature bore inside of the superconducting coil. Together these provide up to 26 T horizontal field, with 30° conical openings at either end for access to neutron scattering. The magnet sits on a rotating table that allows for a maximum of 12° rotation, giving a maximum possible scattering angle of $2\theta_{max} \approx 27°$. The horizontal rotation of the magnet is denoted by the angle ω, similarly defined in previous sections.

5.3.2 Experimental technique and data extraction for EXED/HFM

Temperatures were accessed from 1.3 to 33 K and fields from 14 to 25.5 T. For changing the field the wiggle-cool method was used as previously described for KFe_2As_2 and $(Ba_{0.5}K_{0.5})Fe_2As_2$ at the ILL with a constant wiggle field of $\Delta B = \pm 0.005$ T. Backgrounds were taken for each field accessed at 30 and 45 K. The detector was rotated in the azimuthal plane to the following angles for scans: ω = 2.0°, 1.6°, -1.5°, -2.7°, -3.0°, -3.2°, -3.4°. These scans could be overlapped to provide a contour

High Filed Magnet data (table)

Central Field	> 25 T
Bore	50 mm horizontal warm bore
Opening Angle	30°
Power Resistive Insert	4.4 MW
Field Homogeneity	< 0.5% Cyl. 20 mm ∅ 20 mm length
Operating Current	20 kA
Magnetic Field of Resistive Insert	12 - 13 T (4.4 MW)
Magnetic Field of Supercond. Coil	12 - 13 T
Height	~ 5 m
Total Weight	~ 25 t
Cold Mass (4.5 K)	~ 6 t

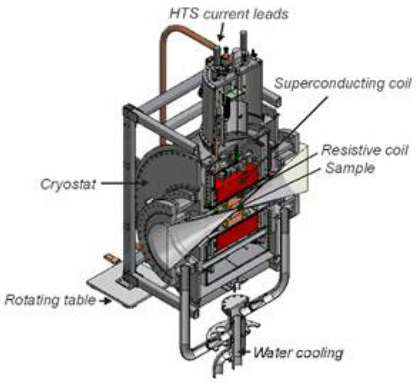

Figure 53: Technical details of the High Field Magnet (HFM). The image shows only the cryomagnet and sample stage of the HFM/EXED beamline. This image was sourced from [103]

region of the diffraction spots in q-space. Accessing these angles is important in order to place measurable diffraction spots onto one of the detector banks. Given the portable nature of the detector banks, there are gaps where neutrons cannot be detected between the positions of the detector banks. A consequence of this setup is that at each angle the beam stop needs to be tracked in order to make sure direct beam does not impinge on the detector banks and cause saturation. This is because the beam stop moves along a straight axis while the cryomagnet rotates, so the beam stop tracking is non-linear and has to be confirmed for each potential angle of measurement. In this case the beam stop position could be fit very reasonably by a second order polynomial with a shallow curve: $bs_y = 0.3672\omega^2 - 69.643\omega + 204.80$, with beam stop positions tested between 157 mm and 461 mm for that fit. The chopper phases were set for $< \lambda >= 6$ Å and $\Delta\lambda = 7$ Å.

An example of a single scan can be seen in Figure 54. Here the angle is set to $\omega = -3.4°$ at base temperature, 1.3 K and a field of 25.5 T. The position of

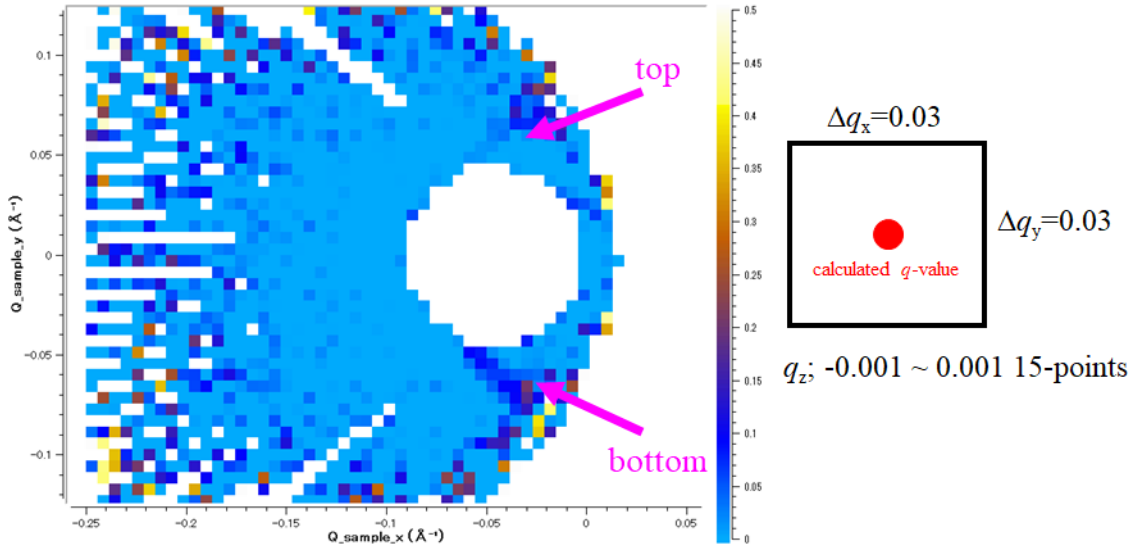

Figure 54: Single contour scan at 1.3 K and 25.5 T for $\omega = -3.4°$. A large area in the centre of the diffraction pattern is the masked-out direct beam. The arrows indicate the approximate positions of two spots, identified as the top- and bottom-right of the hexagonal VL. Included is the q-space square used for analysis of the image in order to extract the integrated intensity. This is much like the sector boxes in GRASP. The q space is in units of Å^{-1}

the spots to be analysed is denoted by the arrows in the image, with most scans during this experiment showing the top- and bottom-right spots of the hexagonal VL to be most prominent. The smearing in the spots in an arc is due to the use of a broader range of neutron wavelengths than in the monochromatic case of the ILL and PSI experiments, given those outlying wavelengths from the average will satisfy the Bragg conditions at different angles of diffraction. Included in Figure 54 is the sector box in q space that is laid over the diffraction image centred on the identified Bragg spots. With this box (in units of Å^{-1}) a curve of the intensity vs q can be plotted from extracting the number of counts per pixel with respect to pixel position in q-space with the background subtracted. The area between the intensity curve and the background is calculated to find the integrated intensity value at that field and temperature. This process is repeated for many diffraction patterns with layered contour plots, like in Figure 55, to improve the resolution of the diffraction spots and the overall signal strength for the VL Bragg spots.

By combining the scans from many angles across several detectors a more com-

prehensive image of the VL can be seen. An example of the contour combination can be seen in Figure 55. Here we see combined scans at 20 T and 1.3 K producing a VL with a visible left- and right-most diffraction spots and an upper and lower spot on the left hand side of the VL diffraction pattern. This data is incompatible with GRASP and so has to be analysed manually by defining the q space bounds of the spots for the same process that GRASP is purpose built for; creating a curve for the intensity of a defined image space then integrating that Gaussian/Lorentzian curve for the integrated intensity. From this basis the data can be taken forward in much the same manner as before with regards to modelling and calculating the form factor. I must acknowledge and thank Minoru Soda, Research Associate of the Institute of Solid State Physics, University of Tokyo for doing the bulk of the initial conversion of the data from raw diffraction patterns to integrated intensities using Mantid© [105, 106, 107, 108] software and Python™, and Maciej Bartkowiak, Helmholtz-Zentrum Berlin, Germany for coding support and later image rendering and analysis.

5.3.3 Integrated intensity at high-field ($B \geq 14$ T)

Figure 56 shows the integrated intensity signals from the EXED/HFM experiment with respect to temperature. We can see that the 25.5 T signal is the smallest, as expected, but it is surprising to see that the 20 T and 25.5 T signals are both persistent up to the range of 25 K to 30 K. This is somewhat unexpected given that we have previously seen that the 16 T signal at D33 dissipated by ≈ 28 T. Another unexpected feature is the additional signal strength seen in the 16 T results for the high temperature regime. This feature is not observed as clearly in the D33 results until normalised and compared to the models in Figure 47, where we see an enhancement of the signal above 17 K. In this case it would appear that the same enhancement is present, but clearer.

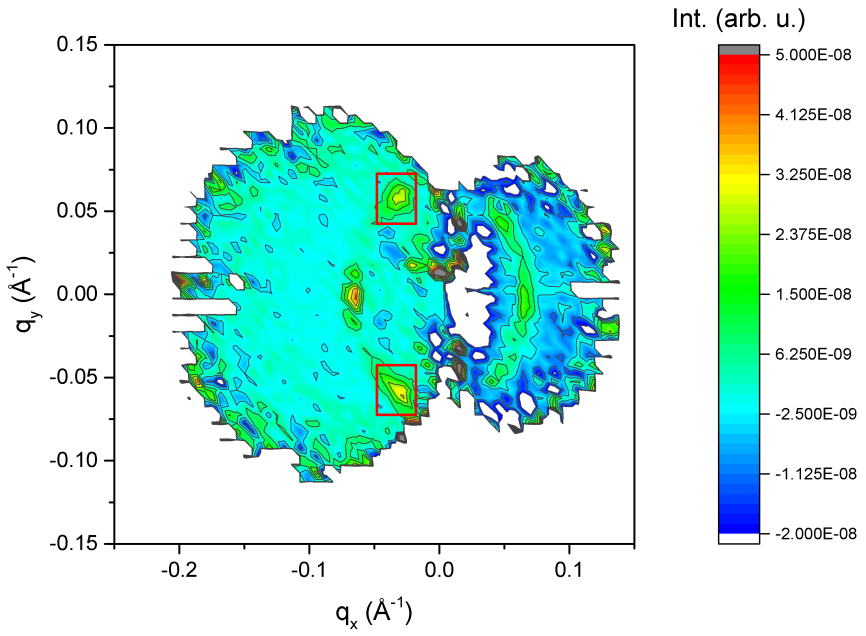

Figure 55: Contour image of overlapped scans of raw data from ω = 2.0°, 1.6°, -1.5°, -2.7°, -3.0° and -3.2°. These scans combine the tracked information about the beam stop as well in order to subtract the background and mask the direct beam. These scans were all taken at 20 T and 1.3 K.

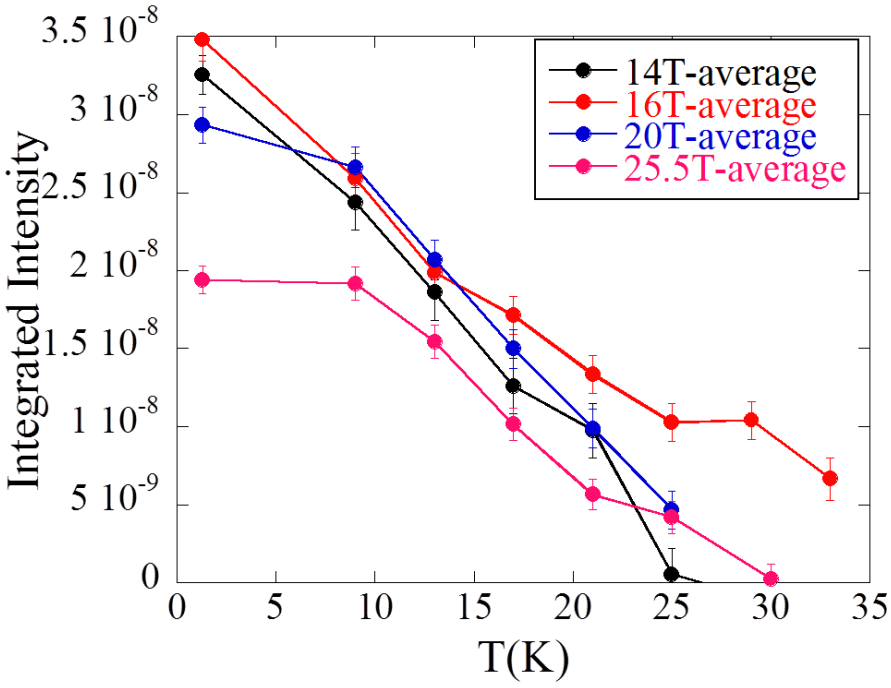

Figure 56: Averaged integrated intensity of the flux lattice of $(Ba_{0.5}K_{0.5})Fe_2As_2$. Results are averaged over the top- and bottom-most spots available for analysis. These spots can be seen in Figures 54 and 55.

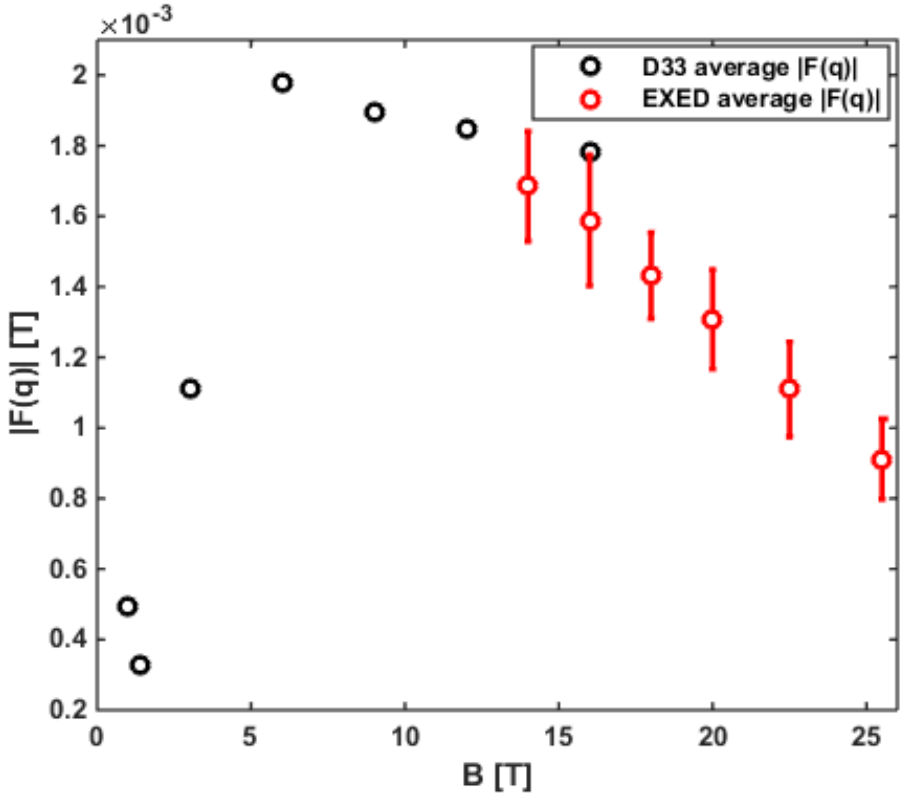

Figure 57: Averaged $|F(q)|$ versus field with the EXED and D33 data combined to show the continuation of the form factor behaviour. The EXED data is averaged over top and bottom spots while the D33 data is averaged over the ω and ϕ scans, as previously discussed in the D33 experiment section.

5.3.4 Field dependence of the form factor: Comparison with low-field data

The field dependent results in Figure 57 show the D33 and EXED results together. The EXED high field data demonstrates a steeper gradient and faster decrease in form factor than the gradient set by the low field data from the D33 investigation, indicating a much faster fall-off in signal strength with field than previously expected. Despite this we are still seeing a form factor signal of ≈ 1 mT for an applied field of 25.5 T. A field of 25.5 T is still only $\approx 18\%$ of the theoretical upper critical field for this material. As such, probing even higher fields could yield an $|F(q,T)|$ signal that behaves unexpectedly with field on approach to the upper critical field (notwithstanding Pauli limiting effects). Given this, there is a reasonable overlap

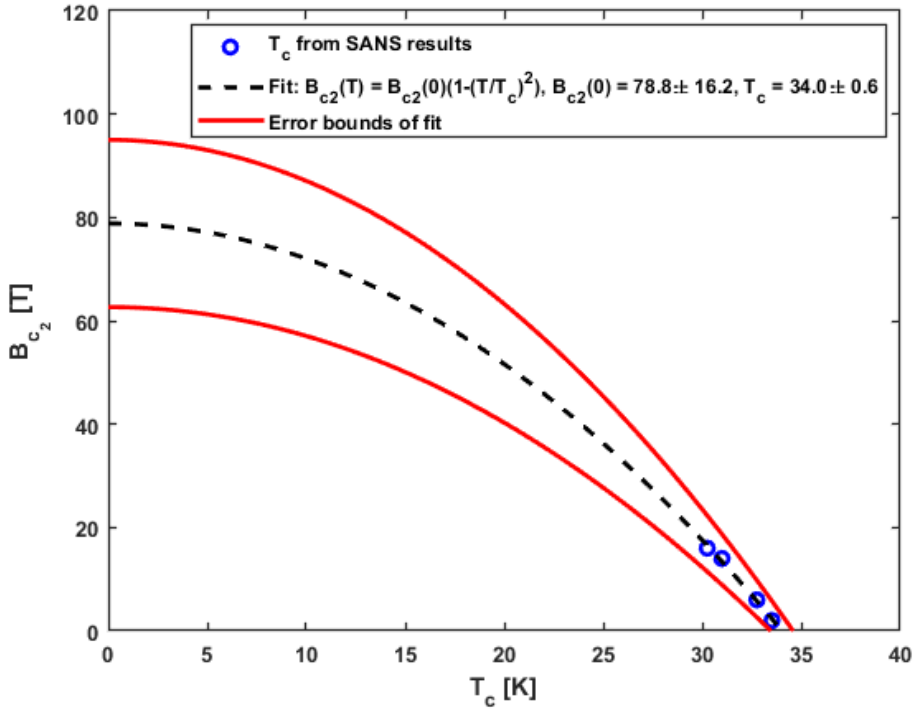

Figure 58: Fit and bounds for the Ginzburg-Landau approximation for upper critical field and critical temperature behaviour fitted to the D33 results for T_c and the 14 T set from the EXED investigation.

between the intermediate fields of 14 T and 16 T (within error); the trend of the EXED high data would suggest a signal suppressed at $\approx$ 50 T if the behaviour remained unchanged for higher fields. This is significantly lower than the 140 T predicted, but the 50 T value is a linear extrapolation, it does not take into account that the $|F(q)|$ might flatten out at even higher fields, or even rise due to Pauli paramagnetism. The likelihood of a persistent signal above 50 T is not insignificant given the large $|F(q)|$ signal at the fields already accessed.

5.3.5 Temperature dependence of the form factor

As a result of the difficulty in establishing the trend of T_c with respect to applied field for the EXED results, the D33 results and the 14 T results of EXED were used to provide four data points to fit a Ginzburg -Landau (G-L) model of the potential behaviour of B_{c_2} and T_c for larger fields. By fitting the values of T_c(2T) = 33.5 K, T_c(6T) = 32.8 K, T_c(14T) = 31.0 K and T_c(16T) = 30.3 K extracted from the

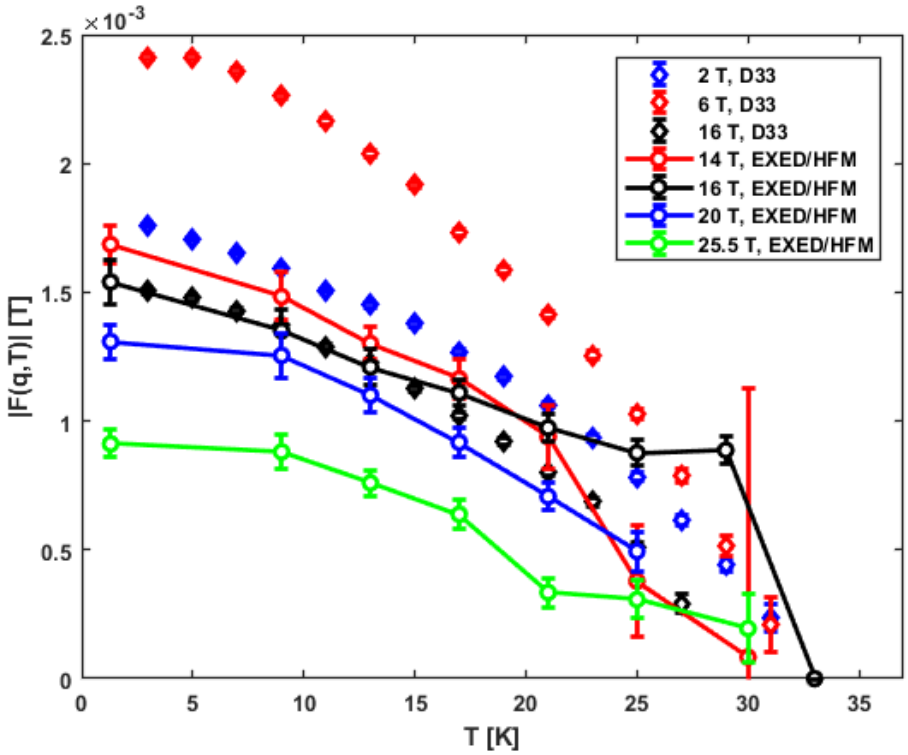

Figure 59: Form factor, $|F(q,T)|$ versus temperature, T for both the EXED and D33 results.

potential intercepts of the D33 form factor data with the x-axis and using the G-L equation $B_{c_2}(T) \approx B_{c_2}(0)(1-(T/T_c)^2)$, we get fits of $B_{c_2}(0) = (78.84 \pm 16.18)$ T and $T_c = (34.03 \pm 0.56)$ K. This fit and the bounds of the fit are plotted in Figure 58. This result is used to gauge the values of T_c for 20 T and 25.5 T, where an estimation of T_c is much more difficult. These values are subsequently predicted to be $T_c(20\text{T}) = 29.4$ K and $T_c(25.5\text{T}) = 28.0$ K and are used in the models for the analysis in this section and later sections. The modelled upper critical field value of $B_{c_2} \approx 78.8$ T is much smaller than the value of 140 T predicted from the coherence length from previous work.

We see from Figure 59 that the high field scans, 20 T and 25.5 T, generally conform to expectations of a decreased overall signal strength for all temperatures accessed. Generally, there is good agreement at low temperature for the overlap fields of 14 T and 16 T. This breaks down somewhat above 20 K for the 16 T EXED data where the signal experiences an unusual enhancement not seen in the previous

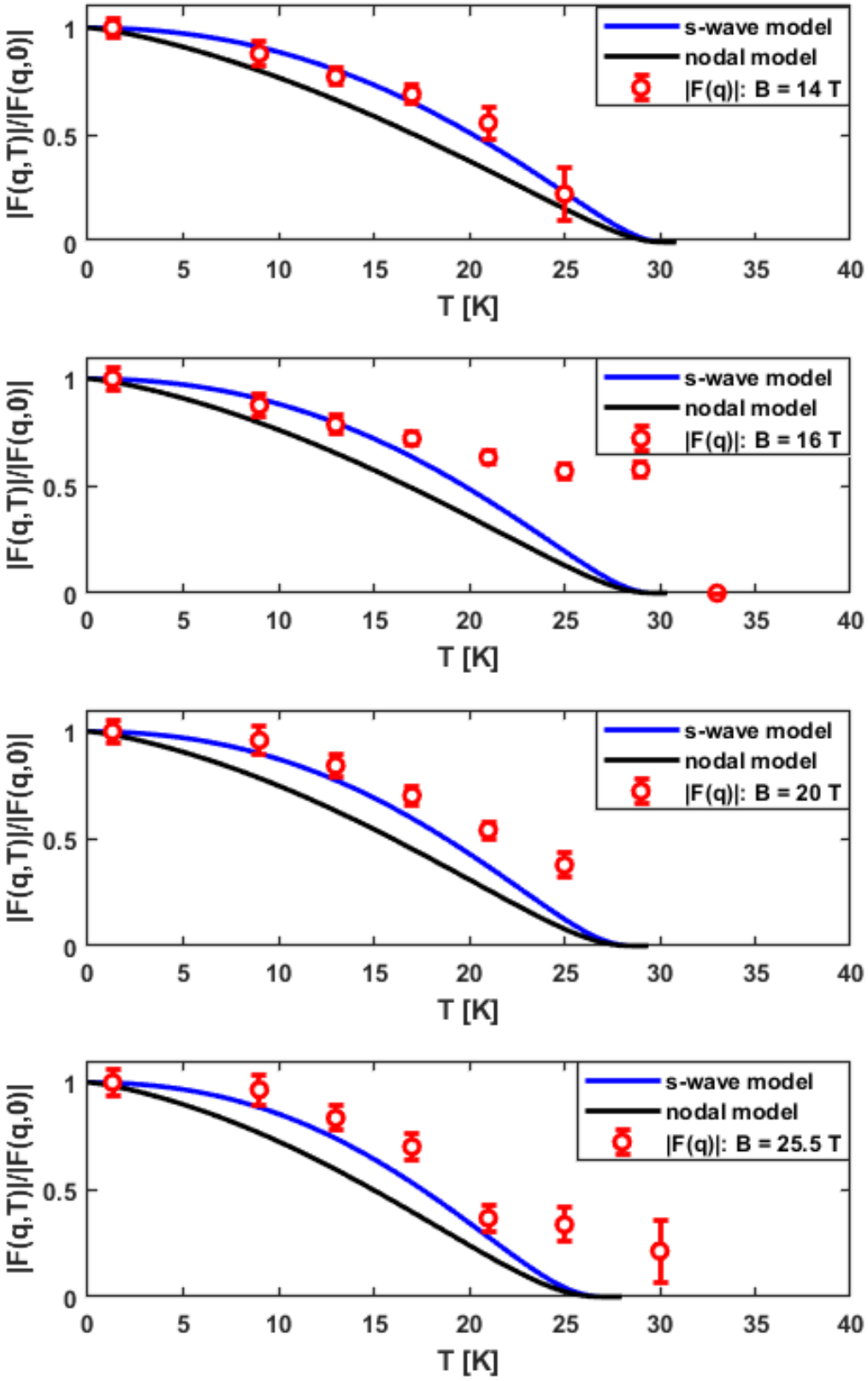

Figure 60: Normalised form factors for each of the applied fields in the high field range. Sets are presented with increasing field in descending order. Data is presented alongside ideal *s*-wave and nodal models for the form factor behaviour.

16 T data set. The high field data continues the expected trend of a flattening-out of the form factor signal over the accessed temperatures, however the T_c for these fields remains high for all fields accessed. This is expected to some extent given we are still below 20% of the predicted B_{c_2} of this material, but the data indicates very little change in T_c for increased applied field.

Similar to the process with the $(Ba_{0.5}K_{0.5})Fe_2As_2$ D33 data, we present here the EXED high-field data normalised alongside ideal models. This null hypothesis approach compares pairing symmetry models of the form factor to the normalised data to establish trends and similarities. We can see from Figure 60 that below 20 K, for all fields, the results broadly adhere to an s-wave model for form factor behaviour. However, above 20 T we see significant deviations from all models with an overall increase in signal for all fields except the 14 T data set (which does not exhibit this behaviour). The adherence to an s-wave model is not unexpected given the lack of observed variation in the VL structure with field variation. This is also expected for the high field results given the low field results showed a very strong correlation with an s-wave interpretation and similarly showed no variation in the VL structure with field variation.

This deviation is consistent with previous observations made on the form factor that showed an enhancement of the temperature dependent signal for $T \to T_c$. The relative enhancement between the fields is more apparent here due to the normalisation process and the comparison to the models. We again see a significantly larger enhancement of the signal for 16 T in the EXED data.

5.3.6 Penetration depth under high-field

The penetration depth, $\lambda(T)$ was calculated from the form factor, using the previous framework outlined using equation 105. The penetration depth for the high field scans are presented in Figure 61. Here, we see the successively high fields producing results consistent with expectations for a material with such a high predicted H_{c_2}.

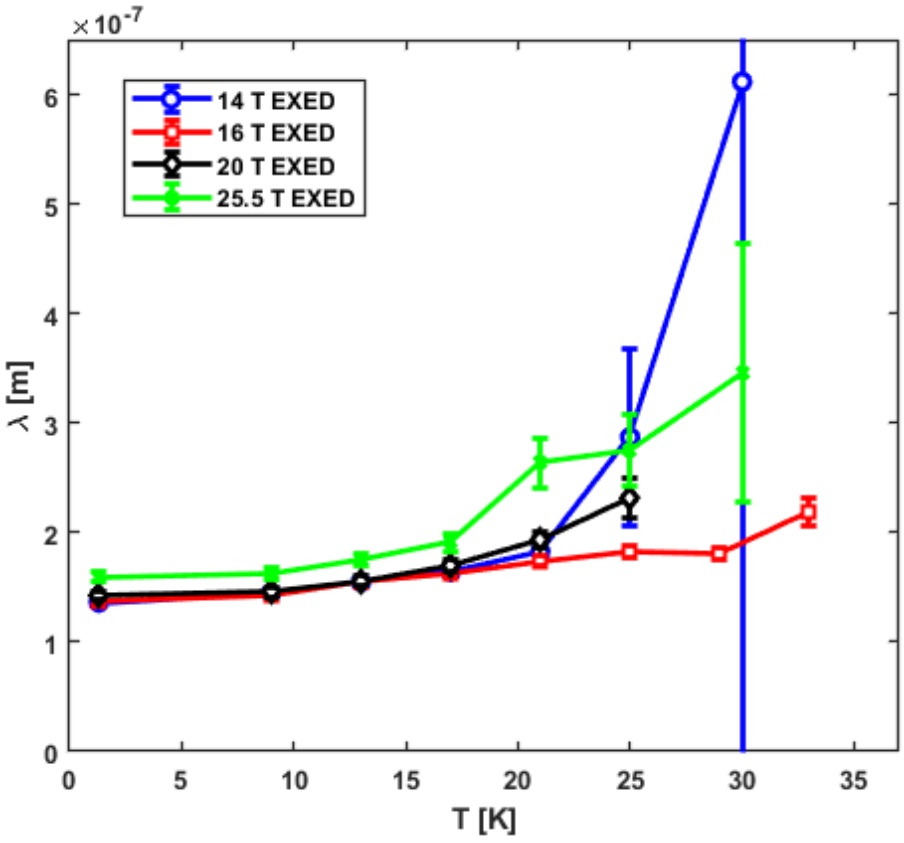

Figure 61: Penetration depth, calculated from the form factor, versus temperature. At the highest temperature, the signal is very weak, hence the large errors.

The previous D33 low field results yielded $\lambda_0^{16T} \approx 140$ nm. In the EXED results the 16 T set gives $\lambda_0^{16T} \approx 133$ nm but with a margin of error of 7.8 nm, placing it broadly in agreement with previous results.

We do see a continuation of trends for the 20 T and 25.5 T results with a fitting procedure. Both 20 T and 25.5 T yield power law fits of $p_{20T} = 1.97 \pm 0.25$ and $p_{25.5T} = 2.00 \pm 0.77$, which puts them very much in line with an s-wave interpretation as expected, but with errors reflecting the greater degree of uncertainty in the EXED results. The 14 T and 16 T fits are not so clear. We can see the consequences of the stronger form factor than expected for the 16 T set at high temperature has produced a much smaller penetration depth than expected for high temperature at this field. The behaviour is not in line with expectations and produces power-law fit parameters outside of the expected bounds for this material's behaviour; with fits giving unconventional behaviour $p < 2$ for 14 T and poor overall fitting for the 16 T set. This is likely due to the large signal enhancement in the EXED results for $T \to T_c$.

We can gain a better picture of the behaviour of the penetration depth by comparing each field set with the Prozorov [92] power-law approach used in previous sections. In Figure 62 we see each of the four fields in the temperature dependent scans compared to power-law models representing the s-wave and nodal cases. We would expect to see parity between the overlap fields of 14 T and 16 T with the low field scans from the D33 investigation. However, there are features that do not align with what we have seen previously. Broadly speaking, the majority of the results conform to the s-wave model but in some cases this breaks down for high temperature. In these cases a mixture of large uncertainty and weak signal make it difficult to interpret penetration depth behaviour at $T \to T_c$. We can say at least that the high field results generally point to the same conclusions supported by the low field data.

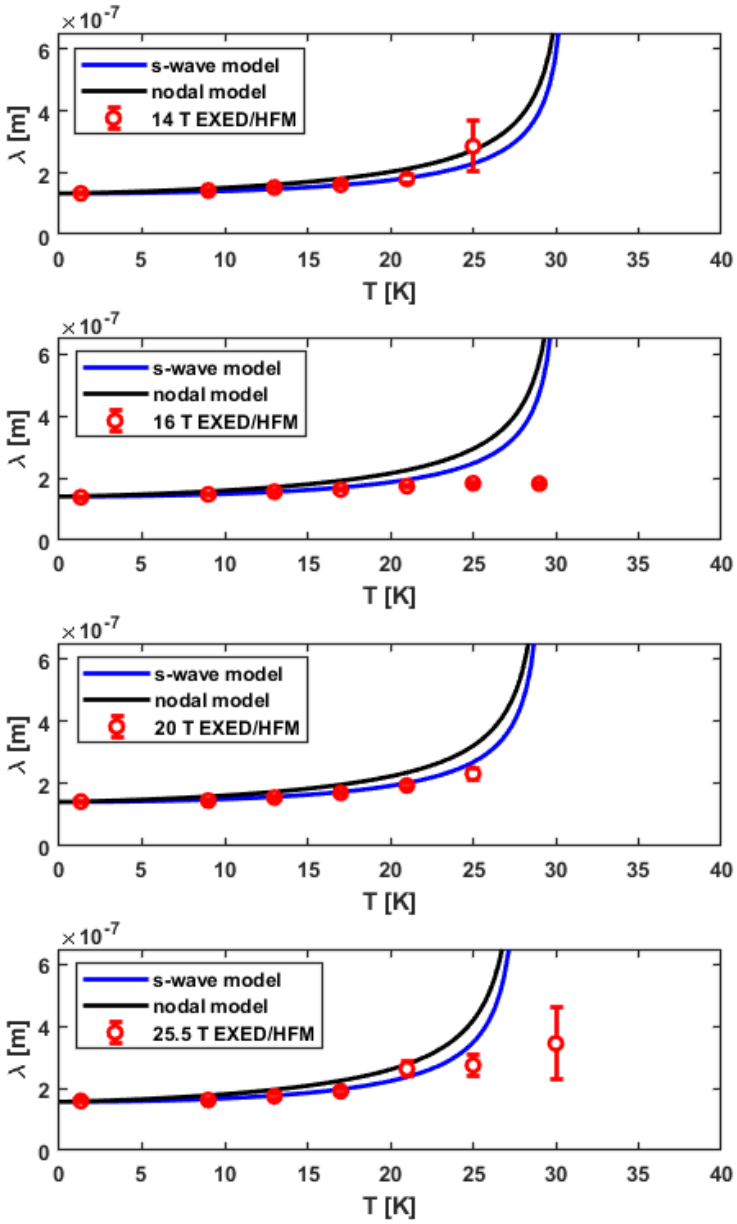

Figure 62: Penetration depths, $\lambda(T)$ versus temperature, T presented separately for each field. These results are presented alongside ideal models for penetration depth behaviour, given a specific dominant pairing mechanism; s-wave or nodal symmetry. Increasing field strength is presented in descending order.

5.3.7 Evidence for Pauli limiting above 16 T

Given the likely s-wave pairing mechanism being dominant in this material we can use the BCS model to describe the gap size for $(Ba_{0.5}K_{0.5})Fe_2As_2$. In BCS theory the zero temperature gap is estimated as $\Delta_0 = 1.76 k_B T_c$ which gives a value of $\Delta_0 \approx 5.6 \pm 0.1$ meV.

If we combine the gap function estimate with the calculation for the Pauli limiting field, equation 74, we get a prediction for when we might see definitive Pauli limiting effects. The predicted Pauli limiting field in this approach is $B_{c_2}^{Pauli} \approx 69$ T. This gives a Maki parameter of $\alpha_M \approx 2$, which is incredibly high, given that for most superconductors $\alpha_M \ll 1$. This indicates that although the orbital field is possibly as high as 140 T, the Pauli limiting field would destroy the superconductivity at fields of 70 T. This falls in line with the trend we see in Figure 57 where the prevailing gradient of the high field data suggests an x-axis intercept above 50 T; but given the limits of applied fields we cannot be certain that this behaviour would persist without probing much higher fields.

The key evidence is the increase in the form factor signal above that of the expected s-wave model in the temperature scan data that evolves with increasing applied field. The increase in signal in the regime of $T \rightarrow T_c$ correlates with an increase in field in the D33 data. In the EXED data we still see this enhancement, more or less, but the proportionality to field increase is unclear in comparison to the D33 data. The field dependent data does not probe high enough fields at the temperature settings applied to probe areas of possible PPE behaviour, unlike in the results in the previous chapter for KFe_2As_2. However, the response in the temperature dependent data is sufficient to reasonably say there is likely PPE behaviour detectable for $B \geq 16$ T.

5.4 Conclusions

In the case of $(Ba_{0.5}K_{0.5})Fe_2As_2$ We have seen a response from low and high field data supporting the interpretation of a BCS, *s*-wave gap. It appears to be no VL rearrangement under field variation and comparison to models shows a strong correlation with an *s*-wave interpretation. However, we have not probed to high enough fields to rule out possible variation of the VL orientation or emerging anisotropy, nor have we subjected the sample to large angular variation under the same experimental conditions as for KFe_2As_2.

Even though the pairing symmetry has not presented any evidence of nodes or unconventional behaviour we have seen some evidence to suggest PPE in this material. The Pauli limiting effects develop from 16 T upwards in applied field and are evident from 17 K upwards in temperature. The D33 results show a smooth increase in this response above 17 K but the EXED results are less consistent, this is in part due to the significant differences in experimental procedure and analysis between the D33 and EXED data sets. However, the high-field EXED data still supports the interpretation of PPE above 17 T for $B \geq 16$ T.

The results of both the EXED and D33 investigations demonstrate that the 50% doping of Ba content not only significantly shifts the upper critical field and critical temperature but also shifts the symmetry of the gap function on the Fermi surface as evidenced by the difference in pairing mechanism, if we compare the results of $(Ba_{0.5}K_{0.5})Fe_2As_2$ with that of KFe_2As_2. It is clear that there are differences between the electron band levels as a function of doping from Section 3, with the pairing symmetry shown to depend on the subtle shifts in energy bands, precluding the presence of nodes in $(Ba_{0.5}K_{0.5})Fe_2As_2$, but permitting them in KFe_2As_2 and $TlNi_2Se_2$.

6 STUDY OF THE PAIRING MECHANISMS IN $TlNi_2Se_2$

6.1 Properties of $TlNi_2Se_2$ and motivation for SANS studies

$TlNi_2Se_2$ is a Type-II superconductor, with the first significant investigation done in 2013 [48], when it was first synthesised as a superconducting single crystal. It is a Ni-chalcogenide with body-centered tetragonal structure and space group *I4/mmm*. $TlNi_2Se_2$ also exhibits heavy fermion behaviour with electron masses measured at $(14-20)m_e$, despite not containing any elements normally associated with this type of behaviour, such as uranium or cerium.

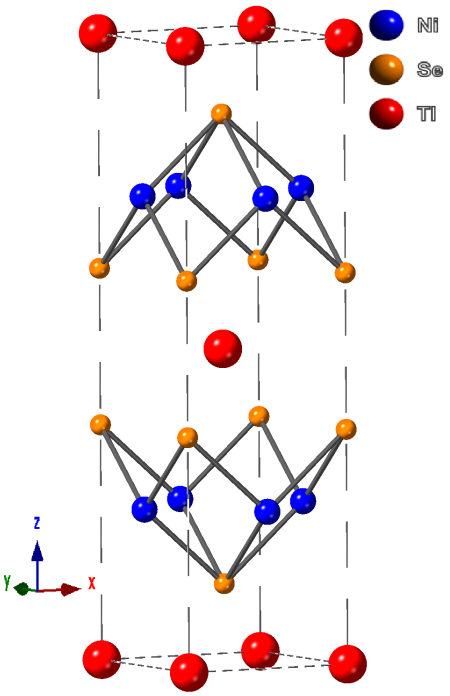

Figure 63: The crystal structure of superconducting $TlNi_2Se_2$ [48]. The crystal has lattice parameters: $a = b = 3.889$ Å and $c = 13.413$ Å.

Figure 63 shows the structure of the compound $TlNi_2Se_2$. There are alternating layers of Tl and Ni-Se, much like the structure of Fe-arsenide superconductors. It has no known structural transitions below 300 K, much like the Ni-pnictides. In the normal state it is a Pauli paramagnet and becomes superconducting at $T_c = 3.7$ K, with an upper critical field of $H_{c_2} = 0.802$ T which is easily accessible experimentally. Conservative estimates using the values for coherence length $\xi = 20.3$ nm and Fermi velocity $v_F = 5.484\times10^4$ ms^{-1} [47][48] give a penetration depth of $\lambda \approx 200$ nm. This was calculated using the London penetration depth equation, $\lambda = \sqrt{(m^*/\mu_0 n_s e^2)}$, with the maximum effective mass of $m^* = 20m_e$, and an estimate of the Cooper pair density, donated by 1.5 free electrons per Ni atom [48], of $n_s \approx 3 \times 10^{28}$ m^{-3}.

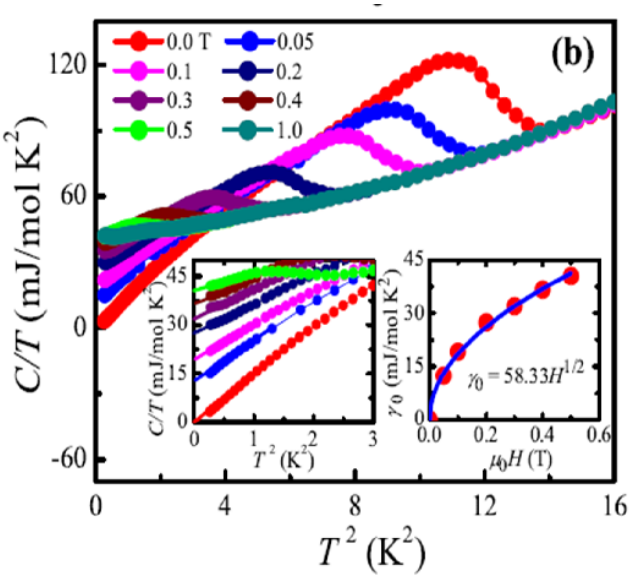

Figure 64: Specific heat results for $TlNi_2Se_2$ at varying fields against T^2. The left hand inset shows the results for below 1.7 K. The right inset shows the magnetic field dependence of the electronic specific heat coefficient, γ_N, also known as the Sommerfeld coefficient. Figure from [48]

There are some considerations to make with this material that limit its use. From an applications perspective the material is difficult to work with as it is brittle and hard and so cannot be formed into many particularly useful shapes. The thallium content is problematic as it is a dangerous, skin-contact, heavy-metal poison. This is compounded by the fact that the crystals available are small and brittle as well as being very sensitive to moisture and air exposure; when not in use they are kept under a He atmosphere to prevent decay. This means handling of these samples must be taken with great care. Crystal manufacture is also problematic from a safety perspective as the thallium and selenium content in powdered form (and to a lesser extent, nickel) makes manufacturing a more hazardous procedure than with most metallic superconducting compounds. It is not feasible to produce these samples on site in Birmingham. We have obtained these samples from Dr Minghu Fang at the Zheijiang University, Hangzhou, China.

6.2 Previous investigations

Previous investigations into $TlNi_2Se_2$ have been almost entirely conducted by Hong *et al.* [47] and Wang *et al.* [48]. They have also grown their crystals to a very high quality and supplied seven single crystal platelet samples for use in Birmingham. These crystals are ≈ 0.13 mm thick, with sides of ≈ 2 mm $\times 3$ mm, but this varies slightly between the samples. The samples have an average mass each of 6 mg.

Wang *et al.* [48] confirmed the basic parameters of $TlNi_2Se_2$ as a superconductor, such as the critical temperature and field, and investigated the specific heat in order to probe the heavy electron behaviour. The normal state specific heat can be modelled by $C_N = \gamma_N T + \beta T^3 + \delta T^5$. Figure 64 shows that for zero field, the specific heat goes to zero as $T \rightarrow 0$ K. At low temperature regions the phonon contribution to the heat capacity is negligible, the electron contribution is largest. This means that the linear electronic contribution of the heat capacity is zero, so therefore almost all the electrons enter the superconducting state. By increasing the field, the linear contribution also increases. The relationship between this coefficient and the applied field indicates how the electrons contribute to the specific heat and may be indicative of what type of electron pairing is occurring in a superconductor, discussed below.

The right inset in Figure 64 shows the field dependence of the linear Sommerfeld coefficient, γ_N, in the mixed state. This contribution in the mixed state is calculated by fitting to the normal state heat capacity for the mixed state region. γ_N is normally attributed to the normal state, in the superconducting state it comes from the unpaired electrons in the vortex cores. For *s*-wave superconductors, this contribution to the heat capacity is like a normal metal as it is proportional to the number of cores containing free, unpaired electrons. This means that γ_N should behave linearly: $\gamma_N(H) = \gamma_0 H/H_{c_2}$. However the inset shows clearly that this is not the case. The fitted line in the inset is $\gamma_N(H) = 58.33H^{0.5}$. This type of behaviour is normally

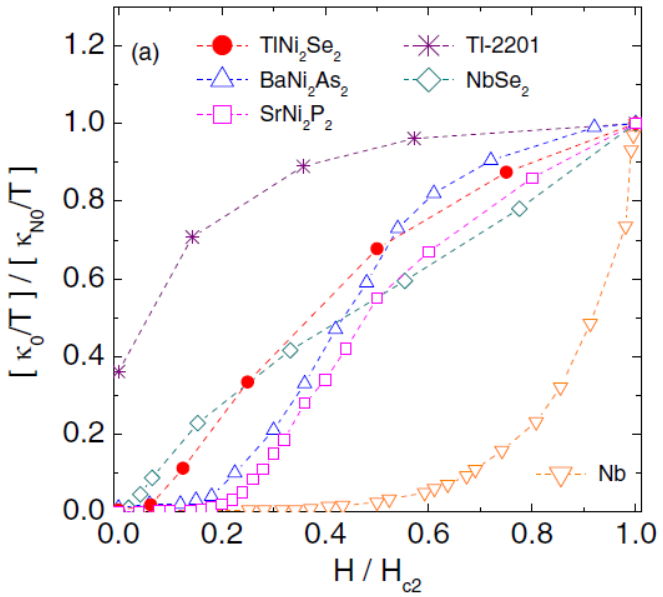

Figure 65: Normalised thermal conductivity per unit temperature of $TlNi_2Se_2$ vs H/H_{c_2}. This graph shows the $TlNi_2Se_2$ data compared to other materials such as the single-band s-wave superconductor, Nb [54], the multiband s-wave superconductor, $NbSe_2$ [55] and the d-wave superconductor, Tl-2201 [56]. Additionally there are two nickel-pnictide superconductors $BaNi_2As_2$ [57] and $SrNi_2P_2$ [58]. Image is taken from work in [47].

observed in *d*-wave cuprate and some heavy fermion superconductors [49, 50, 51]. This behaviour can be indicative of *d*-wave behaviour, however we must be cautious as there are *s*-wave superconductors that also exhibit this behaviour such as $NbSe_2$ [52, 53].

Wang *et al.* used the data to estimate the effective mass of the electrons. Starting from an estimated coherence length of $\xi_0 = \sqrt{(\Phi_0/2\pi H_{c_2})} = 20.3$ nm, we may then calculate the Fermi velocity, $v_F = k_B T_c \xi_0 / 0.18\hbar = 5.484 \times 10^4$ ms^{-1}. If we assume a spherical Fermi surface, the Fermi wave vector is $k_F = (3\pi^2 Z/\Omega)^{1/3}$ where Ω is the unit cell volume and Z is the electrons per unit cell. Assuming $Z = 6$ (1.5 electrons per Ni atom) we obtain $k_F = 9.6 \times 10^9$ m^{-1}. By combining this result with $m^* = \hbar k_F / v_F$ we get $m^* \approx 20 m_e$, confirming the heavy fermion behaviour.

The later investigation by Hong *et al.* focused on the nature of the gap structure. This investigation also looked at the thermal conductivity and combined it with the

specific heat data to provide more information on the electron pairing in $TlNi_2Se_2$. A measurement of the thermal conductivity can be modeled by $\kappa/T = \kappa_0/T + b/T^2$. Figure 65 shows the normalised Wiedemann-Franz Law expectations for the superconducting state, κ_0/T and normal state, $\kappa_{N0}/T = L_0/\rho_0 \approx 40$ mWK^{-2}cm^{-1}, where the latent heat, $L_0 = 2.45\times10^{-8}$ WΩK^{-2} and the residual resistivity is $\rho = 0.6$ $\mu\Omega$cm. The Wiedemann-Franz Law in general states that the ratio of the thermal conductivity to the electrical conductivity is proportional to the temperature: $\kappa/\sigma = LT$ [59]. This is important as it identifies the role of heat and electrical transport on the free electrons in a material. The Wiedemann-Franz Law is not entirely accurate for all materials (it was developed before quantum mechanics to describe metals) but does provide a way of comparing materials based on their ratio of thermal to electrical conductivity with respect to temperature. By comparing values of the normalised thermal conductivity with other materials we can move closer to a classification of the type of superconductivity in $TlNi_2Se_2$. The ratios between superconducting and normal state near 0K of the measured Wiedemann-Franz Law values, ($[\kappa_0/T]/[\kappa_{N0}/T]$) are 0.44% and 0.12% for two independent samples.

Using these values we can make a comparison between $TlNi_2Se_2$ and d-wave superconductors. The value of κ_0/T in zero field for a d-wave superconductor can be estimated for $TlNi_2Se_2$ using the quasi-two-dimensional approximation [60, 61, 59]:

$$\frac{\kappa_0}{T} \simeq \frac{\hbar\gamma_N v_F^2}{2\pi\Delta_0} \tag{118}$$

Where v_F is the same as given above, γ_N is similarly calculated in a fitting procedure as 40 mJmol^{-1}K^{-2} and Δ_0 is the maximum superconducting gap which Wang *et al.* predicted as the upper of the two fitted gaps, $\Delta_2 = 2.01 k_B T_c$. If $TlNi_2Se_2$ is a quasi-two-dimensional d-wave superconductor then we should obtain a value of $\kappa_0/T \simeq 3.22$ mWK^{-2}cm^{-1} which is a ratio of $\approx 8\%\kappa_{N0}/T$. This is ≈ 20 times higher than observed in the samples, making a d-wave interpretation inconsistent from this comparative perspective. Additionally, the ($[\kappa_0/T]/[\kappa_{N0}/T]$) curve is shaped

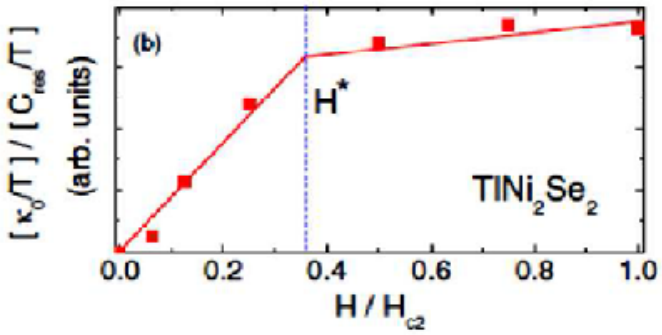

Figure 66: Combined heat capacity and thermal conductivity results against field showing a two gap structure in the electron pairing with the smaller energy gap overcome at field $H^* \approx 0.36$ T. Image is taken from work in [47].

ambiguously insofar as it could be compared easily to the multigap and nodal s-wave superconductors. But it is clearer in Figure 65 that it does not align with the d-wave Tl-2201 superconductor or the strongly s-wave superconductor, Nb. These observations suggest the pairing symmetry is less likely to be d-wave whilst not ruling out an unconventional case.

It is conceivable that the sample is dirty, which has affected its properties. Superconductors can be classified as clean or dirty, as covered in section 1.5.To determine this for $TlNi_2Se_2$, we calculate the mean free path of the electron, $l_e = \tau v_F$ where τ is the time between collisions. We then compare the l_e in the normal state with ξ_0 to find the clean and dirty limits, $l_e \gg \xi_0$ and $l_e \ll \xi_0$ respectively. We can estimate the mean free path and use the previously calculated coherence length, $\xi_0 = 20.3$ nm. We can calculate the mean free path using the following:

$$\frac{\kappa}{T} = \frac{1}{3}\gamma_N v_F l_e. \tag{119}$$

This yields the electron mean free path $l_e \simeq 677$ nm. We compare this value to the clean limit of $l_e/\xi \gg 1$, which gives $l_e/\xi \simeq 33.3$. We can therefore be sure that the samples are in the clean limit.

Figure 66 is the second part of the investigation by Hong *et al.*. This combines the thermal conductivity as a ratio with the residual specific heat, measured by Wang

et al. at varying fields, where we have already shown that this has a value of zero at zero field. Figure 66 shows a rapid increase up to a field H^*, whereupon the smaller gap is suppressed. One can estimate the ratio of the smaller gap, Δ_s to the larger gap Δ_l, by plotting the data in Figure 66. In the region of $H^* < H < H_{c_2}$, the Fermi sheet with the smaller gap energy is suppressed by the applied field, and so only the larger gap contributes to the rise in $(\kappa_0/T)/(C_{res}/T)$, resulting in the change in gradient above H^*, where $H^* \simeq 0.36 H_{c_2} = 0.29$ T. Given that $H_{c_2} \propto \Delta^2/v_F^2$, we can estimate that $\Delta_{small}/\Delta_{large} \approx 0.6$.

6.3 Heat capacity studies of $TlNi_2Se_2$

To supplement the SANS work conducted on these samples, an additional investigation was conducted to compare with the previous investigations into the heat capacity with respect to field and temperature. The key previous findings were that the heat capacity phase transition peak in the superconducting phase could be better modelled by a two-gap system and that the Sommerfeld constant followed a field dependent behaviour of $\gamma_N \propto H^{0.5}$, typically associated with d-wave systems [48].

The subsequent heat capacity investigation presented here was conducted in situ at the University of Birmingham using a Quantum Design Physical Property Measurement System (PPMS). The PPMS has a heat capacity puck calibrated down to 1.81 K, setting the available temperature range for measurement. This is in comparison to the 0.5 K accessed in previous work [48]. Initially the heat capacity was measured for the superconducting state over a temperature range of 2-4 K at 0 T, compared to the normal state measured over the same temperature range but for 0.9 T, well above H_{c_2}. These results are shown in Figure 67. The results show a comparable value of the peak heat capacity, with peak heat capacity after the superconducting transition reaching $C/T \approx 140$ mJ mol^{-1} K^{-2} for 0 T. This is compared to Figure 64 which shows a heat capacity peak of $C/T > 120$ mJ mol^{-1} K^{-2}.

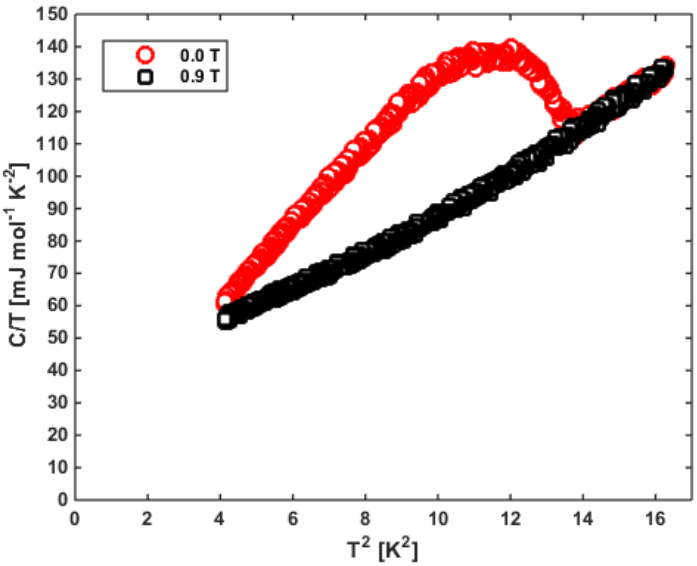

Figure 67: Heat capacity per unit Kelvin, C/T at 0 T (superconducting phase) and 0.9 T (normal phase) versus T^2; these units are chosen to maintain parity with Figure 64.

To recap from earlier discussions of the heat capacity results in the work of Wang, Hong *et al.*, the heat capacity can be modelled in the normal state by $C_N(T) = \gamma T + \delta T^3 + \beta T^5$, γ_N is the Sommerfeld constant and δ and β are other numerical fitting constants. By solving for C/T we can fit the data with γ as the zero temperature intercept of the y-axis, γ_0. By establishing the value of γ_0 for each field we can develop a description of the behaviour of the Sommerfeld coefficient, γ_N. To establish the superconducting behaviour of the heat capacity we measure the normal state heat capacity and the heat capacity with the superconducting transition as shown in Figure 67. We must then normalise the data that includes the phase transition to the background of the normal state: $C_{es} = C - C_{latt}$, this effectively removes the contribution of the ion lattice leaving only the contribution of the electrons to the heat capacity.

Results in Figure 68a demonstrate the heat capacity response over the temperature range of 2 K to 4 K for fields up to 0.3 T. We can see a clear suppression of the superconducting phase as the field strength increases. Unfortunately we were unable

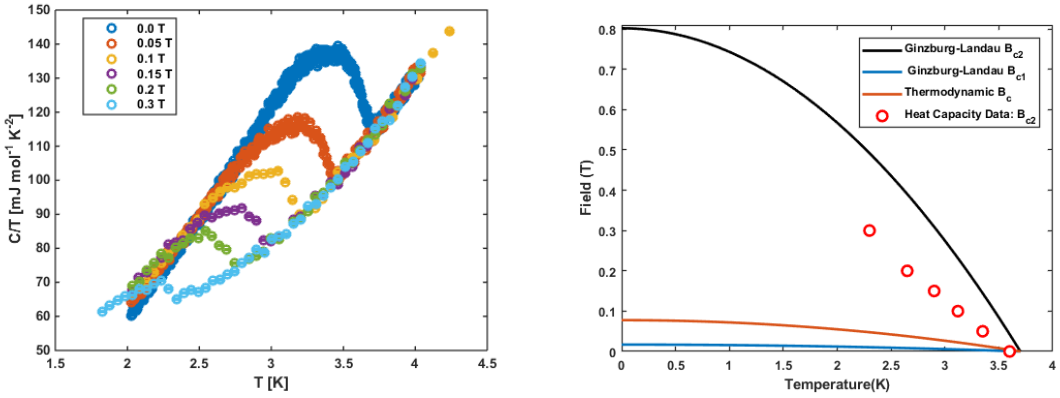

(a) (b)

Figure 68: (a) Heat capacity per unit Kelvin versus temperature for fields up to 0.3 T. Above this field the superconducting phase was suppressed to temperatures below the accessibility of the PPMS, which was calibrated down to 1.81 K. (b) Theoretical calculation of B_{c_2}, B_{c_1} and B_c compared to the results form the heat capacity scans. The value for the critical temperature associated with the applied field is take from the centre of the initial slope increase of the heat capacity, representing the middle of the phase transition.

to probe to lower temperatures due to calibration limits on the heat capacity puck, this means fields were only probed up to 0.3 T. Above 0.3 T the superconducting state was suppressed below the calibration temperature for measurement. We see in Figure 68a that there is uniform overlapping of the normal state part of the curve for each applied field.

The results of analysing the field sets in Figure 68a give the values for B_{c_2} versus temperate by finding the mid-point of the initial heat capacity slope as the peak develops from the phase transition upon cooling to the superconducting state. The values for the upper critical field are presented in Figure 68b alongside the theoretical predictions from earlier work, using the coherence length calculated in [48] and using the Ginzburg-Landau framework [10].

The results of the measured upper critical field indicate a more suppressed superconducting state than expected, suggesting a more linear phase diagram than the Ginzburg-Landau prediction for the upper critical field behaviour in the low-field regime, explored by the heat capacity study. According to theoretical calculations

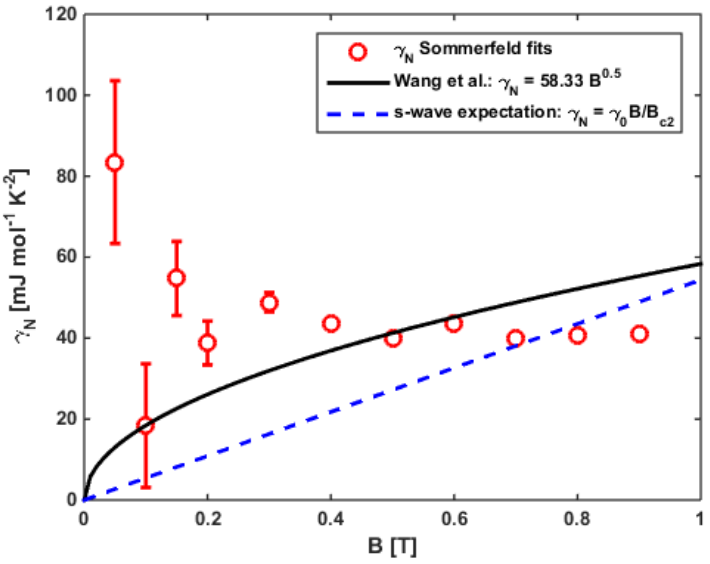

Figure 69: Sommerfeld coefficient, calculated from the normal state data points, versus applied field. Shown are the expected Sommerfeld behaviour for BCS superconductors [10, 48] and the behaviour observed by Wang *et al.* [48].

we are in the superconducting mixed state at that field and temperature.These results are somewhat in disagreement to previous resistivity and magnetisation results which confirmed an upper critical field of 0.8 T. This could suggest that the behaviour of the B_{c_2} curve versus temperature deviates from expectations. If the behaviour does in fact deviate at much higher fields in the low-T regime this would explain why the conditions of 0.5 T and 0.15 K act as if they are much closer to the boundary line between the normal and superconducting states while still approximately maintaining a zero temperature value of $B_{c_2} = 0.8$ T. It is also reasonable that the experimental conditions made it difficult to detect a weak but present signal for fields much closer to B_{c_2}, and with a longer count time a VL may have been resolvable for fields above 0.5 T. It would also be possible to resolve this by measuring the heat capacity at higher fields, however this would require having calibration for lower temperatures, which has not been possible.

A key indicator, identified in the literature [48], of unconventional superconductivity is the unusual behaviour of the Sommerfeld constant in the heat capacity in

the normal state. Previously the Sommerfeld coefficient had exhibited a relationship with the field of $\gamma_N = 58.33H^{0.5}$; this is often associated with d-wave behaviour [48]. Typically we would expect the Sommerfeld coefficient to be linear with field, $\gamma_N = \gamma_0 B/B_{c_2}$ in a standard BCS case as the number of free electrons contributing to the heat capacity is proportional to the strength of the applied field, as previously discussed at the beginning of this chapter regarding the work of Wang *et al.* We see in Figure 69 the difference between the previous fit and the BCS case, but what is more apparent is that the new Sommerfeld coefficient data does not conform to either model and appears to be (for most of the field range) independent of the field and hold a roughly constant average value of $\gamma_N \approx 43$ mJ mol^{-1} K^{-2}.

The low field behaviour is unreliable due to the number of data points in the normal state being minimal for the full scan width in T and the lowest point of the normal state being further from $T = 0$ K. This introduces a lot of uncertainty in a fit for the y-axis intercept to acquire the γ_0 value. As such it is reasonable to distrust the data range of $B \leq 0.2$ T. Attempted fits using the power law framework to these results has produced untenable results with high margins of error and unphysical behaviour. Further investigation of the heat capacity, specifically the Sommerfeld coefficient, would be prudent in order to establish the free electron behaviour under field and temperature variation. As the investigation currently stands, these results do not conform to the behaviour seen in [48] whilst also clearly not conforming to a conventional model, however they are of an agreeable magnitude with the previous normal state fit at 6 T in [48] yielding $\gamma_N \approx 40$ mJ mol^{-1} K^{-2} compared to an average value in this investigation of $\gamma_N \approx 43$ mJ mol^{-1} K^{-2}. This at least supports the previous discussions in this investigation that clearly point to an unconventional model to describe the superconductivity in this material.

As previously discussed in this section, we may extract just the free electron component of the heat capacity, C_{es} by normalising to the background (the normal state). Figure 70 shows the adjusted free electron component of the heat capacity

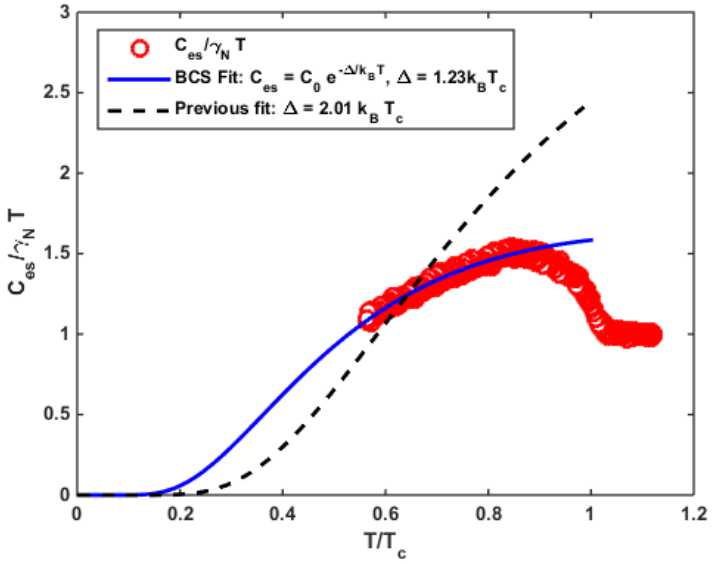

Figure 70: Unitless adjusted heat capacity per unit temperature, $C_{es}/\gamma_N T$ versus reduced temperature, T/T_c. These results are modeled in the same manner as in [48] using $C_{es}(T) = C_0 e^{-\Delta/k_B T}$. The results are presented with the fit applied in [48] and a fit to this new data set.

calculated from the 0 T data set and the background at 9 T in Figure 67. The dotted black line represent the two-gap fit from [48], $\Delta_0 = 2.01 k_B T_c$, while the blue line represents the fit to the calculation of C_{es} from the new data, $\Delta_0 = 1.23 k_B T_c$. We also find very different values of the pre-factor, C_0 with the previous results yielding $C_0 = 65.69$ mJ mol^{-1} K^{-1} and the new fit giving $C_0 = 19.53$ mJ mol^{-1} K^{-1}.

This new calculation and fit for the unitless representation of the free electron behaviour in the superconducting state deviates fairly significantly from previous results. We see a more suppressed gap function that does not conform to standard predictions for the gap function for unconventional behaviour. Prozorov *et al.* [92, 101, 30] outlined limits for the gap function given certain pairing symmetries for the Cooper pairs. The standard BCS fit is $\Delta_0^{s-wave} = 1.76 k_B T_c$, but for nodal and d-wave behaviour is enhanced; two-dimensional d-wave behaviour can be described by $\Delta_0^{d-wave} = 2.14 k_B T_c$.

Given that all our current analysis thus far points to an enhanced gap function it seems there are limitations to our data and with the approach to the analysis. Pri-

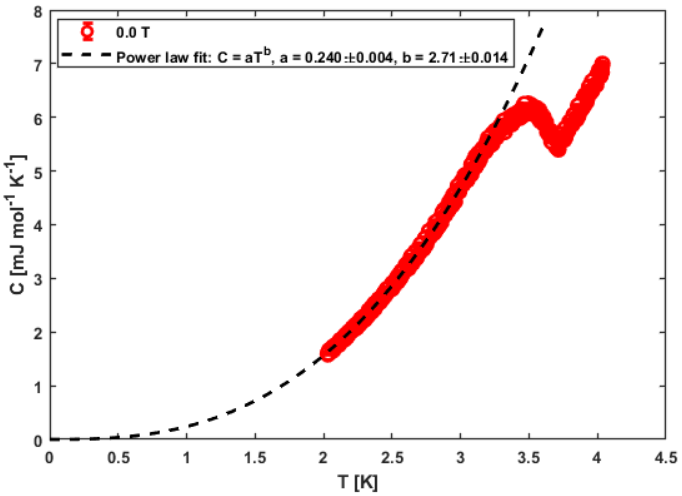

Figure 71: Heat capacity at 0 T from 2 K to 4K showing the superconducting transition upon cooling. Heat capacity data has been fit with a power law model, $C = aT^b$ to check for unconventional behaviour in the superconducting state [10, 48].

marily we are lacking in low temperature data for a fuller comparison; the previous work on heat capacity was able to access almost double the low temperature regime that we have been able to access. This makes fitting functions more challenging as the data set ends further from the y-axis, so a greater amount of uncertainty is incurred when attempting to establish a fitting model and parameters with a great degree of accuracy. As a result we take the analysis in Figure 70 with some degree of skepticism until a larger temperature range is accessed; it is possible that at low temperatures the data still conforms to the previous fit but near T_c there is some artificial suppression of the gap function.

If we return to fitting the heat capacity data under zero field, we have another option besides the BCS fit of $C(T) \propto e^{-\Delta/k_B T}$. Instead we can use a power law fit of $C(T) = aT^b$, which corresponds to unconventional effects that make the superconductor more sensitive to temperature variation in the low-T regime [32]. In Figure 71 we show the heat capacity results at zero field cooling through the superconducting transition with a power law fit made to the superconducting state curve up to the transition peak. In a power law fit, the size of the power can tell

you about what kind of unconventional system you are looking at, with the general interpretation being $C(T) \propto T^2$ for line nodes and $C(T) \propto T^3$ for point nodes in the gap [10]. In this case we see a fit of $C(T) \approx 0.24T^{2.71}$, where we have the specific power fit of $b = 2.710 \pm 0.014$. This is a good fit with small errors, indicating a tendency towards the point nodes interpretation of the gap structure.

6.4 Preliminary results for $TlNi_2Se_2$: SANS-I, PSI, November 2015

In order to test whether a signal was detectable for the SANS-I experiment, the six available samples were aligned using X-ray diffraction (XRD) with the Brüker D5000 available at the University of Birmingham. This method uses Bragg diffraction to determine the inter-atomic spacing in crystals. By looking for Bragg peaks at the [004], [404] and [044] vectors, the alignment of the crystal could be determined ([004] etc were chosen due to structure factor considerations). The samples are flat platelets. We confirmed that the largest flat face of the platelet samples was perpendicular to the **c**-axis. As the samples are tetragonal down to the lowest temperatures, their **a** and **b** axes are equal, so as long as these are aligned at 90° with each other. Then there will be a clear diffraction pattern when conducting a SANS investigation. Otherwise a rotation in a sample out of alignment would produce a pattern where, rather than a hexagonal pattern for the VL being seen, slightly rotated hexagonal VLs would produce an azimuthally smeared diffraction pattern.

Figure 72 shows the diffraction pattern produced by the D11 instrument at the Institute Laue-Langevin (ILL) in Grenoble in July 2015. These scans were performed at the end of a different experiment by Randeep Riyat. This image is compiled from twenty one scans of 180 s each that rock the sample ϕ from $-2°$ to $2°$ in steps of $0.2°$, where ϕ is the polar angle of the sample. This rock in ϕ is why the spots on the left and right hand side of the image are brightest because these sides have been sampled

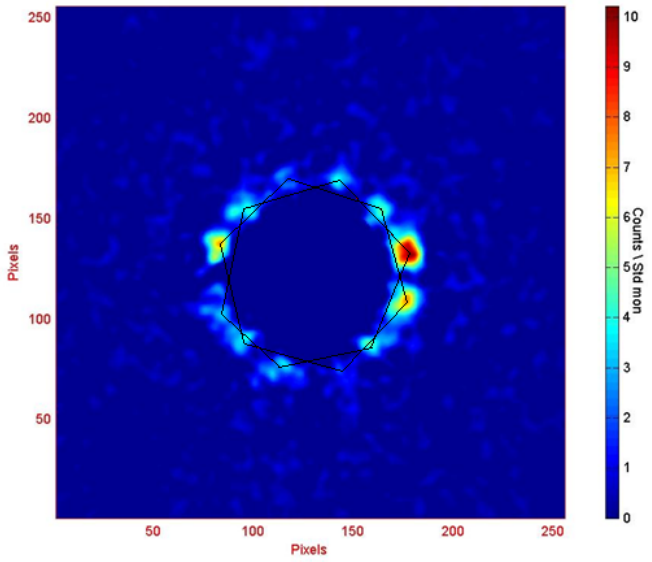

Figure 72: Diffraction pattern from D11 at the ILL of $TlNi_2Se_2$, wiggle cooled ϕ rock of $-2°$ to $2°$ in steps of $0.2°$ counting for 180 s at 150 mT. Field was wiggled at ± 5 mT from 5 K to 1.4 K. The two degenerate hexagonal VLs are drawn in black for clarity. These scans were conducted by Randeep Riyat, from the Condensed Matter Group, University of Birmingham.

more often compared to the top and bottom of the sample due to the rocking curve measurement. Twelve spots are seen with no obvious smearing evident. This points to two degenerate hexagonal VLs, this means the VL is twofold degenerate; the same twofold degeneracy is seen in KFe_2As_2 [12]. The degeneracy in KFe_2As_2 becomes interesting when the sample is rotated relative to the field and neutron beam or the field is varied in strength, as both VL domains rotate at different rates until they become one VL domain and then the single domain will distort with increasing angle or field strength. It is possible this effect could be observable in $TlNi_2Se_2$ with variation in field and angle.

For the preliminary experimental investigation at PSI we used a collimation of 18 m and a wavelength of 8 Å. Our beam intensity, according to Figure 73, is $\approx 10^5$ counts $s^{-1}cm^{-2}mA^{-1}$. However, we need to take into account the rocking curve width and move to a more standard unit of length than cm. Assuming a rocking curve width of $1°$, yielding $\approx 2 \times 10^7$ counts $s^{-1}m^{-2}mA^{-1}$. Next we must divide

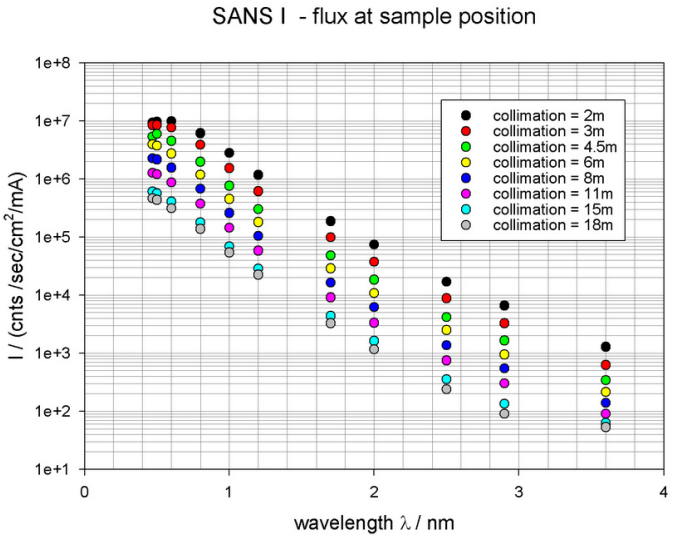

Figure 73: The SANS-I beam intensity values vs neutron wavelength for selected values of collimation. Image taken from [38].

by the PSI neutron current for SANS-I, 2000 mA. This gives a predicted integrated intensity of $\approx 10^4$counts $s^{-1}m^{-2}$, which can be applied as an approximated solution using the Christen formula in order to find a predicted value for $|F(q)|$. This predicted intensity is sufficient for a signal to be detected at SANS-I for a 1° rocking curve width at $q = 0.0105$ Å^{-1} in a 0.5 T field.

The results from the ILL and preliminary scans at PSI indicated that the clearest results, that is the best spot intensity in a given time, was found to be with a rocking curve of ±1.4°. This gave the best image for representing the results as well as providing enough intensity for the scan time.

Results from PSI in November 2015 were sparse, there were problems with the target station and the dilution mixture stability over the range of 0.1 K to 4 K leading to a loss of a significant amount of scanning time. Nonetheless they were useful for motivating subsequent investigations at the ILL, with four clear diffraction patterns that confirmed estimations of the penetration depth of the order ≈ 200 nm but the investigation had insufficient evidence to conclusively demonstrate whether a second gap function is suppressed at around 0.29 T or not.

Figure 74 shows the first of four scans with a clear diffraction pattern of two

hexagonal VL domains. This image is the clearest of the four with the strongest signal and highest integrated intensity. This scan also yields the largest form factor for the VL, which we will compare with the other scans later in this section.

Figure 76a shows a much weaker signal for the two degenerate diffraction patterns, however it is still visible with a q value consistent with predictions. It is here that we can make a reasonably informed comment on the suppression of the smaller gap function. It is possible that this is the explanation for the rapid drop in integrated intensity between the 0.2 T results and the 0.3 T result with the 0.4 T and 0.6 T results in Figures 76b and 76c, respectively, showing a steady decline in signal strength compared with the difference between the 0.2 T and 0.3 T signal difference. However, this is not thoroughly conclusive in showing the suppression of the lower gap function below 0.3 T, but it is complementary to previous results by Hong *et al.*. Given the evidence supporting the suppression of the smaller gap is dependent on the relatively low $|F(q)|$ signal at 0.4 T or the higher signal at 0.6 T, we cannot conclusively say that this data is in support of two gaps.

By 0.6 T the signal is very weak and extracting a q value using GRASP from this data set proved difficult. However from this set we were able to generate FF values for all four fields and a calculation of the London penetration depth using the 0.2 T data. The London penetration depth was initially estimated, assuming a spherical Fermi surface, using the Wang *et al.* calculations for coherence length to be of the order of 200 nm. Using Equation 105 (without the exponential term) the London penetration depth was calculated as $\lambda_L \approx 212$ nm. This falls very close to our initial predictions and allows us to make better estimates of the Cooper pair number density and effective mass of the electrons in this heavy fermion superconductor. However more data is required before we may make an accurate calculation of the penetration depth, or other characteristic parameters, with any degree of certainty or with a reasonably small error.

The calculated $|F(q)|$ results from the measured integrated intensity are shown

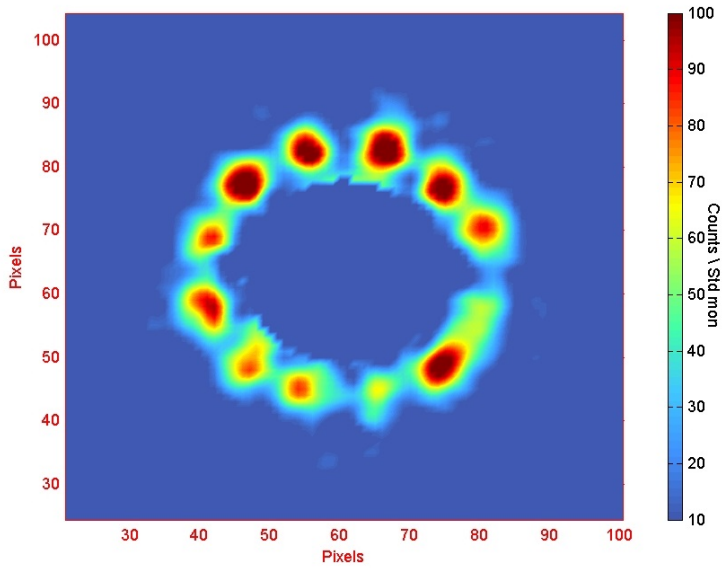

Figure 74: Diffraction pattern of the VL in $TlNi_2Se_2$ at 0.2 T and 0.1 K. The pattern shows intensity in counts per standard monitor, with a monitor of 100 for this scan (monitors of 50 were taken for the background scans). Two hexagonal VL domains are clearly visible with the top two spots at approximately $\pm 15°$. This scan does not indicate any anisotropy in the system, however the lower gap function is not yet suppressed, according to previous investigations. The top-most right and bottom-most left spot were combined to find the q value for the peaks. Theses peaks had the most exposure to the neutron beam as they lie approximately along the axis of rotation for the rocking curve. The q-value was found at $q = 6.75 \times 10^7$ m^{-1}.

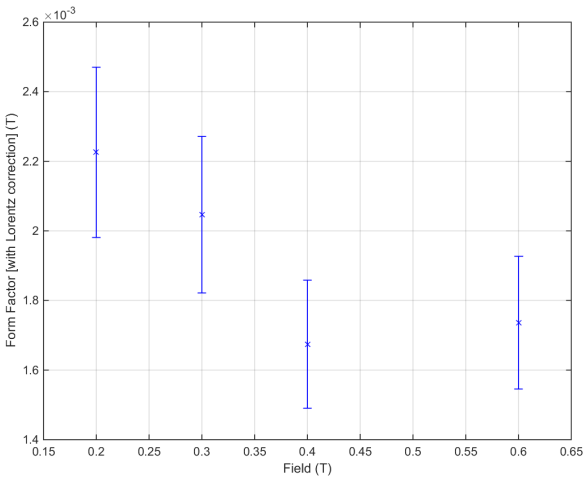

Figure 75: The averaged and Lorentz corrected $|F(q)|$. The results show a marked decline in $|F(q)|$ above 0.2 T. However there is a lack of results around the predicted transition point to see the suppression of the smaller gap function. This is predicted to be at $\simeq 0.29$ T.

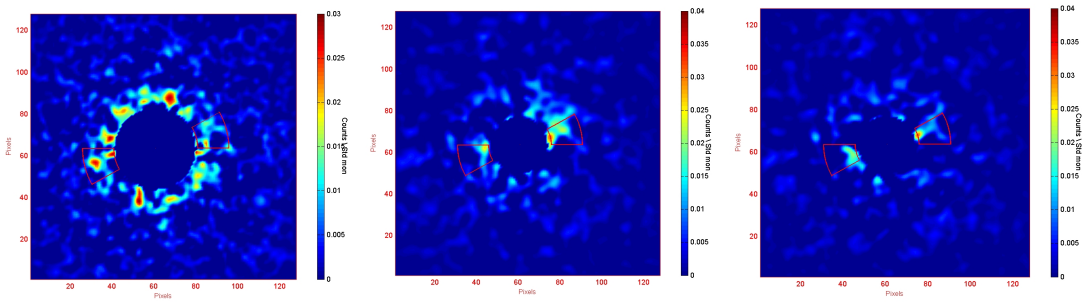

(a) (b) (c)

Figure 76: Diffraction patterns produced from the preliminary results at PSI on SANS-I for $TlNi_2Se_2$ for fields of 0.3 T to 0.6 T and a temeprature of 0.1 K to 0.13 K for all scans. (a) Diffraction pattern of the VL in $TlNi_2Se_2$ at 0.3 T and 0.1 K. The pattern has the same monitor settings as previously described. Two hexagonal VL domains are partially visible. The q-value was found at $q = 8.3 \times 10^7$ m^{-1}. (b) Diffraction pattern of the VL in $TlNi_2Se_2$ at 0.4 T and 0.1 K. The pattern has the same monitor settings as previously described. The q-value was found at $q = 9.84 \times 10^7$ m^{-1}. (c) Diffraction pattern of the VL in $TlNi_2Se_2$ at 0.6T and 0.1K. The pattern has the same monitor settings as previously described. The q-value was found to be $q = 1.15 \times 10^8 m^{-1}$.

in Figure 75. The results show a decline in $|F(q)|$ above 0.2 T. There is insufficient evidence to point to Pauli paramagnetic effects, however this is not entirely ruled out due to the low number of data points acquired overall in this preliminary investigation. The suppression of a gap function in a multi-gap superconductor will destroy Cooper pairs associated with that gap energy, reducing the variation of the magnetic field associated with the VL as there are less Cooper pairs able to screen out the penetrating field lines. However, the lack of data above 0.6 T as well as below 0.2 T and intermediate fields means we do not have a clear indication of the transition point where a smaller gap function might be suppressed if present in the manner predicted by Wang, Hong *et al.*. Also we cannot see how $|F(q)|$ behaves at small and large field ranges, relative to B_{c_2}, as well as across broad temperature ranges. All of these factors were strong motivators to continue investigation into this material at the ILL with a more intense beam and more stable low-temperature control.

6.5 Results for $TlNi_2Se_2$: D33 beamline, ILL, December 2016

The following section represents the results and analysis for the investigation on $TlNi_2Se_2$ on the D33 beamline, ILL in December 2016. The sample was subjected to fields up to 0.6 T, and a temperature range of 100 mK to 3.5 K. The sample was also rotated with respect to the applied field from 0° to 30°, with the applied field aligned parallel to the neutron beam and the sample aligned approximately parallel to the neutron beam at 0° rotation of the sample **c**-axis with respect to the field.

In this investigation the sample was subjected to fields up to 0.5 T across four angles of rotation in Ω: 0°, 10°, 20° and 30°. However, for the 20° results a problem was encountered. At this angle a large, asymmetric spot of reflection on the left-hand side of the diffraction patterns was observed. The position and intensity of the spot varied slightly with the rocking of the sample and as such it was concluded that this was caused by a canted edge of the cadmium window surrounding the mosaic. The right hand spot of the VL was not affected or obscured, however the left-hand spots were. Point-by-point subtraction in GRASP was able to eliminate some of the effects of the cadmium reflection, however this still left some spots with poorer statistics in each of the rocking curves at this angle. This was especially problematic at low field, where the VL left-hand spots were in the exact same region of q-space as the Cd reflection. For higher fields this was partly mitigated by the increasing value of q for the VL spot. The net effect of this made the 20° unreliable for comparison to the other angles, given that any unusual or interesting behaviour would not be reasonably separate from the varying reflection noise in the signal. This resulted in this set of data being omitted from the analysis here.

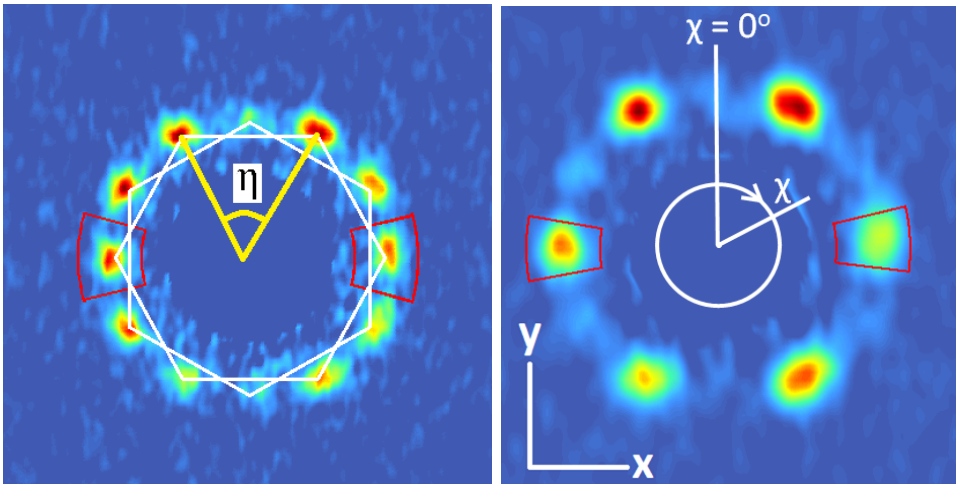

(a) (b)

Figure 77: (a) Diffraction pattern of the VL under an ω (san) rock of $\pm 0.8°$ in steps of $0.05°$ at 2 minutes per point. As there is no rotation of the centre of the rock relative to the field, the secondary domain is still visible. Hexagons in white indicate the two domains in the diffraction pattern. The red sectors indicate the sector boxes used for extracting the integrated intensities from the diffraction images in GRASP software. See section 8.1, Appendix A for details on the use of GRASP and sector boxes. (b) Similar to (a) but at a fixed rotation of $\Omega = 10°$ to remove the second domain (see Figure 78b). Here the diffraction pattern χ is defined relative to the $y - x$ axes of the image. The opening angle η in (a) is defined in the χ coordinate system.

6.5.1 Vortex lattice structure

Preliminary data highlighted the prevalence of a strong signal for a secondary domain of the VL, visible for the majority of the field ranges and temperatures accessed. In order to clearly see the evolution of any structural changes in the VL, the secondary domain needs to be suppressed. To do this the sample mosaic is altered compared to the preliminary setup. Here the single crystals are arranged such that the **a** and **b** axes are no longer aligned parallel to the ϕ and ω axes of rotation, respectively but instead the samples are rotated such that the **a** and **b** axes are at 45° to the normal of the ω and ϕ planes. This rotation was made in order to break the symmetry between the second domain and the crystal structure for rotations away from $\mathbf{c} \parallel \mathbf{B}$ and thus suppress the second domain by angular variation. This arrangement is illustrated in Figure 78a. In this investigation we also rotated the sample by a fixed

displacement in ω with respect to the field, about which point the ω and ϕ rocks were conducted. These fixed displacement angles are denoted by Ω and were taken at 0°, 10°, 20° and 30°. At $\Omega = 0°$ the second domain is preserved but for larger angles the second domain integrated intensity rapidly falls as the secondary VL no longer satisfies the same symmetry conditions of the underlying crystal symmetry upon rotation in ω with the initial rotation of 45° normal to ω, previously outlined.

Figure 77a shows a very clean signal of a well ordered primary and secondary domain, with only a low intensity signal for the top- and bottom-most spots due to these spots being approximately parallel to the axis of the rocking angle ω, so these spots underwent the least amount of rocking of all the VL spots. The two hexagonal lattices are clearly well aligned, which is prevalent through all results with a 0° rotation in Ω. The left- and right-most spots are highlighted by red sector boxes to define the region of analysis in GRASP software, a process fully explained in Section 8.1, Appendix A. These two highlighted spots have a Lorentz factor of approximately unity in the ω scans and therefore are very useful for preliminary analysis and establishing q values for the VL for this rocking orientation. For ϕ scans there are no spots in the first domain that have alignment to the plane normal to the ϕ rocking angle and so a Lorentz factor is of much more importance in that case.

Observation of the VL structure evolution with field and temperature indicated only small structural changes with no definitive shift to a rhombus or square shape, as is characteristic for d-wave superconductors [89]. What we observe is the standard evolution of the VL as a function of q in relation to the applied field $\mathbf{B}$, as demonstrated in equation 84. Instead the VL shows a remarkable stability and maintains an isotropic hexagonal arrangement throughout despite evidence to suggest multiple gaps and/or d-wave pairing symmetry. This provides very strong evidence from the outset that a d-wave pairing mechanism or d-wave contribution is perhaps unlikely here.

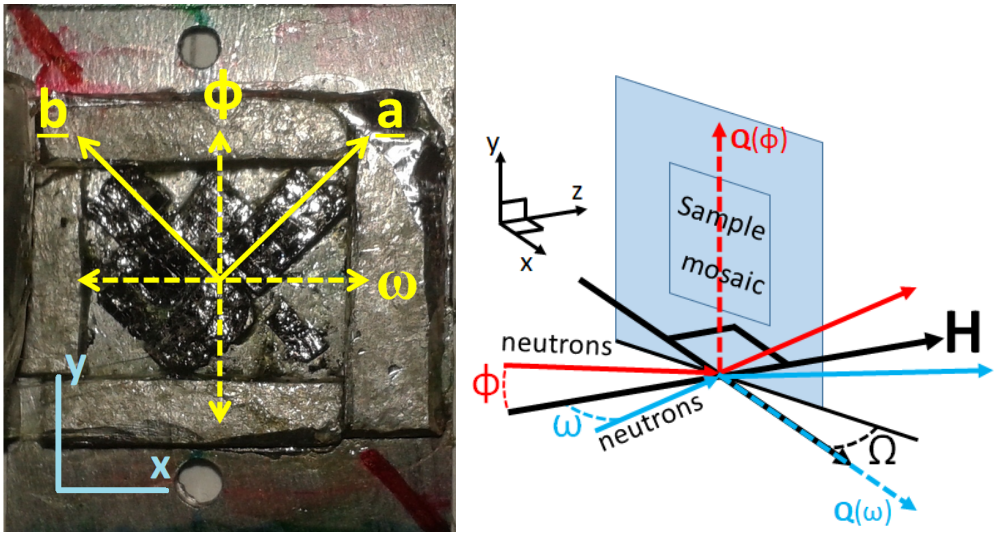

(a) (b)

Figure 78: (a) Image of the mosaic of the seven single crystal samples. These samples are approximately 0.13mm thick and have a total volume of 4.68×10^{-9}m^3. The solid lines indicate the **a**-plane alignment of the crystals, rotated to 45°. The dashed lines indicate the rocking axes relative to the crystal axes, with ϕ rocks being a rotation about the horizontal x-axis and ω rocks a rotation about the vertical y-axis. Fixed displacements in ω, which act as a new zero point for rocking, are denoted by Ω. (b) Orientation and angles of the sample with respect to the applied field and neutron beam. Included are the rocking angles (ϕ and ω) and displacement angle (Ω).

6.6 Field- and angle-dependent anisotropy of the VL in $TlNi_2Se_2$

During this investigation all the diffraction spots of the VL hexagonal pattern were used for calculations and data analysis. In the case of the anisotropy however, we do not want to take an average over all Q values, because this will partly mask any anisotropy present in the VL. Instead we must choose an axis over which to measure the Q values, here we choose the left- and right-most spots which sit on the x-axis, see Figure 77a. These spots have a Lorentz factor of almost unity with respect to the ω scan angle and thus the smallest error factor in that regard while the top spots would have a Lorentz factor for either the ϕ or ω scans and thus a slightly larger error associated with them, as well as a smaller signal size. However, other neighbouring spots in the VL are also used to improve the statistics and interpretation for the

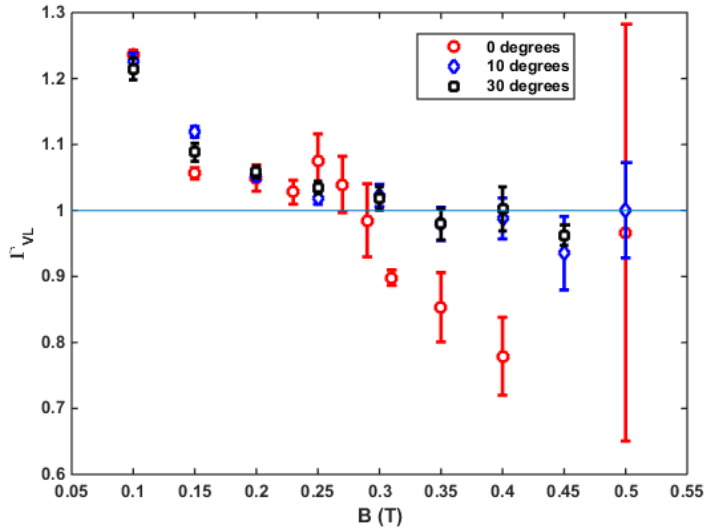

Figure 79: Anisotropy of the VL as calculated using equation 111. Reference line at $\Gamma_{VL} = 1$ indicates the area where there is no anisotropy in the VL. All three values of Ω indicate the same behaviour of a linear relationship of the anisotropy with respect to the field with a negative gradient.

purposes of an anisotropy investigation, such as for the calculation of angles between spots, which will be explored later in this work.

An anisotropy value greater than 1 would suggest that the Q_{VL} value for these spots is much smaller than expected, while a value of anisotropy smaller than 1 suggests a much larger value of Q_{VL} than expected. This can be understood as a contraction or expansion, respectively, of the VL hexagon along the x-axis in reciprocal space.

The anisotropy of the underlying crystal structure has been measured to be $c/a = 3.47$. In addition, previous resistivity measurements by Wang *et al.* suggest an anisotropy of $\rho_c/\rho_{ab} = 1.57$, which lend validity to the idea that the VL should experience anisotropy when the field or angle, Ω, is maximised due to underlying anisotropy in the system. What we observe from Figure 79 indicates that the anisotropy is weak but not insignificant, with the results for Γ_{VL} demonstrating a range of $1.3 < \Gamma_{VL} < 0.6$ (including errors), with the low field results having small errors and thus demonstrating that there is anisotropy in the system related

to field modulation. A common behaviour for all the results at the accessed angles is the generally negative linear gradient of the anisotropy, crossing from $\Gamma_{VL} > 1$ to $\Gamma_{VL} < 1$ around 0.3 T. For the spots in question this means that the VL is slightly contracted at low fields and slightly stretched at higher fields along the x-axis. This effect is small, with some results for the higher fields still sitting within error of $\Gamma_{VL} = 1$. This drift of the top/bottom pairs of spots suggests a weak interaction of the VL with some underlying preference with field modulation.

In order to establish an understanding of the anisotropy in a superconductor, the relationship between Ω and Γ_{VL} must be investigated. In this case we have a poor correlation between the data points to support anisotropy in the VL, according to fits using equation 113. If we look at the results in Figure 80 we can see that the fit for 0.3 T is very poor, while the fits for 0.1 T and 0.2 T are fair at best. Overall we can see that the anisotropy in this system is not absent but it is small and doesn't follow a clear model of behaviour; the fits for Γ_{VL} do not entirely conform to observed behaviour in all instances. The 0.3 T data demonstrates the weakest adherence to the model. This is likely due to the difficulty of defining the centre and drift of a VL diffraction spot with a weak signal for this higher field. We can say that the anisotropy exists, but is weak and more sensitive to field rather than angle variation. This picture may change with more data at higher or intermediate angles.

If we revisit the field dependent anisotropy we can extend our analysis of the $\Gamma_{VL}(B)$ data by applying linear fits; this will not only highlight the evolution with respect to field but also allow comparisons between the angles. The fits are as follows: $\Gamma_{VL}(0°) \approx -0.82B + 1.2$, $\Gamma_{VL}(10°) \approx -0.54B + 1.2$ and $\Gamma_{VL}(30°) \approx -0.58B + 1.2$. These fits reiterate the consistent negative gradient of the anisotropy across all angles. There is a clear tendency for the anisotropy to consistently intercept at zero field around $\Gamma_{VL} = 1.2$ and for the anisotropy gradient to be larger for $\Omega = 0$. It is clear that more angles and larger angles are needed to complement the

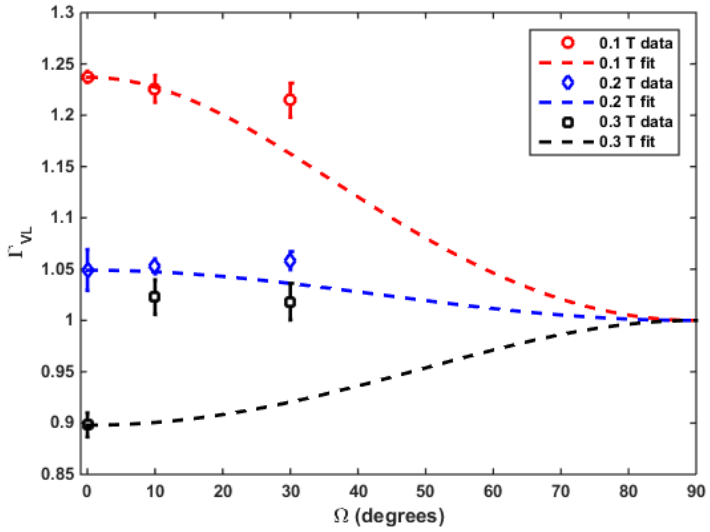

Figure 80: Anisotropy of the VL with respect to Ω, at 0.1 T, 0.2 T and 0.3 T. The data is fitted to equation 113 with the values for Γ_{ac} taken from the measured values of $\Gamma_{VL}(\Omega = 0)$ in Figure 79.

investigation into anisotropy in order to provide more definitive angle- and field-dependent analyses of the behaviour of the VL in $TlNi_2Se_2$.

Another method of assessing the anisotropy is to look at the opening angle between two spots. This angle should be 60° for an isotropic VL, where the opening angle η is defined in Figure 77 and used for the top and bottom spot pairs (Figure 77a) then averaged to assess the general trend to reduce sensitivity to fluctuations. The orientation of the VL spots, from the observations of η in Figure 81, do undergo an evolution with respect to field; this behaviour of η is not what is typically expected with regards to other examples of anisotropic VLs. If we refer to the work in [12] by Kawano-Furukawa *et al.* on KFe_2As_2 we see an evolution of η (β in [12]) from an approximately isotropic case to on average an increase of $\Delta\eta \approx 5°$. However, this η data is consistent with figure 79 as it shows the excess drift of the top/bottom spot pairs. The opening angle is compressed below 0.3 T, and expanded above 0.3 T. This infers that the top/bottom spot pairs are moving along the x-axis more rapidly with changes in field than for a purely isotropic VL case. Given this consistency we can say that there is a weak anisotropy in the VL.

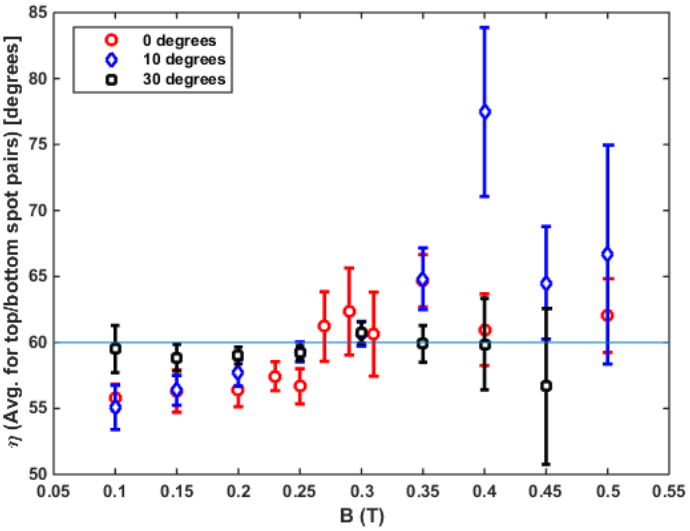

Figure 81: Calculation of the average opening angle η for the top and bottom spot angular gap. A deviation from 60° would indicate a contraction or expansion in the shape of the hexagonal VL along one of the axes. Generally, the results sit within error of isotropy, while at high fields the larger deviations in angle are also accompanied by much larger errors due to the weak VL signal here.

This drifting of the VL, especially the expansion of the VL above 0.3 T, is likely due to the VL spots weakly coupling to the **ab**-axes of the crystal (Figure 78a). This is more probable when we consider that work by Xu *et al.* [83] demonstrates that the nodes in the gap structure are concurrent with the fourfold symmetry of the underlying crystal axis. This makes it reasonable that the VL spots would try to align with this underlying symmetry with applied field modulation. However, this effect is still very small and requires further investigation. Expansion on the case of the nodal structure is discussed earlier in Section 3.

Overall the relationship between field and angle with the anisotropy of the VL is weak in $TlNi_2Se_2$ Anisotropic behaviour is often considered a clear indicator that a superconductor is unconventional [89] (but this argument is not exclusive). If we refer back to the resistivity measurements in [48], it is reasonable to expect some anisotropy evolving with angle due to the greater resistivity in the **c**-axis of the crystal. This complements the clear anisotropy of the crystal structure between

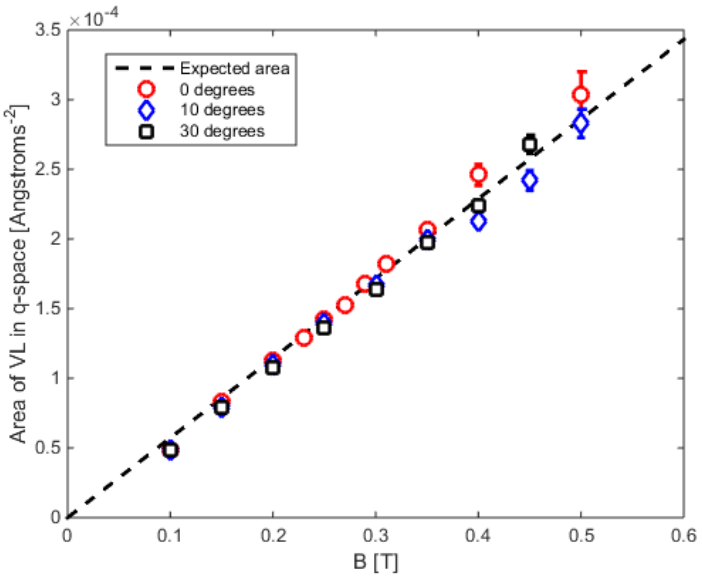

Figure 82: Area of the hexagon made by the six VL spots evolving with field. The area was calculated by summing the areas of each of the six triangles in the VL using the η and Q values for each spot-pair.

the **ab** plane and **c**-axis. But, the anisotropy maximum peak for the 0.1 T data is $\Gamma_{VL} \approx 1.24$ for variation with Ω. We see similar values with respect to B as well in Figure 79. The value of 1.24 for the anisotropy is not unity, and as such we must pursue more intermediate fields and angles in order to fully explore the evolution of the VL structure and the existence of weak anisotropy in this material. Overall the anisotropy is very low in comparison to structural equivalents like KFe_2As_2 [86], but this does not rule out the case of unconventional superconductivity being present in this material, of which we have presented ample evidence previously in this work.

The final part of the anisotropy investigation regards the overall area of the hexagonal VL created by the visible six spots in reciprocal space. The total area of the unit cell VL is conserved due to flux quantization, even under anisotropy. The total VL area is only dependent on the strength of the applied magnetic field. It is possible that any fluctuations measured in the anisotropy are due to fluctuations in the applied magnetic field, such as deviations from the intended target field or additional field contributions under the experimental conditions. If this is the case

then the measured area of the VL will deviate from the expected VL area as it is conforming to the real field rather than the set field.

The side of the regular hexagonal VL is defined by equation 84. The area of a hexagon is given as $A = 3\sqrt{3}a^2/2$. This means the area of a hexagonal VL with regular and equal sides $q = 2\pi/a$, in reciprocal space should evolve linearly with the field in reciprocal space, $A_q = 6\pi B/\Phi_0$. We see the area behaves linearly, as expected for the full field range accessed. In fact, the area conforms very closely to the expected area for the fields applied, which suggests there is only minimal error on the value of the applied field.

There is some divergence in area between the angle sets above 0.35 T. The 10° set undergoes a slight decrease in area, the 0° experiences a slight enlargement and the 30° data fluctuates partially around the expected line of area. Some of the fluctuations are explainable alongside the larger errors; the signal here is somewhat weaker and so the centre of the spots used to define the Q values is less well-defined but some of the fluctuations are outside of the error bounds. Further measurements at larger and intermediate angles of Ω could perhaps indicate whether this is indeed a feature above 0.35 T, or are just fluctuations. Analysis of the form factor did not clearly indicate any large deviations in the expected applied field.

6.6.1 Field dependence of the vortex lattice form factor

Figure 83 shows the measured integrated intensity with the first and second domain data summed together for a total integrated intensity signal from the ω and ϕ rocks. The errors in the 2nd domain signal are large due to their small signal size in comparison to the background. In some cases a signal above the background could not be obtained for the second domain for $\Omega = 10°, 30°$. The signal for the 2nd domain was significantly stronger for $\Omega = 0°$ and comparable in magnitude to the 1st domain signal.

It is clear from Figure 84 that the signal strength and resolution for the 2nd

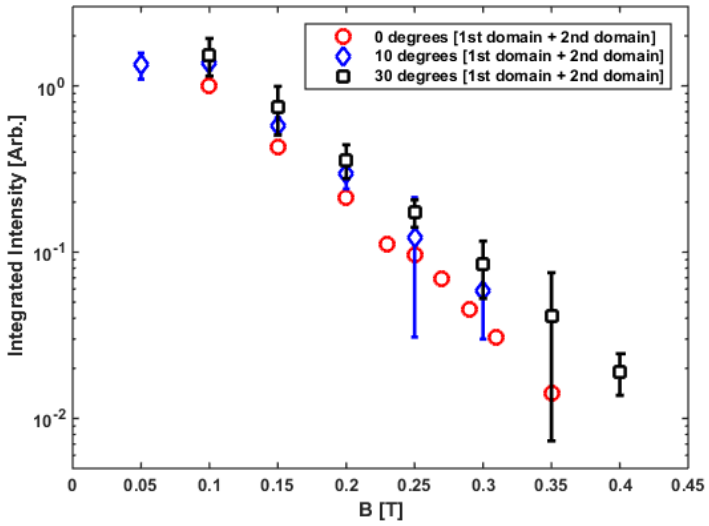

Figure 83: Integrated intensity measurements vs field (B) for varying Ω, averaged over the ω and ϕ rocks, under field variation with 1st and 2nd domains summed to a total intensity.

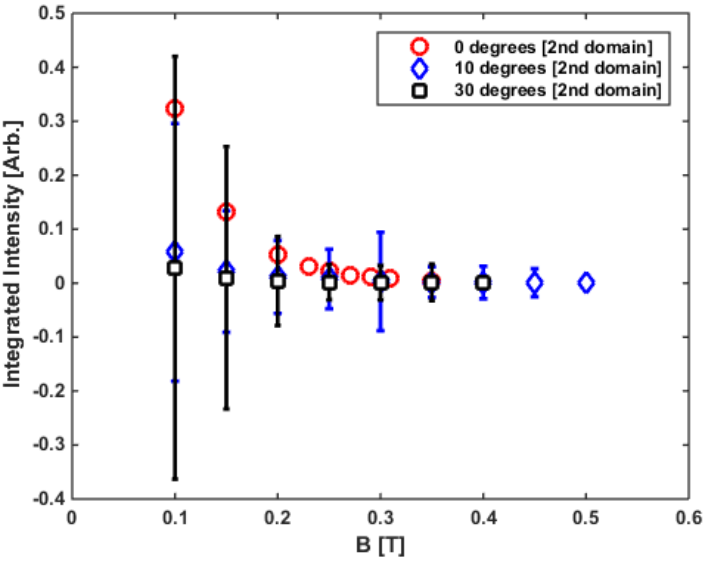

Figure 84: Integrated intensity measurements vs field (B) for varying Ω, averaged over ω and ϕ rocks, under field variation with just the 2nd domain contributions.

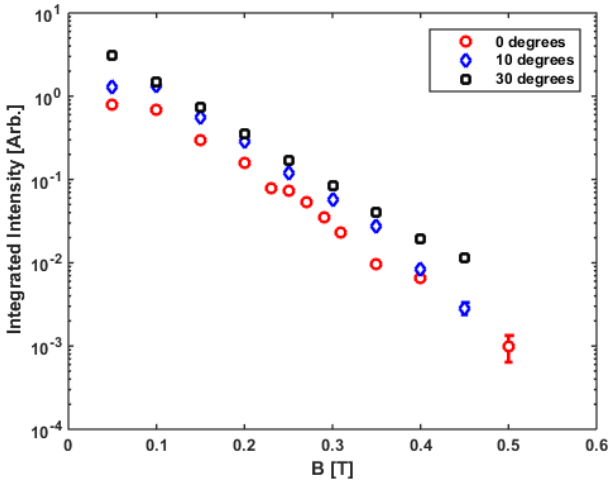

Figure 85: Integrated intensity measurements vs field (B) for Ω scans with only the 1st domain contributions. We see a signal strength increase for greater displacement angles of Ω.

domain rapidly falls with increasing angle; as expected for a second domain signal. Interestingly, when summed for both domains, we see that the 30° signal is still slightly enhanced over the 10° and 0°. Either there is some mechanism occurring that we are not aware of, such as the presence of some anisotropy in the VL, or there is a discrepancy between the set field and the actual field applied that creates the VL.

In the case of the 1st domain only we also see a slight increase in integrated intensity for increasing Ω in Figure 85. This change in integrated intensity could be due to an error in the applied field, meaning the field we expect is not the field applied during the experimentation. To check this we can plot Q versus the applied field B and check the results alongside the expected Q values.

The results in Figure 86 indicate that for almost the whole field range, for most values of Ω, the Q value is as expected. However, in the case of the 0° data between 0.25 T and 0.4 T there is a noticeable discrepancy. If this is calculated backwards to find the experienced field at that point we find an almost constant field discrepancy of $39 - 42\%$ higher field for that segment. It is not clear whether this is due to anisotropy or a systematic error during experimentation, but it seems unlikely that

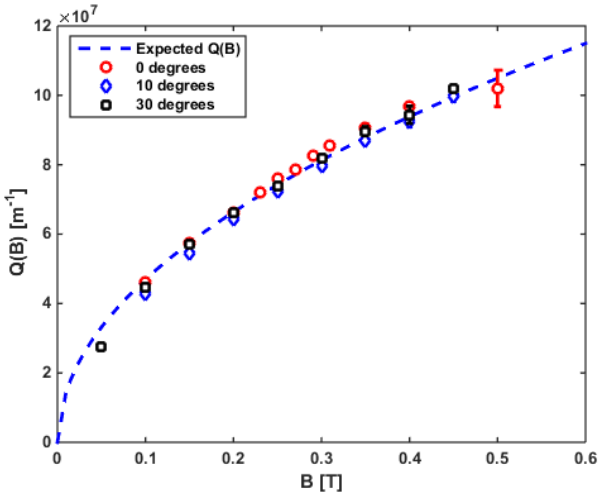

Figure 86: Measured Q values of the field dependent data versus the applied field. If there was a discrepancy in the applied field or any anisotropy, there would be a deviation from the expected Q line. There is some deviation from the expected Q for the 0° data set between 0.25 T and 0.4 T, but not for the whole range nor all values of Ω.

an incorrect field was applied for a small segment of one set of scans for one angle.

The field dependent results are presented in Figure 87. The results are presented with a logarithmic y-axis for the form factor; this is because a trend of linear or non-linear relation to the field in a logarithmic representation indicates how the exponent in the Gaussian correction term in equation 105 varies with field. The most obvious change in the form factor is the increase of the signal strength with increasing angle. Effectively the increase of Ω seems to improve the order of the VL and increase the signal of the form factor by a small factor; as previously highlighted and discussed for the integrated intensity. There is no visible feature in the data around 0.3 T, which would correspond to the suppression field of $H^* = 0.36H_{c_2} = 0.29$ T for the smaller gap predicted by Wang *et al.* as shown in Figure 66.

6.6.2 Temperature dependence of the vortex lattice form factor

Observing changes in the VL with respect to temperature tends to produce results that can be indicative of the pairing mechanism and the nature of the superconductivity in a material due to the strong temperature dependence of the characteristic

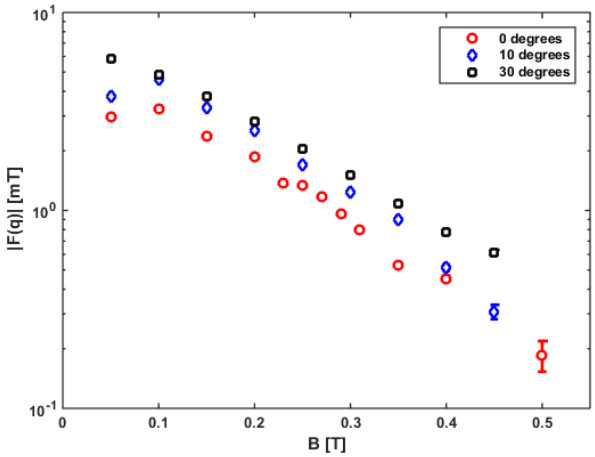

Figure 87: Form factor ($|F(q)|$) measurements vs field (B). Note the increase in the form factor signal with increased angle carried through from the integrated intensity. The results show a slight deviation from linear behaviour with a log(y) axis. This is indicative of a non-constant Gaussian term for the core correction, which could suggest a coherence length value that varies more than just at the regime of $T \to T_c$ as we would normally expect.

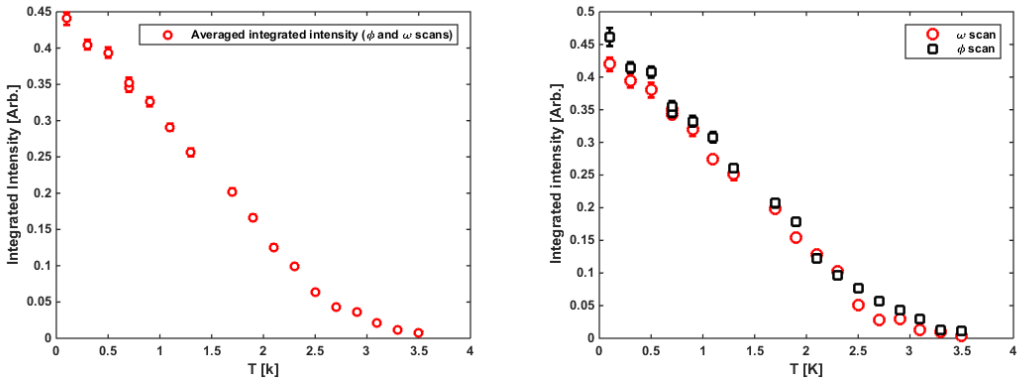

(a) (b)

Figure 88: (a) Integrated intensity versus temperature (T) averaged over the ω and ϕ scans. The scans were taken at 0.15 T as this presented the largest integrated intensity signal from the field dependent results, see Figure 85. (b) Integrated intensity versus temperature for the ω and ϕ scans separately. For the majority of the temperature range there is good agreement between the scans, with most of the temperature scan points for ω and ϕ within error of each other. At the extremes of the temperature range there is somewhat more divergence.

parameters $\lambda(T)$, $\xi(T)$ and $\Delta(T)$. As part of the investigations at ILL, sets of ω and ϕ scans were taken at a displacement angle of $\Omega = 30°$ rotation and 0.15 T with the temperature varied from 0.1 K to 3.5 K. The rotation angle (Ω) was chosen as it had

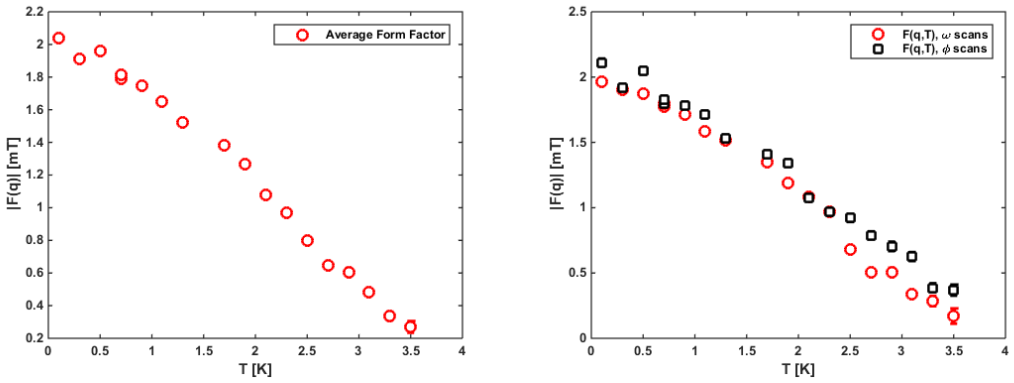

(a) (b)

Figure 89: (a) Average form factor versus temperature calculated using the Christen formula (equation 104) and averaged over the ω and ϕ scans. (b) Form factor versus temperature for the separate ω and ϕ scan results; also calculated using equation 104. These results highlight some divergence in behaviour above $T = 2.3$ T.

given the largest integrated intensity signal in the previous sets of field dependent data (see Figure 85). The field of 0.15 T was also chosen for the large integrated intensity signal in the field dependent data, as seen in Figure 85, whilst the spots of the VL in q-space are not too close to the beam-stop for 7Å. A wavelength of 12 Å was used for some of the field dependent data for very low fields but this was not used in the temperature dependent scans for expediency and consistency during experimentation.

The results in Figure 85 show the temperature dependent integrated intensity averaged over the ω and ϕ scans. For this work we will make calculations using both the averaged and split results in order to highlight discrepancies in the split data that might be indicative of anisotropy or multi-gap behaviour, whilst also producing averaged behaviour alongside.

Figures 89a and 89b represent calculations using the Christen formula. The results of the separate ω and ϕ scans show a divergence between the scan angle results for $T > 2.3$ K. This divergence has not been hinted at in previous literature regarding the heat capacity or thermal conductivity, it could be evidence of anisotropy in the superconducting state or a disparity in the size of the gap between two different

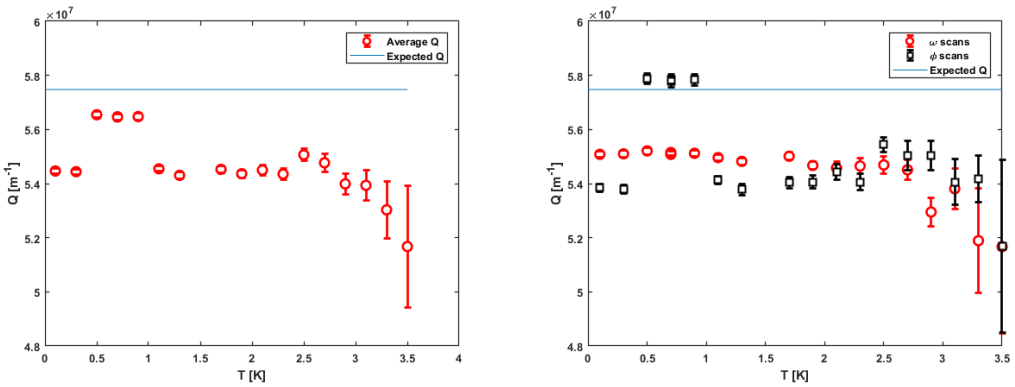

(a) (b)

Figure 90: (a) Measured Q value averaged over the ω and ϕ scans with respect to temperature. A reference line is also added showing the expected Q value for the applied field, $Q = 5.7474 \times 10^7$ m^{-1} for $B = 0.15$ T. (b) Separate ω and ϕ scan values for Q. There is generally good agreement except for the anomalously different values at 0.5, 0.7 and 0.9 K for ϕ that are much closer to the expected value.

directions in the crystal. It is possible this is representative of a feature or some mechanism of the superconductivity. However, we must rule out that there isn't a systematic error in the applied field for these scans. If the field deviated from the set field during experimentation, this would affect the Q value of the VL spots, the integrated intensity and thus any calculations made using $I(Q)$. In order to check this we must compare the Q values of the scans to the expected Q for the applied field.

The values presented in Figures 90a and 90b show a clear and near-consistent deviation of both sets of scans from the intended applied field, apart form three anomalous results at low temperature (0.5-0.9 K) in the ϕ scan set. The rough average of the scans is $Q \approx 5.5 \times 10^7$ m^{-1}, this translates into a field of $B = 0.14$ T; this is $\approx 8\%$ smaller field than expected, but the differences between the ω and ϕ scans are minor compared to the overall difference between the expected Q and the average Q of both sets. This isn't concurrent with the field dependent Q discrepancies from Figure 86 that show the applied field was larger than expected but only for the regime of 0.25 T to 0.4 T. The excess field for the field dependent investigation may likely be due to an additional remnant field adding to the applied

field during scanning. Alternatively there may have been some discrepancies with the VL lattice preparation in this temperature regime.

The discrepancy for the temperature dependent scans is much smaller and fairly consistent in size for all temperatures accessed. The decline in the Q value at high temperatures coincides with a dramatic increase in error size and so indicates that the drop off in Q is likely tied to the difficulty of measuring a signal and ascertaining the Q value of diffraction spots with weak signals. As such, the majority of the Q values presented here broadly conform to a constant applied field within 8% of the target applied field of 0.15 T. This is fairly significant however, analysis of the overall area of the VL with respect to the Q in Figure 82 demonstrates that for the field dependent results these problems were not mirrored. If we also look to the impact of anisotropy on the measured values of Q in the previous section, it is conceivable that anisotropic variation of the VL had a role in the deviations observed here.

6.6.3 FWHM of the VL spots vs field and temperature

For both the $|F(q)|$ vs B and $|F(q)|$ vs T results, the full-width half-maximum (FWHM) of the rocking curves that generate these results can give some indication as to whether the application of stronger magnetic fields or an increase in temperature affect the disorder in the VL. Typically we would expect increasing temperature to cause greater disorder in the VL and thus increase the FWHM as the number of screening electrons (Cooper pairs) is reduced for a given field.

The FWHM of the temperature scan data in Fig. 92 taken from the rocking curves indicates a slight decrease in the FWHM with increased field. The behaviour of the FWHM with respect to the field is comparable to that of the integrated intensity with respect to field. This suggests the FWHM is tied to the size of the overall signal of a VL spot above the background, rather than being proportional to the applied field strength.

From Figure 91 we can see a rapid drop in the FWHM between 0.05 T and

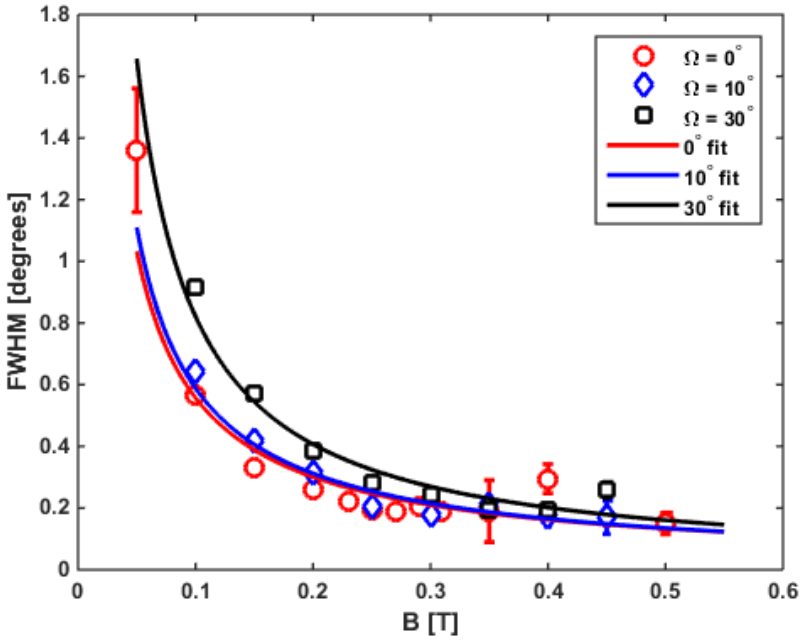

Figure 91: FWHM of the VL spots in ω with respect to applied field (B) for the full range of angles accessed. The results broadly conform to a power law relation, with the 30° results showing a marginally broader FWHM.

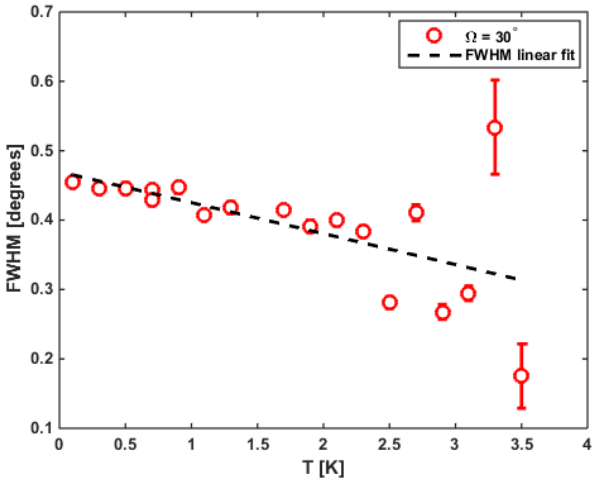

Figure 92: FWHM of the VL spots in ω with respect to temperature (T) at $\Omega = 30°$. Overall there is a linear decrease in the FWHM with respect to temperature.

0.3 T, with the FWHM leveling out above 0.3 T. The results are fitted as follows: $y_{0^\circ}^{FWHM} = 0.0720B^{-0.889}$, $y_{10^\circ}^{FWHM} = 0.0716B^{-0.915}$ and $y_{30^\circ}^{FWHM} = 0.0797B^{-1.013}$, essentially $FWHM \propto 1/B$. With increasing angle the overall FWHM increases slightly while the rate of decrease of the FWHM also goes up with increasing angle; this is consistent with the slight increase in signal strength with Ω. We see that the pre-factor increases from 0.0716 to 0.0797 from 0° to 30° and the power goes from -0.889 to -1.013 within the same interval. This might suggest that at smaller angles we see less disorder in the form of a smaller FWHM. However, this effect is only strong for low fields as the high field results generally tend towards a levelling-out of the FWHM, with some fluctuation and larger errors. This is indicative of a weak VL signal, with results fluctuating around an equilibrium for the FWHM at the highest fields. The fluctuations at high fields could indicate a slight increase in overall signal size but are much more likely reflecting the large noise to signal ratio at these high fields (as indicated by $|F(q)|$, where at high fields the form factor signal is very small compared to the background).

What we can say is that the very large FWHM at very low fields may not entirely be due to the larger signal overall, it is possible there is a contribution of larger disorder in the VL for weaker magnetic fields. We see a different effect for the FWHM with respect to the temperature. Figure 92 indicates that the FWHM falls approximately linearly with T and can be fitted as $FWHM = -0.0446T + 0.4697$. This small but steady reduction in FWHM with increasing temperature may suggest that there is actually a slight decrease in disorder for the VL for the higher temperature regime. If this is the case, it could be due to a higher temperature freeing pinned flux lines and thus increasing the order of the VL as it rearranges towards a more energetically favourable arrangement. However, we have outlined already a wiggling procedure for cooling that normally mitigates any pinning issues. In the case of the ILL investigation in December 2016 some scans were performed without the wiggle-cooling procedure and the VL signal was significantly more disordered,

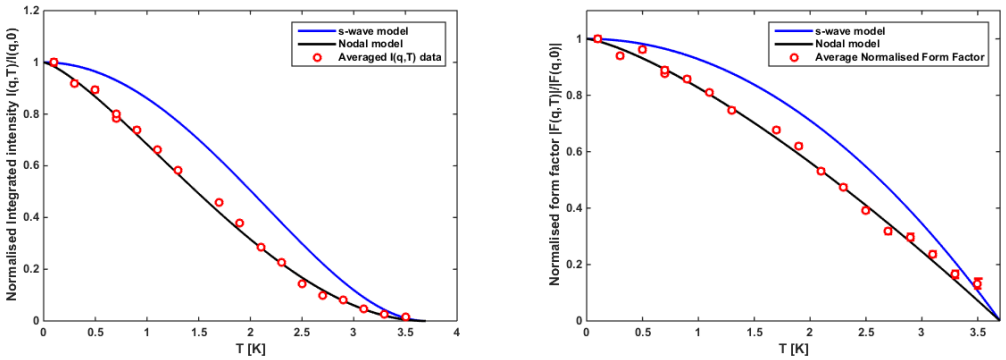

(a) (b)

Figure 93: (a) Integrated intensity vs temperature (T) with null hypothesis approach using the Prozorov *et al.* [92] models. (b) Same approach as in (a) but for the form factor, $|F(q,T)|$. These graphs are the same approach for modelling the data as in the chapter investigating $(Ba_{0.5}K_{0.5})Fe_2As_2$, with the data sets of the rocking scans averaged together in order to see the integrated intensity and form factor behaviour of the whole VL. This approach does, to some extent, screen out potential anisotropy and multiple pairing mechanisms tied to different crystal axes, however.

with a weaker, smeared VL signal. It is likely that the small linear decrease in the FWHM is in line with the clear linear decrease in the form factor signal, as illustrated in Figure 89a, and as such the FWHM is scaling with the total signal size with respect to temperature.

6.6.4 Comparison of the integrated intensity data with ideal models

Figures 93 and 94 illustrate the application of the null hypothesis discussed earlier (section 2.7). These figures show the comparison of the integrated intensity data and form factor calculations (both split sets and averaged) compared to their respective models, given a particularly strong emphasis of a pairing mechanism; either s-wave or nodal.

It is immediately obvious in the case of Figure 93a and Figure 93b that the data does not support a simple BCS, s-wave interpretation. Given the smaller errors in the integrated intensity data, this can be used more reliably to state what kind of pairing mechanism is dominant. Overall, it appears that the data strongly tends towards a nodal behaviour for the the full range of the accessed temperature range

at this angle of rotation ($\Omega = 30°$). It is very clear from the integrated intensity that there are nodes in the gap structure but not necessarily d-wave pairing symmetry. The form factor data in Figure 93b has slightly larger errors but still very strongly aligns with the nodal model, even with some small fluctuations at the extremes of the temperature range. As there appears to be no variation in alignment to the nodal pairing symmetry model, and there are no discontinuities in the data, this might lend one to think this points to a single nodal gap rather than multiple gaps which was strongly indicated in previous work [48, 47]. Multiple gaps could take the form of a large nodal gap and a smaller nodal or s-wave gap or vice versa or a pair of the same symmetry. Any of these combinations could manifest when one of these gaps is suppressed at a temperature below T_c for a non-zero magnetic field. However, this is not observed. This does not rule out multiple gaps, in fact the previous field-dependent anisotropy data makes multiple gaps a possibility, as previously discussed. Obviously the data points at the lowest and highest temperatures in the range do have some error overlap with the BCS model, this does not indicate any kind of transition between symmetries because the superconducting state will be suppressed at T_c regardless of the pairing symmetry and converges to the same value at $T = 0$ K.

The separate ω and ϕ results in Figure 94a for the integrated intensity show good agreement with each other; there is a good indication that the dominant pairing symmetry is strongly nodal from this data. We do see some fluctuations around the models but in general the integrated intensity null hypothesis is consistent and clear. The ω and ϕ results for $|F(q)|$ present a similar picture with regards to agreement to the models but with a greater degree of divergence of the ω and ϕ scans from each other. In Figure 94b we see more fluctuation in the value of the $|F(q)|$ and a not insignificant divergence between the scans at temperatures above 2 K where there is a slight splitting between the data sets. The ϕ scans present a slightly stronger overall form factor signal than the ω scans. There is also a section of divergence

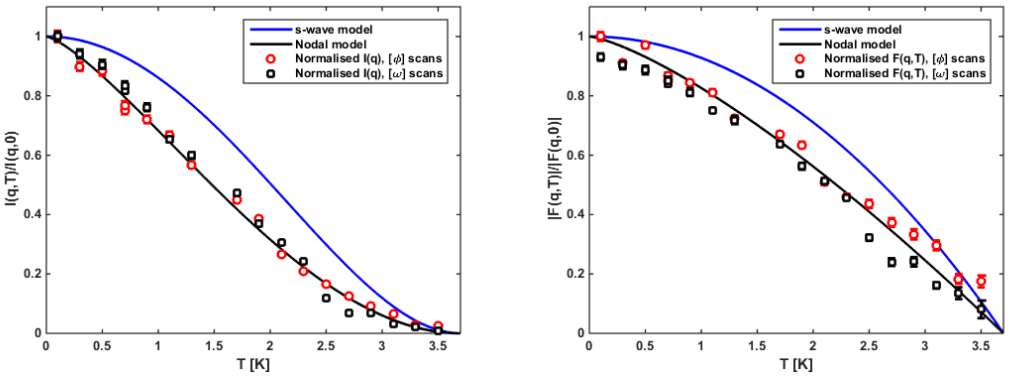

(a) (b)

Figure 94: Models for each pairing mechanism as outlined previously compared to the integrated intensity data and form factor calculations for ϕ scans and ω scans. (a) is the comparison between the integrated intensity calculated from the raw data in GRASP with the models for the integrated intensity for s-wave and nodal gap structures, as outlined in the previous section. (b) is the same approach as in (a) but for the form factor; where the data is calculated from a rearranged Christen Formula.

between the scan results for $T > 2.3$ K. These results are illuminating, as they hint at potential anisotropy or multi-gap behaviour, but with the smaller gap looking to be similar in size compared to the larger gap if this is the case. This is not fully in line with what has been previously discussed about this material [48, 47] but does lend some evidence towards a multigap picture of the superconducting state.Further analysis of the penetration depth and gap function can provide the necessary clarity regarding the pairing symmetry of the gap function.

Previous investigations covered in this thesis by Wang *et al.* have demonstrated that multiple gaps are possible in the gap structure of this material, while also demonstrating conflicting evidence on the presence of d-wave contributions from the behaviour of the free electron term in the heat capacity behaviour [48, 47]. However, even in the low-T regime there are minimal observable structural changes in the VL (insofar as no change to rhombus or square VL or easily identifiable large shifts in anisotropy), which is unusual if there is unconventional pairing under those conditions given that d-wave superconductivity is often identified by structural changes in the VL with field and temperature, as seen in $CeCoIn_5$ [89]. But unusually the

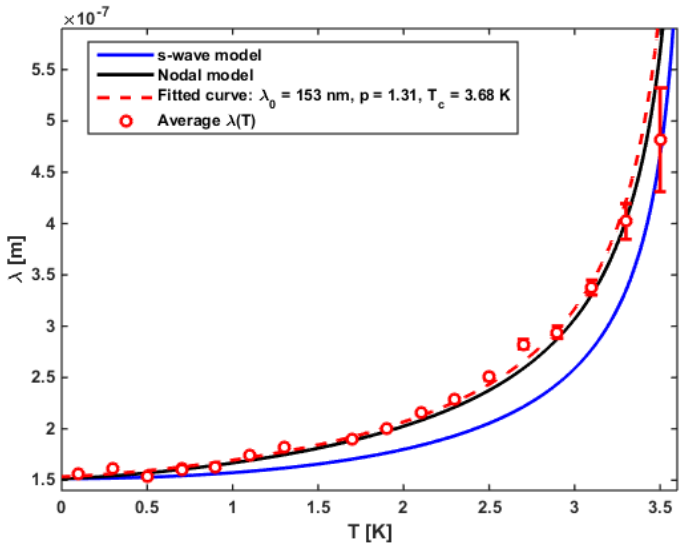

Figure 95: The averaged penetration depth, $\langle\lambda(T)\rangle$ vs T, for the whole of the VL calculated from $|F(q,T)|$ and fitted using a power law relation from the Prozorov framework, equation 108. The results for the ϕ and ω scans have been averaged over both data sets with a fit line for the average. The full fits are: $\lambda_0 = 153.42 \pm 2.08$ nm, $T_c = 3.68 \pm 0.09$ K and $p = 1.31 \pm 0.11$.

evidence from the null hypothesis demonstrated in Figure 93a is strongly indicative of unconventional, potentially d-wave pairing symmetry; or otherwise some arrangement of line and/or point nodes in the superconducting gap (given the lack of VL rearrangement).

6.6.5 Calculation of the penetration depth and the superfluid density

An alternative method of arriving at a picture of the pairing mechanisms in a superconductor is trying to calculate or express the behaviour of the penetration depth, $\lambda(T)$. If, as before, we calculate the form factor with respect to temperature as seen in Figure 93b, we may then calculate the penetration depth. This is done by inserting equation 105 into equation 104, then rearranging for $\lambda(T)$. This requires values for some parameters that we don't know very much about, or are known to vary with temperature but for which we have no data to describe such a relationship. Thus we must accept for this method that some assumptions at this stage must be made for simplification. Firstly, we must use the value of the coherence length

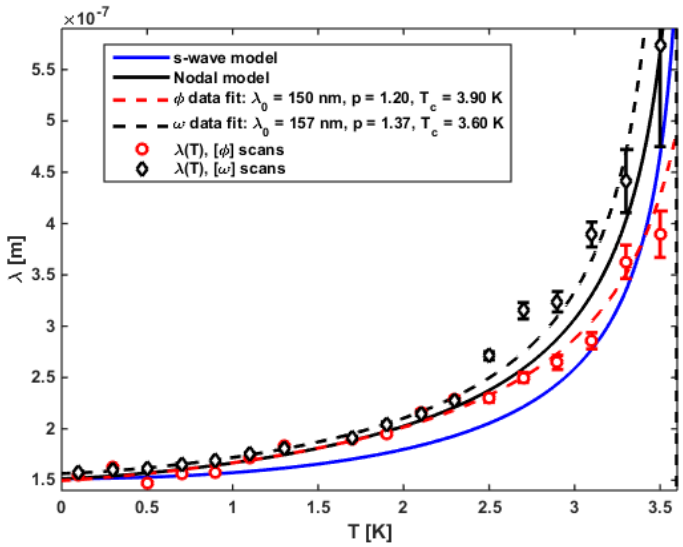

Figure 96: Figure showing the penetration depth ($\lambda(T)$) vs T calculated separately for the ϕ and ω scans from $|F(q,T)|$ for the separate ϕ, ω scans and fitted using a power law relation from the Prozorov framework, equation 108. The graph shows the data sets for the ϕ scans and the ω scans separately and includes fitted curves for both. The full fits are: $\lambda_0^{\omega} = 156.52 \pm 1.75$ nm, $T_c^{\omega} = 3.60 \pm 0.05$ K, $p^{\phi} = 1.37 \pm 0.09$ and $\lambda_0^{\phi} = 149.60 \pm 4.58$ nm, $T_c^{\phi} = 3.90 \pm 0.25$ K, $p^{\phi} = 1.20 \pm 0.24$

calculated in [48] from the heat capacity data; $\xi_0 = 20.3$ nm. Then we must assume that this remains approximately constant for the accessible temperature range over which we will be making the numerical calculations.

Once a calculation of the penetration depth is made, it can be compared in a null hypothesis as before or modeled by the previously outlined Prozorov framework using the power law description from equation 108. In Figure 95 the fit for the average penetration depth over the whole VL gives the following values: $\lambda_0 = 153.42 \pm 2.08$ nm, $T_c = 3.68 \pm 0.09$ K and $p = 1.31 \pm 0.11$. This fit in relation to the models leaves p very close to the nodal model value of $p = 1.333$. This places the fit, as can be seen in the figure, very definitively in the realm of an unconventional nodal or d-wave interpretation. If we take the ϕ and ω scans separately, and then plot a fitting curve we get the results presented in Figure 96. Here we have the fitting parameters for the ω scans: $\lambda_0^{\omega} = 156.52 \pm 1.75$ nm, $T_c^{\omega} = 3.60 \pm 0.05$ K and $p^{\phi} = 1.37 \pm 0.09$ and for the ϕ scans: $\lambda_0^{\phi} = 149.60 \pm 4.58$ nm, $T_c^{\phi} = 3.90 \pm 0.25$ K and $p^{\phi} = 1.20 \pm 0.24$. As

shown in the figure, these data sets diverge considerably for $T > 2$ K, which could suggest a growing separation between pairing symmetries at higher temperatures. But, within the Prozorov framework both the ω and ϕ scan results indicate a very close adherence to nodal behaviour up until 2 K, with the parameter that seems responsible for the divergence being the split in T_c. The fitted values of T_c differ by 0.3 K, and $\approx 8\%$ difference, which primarily accounts for the splitting between these scan sets.

This penetration depth disparity between the scans is less likely to be evidence of an evolution of the gap function symmetry and more indicative of a disparity in the penetration depth given whichever angle is being rocked in the scan. These penetration depth calculations suggest that in the vertical rocking case for the ϕ scans, the penetration depth is more suppressed at high temperature, while the opposite is true of the horizontal rocking case for the ω scans. The net effect in Figure 95 is that the average data and the average fit as a result align very closely with the middle of these two sets, which is the unconventional nodal model. Given that the fitted parameters for the ω and ϕ scans, λ_0, T_c and p are all in very close agreement of each other and the average penetration depth, thus it is reasonable to say that the overall behaviour indicated by this analysis is that of a nodal, possibly d-wave, pairing symmetry. Of course the cause of this disparity could be due to the previously suggested multigap interpretation of $TlNi_2Se_2$. Mulitple gaps with separate T_c and H_{c_2} values could manifest in a spacial separation of the penetration depth.

These fits indicate that perhaps there are multiple gaps, with the difference between the two becoming apparent and outside error overlap above $T = 2.5$ K as one is suppressed at a slightly smaller critical temperature. The separate power law fits for p indicate that both the ϕ and ω fits sit fairly well aligned still to a nodal interpretation despite the divergence. Something that is confirmed is the lack of intrinsic anisotropy between the y and x axes (between the ϕ and ω scans,

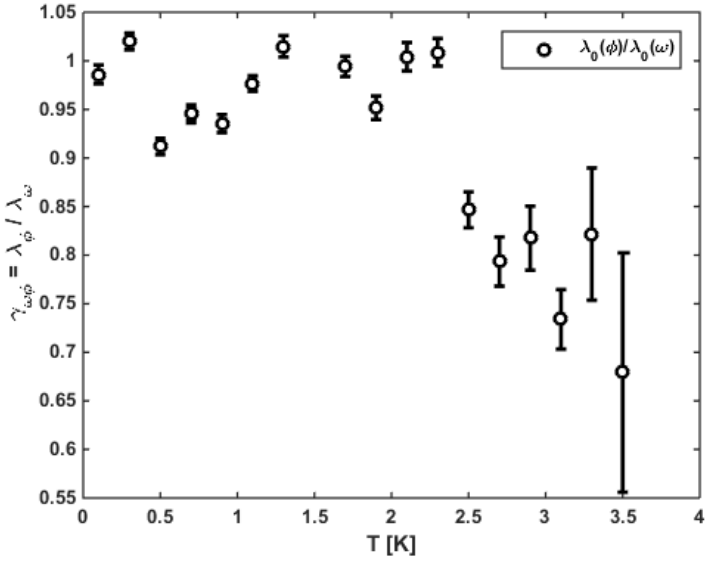

Figure 97: Penetration depth anisotropy, $\gamma_{\omega\phi}$ with respect to temperature, T between the ϕ and ω scans, or the y and x axes of the VL diffraction pattern. Calculated by the ratio of $\lambda(T)$ for the ϕ and ω scans; which correspond to the [110] and $[\bar{1}10]$ planes, respectively. This calculation suggests isotropy dominates for the majority of the temperature range as expected for a tetragonal crystal, up to 2.5 K. Above this point in reciprocal space the x axis of the VL overtakes that of the y axis up to $\gamma_{\phi\omega}(T) \approx 0.7$.

respectively). If we take the λ_0 fits for each scan and take the ratio, the anisotropy is $\gamma_{\phi\omega} = \lambda_0^\phi(T)/\lambda_0^\omega(T)$. The results for this ratio of the VL anisotropy in reciprocal space is shown in Figure 97. In this Figure we see that an isotropic VL remains roughly steady, which is what we would expect for a tetragonal crystal where $a = b$. However, from 2.5 K upwards anisotropy appears. In this high-T regime the $y - x$ anisotropy drops linearly to roughly 0.7. This suggests that the penetration depth in the x axis (the ω scans) overtakes that of the y axis (the ϕ scans). However, the sample has been rotated by 45° within the $a - b$ plane. This means that **a** is no longer normal to the ϕ rock axis and **b** to the ω rock axis, respectively; they are now 45° to the rocking axes, meaning we are rocking in the $[11l]$ and $[\bar{1}1l]$ planes.

It is a surprising result to see this divergence then between the two rocking directions above 2.3 K. This sudden shift in $\gamma_{\phi\omega}(T)$ is a measure of the divergence in the penetration depth that we see at $T \geq 2.5K$ in Figure 96. This could indicate

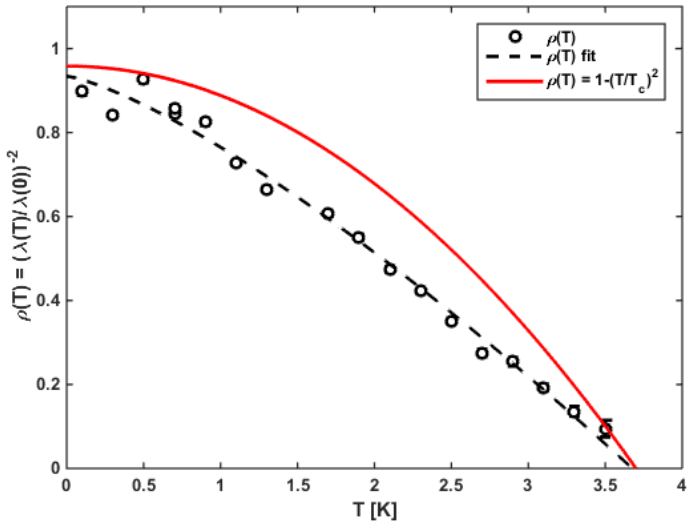

Figure 98: The superfluid density, $\rho(T)$ versus T. The results here are calculated from the averaged $\lambda(T)$ from Figure 95 and the fitting line is also a rearrangement of the averaged $\lambda(T)$ fit. The red $\rho(T)$ line is the BCS theory for the superfluid density: $\rho(T) = 1 - (T/T_c)^2$.

that at around 2.5 K one of the gaps in this multigap system is suppressed. If this were the case, a sudden shift in anisotropy would make sense as one direction in the crystal associated with one of the gaps would become more energetically preferential for the Cooper pairs. Given that **a** has been rotated by 45°, this could suggest there is a difference in gap structure between the [110] and the [$\bar{1}$10] directions.However, the difference that becomes apparent between the ϕ and ω scans could very likely be an experimental artifact, given the small margin of difference between the scans and the weaker signal at $T \to T_c$ where the signal to noise ratio becomes poorer.

The penetration depth, specifically the results shown in Figure 95, can be further utilised to look at the superfluid density behaviour. Using equation 117 for fitting gives $\lambda_0 \approx 153$ nm from Figure 95. The superfluid density is normalised as a ratio and so unitless and has a value ≤ 1, rather than an absolute measurement of the number of superconducting electrons per unit volume of the material as this would require exact knowledge of the effective electron mass. The effective mass is estimated in [48] to be 14-20m_e, which would put the zero temperature number of Cooper pairs to be of the order of 10^{27} per unit volume of the material. In this case

we will remain with a ratio as it more accurately reflects the behaviour and can be used in later calculations of the actual superfluid density in volume density of carriers. From Figure 98 we can see that the superfluid density calculations are much more linear compared to the BCS theory but with some variation at the extremes of the temperature range. In general for a BCS superfluid density we would expect little variation at low-T and a more rapid suppression at $T \to T_c$. In the case of $TlNi_2Se_2$ the superfluid density is much more linear, indicating a greater sensitivity at low-T. This follows consistently from the modelling of unconventional behaviour which shows much more sensitivity of the superconducting state at low-T.

6.7 Non-local corrections to the superfluid density

Although the possibility of a d-wave gap has been shown by the $|F(q)|$ results and the penetration depth fits, there is still some uncertainty surrounding the nature of the pairing symmetry. We can investigate this further by taking into account non-local effects from strongly coupled d-wave pairing in order to see the extent to which unconventional pairing mechanisms are affecting the superfluid density. Even a small contribution of the non-local coupling could be very indicative of strongly coupled d-wave pairing in the system.

As previously discussed for $(Ba_{0.5}K_{0.5})Fe_2As_2$, there are sometimes non-local coupling effects that influence the superfluid density below a certain temperature in a superconductor. Once again to analyse the non-local coupling contribution we must begin with the superfluid density itself, calculated from the penetration depth, to develop the description of the non-local coupling.

The calculated values in Fig. 99 demonstrate a weaker non-local coupling contribution compared to the modeled expectation. The non-local contributions decrease quickly at low temperature but overall follow a more linear relationship with respect to temperature in comparison to the quadratic model. The non-local contribution is predicted to persist right up to T_c. Instead we see it goes to unity just below T_c

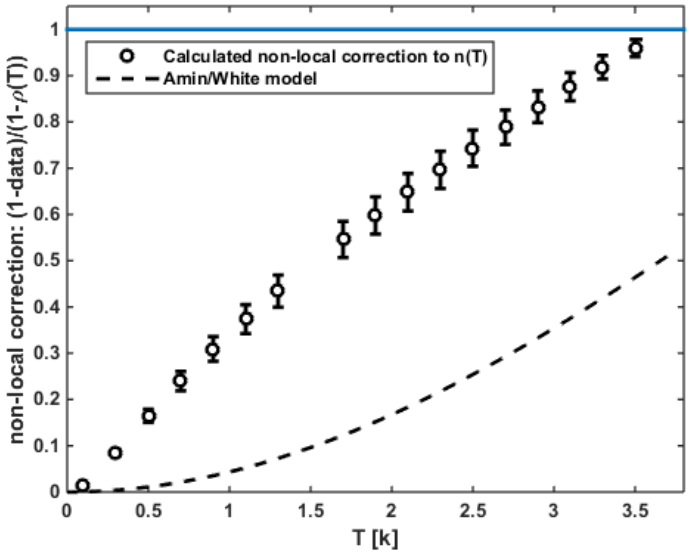

Figure 99: The non-local contribution towards the superfluid density. This is calculated using equation 64 to create a ratio of the non-local and local superfluid densities. The solid blue line represents the point at which the ratio reaches unity, $n(T) = \rho(T)$. The local superfluid density is taken as the simple BCS model, assuming s-wave behaviour, while the non-local superfluid density is calculated from the data. Included is the Amin/White model, which is the ideal ratio if there are strong non-local coupling effects.

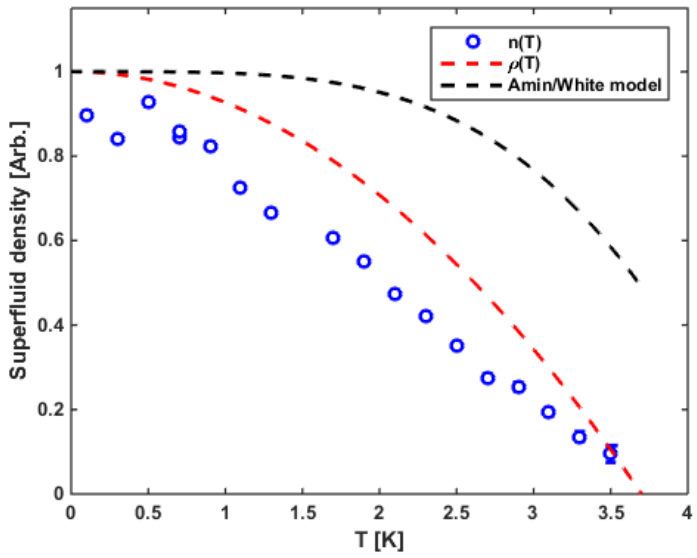

Figure 100: Superfluid density calculations comparing the $n(T)$ calculated from the data with a BCS model of $\rho(T) = 1 - (T/T_c)^2$. Included is the Amin/White model of maximal non-local coupling contributions.

and decreases very quickly with increasing temperature compared to the non-local model. This means non-local coupling contributions are present but contribute very little compared to a strong coupling case. This does not rule out unconventional pairing mechanisms but does show a strong coupling d-wave interpretation like that for the cuprates [96, 101, 102] is very unlikely for $TlNi_2Se_2$. The evidence in Figure 99 indicates that the contributions are weaker than anticipated given the previous evidence [48] suggesting a possible weakly coupled d-wave symmetry presence; this is principally due to the overall weaker superfluid density than expected at low-T. The behaviour of the superfluid density is also responsible for the more linear response of the non-local contributions here and more in line with a local, s-wave, nodal superconductor.

When we compare the ideal non-local model with the BCS model and the data for the superfluid density we see some stark differences in Figure 100. We have already seen that when compared with the models the data falls below the values of the the BCS model. This demonstrates a suppression of the superfluid density,

rather than an enhancement. However, having an almost linear superfluid density is also unusual and indicative of non-BCS behaviour and in line with the low-T sensitivity of nodal systems [32]. Overall, this presents a complex picture of the pairing symmetry and the resultant effects for the superconductivity. Given that this approach is an empirical one and is insensitive to fitting procedures it is entirely reasonable that the superfluid density is suppressed (which is consistent with the enhanced penetration depth for an unconventional superconductor), supporting the picture of unconventional pairing symmetry from the framework of Prozorov. What this shows is that the strongly coupled d-wave case is ruled out, so we are most likely looking at a weakly coupled nodal superconductor.

6.8 Conclusions

The field dependent data indicates a small deviation in behaviour from the expected form factor. This however, is coupled with the unexpected deviation of Q from expectations in the intermediate field range for the 0° case and thus small deviations could likely be fluctuations in the applied field or the VL order. As such the field dependent data does not tell us much about the nature of the superconductivity except for the consistent response of a slightly better signal for higher values of Ω.

The temperature dependent data is much more informative. We see a strong correlation with nodal modelling for the integrated intensity, form factor and penetration depth. Despite the lack of clearly observable rearrangement of the VL with field or temperature, the temperature-dependent data is very clear in its support of unconventional pairing mechanisms. This makes this material a strong candidate for nodal s-wave pairing (but with the possibility still open for weakly coupled d-wave pairing) similar to the structurally similar iron-arsenide superconductor KFe_2As_2 [109, 12, 86]. This type of pairing is sometimes denoted as $s\pm$-wave to reflect the changing sign of the gap over the Fermi surface.

What we can gather from the results is an interpretation of a very weak rela-

tionship for the VL anisotropy. With respect to field we can see a general negative gradient, passing through ≈ 0.3 T at the point of isotropy. However, with respect to Ω a pattern is difficult to interpret. Given that there is some weak trend of a negative gradient to Γ_{VL} with respect to applied field and the same results indicating that there is almost a crossover at around 0.3 T from $\Gamma_{VL} > 1$ to $\Gamma_{VL} < 1$ it would be reasonable to suggest that herein lies evidence of an anisotropic relationship with field. The anisotropy reaches a maximum of ≈ 1.24 for the lowest fields, which is not insignificant and not within error of isotropy. There is no visible, significant reordering of the VL with field or angle as we would expect for d-wave superconductivity. One could be tempted to suggest that the lack of reordering is due to pinning mechanisms, but given the wiggling procedure and the consistent evolution of Q with respect to the applied field, this rules out the hypothesis of pinning effects being the cause. The evidence does not rule out unconventional gap structure given the strength of the form factor analysis and the existence of a small anisotropic relationship of the VL with respect to field. Given the current understanding of d-wave symmetry and VL behaviour in d-wave materials [89], it is unlikely that this material is d-wave. Obviously this is not an exclusive argument and further evidence could highlight the existence of d-wave pairing.

Overall the available evidence suggests weak anisotropy with respect to field. The evidence does not support a clear relationship between Ω and Γ. This compares starkly with the previously mentioned KFe_2As_2 that has a very high anisotropy of up to $\Gamma_{VL} > 5$ under appropriate field and angle settings. It seems that the I4/mmm symmetry, despite having high crystal anisotropy between the **a**-**b** plane and **c** axis, doesn't automatically lend itself to large VL anisotropy under field or rotation in Ω.

From the heat capacity investigation we have established that the relation between the upper critical field and the critical temperature is not as expected from a pure Ginzburg-Landau description of H_{c_2}. We see for the accessed low field regime that the superconducting state is actually slightly more suppressed and the be-

haviour of the upper critical field as a function of temperature is more linear than expected. This is partly supported by the SANS results which showed very weak signals for scans with fields of $0.6H_{c_2}$ and higher. The overall magnitude of the heat capacity and the variation of the superconducting transition with respect to field in the new data sets broadly conforms well to the previous investigations conducted on this material. However, there is some deviation from previous results with regards to the Sommerfeld coefficient and the free electron heat capacity in the superconducting phase. These discrepancies could likely be resolved with further investigation at much lower fields. Despite this the heat capacity data does suggest unconventional behaviour from the Sommerfeld coefficient as well as the power law fit which characterises point nodes in the gap structure as the source of the unconventional behaviour.

7 FINAL SUMMARY

In this thesis we have primarily used SANS techniques to study the VL of heavy fermion $TlNi_2Se_2$ and the iron-arsenides $(Ba_{0.5}K_{0.5})Fe_2As_2$ and KFe_2As_2. All three materials belong to the same crystal structure symmetry group of I4/mmm with a 122 chemical formula. Whilst having this common structure these three materials differ in other respects. $TlNi_2Se_2$ is a heavy fermion material with potential d-wave pairing and possibly multiple gaps, $(Ba_{0.5}K_{0.5})Fe_2As_2$ has an exceedingly high upper critical field of $H_{c_2} \approx 62.7 - 140$ T (depending on whether you're looking at the G-L model from Figure 58 or the coherence length calculation) while KFe_2As_2 has a highly anisotropic VL.

Observations of the VL in $TlNi_2Se_2$ showed a small but not insignificant relationship between the anisotropy in the VL with respect field changes, but with more uncertainty on the relation with angle. There is distinct lack of discontinuities in the form factor to suggest a sudden suppression of a smaller gap in a multigap system. Typically morphological transitions of the VL structure with field and angle are hallmarks of unconventional and especially d-wave behaviour. KFe_2As_2 has been identified as a highly anisotropic, nodal s-wave superconductor. This compares with $TlNi_2Se_2$ which appears to have similar nodal s-wave gap structure but with significantly weaker anisotropic VL behaviour. Distinctly, $(Ba_{0.5}K_{0.5})Fe_2As_2$ shows no signs of anisotropy or morphological changes to the VL with field at all. This is less surprising given the strong adherence to a BCS model of superconductivity for the field range accessed during this work. However, the maximum field accessed was only $\approx 0.18H_{c_2}$. This means it is conceivable that there are features we have not seen due to the limitations of accessing steady state (DC) horizontal fields greater than 25 T for SANS studies. Although the material has a strong adherence to BCS, s-wave, behaviour there is good evidence of Pauli limiting effects from $B \geq 16$ T similarly seen in KFe_2As_2 but not in $TlNi_2Se_2$

Review of the literature presents a common thread of van Hove singularities in these materials but varying in tuning level, with d-electrons identified as the determining factor of the electron effective mass. The van Hove singularities, and their position relative to E_F, is suggested as the deciding factor in the structure of the gap function and the presence of nodes in the gap. In the case of $TlNi_2Se_2$, the Fermi level almost exactly bisects the saddle points of the electron energy bands, creating a nested electron-like pocket inside a concentric hole-like pocket with four-fold concurrent symmetry with the underlying crystal axes. This is highly likely to be responsible for the nodal behaviour observed in this material and the weak VL anisotropy with respect to field. For KFe_2As_2 we observe the same bisection, in the saddle points of the electron bands, but with the additional feature that there are four van Hove singularities around a single point in the Fermi surface that corroborate very well with the suspected line-node gap function of $\cos k_x \cos k_y$. In $(Ba_{0.5}K_{0.5})Fe_2As_2$ the Lifshitz transition has shifted E_F above the peaks of the electron band saddle point features. This means that the van Hove singularities in the electron band structure no longer create nested hole-like or electron-like pockets but the common feature is still responsible for the measured high effective masses and specific heat coefficients for $(Ba_{1-x}K_x)Fe_2As_2$, $x < 0.9$.

In order to create greater understanding of the similarities between these materials, $(Ba_{0.5}K_{0.5})Fe_2As_2$ should be subjected to angle variation in Ω under SANS conditions for comparison to $TlNi_2Se_2$ and KFe_2As_2 as well as higher DC fields if possible. Also, in order to understand more fully the effects of the Lifshitz transitions on the gap structure, a compound of $(Ba_{1-x}K_x)Fe_2As_2$ near the $x = 0.9$ transition should be similarly investigated in SANS looking at the VL behaviour. Equally, there have been some ARPES studies conducted of $TlNi_2Se_2$, as well as S- and K-doped compounds, but no SANS studies. By investigating the variations on this compound under the same experimental conditions we may understand more about the connection between the van Hove singularities and their relation to de-

termining the gap structure and pairing symmetry. Additionally, $TlNi_2Se_2$ should be subjected to larger displacement angles (Ω) for SANS investigations.

8 APPENDICES

8.1 Appendix A: Analysis using GRASP

The source of the bulk of the analysis presented in this thesis, including the integrated intensity, q values and angular positions, is from the use of GRASP software. This is a Matlab® based software environment developed by C. D. Dewhurst, based at the ILL [67]. The Matlab® basis makes the software very adept at handling two-dimensional pixelated data from multidetectors, as is acquired from SANS experiments.

The user interface is shown in Figure 101. The central colour-graded image is a representation of the intensity of the diffracted neutrons incident on the multidetector, with each single 2-D image representing a single angle at which the intensity was measured. These single images of summed intensity at one angle are assigned a number known as a numor. In the case of the diffraction pattern in Figure 101 multiple angles have been loaded in to show the intensity distribution for many angles summed into one image. This gives the intensity distribution of the diffraction pattern for a whole rocking curve (or for what part of the curve is input as numors). In essence this shows all the Bragg spots satisfied at multiple different angles in one image (for first-order), giving the image of the VL.

Background data is taken by setting the sample in the normal state by warming to $T > T_c$. This is preferred over raising the field to $B > B_{c_2}$ as a change in field creates a change in flux line density. If there are any pinning effects present in the material, this will resist the motion of the flux lines as the field is changed. Thus a change in field in the superconducting state runs the risk of damaging or even destroying the sample (for all field changes the sample is warmed to the normal state first). By scanning at identical angles but for the normal state (with low and high field backgrounds set) we can subtract this from the foreground data to remove

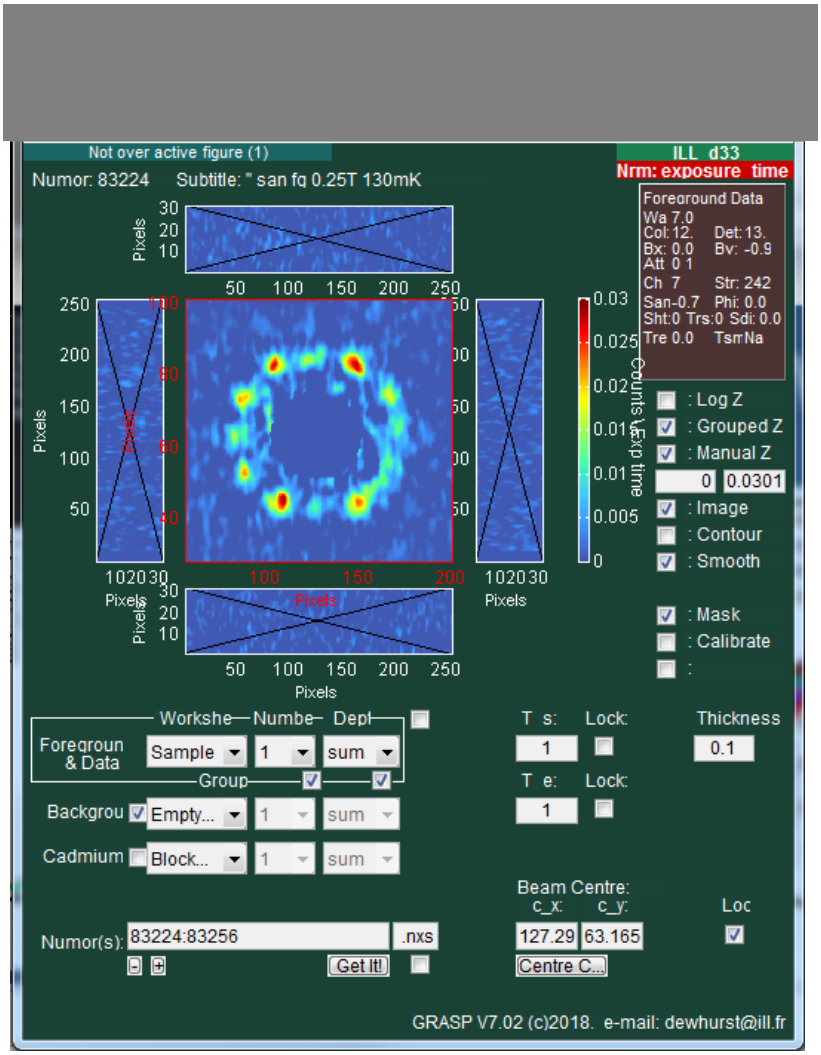

Figure 101: Image of the main user interface (UI) window for GRASP (version 7.02). SANS data is loaded as numors, a number designating a single measurement point in a rocking angle. The first order Bragg spots are visible, with a central mask covering the direct beam noise. The window panels are available for ILL scans for higher q events but are not used in this investigation. A sector box can be chosen over any of the spots for analysis (or any space on the diffraction image), defined by an inner and outer radius and an angular width.

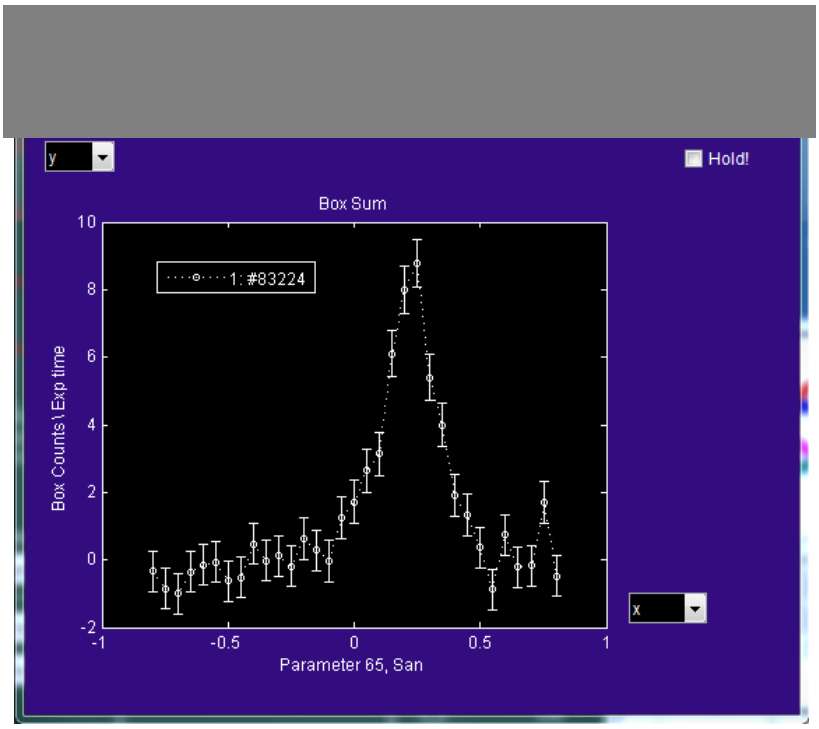

Figure 102: Image of a sans angle (ω) rocking curve output by GRASP. This graph is generated by a parameter analysis over a sector box. The y-axis is measured in total sector box counts per unit of experimental time, in the case of ILL the scan time is unchanged due to the stability of the beam. The x-axis has a direct equivalence with ω, such that zero corresponds to a direct beam straight through the sample.

any effects of the neutrons diffracting from a feature that is not the VL. A direct beam measurement is also taken with a different aperture in the background state in order to centre the scans to the beam. This is important for thermal neutrons used in SANS, at these wavelengths the neutrons are moving slowly enough to be affected by gravity.

The direct beam in all the scans, even with attenuation, provides a lot of noise, this is mitigated by a mask function which can manually screen a part of the diffraction image allowing the colour scale of the diffraction pattern to be adjusted in its absence, for clarity. In this case a 20 pixel diameter mask centred on the direct beam is masked out in Figure 101. A smooth function can also be applied to the diffraction image. The smooth function is an applied Gaussian envelope from 1x1 pixels up to 5x5 pixels. The image in Figure 101 uses a 2x2 pixel Gaussian envelope, this setting for smoothing is used for the majority of the analysis presented in this

work. The use of a smooth function on the image improves the presentation and clarity of the diffraction image but does not actually influence the statistical analysis of the data, it is a visual tool only.

To acquire the rocking curve seen in Figure 102, a sector box is selected over the image area of a spot. The sector box is defined by an inner and outer radius and an angular width. To generate the rocking curve the pixel counts are summed for each angle of the rocking curve within the selected box, generating an angular dependent intensity curve for that sector box. In order to obtain the raw integrated intensity for the rocking curve, one must fit the rocking curve with a suitable function and integrated for the area between the curve and the background. For a strong, clear signal a Lorentzian is desirable but for all of the scans presented here a Gaussian was primarily used as it gave smaller errors in fitting, especially where signals were comparatively weak.

The integrated intensity can then be used to find the form factor of the VL by rearranging equation 104, which we will give again here for clarity:

$$I(q) = 2\pi V \lambda_n^2 \phi_n \left(\frac{\gamma}{4}\right)^2 \frac{|F(q)|^2}{\Phi_0^2 q \cos\zeta}. \tag{120}$$

Once again $I(q)$ is the integrated intensity, V is the volume of the sample, λ_n is the neutron wavelength, ϕ_n is the incident neutron beam flux, γ is the gyromagnetic ratio of a neutron (≈ 2), $|F(q)|$ is the form factor, Φ_0 is the flux quantum, q is the magnitude of the reciprocal lattice vector and ζ is the Lorentz angle. The Lorentz angle is a correction for the reciprocal lattice vector if the spot position being analysed does not align with the normal of the rocking axis. If the spot being analysed is not perpendicular to the normal of the rocking axis then Ewald sphere does not cut through this reciprocal spot directly; the correction angle accounts for this. This angle can be determined by finding the centre of a spot with a Gaussian fit for it's angular position relative to the direct beam centre and the $x-y$

coordinates of the diffraction image. The Lorentz angle is then that made between the spot position and the normal of the rocking axis. GRASP can give the χ angular position of a spot relative to the direct beam as (0,0) coordinates and the x-y axes passing through this. The y-axis is taken as $\chi = 0°$.

8.2 Appendix B: Suitably modelling the integrated intensity, form factor and penetration depth

The bulk of the analysis conducted for the $TlNi_2Se_2$ and $(Ba_{0.5}K_{0.5})Fe_2As_2$ results to ascertain a pairing symmetry for the Cooper pairs was the use of a null hypothesis approach combined with the Prozorov *et al.* [92] framework and least-squares power-law fits. For clarity we will redress the equations used in this process. The process for obtaining a fit for the penetration depth and a representation of what the pairing symmetry likely is begins with the Christen formula,

$$I(q) = 2\pi V \lambda_n^2 \phi_n \left(\frac{\gamma}{4}\right)^2 \frac{|F(q,T)|^2}{\Phi_0^2 q \cos\zeta} \tag{121}$$

with the data from GRASP providing the raw integrated intensity data. This equation rearranged provides the previously defined form factor $F(q)$,

$$|F(q,T)| = \frac{4\Phi_0}{\lambda_n \gamma} \sqrt{\frac{I(q) q \cos\zeta}{2\pi V \phi_n}} \tag{122}$$

which can also be described by the following,

$$F(q,T) = \frac{B e^{-c\xi(T)^2 q^2}}{1 + q^2 \lambda(T)^2}. \tag{123}$$

Once we have values for the form factor from the Christen formula, we rearrange equation 121 to solve for the penetration depth as follows

$$\lambda(T) = \frac{1}{q}\sqrt{\frac{Be^{-c\xi(T)^2q^2}}{F(q,T)} - 1}. \tag{124}$$

It is at this point that a judgement should be made regarding the core correction factor: $e^{-c\xi^2q^2}$. If enough detail is known about the coherence length, $\xi(T)$ and how it varies with temperature and the material is very strongly Type-II ($\kappa \gg \sqrt{2}$) then the core size does not conform well to the London assumption of δ-like (infinitesimally small width). This will make the inclusion of the core-correction exponent necessary as the existence of finite flux cores means interactions will not be confined locally to the core, there will be non-local interactions between the inside and outside of the core over the distance ξ_0. However, if this is included then one may decide on either using ξ_0 (with the assumption that ξ only varies near $T \to T_c$) or $\xi(T)$ and a guess or fit for the value of c. This is a correction term that is material specific, with examples for KFe_2As_2 being fitted at $c = 0.52$ [109, 12] and $c = 0.44$ for $YBa_2Cu_3O_{7-x}$ [96, 120]. This term is difficult to fit without a great deal of data available or a similar material from which to base this value. In the case of $(Ba_{0.5}K_{0.5})Fe_2As_2$, the value of $c = 0.52$ from the related compound KFe_2As_2 is used. However, $TlNi_2Se_2$ is very new and as such there is no previous SANS studies or VL studies with which to base this value. Given that we approximated $\kappa \approx 7.5$, and we only have an initial calculation of ξ_0 from the heat capacity results in [48] but no temperature variation data, the exponent would simply be a constant multiplying factor of value < 1. With the null hypothesis an exponent of constant value will be multiplied out for $I(q,T)/(I(q,0))$, for example. Thus we may set the exponent for the case of $TlNi_2Se_2$ to be ≈ 1 for the majority of the analysis.

Following from the calculation of the penetration depth, this data can be fitted

with a least-squares approach for the penetration depth equation defined previously:

$$\lambda(T) = \frac{\lambda_0}{\sqrt{1 - \left(\frac{T}{T_c}\right)^p}} \tag{125}$$

where the fitting procedure requires guesses for the variable parameters λ_0, T_c and p. If the data has large errors or a great deal of variance then it is prudent to switch to a fixed value of T_c, as this is usually well known, and allow only λ_0 and p to vary. Once a fit is given, with reasonable uncertainties on the parameters, the value of p can be compared to the Prozorov framework directly. This provides an initial analysis based on the penetration depth calculations, however the more powerful comparison of the integrated intensity and form factor to modelled behaviours is provided by substituting the equation for $\lambda(T)$, with fixed values of $p = 2$ for s-wave and $p = 4/3$ for nodal/d-wave, back into the equations for $F(q)$ and $I(q)$. By doing this and normalising the models to a unitless ratio of $f(x)/max(f(x)) \approx f(x)/f(0)$ alongside a similar procedure for the data we can look at how the data varies with T accordingly alongside the models. This has proved to be a powerful method of analysis, especially in the case of $TlNi_2Se_2$ where there has not been previous similar studies of the VL.

8.3 Appendix C: Numerical method for modelling the gap function

A complementary method of establishing the pairing mechanism in a material is to directly find the gap function itself with respect to temperature. However, this is very difficult, with much of the framework relying on equations that are approximations or not analytically solvable. Presented in this appendix is a potential numerical approach to finding and fitting the gap function from available form factor data. This method has limitations however, and as such was not used as part of

the main argument for defining the pairing symmetry in the materials in this work. The work presented in this appendix only attempts to fit the gap function for the $TlNi_2Se_2$ data.

It is possible to establish a connection between the superfluid density ratio and the gap function. To do so we must calculate the ideal model for a given pairing mechanism by calculating the parameter which best represents the gap structure, which is the gap function itself. The temperature dependent gap function is outlined by Gross-Alltag [95] and White *et al.* [96] in a simplified form to be

$$\Delta(T) = \Delta_0 \tanh\left(\frac{\pi k_B T_c}{\Delta_0}\sqrt{a\left(\frac{T_c}{T}-1\right)}\right), \tag{126}$$

where Δ_0 is the gap function at $T = 0$, k_B is the Boltzmann constant, T_c is the critical temperature and a is a unitless coefficient that alongside Δ_0 is indicative of the pairing mechanism. In the case of a, the following values are used: s-wave, $a = 1$; two-dimensional d-wave, $a = 4/3$; nodal s-wave [97], $a = 2$ and non-monotonic d-wave [98], $a = 0.38$. Similarly for Δ_0 we can apply pairing mechanism variations with the following: s-wave; $\Delta_0 = 1.76k_BT_c$ [10], d-wave; $\Delta_0 = 2.14k_BT_c$ and nodal s-wave; $\Delta_0 = 2.77k_BT_c$ [92]. By setting the values for these two parameters and applying the known value of $T_c = 3.7$ K a function for the gap with respect to temperature, for the relevant temperature range, can be generated. A major drawback of this equation is it is not analytically solvable for Δ_0 and so a ratio of $\Delta(T)/\Delta_0$ cannot be obtained as a normalised starting point for a fit.

Getting the gap function from the superfluid density requires the same framework as equation 126 using the process outlined in [95] and more clearly in [96]. We define the following relationship

$$\rho_s(T) = 1 - \frac{1}{4\pi k_B T} \times \int_0^{2\pi}\int_0^{\infty} \cosh^{-2}\left(\frac{\sqrt{\epsilon^2+\Delta_k^2(T,\phi)}}{2k_BT}\right) d\phi d\epsilon. \tag{127}$$

where $\sqrt{\epsilon^2+\Delta_k^2(T,\phi)}$ is the excitation spectrum, $\Delta_k(T,\phi) = \Delta(T)\Delta_k(\phi)$ such that

$\Delta(T)$ is the BCS gap function that can be modelled by the empirical formula in equation 126 and $\Delta(\phi)$ is the angular gap function. The angular gap function is unitless but describes the azimuthal angular variation of the cylindrical Fermi surface. For a completely cylindrical Fermi surface, $0 < \phi < 2\pi$ describes the rotation about the azimuthal angle, but for unconventional or nodal superconductors the cross-section of the Fermi surface is no-longer a perfect circle to make a cylindrical Fermi surface with. Thus $\Delta(\phi)$ is heavily dependent on the pairing mechanism in the material.

As equation 127 is not analytically solvable for Δ and requires a numerical approach we must construct a numerical method for solving the gap function. We have already established $\rho_s(T)$ with equation 117, and so must insert the values for the energy ϵ with a large range, with respect to the size of the increment that ϵ will count with in order to simulate the integral from zero to infinity. An array of values for $\Delta(T)$ is guessed and inserted into equation 127 for each step in temperature, such that a set of values for the gap is tried for each single value of T and $\rho(T)$. The values of ρ as a function of Δ are then plotted against the value of ρ for that temperature with error lines as limiting bounds for values of Δ that satisfy the numerical analysis. It is then a case of determining the intercept of the two as shown in Figure 103. A drawback of this method is analysis of low-T gap functions. The gradient of the fitting function for this process is very shallow around the intercept with ρ, practically zero gradient upon crossing the $\rho(T)$ line. Consequently, the number of values that can satisfy this intercept reasonably is very broad with a large error associated with any value chosen from this procedure in this temperature regime. As such the temperature range is approximately half of the full set.

In order to have a robust numerical solution in this case, functions for $\Delta(\phi)$ also need to be taken into account. These are typically broken down into 2-D pairing mechanism functions for the variation in the polar or azimuthal axis in the Fermi surface. For a BCS, s-wave interpretation $\Delta(\phi) = 1$. For d-wave pairing the Fermi

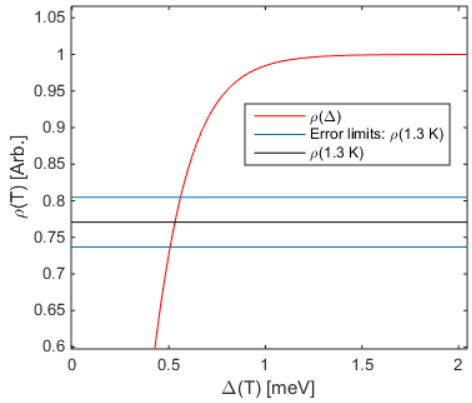

Figure 103: Graph illustrating the numerical process for solving the gap function from the calculated superfluid density. The red line is generated from values of the superfluid density at a single temperature but an array of values for the gap. The black line indicates the calculated value of $\rho(T)$ from the form factor data with the blue lines indicating the error limits from that value. The intercept between the black and red lines traced to the x-axis gives the best numerical guess value for the gap at that temperature. The limits are determined by the same process; by looking at where the red line intercepts the blue lines then extrapolating that to an upper and lower value on the x-axis for the errors on the value of the gap. In the case above, the temperature is 1.3 K. This process must be done for each temperature in the array of values for ρ.

surface becomes more complex and is described by $\Delta(\phi) = \cos(2\phi)$, creating point nodes in the Fermi surface due to the variation in ϕ for a cylindrical Fermi surface. For a nodal s-wave description we introduce the polar angle $0 < \theta < 2\pi$ and use $\Delta(\phi) = (1 - \sin^4(\theta)\cos(4\phi))$ to describe the existence of point and line nodes for a three dimensional case.

The data for the numerical fits is presented in Figure 104. This fit is only an attempt with an s-wave model. The value for T_c comes very close to the measured values (within 2σ), but the fit for $\Delta_0 = 0.53$ meV falls short of the previously calculated $\Delta_0 = 0.6375$ meV by $\approx 10\sigma$. The numerical results produce fairly small errors but are far below expectations of the gap function. This indicates that the s-wave model for gap behaviour is insufficient in describing the gap function from the available data, lending more evidence to the interpretation of a nodal/d-wave model as this necessitates a larger gap function overall.

It is a common problem with this method for the numerical results to break down

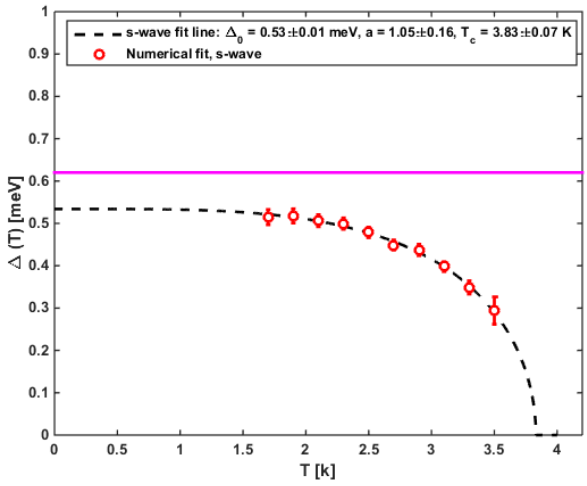

Figure 104: Numerical fitting results for the gap function for each of the three pairing mechanisms. The pink reference line is the value of $\Delta_0 = 2.01 k_B T_c = 0.6375$ meV, determined in [48]. The low temperature values for all of the pairing symmetries are omitted as their errors blow up and the value of the gap drops unphysically due to the nature of the fitting procedure, as previously described. The fit lines are generated by a least squares fit of equation 126 to the data from the numerical fitting procedure.

at low temperature. Consistently we see the errors blow up and the intercept outputs decrease in a manner unsupported by the physics of the gap function. The source of the issue with the outputs, for Figure 103, is due to the fact that at low temperature an intercept between $\rho(\Delta)$ and $\rho(T = x)$ provides a wide range of values that are capable of satisfying this intercept. This is particularly problematic given that at low temperature the values of ρ tend asymptotically towards a constant value for many values of Δ. This is seen in Figure 105, where the upper error bar intercept essentially approaches infinity and at some values the fit line is so close to the value of the superfluid density that an extremely large number of gap values satisfies the numerical fit. In Figure 105 we can easily argue that above the intercept, all the values of the gap essentially satisfy the numerical procedure.

Although fitting the gap function from the superfluid density can be a powerful method of understanding the nature of the superconductivity in this material, this method has limitations for certain temperature ranges and relies in this case on an assumption of a constant value for the coherence length; which is a fair approxima-

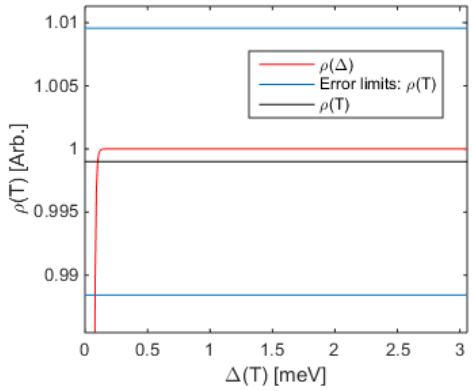

Figure 105: Graph of the numerical fits for ρ at $T = 0.1$ K for an s-wave integral representation of ρ. Here it is clear that the numerical solutions produce many values of Δ that could satisfy the superfluid density, such that the upper error limit on values of $\Delta(T)$ for low temperature approaches infinity.

tion as long as we aren't close to T_c. This method is likely to be somewhat more powerful if more information on the evolution of the coherence length or the gap function itself was available in order to supplement a numerical solution.

So far only an s-wave fit has been presented. Attempts to fit with the unconventional gap structures using polar and/or azimuthal angle variation had other issues for fitting. Using these additions requires nested loops for fitting to account for one or more angles per energy increment. During the course of this work attempts were made to fit the data using unconventional models for d-wave and nodal structures but these had a tendency to produce unphysical features in the fitting and as such did not produce enough data points to make a clear fit for comparison. What we can say is that the s-wave fit highlights that a BCS approach is insufficient in this case, however this approach is not as robust as the null hypothesis and analytical approaches developed and presented earlier in this work.

8.4 Appendix D: Publications

8.4.1 Publications arising from work in this thesis

S. J. Kuhn, H. Kawano-Furukawa, E. Jellyman, R. Riyat, E. M. Forgan, M. Ono *et al.*, *Simultaneous evidence for Pauli paramagnetic effects and multiband superconductivity in KFe_2As_2 by small-angle neutron scattering studies of the vortex lattice*, Phys. Rev. B **93**, 104527 (2016).

E. Jellyman, P. Jefferies, S. Pollard, E. M. Forgan, E. Blackburn, A. T. Holmes, *et al.*, *Unconventional superconductivity in the nickel-chalcogenide superconductor, $TlNi_2Se_2$*, arXiv:1808.03207 [cond-mat.supr-con], 9th August 2018.

E. Jellyman, R. Riyat, A. T. Holmes, E. M. Forgan, E. Blackburn, H. Kawano-Furukawa *et al.*, *High-field studies of the vortex lattice in superconducting $(Ba_{0.5}K_{0.5})Fe_2As_2$ by small-angle neutron scattering*, Pending.

8.4.2 Other publications arising during the thesis period

L. Shen,* E. Jellyman, E. M. Forgan, E. Blackburn, M. Laver, E. Canévet *et al.*, *Unconventional magnetic phase separation in γ-CoV_2O_6*, Phys. Rev. B **96**, 054420 (2017).

L. Shen, O. Zaharko, J. O. Birk, E. Jellyman, Z. He, E. Blackburn, *Magnetic order in the quantum spin chain compound $SrCo_2V_2O_8$: a single-crystal neutron diffraction study in magnetic field*, arXiv:1801.10237 [cond-mat.str-el], 30th January 2018.

R. Riyat, E. Blackburn, E. M. Forgan, y A. S. Cameron, A. T. Holmes, E. Jellyman, *et al.*, *Field-dependent superconducting anisotropy and Pauli paramagnetism in $YBa_2Cu_3O_7$*, Pending.

References

[1] F. London and H. London, *The electromagnetic equations of the supraconductor*, Proc. Roy. Soc. (London) **A149**, 71 (1935)

[2] H. K. Onnes, *The Superconductivity of Mercury*, Comm. Phys. Lab. Univ. Leiden, Nos. 122 and 124 (1911)

[3] W. Meissner and R. Oschenfeld, *Ein neuer Effekt bei eintritt der Supraleitfähigkeit*, Naturwissenschaften **21**, 787 (1933)

[4] H. W. Lewis, Phys. Rev. 102 15081 (1956)

[5] J. Bardeen, *Two-Fluid Model of Superconductivity*, Phys. Rev. Lett. 1, 399 (1958)

[6] B. S. Deaver and W. M. Fairbank, *Experimental Evidence for Quantized Flux in Superconducting Cylinders*, Phys. Rev. Lett. **7**, 43 (1961)

[7] R. Doll and M. Nabäuer, *Experimental Proof of Magnetic Flux Quantization in a Superconducting Ring*, Phys. Rev. Lett. **7**, 51 (1961)

[8] W. A. Little and R. D. Parks, *Observation of Quantum Periodicity in the Transition Temperature of a Superconducting Cylinder*, Phys. Rev. Lett. **9**, 9 (1962)

[9] M. Tinkham, *Effect of Fluxoid Quantization on Transitions of Superconducting Films*, Phys. Rev. **129**, 2413 (1963)

[10] M. Tinkham, *Introduction to Superconductivity*, Dover republication (2004) second edition, ISBN-13: 978-0-486-43503-9

[11] V. G. Kogan, *London approach to anisotropic Type-II superconductors*, Phys. Rev. B **24**, 1572 (1981)

[12] H Kawano-Furukawa, L. DeBeer-Schmitt, H. Kikuchi, A. S. Cameron, A. T. Holmes, R. W. Heslop *et al.*, *Probing the anisotropic vortex lattice in the Fe-based superconductor KFe_2As_2 using small-angle neutron scattering*, Phys. Rev. B **88**, 134524 (2013)

[13] L. J. Campbell, M. M. Doria and V. G. Kogan, *Vortex lattice structures in uniaxial superconductors*, Phys. Rev. B **38**, 2439 (1988)

[14] A. B. Pippard, *An experimental and theoretical study of the relation between magnetic field and current in a superconductor*, Proc. Roy. Soc. (London) **A216**, 547 (1953)

[15] T. E. Faber and A. B. Pippard, *The penetration depth and high-frequency resistance of superconducting aluminium*, Proc. Roy. Soc. (London) **A231**, 336 (1955)

[16] V. G. Kogan, A. Gurevich, J. H. Cho, D. C. Johnson, M. Xu, J. R. Thompson *et al.*, *Nonlocal electrodynamics and low-temperature magnetization of clean high-κ superconductors*, Phys. Rev. B **54**, 12386 (1996)

[17] V. G. Kogan, M. Bullock, B. Harmon, P. Miranovic, L. Dobrosavljevic-Grujic, P. L. Gammel *et al.*, *Vortex lattice transitions in borocarbides*, Phys. Rev. B **55**, R8693 (1997)

[18] V. G. Kogan, P. Miranovic, L. Dobrosavljevic-Grujic, W. E. Pickett and D. K. Cristen, *Vortex Lattices in Cubic Superconductors*, Phys. Rev. Lett. **79**, 741 (1997)

[19] G. Eilenberger, *Transformation of Gorkov's equation for Type II superconductors into transport-like equations*, Z. Phys. **214**, 195 (1968)

[20] A. A. Abrikosov, *On the Magnetic Properties of Superconductors of the Second Group*, Soviet Physics JETP **5**, 1174 (1957)

[21] J. B. Ketterson and S. N. Song, *Superconductivity*, Cambridge University Press, 1st edition (1999)

[22] W. H. Kleiner, L. M. Roth and S. H. Autler, *Bulk Solution of Ginzburg-Landau Equations for Type-II Superconductors: Upper Critical Field Region*, Phys. Rev. **133**, A1226 (1964)

[23] E. H. Brandt, *The flux-line lattice in superconductors*, Rep. Prog. Phys. **58**, 345 (1995)

[24] E. M. Forgan, S. J. Levett, P.G. Kealey, R. Cubitt, C. D. Dewhurst, D. Fort *et al.*, *Intrinsic behavior of flux lines in pure niobium near the upper critical field*, Phys. Rev. Lett. **88**, 167003 (2002)

[25] J. R. Clem, *Simple model for the vortex core in a Type II superconductor*, J. Low Temp. Phys. **18**, 427 (1975)

[26] J. Bardeen, L. N. Cooper and J. R. Schrieffer, *Microscopic Theory of Superconductivity*, Phys. Rev. **106**, 162 (1957)

[27] L. N. Cooper, *Bound Electron Pairs in a Degenerate Fermi Gas*, Phys. Rev. **104**, 1189 (1956)

[28] H. Fröhlich, *Theory of the Superconducting State. I. The Ground State at the Absolute Zero of Temperature*, Phys. Rev. **79**, 845 (1950)

[29] L. P. Gor'kov, *On the Energy Spectrum of Superconductors*, Sov. Phys. JETP **7**, 505 (1958)

[30] G. Goll, *Unconventional Superconductors: Experimental Investigation of the Order-Parameter Symmetry*, Springer Tracts in Modern Physics, Vol. 214 (2006)

[31] H. Aoki, T. Sakakibara, H. Shishido, R. Settai, Y. Onuki, P. Miranovic *et al.*, *Field-angle dependence of the zero-energy density of states in the unconventional*

heavy-fermion superconductor $CeCoIn_5$, J. Phys.: Condens. Matter **16**, L13-L19 (2004)

[32] G.E. Volovik and L.P. Gor'kov, *Superconducting classes in heavy-fermion systems*, Sov. Phys JETP **61**(4), 843 (1985). (Zh. Eksp. Teor. Fiz. **88**, 1412 (1985))

[33] B. S. Chandrasekhar, *A Note on the Maximum Critical Field of High-Field Superconductors*, Appl. Phys. Lett. **1**, 7 (1962)

[34] A. M. Clogston, *Upper Limit for the Critical Field in Hard Superconductors*, Phys. Rev. Lett. **9**, 266 (1962)

[35] I. Askerzade, *Unconventional Superconductors: Anisotropy and Multiband Effects*, Springer Series in Materials Science, Vol. 153 (2012)

[36] N. V. Orlova, A. A. Shanenko, M. V. Milošević, F. M. Peeters, A. V. Vagov, and V. M. Axt, *Ginzburg-Landau theory for multiband superconductors: Microscopic derivation*, Phys. Rev. B **87**, 134510 (2013)

[37] G. L. Squires, *Introduction to the theory of thermal neutron scattering*, Dover Publications (1996)

[38] http://www.psi.ch/sinq/sansi/components (accessed 07/04/2017 at 15:45)

[39] P. P. Ewald, *Introduction to the Dynamical Theory of X-Ray Ditfraetion*, Acta Cryst. A **25**, 103 (1969)

[40] https://www.psi.ch/bsq/spallation-target (accessed 16/07/2018 at 12:05)

[41] https://neutrons.ornl.gov/content/how-sns-works (accessed 16/07/2018 at 12:05)

[42] https://eic.rsc.org/section/feature/research-at-isis/2020219.article (accessed 08/10/2018 at 11:39)

[43] https://www.ill.eu/instruments-support/instruments-groups/instruments/d33/description/layout/ (accessed 07/04/2017 at 15:59)

[44] https://www.ill.eu/users/instruments/ (accessed 08/10/2018 at 12:04)

[45] National Institute of Standards and Technology: Centre for Neutron Research, https://www.ncnr.nist.gov/resources/activation/ (accessed 12/07/2018 at 15:19)

[46] Z. Fisk, H. R. Ott, T. M. Rice and J. L. Smith, *Heavy-electron metals*, Nature 320, 124 (1986)

[47] X. C. Hong, Z. Zhang, S. Y. Zhou, J. Pan, Y. Xu, H. Wang *et al.*, *Multigap nodeless superconductivity in nickel chalcogenide $TlNi_2Se_2$*, Phys. Rev. B 90, 060504 (2014)

[48] H. Wang, C. Dong, Q. Mao, R.Khan, X. Zhou, C. Li *et al.*, *Multiband Superconductivity of Heavy Electrons in a $TlNi_2Se_2$ Single Crystal*, Phys. Rev. Lett. 111, 207001 (2013)

[49] D. A. Wright, J. P. Emerson, B. F. Woodfield, J. E. Gordon, R. A. Fisher, and N. E. Phillips, *Low-Temperature Specific Heat of $YBa_2Cu_3O_{7-\delta}$, $0 \leq \delta \leq 0.2$: Evidence for d-Wave Pairing*, Phys. Rev. Lett. 82, 1550 (1999)

[50] H. D. Yang and J-Y. Lin, J. Phys. Chem. Soc. **62**, Issues 9-10, p. 1861-1870 (2001)

[51] H. P. van der Meulen, Z. Tarnawski, A. de Visser, J. J. M. Franse, J. A. A. J. Perenboom, D. Althof *et al.*, *Specific heat of UPt_3 in magnetic fields up to 24.5 T*, Phys. Rev. B 41, 9352 (1990)

[52] D. Sanchez, A. Junod, J. Muller, H. Berger and F. Lévy, *Specific heat of 2H-$NbSe_2$ in high magnetic fields*, Physica B: Condensed Matter, Vol. **204**, Issues 1-4, p. 167-175 (1995)

[53] J. E. Sonier, M. F. Hundley, J. D. Thompson, and J. W. Brill, *Low Field Anomaly in the Specific Heat of s-Wave Superconductors due to the Expansion of the Vortex Cores*, Phys. Rev. Lett.**82**, 4914 (1999)

[54] J. Lowell and J. B. Sousa, *Mixed-state thermal conductivity of Type-II superconductors*, J. Low Temp. Phys. 3, 65 (1970)

[55] E. Boaknin, M. A. Tanatar, J. Paglione, D. Hawthorn, F. Ronning, R. W. Hill *et al.*, *Heat Conduction in the Vortex State of $NbSe_2$: Evidence for Multiband Superconductivity*, Phys. Rev. Lett. 90, 117003 (2003)

[56] C. Proust, E. Boaknin, R. W. Hill, L. Taillefer, and A. P. Mackenzie, *Heat Transport in a Strongly Overdoped Cuprate: Fermi Liquid and a Pure d-Wave BCS Superconductor*, Phys. Rev. Lett. 89, 147003 (2002)

[57] N. Kurita, F. Ronning, Y. Tokiwa, E. D. Bauer, A. Subedi, D. J. Singh *et al.*, *Low-Temperature Magnetothermal Transport Investigation of a Ni-Based Superconductor $BaNi_2As_2$: Evidence for Fully Gapped Superconductivity*, Phys. Rev. Lett. 102, 147004 (2009)

[58] N. Kurita, F. Ronning, C. F. Miclea, E. D. Bauer, K. Gofryk, J. D. Thompson *et al.*, *Fully gapped superconductivity in $SrNi_2P_2$*, Phys. Rev. B 83, 094527 (2011)

[59] H. M Rosenberg, *The solid state*, Oxford University Press, 3rd edition (2009)

[60] M. J. Graf, S-K. Yip, J. A. Sauls and D. Rainer, *Electronic thermal conductivity and the Wiedemann-Franz law for unconventional superconductors*, Phys. Rev. B 53, 15147 (1996)

[61] A. C. Durst and P. A. Lee, *Impurity-induced quasiparticle transport and universal-limit Wiedemann-Franz violation in d-wave superconductors*, Phys. Rev. B 62 1270 (2000)

[62] D. K. Christen, F. Tasset, S. Spooner, and H. A. Mook, *Study of the intermediate mixed state of niobium by small-angle neutron scattering*, Phys. Rev. B 15, 4506-4509 (1977)

[63] A. Holmes, G. R. Walsh, E. Blackburn, E. M. Forgan and M. Savey-Bennett, *A 17T horizontal field cryomagnet with rapid sample change designed for beamline use* The Review of scientific instruments **83**, 023904 (2012)

[64] F. Pobell, *Matter and Methods and Low Temperatures*, Third, Revised and Expanded Edition, Springer (2007)

[65] *http://www.cresst.de*, accessed at 11:21, 11/04/2018.

[66] J. S. White, *SANS investigations of the flux line lattice in unconventional superconductors*, Thesis, University of Birmingham, October 2009

[67] C. D. Dewhurst *et al.*, *The effects of vortex 'shaking' on lattice perfection in* YNi_2B_2C *and* $Ca_3Rh_4Sn_{13}$, 2006 (Unpublished)

[68] C. Kranenberg, D. Johrendt, A. Mewis, R. Pöttgen, G. Kotzyba, H. Trill, *et al.*, *New compounds of the* $ThCr_2Si_2$*-type and the electronic structure of* CaM_2Ge_2 *(M: Mn - Zn)*, Journal of Solid State Chemistry **167**, 107-112 (2002)

[69] A. Mani, N. Ghosh, S. Paulraj, A. Bharathi and C. S. Sundar, *Pressure-induced superconductivity in* $BaFe_2As_2$ *single crystal*, EPL **87**, 17004 (2009)

[70] O. K. Anderson and L. Boeri, *On the multi-orbital band structure and itinerant magnetism of iron-based superconductors*, Annalen der Physik **523(1-2)**, 8 (2011)

[71] L. van Hove, *The Occurrence of Singularities in the Elastic Frequency Distribution of a Crystal*, Phys. Rev. **89**, 1189-1193 (1953)

[72] D. Fang, X. Shi, Z. Du, P. Richard, H. Yang, X. X. Wu *et al.*, *Observation of a van Hove singularity and implication for strong coupling induced Cooper pairing in KFe_2As_2*, Phys. Rev. B **92**, 144513 (2015)

[73] S. Doniach, and M. Sunjic, *Many-electron singularity in X-ray photoemission and X-ray line spectra from metals*, J. Phys. C **3**, 285 (1970)

[74] K. Okazaki, Y. Ota, Y. Kotani, W. Malaeb, Y. Ishida, T. Shimojima *et al.*, *Octet-line node structure of superconducting order parameter in KFe_2As_2*, Science **337**, 1314-1317 (2012)

[75] M. Rotter, M. Pangerl, M. Tegel and D. Johrendt, *Superconductivity and Crystal Structures of $(Ba_{1-x}K_x)Fe_2As_2$ $(x = 0-1)$*, Angew. Chem., Int. Ed. **47**, 7949 (2008)

[76] J. P. Hu and H. Ding, *Local antiferromagnetic exchange and collaborative Fermi surface as key ingredients of high temperature superconductors*, Scientific Reports **2**, 381 (2012)

[77] K. Seo, B. A. Bernevig, and J. P. Hu, *Pairing Symmetry in a Two-Orbital Exchange Coupling Model of Oxypnictides*, Phys. Rev. Lett. **101**, 206404 (2008)

[78] H. Ding, K. Nakayama, P. Richard, S. Souma, T. Sato, T. Takahashi *et al.*, *Electronic structure of optimally doped pnictide Ba0.6K0.4Fe2As2: a comprehensive angle-resolved photoemission spectroscopy investigation*, J. Phys.: Condens. Matter **23**, 135701 (2011)

[79] I. M. Lifshitz, *Anomalies of Electron Characteristics of a Metal in the High Pressure Region*, Sov. Phys. JETP **11**, p. 1130-1135 (1960)

[80] J. K. Dong, S. Y. Zhou, T. Y. Guan, H. Zhang, Y. F. Dai, X. Qiu *et al.*, *Quantum Criticality and Nodal Superconductivity in the FeAs-Based Superconductor KFe_2As_2*, Phys. Rev. Lett. **104**, 087005 (2010)

[81] J.-Ph. Reid, M. A. Tanatar, A. Juneau-Fecteau, R. T. Gordon, S. René de Cotret, N. Doiron-Leyraud *et al.*, *Universal Heat Conduction in the Iron Arsenide Superconductor KFe_2As_2: Evidence of a d-Wave State*, Phys. Rev. Lett. **109**, 087001 (2012)

[82] N. Xu, P. Richard, X. Shi, A. van Roekeghem, T. Qiam, E. Razzoli *et al.*, *Possible nodal superconducting gap and Lifshitz transition in heavily hole-doped $Ba_{0.1}K_{0.9}Fe_2As_2$*, Phys. Rev. B **88**, 220508(R) (2013)

[83] N. Xu, C. E. Matt, P. Richard, A. van Roekeghem, S. Biermann, X. Shi *et al.*, *Camelback-shaped band reconciles heavy-electron behavior with weak electronic Coulomb correlations in superconducting $TlNi_2Se_2$*, Phys. Rev. B **92**, 081116(R) (2015)

[84] N. Xu, P. Richard, A. van Roekeghem, P. Zhang, H. Miao, W.-L. Zhang *et al.*, *Electronic Band Structure of $BaCo_2As_2$: A Fully Doped Ferropnictide Analog with Reduced Electronic Correlations*, Phys. Rev. X **3**, 011006 (2013)

[85] M. Abdel-Hafiez, S. Aswartham, S. Wurmehl, V. Grinenko, C. Hess, S.-L. Drechsler *et al.*, *Specific heat and upper critical fields in KFe_2As_2 single crystals*, Phys. Rev. B **85**, 134533 (2012)

[86] S. J. Kuhn, H. Kawano-Furukawa, E. Jellyman, R. Riyat, E. M. Forgan, M. Ono *et al.*, *Simultaneous evidence for Pauli paramagnetic effects and multiband superconductivity in KFe_2As_2 by small-angle neutron scattering studies of the vortex lattice*, Phys. Rev. B **93**, 104527 (2016)

[87] F. F. Tafti, A. Juneau-Fecteau, M-È. Delage, S. René de Cotret, J-Ph. Reid, A. F. Wang *et al.*, *Sudden reversal in the pressure dependence of Tc in the iron-based superconductor KFe_2As_2*, Nature Phys. **9**, p. 349-352 (2013)

[88] T. Terashima, N. Kurita, M. Kimata, M. Tomita, S. Tsuchiya, M. Imai, *et al.*, *Fermi surface in KFe_2As_2 determined via de Haas–van Alphen oscillation measurements*, Phys. Rev. B **87**, 224512 (2013)

[89] A. D. Bianchi, M. Kenzelmann, L. DeBeer-Schmitt, J. S. White, E. M. Forgan, J. Mesot *et al.*, *Superconducting Vortices in $CeCoIn_5$: Toward the Pauli-Limiting Field*, Science **319**, 5860, pp. 177-180 (2008)

[90] P. Burger, F. Hardy, D. Aoki, A. E. Böhmer, R. Eder, R. Heid *et al.*, *Strong Pauli-limiting behavior of H_{c_2} and uniaxial pressure dependencies in KFe_2As_2*, Phys. Rev. B 88, 014517 (2013)

[91] D. A. Zocco, K. Grube, F. Eilers, T. Wolf, and H. v. Löhneysen, *Pauli-Limited Multiband Superconductivity in KFe_2As_2*, Phys. Rev. Lett. 111, 057007 (2013)

[92] R. Prozorov and R. W. Gianetta, *Magnetic penetration depth in unconventional superconductors*, Supercond. Sci. Technol. **19**, R41 (2006)

[93] J. Mao, D. H. Wu, J. L. Peng, R. L. Greene and S. M. Anlage, *Electronic band structure of the superconductor Sr_2RuO_4*, Phys. Rev. B **51**, 3316 (1995)

[94] H. W. Lewis, *Two-Fluid Model of an "Energy-Gap" Superconductor*, Phys. Rev. 102 15081 (1956)

[95] F. Gross-Alltag, B. S. Chandrasekhar, D. Einzel, K. Andres, P. J. Hirschfeld, H. R. Ott *et al.*, *Anomalous temperature dependence of the magnetic field penetration depth in superconducting uranium-beryllium (UBe_13)*, Zeitschrift fuer Physik B: Condensed Matter **64**, 175-88 (1986)

[96] J. S. White, R. W. Heslop, A. T. Holmes, E. M. Forgan, V. Hinkov, N. Egetenmeyer *et al.*, *Magnetic-field-induced nonlocal effects on the vortex interactions in twin-free $YBa_2Cu_3O_7$*, Phys. Rev. B **84**, 104519 (2011)

[97] H. Won, H. Jang, D. Parker, S. Haas and K. Maki, *Panorama of Nodal Superconductors*, arXiv:cond-mat/0405099v1 [cond-mat.supr-con], 5 May 2004

[98] H. Matsui, K. Terashima, T. Sato, T. Takahashi, M. Fujita and K. Yamada, *Direct Observation of a Nonmonotonic $d_{x^2-y^2}$-Wave Superconducting Gap in the Electron-Doped High-T_c Superconductor $Pr_{0.89}LaCe_{0.11}CuO_4$*, Phys. Rev. Lett. **95**, 017003 (2005)

[99] K. Izawa, K. KAmata, Y. Nakajima, Y. Matsuda, T. Watanabe, M. Nohara *et al.*, *Gap Function with Point Nodes in Borocarbide Superconductor YNi_2B_2C*, Phys. Rev. Lett. **89**, 137006

[100] K. Maki, P. Thalmeier and H. Won, *Anisotropic s-wave superconductivity in borocarbides $LuNi_2B_2C$ and YNi_2B_2C*, Phys. Rev. B **65**, 140502(R) (2002)

[101] M. H. S. Amin, I. Affleck and M. Franz, *Effective "Penetration Depth" in the Vortex State of a D-Wave Superconductor*, Phys. Rev. B **58**, 5848 (1998)

[102] M. H. S. Amin, M. Franz and I. Affleck, *Low-temperature behavior of the vortex lattice in unconventional superconductors*, Phys. Rev. Lett. **84**, 5864 (2000)

[103] https://www.helmholtz-berlin.de/pubbin/igama_output?modus=einzel&gid=1939&sprache=en, Accessed at 12:23, 30/04/18

[104] O. Prokhnenko, P. Smeibidl, W-D. Stein, M. Bartkowiak and N. Stüsser, Journal of large-scale research facilities **3**, A115 (2017)

[105] J. Taylor, O. Arnold, J. Bilheaux, A. Buts, S. Campbell, M. Doucet, et al. *Mantid, A high performance framework for reduction and analysis of neutron scattering data*, Bulletin of the American Physical Society 57 (2012)

[106] T. M. Michels-Clark, A. T. Savici, V. E. Lynch, X. P. Wang and C. M. Hoffmann, J. Appl. Cryst. **49**, 497-506 (2016)

[107] Mantid (2013): Manipulation and Analysis Toolkit for Instrument Data.; Mantid Project. http://dx.doi.org/10.5286/SOFTWARE/MANTID

[108] O. Arnold, J. C. Bilheux, J. M. Borreguero, A. Buts, S. I. Campbell, L. Chapon *et al.*, Physics Research Section A **764**, pp 156-166 (2014)

[109] H. Kawano-Furukawa, C. J. Bowell, J. S. White, R. W. Heslop, A. S. Cameron, E. M. Forgan *et al.*, *Gap in KFe_2As_2 studied by small-angle neutron scattering observations of the magnetic vortex lattice*, Phys Rev. B **84**, 024507 (2011)

[110] Y. Kamihara, T. Watanabe, M. Hirano, and H. Hosono, *Iron-Based Layered Superconductor $La[O_{1-x}Fx]FeAs$ ($x = 0.05 - 0.12$) with $T_c = 26$ K*

[111] H. Hosono and K. Kuroki, *Iron-based superconductors: Current status of materials and pairing mechanism*, Physica C: Superconductivity and its Applications **514**, pp. 399-422 (2015)

[112] K. Hashimoto, M. Yamashita, S. Kasahara, Y. Senshu, N. Nakata, S. Tonegawa *et al.*, *Line nodes in the energy gap of superconducting $BaFe_2(As_{1-x}P_x)_2$ single crystals as seen via penetration depth and thermal conductivity*, Phys. Rev. B **81**, 220501(R) (2010)

[113] Y. Nakai, T. Iye, S. Kitagawa, K. Ishida, S. Kasahara, T. Shibauchi *et al.*, *^{31}P and ^{75}As NMR evidence for a residual density of states at zero energy in superconducting $BaFe_2(As_{0.67}P_{0.33})_2$*, Phys. Rev. B **81**, 020503(R) (2010)

[114] S. L. Thiemann, Z. Radovic, and V. G. Kogan, *Field structure of vortex lattices in uniaxial superconductors*, Phys. Rev. B **39**, 11406 (1989)

[115] Y. Amano, M. Ishihara, M. Ichioka, N. Nakai, and K. Machida, *Eilenberger and London theories for transverse components of flux line lattice form factors in uniaxial superconductors*, Phys. Rev. B **90**, 144514 (2014)

[116] P. G. Kealey, D. Charalambous, E. M. Forgan, S. L. Lee, S. T. Johnson, P. Schleger *et al.*, *Transverse-field components of the flux-line lattice in the anisotropic superconductor* $YBa_2Cu_3O_{7-\delta}$, Phys. Rev. B **64**, 174501 (2001)

[117] C. Rastovski, C. D. Dewhurst, W. J. Gannon, D. C. Peets, H. Takatsu, Y. Maeno *et al.*, *Anisotropy of the Superconducting State in* Sr_2RuO_4, Phys. Rev. Lett. **111**, 087003 (2013)

[118] L. DeBeer-Schmitt, M. R. Eskildsen, M. Ichioka, K. Machida, N. Jenkins, C. D. Dewhurst *et al.*, *Pauli Paramagnetic Effects on Vortices in Superconducting* $TmNi_2B_2C$, Phys. Rev. Lett. **99**, 167001 (2007)

[119] M. Ichioka and K. Machida, *Vortex states in superconductors with strong Pauli-paramagnetic effect*, Phys. Rev. B **76**, 064502 (2007)

[120] J. S. White, P. Das, M. R. Eskildsen, L. DeBeer-Schmitt, E. M. Forgan, A. D. Bianchi *et al.*, *Observations of Pauli paramagnetic effects on the flux line lattice in* $CeCoIn_5$, New J. Phys. **12**, 023026 (2010)

[121] Y. Amano, M. Ishihara, M. Ichioka, N. Nakai, and K. Machida, *Pauli paramagnetic effects on mixed-state properties in a strongly anisotropic superconductor: Application to* Sr_2RuO_4, Phys. Rev. B **91**, 144513 (2015)

[122] R. Cubitt, M. R. Eskildsen, C. D. Dewhurst, J. Jun, S. M. Kazakov, and J. Karpinski, *Effects of Two-Band Superconductivity on the Flux-Line Lattice in Magnesium Diboride*, Phys. Rev. Lett. **91**, 047002 (2003)

[123] M. R. Eskildsen, E. M. Forgan and H. Kawano-Furukawa, *Vortex structures, penetration depth and pairing in iron-based superconductors studied by small-angle neutron scattering*, Rep. Prog. Phys. **74**, 124504 (2011)

[124] M. R. Eskildsen, *Vortex lattices in Type-II superconductors studied by small-angle neutron scattering*, Front. Phys. **6**(4), p. 398-409 (2011)

[125] S. Demerdiş, C. J. van der Beek, S. Mühlbauer, Y. Su and Th. Wolf, *SANS study of vortex lattice structural transition in optimally doped* $(Ba_{1-x}K_x)Fe_2As_2$, J. Phys.: Condensed Matter **28**, 42 (2016)

[126] H. Q. Yuan, J. Singleton, F. F. Balakirev, S. A. Baily, G. F. Chen, J. L. Luo *et al.*, *Nearly isotropic superconductivity in* $(Ba,K)Fe_2As_2$, Nature **457**, 07676 (2009)

[127] K. Kihou, T. Saito, S. Ishida, M. Nakajima, Y. Tomioka, H. Fukazawa *et al.*, J. Phys. Soc. Jpn. **79**, 124713 (2010)

[128] K. Kihou, T. Saito, K. Fujita, S. Ishida, M. Nakajima, K. Horigane *et al.*, J. Phys. Soc. Jpn. **85**, 034718 (2016)

[129] T. Terashima, M. Kimata, H. Satsukawa, A. Harada, K. Hazama, S. Uji *et al.*, *Resistivity and Upper Critical Field in* KFe_2As_2 *Single Crystals*, J. Phys. Soc. Jpn. **78**, 063702 (2009)

[130] C. Fang, Y.-L. Wu, R. Thomale, B. A. Bernevig, and J.-P. Hu, *Robustness of s-Wave Pairing in Electron-Overdoped* $A_{1-y}Fe_{2-x}Se_2$ *(A = K, Cs)*, Phys. Rev. X **1**, 011009 (2011)

[131] Y. Zhou, D.-H. Xu, F.-C. Zhang and W.-Q. Chen, *Theory for superconductivity in* $(Tl,K)Fe_xSe_2$ *as a doped Mott insulator*, Europhys. Lett. **95**, 17003 (2011)

[132] J.-P. Hu and N.-N. Hao, S_4 *Symmetric Microscopic Model for Iron-Based Superconductors*, Phys. Rev. X **2**, 021009 (2012)

[133] J. R. Neilson, A. Llobet, A. V. Stier, L. Wu, J. Wen, J Tao *et al.*, *Mixed-valence-driven heavy-fermion behavior and superconductivity in* KNi_2Se_2, Phys. Rev. B **86**, 054512 (2012)

[134] S. K. Goh, H. C. Chang, P. Reiss, P. L. Alireza, Y. W. Cheung, S. Y. Lau *et al.*, *Anomalous pressure dependence of the superconducting transition temperature in* $TlNi_2Se_{2-x}S_x$, Phys Rev. B **90**, 201105(R) (2014)